The Dissertation Committee for Marcel Peter Bergmann
certifies that this is the approved version of the following dissertation:

Galaxy Evolution: The Relationship Between Structure, Star Formation, and Environment

Committee:

Gary Hill, Supervisor

J. Craig Wheeler, Supervisor

Inger Jørgensen

Karl Gebhardt

Chris Sneden

Ralf Bender

Galaxy Evolution: The Relationship Between Structure, Star Formation, and Environment

by

Marcel Peter Bergmann, B.S., M.A.

DISSERTATION
Presented to the Faculty of the Graduate School of
The University of Texas at Austin
in Partial Fulfillment
of the Requirements
for the Degree of

DOCTOR OF PHILOSOPHY

THE UNIVERSITY OF TEXAS AT AUSTIN
December 2002

Dedicated to Peter, Margot, Marianne, and Ernest Bergmann
who taught me the equal importance of hard work and
creativity in science, and in life.

Acknowledgments

I enjoyed my time during grad school, and have many people to thank. First and foremost, I am deeply grateful to my advisors Inger Jørgensen and Gary Hill for mentoring me in the ways of research and the forging of a scientific career. Their never-wavering support was invaluable as I struggled through the process of writing papers and this dissertation. I would also like to thank Craig Wheeler, my faculty supervisor, for many good suggestions regarding writing and the job hunt. Karl Gebhardt, though not formally one of my supervisors, has been a great teacher and collaborator since his arrival in Texas two years ago. I look forward to many years of continued collaboration with all of these great scientists.

I also discovered during graduate school that I am a social person, and rely greatly on social interaction with others to maintain my spirit and sanity. I hesitate to list names, for fear of forgetting someone, but I desperately want to express my appreciation to my fellow students, including Andy, Greg, Travis, Inese, Luke, Peter, Dave, Steve, Osamu, Claudia, Eva, Katelyn, the many postdocs (Don and Russel, especially), and friends from outside the department. Thanks to Tom, for being a great friend, and keeping my belly full of barbecue and margaritas (and maui sunshine). Thanks to Jaime for everything! And thanks to the staff of the Crown and Anchor for (almost) always remembering my name.

I would be nothing without the love and support of my parents, Marianne

and Ernest, and my two sisters, Dominique and Gabrielle. Thanks most especially to the four of you, for always being there, always understanding, and for doing everything within your power to help me to succeed.

Galaxy Evolution: The Relationship Between Structure, Star Formation, and Environment

Publication No. ____________________

Marcel Peter Bergmann, Ph.D.
The University of Texas at Austin, 2002

Supervisors: Gary Hill
J. Craig Wheeler

I have conducted two separate observational tests of the current theoretical paradigm for galaxy formation and evolution, hierarchical galaxy formation in a Cold Dark Matter dominated universe. The first project is a spectroscopic study of nineteen low surface brightness galaxies observed with the 9.2m Hobby-Eberly Telescope. I determine redshifts to all the galaxies, and report both emission line and absorption line index strengths, where appropriate. Correlations are found between the gas-phase metallicity indicators and the stellar indices which are sensitive to both metallicity and age. I interpret the star formation and chemical evolutionary histories of these galaxies using a combination of simple stellar population models and nebular emission models. The correlations observed between emission and absorption measurements place strong constraints on possible star formation histories. We find that low surface brightness galaxies are a diverse class, with properties as broad as those exhibited by the full range of high surface brightness galaxies.

The second project is a study of the ages in early-type field galaxies, and a comparison with the ages found for a sample of cluster galaxies. I present preliminary results and interpretations based on new stellar population modelling methods. The new model explicitly accounts for age, metallicity, and α–abundance ratios for the stellar population, by making predictions for low resolution line indices. I measure the ages, metallicities, and α–abundance as a function of radius, from the center of each galaxy to beyond one effective radius. The gradients are consistent with younger, more metal rich stellar populations in the centers of most of the galaxies, but a constant α–abundance ratio within any one galaxy.

I have generated an all-sky catalog which measures the local density of galaxies around every galaxy at cz$<$10,000 km s^{-1}. This facilitates the creation of low redshift field galaxy samples for follow-up study, in particular to study the effects of environment on galaxy evolution. I attempt to quantify the effects on the catalog of the varying spectroscopic survey completeness across the sky, and compare my local density measures with published field galaxy samples. The full catalog (42,024 galaxies, with $\sim$ 50 parameters per galaxy) is included in the electronic version of this dissertation.

Table of Contents

List of Tables

List of Figures

Chapter 1

Introduction and Overview

The formation and evolution of galaxies remains an open question. The processes involved no doubt include gravitational collapse, star formation, gas depletion, energy feedback through stellar winds and supernovae, chemical enrichment, galaxy merging and long range gravitational interactions. The relative importance of these processes, however, is still poorly constrained. The observational attack on this problem has taken a multi-faceted approach, each with its own strengths and weaknesses. Early theory on the formation process broke into two camps: monolithic collapse (top-down) and heirarchical merging (bottom-up). Observers have attempted to differentiate between these two possibilities both by detailed studies of galaxies in the local universe, and by more gross studies of galaxy properties as a function of look-back time (redshift or distance). The most detailed studies are done wholly within our Galaxy, using the overall metallicities and relative metal-abundance ratios of stars, combined with some knowledge of their spatial distribution and kinematics, to describe the formation of the Milky Way, and its constituent bulge, disk, and halo. This understanding is then applied to other (predominantly spiral) galaxies. The high-resolution spectroscopic techniques used within the Milky Way can only be extended to the nearest of neighboring galaxies. Instead, analysis is made of the integrated light from galaxies, studying both the stellar and gaseous component. The loss of resolution, both spatial due to the greater distances to these galaxies, and spectral due to the fainter apparent brightness passing through spectrograph entrance slits, is reflected by a loss of detailed information in the data. Of course, creative observers work very hard to limit these losses (e.g. through adaptive optics studies of globular cluster systems, or high resolution spectroscopy of quasar absorption line systems), but nonetheless they remain. When studying galaxies outside the Local Group, we talk about stellar populations, not single stars, and these populations are characterized with only a few parameters for an entire galaxy: the ”age”, the ”metallicity”, the ”alpha-abundance”, the ”star-formation timescale”. At best, one or two dimensional gradients of these parameters are derived. Similarly for the gaseous constituent of the galaxies, ”temperature” and ”metallicity” are derived for HII regions or globally for all the gaseous emission smeared together. Motions of the stars and gas are measured and quantified as rotation, dispersion, and in some cases higher order moments of the velocity distribution. While it is ideal to have a full two-dimensional spatial map of the kinematic structure of galaxies, this is a rare feat; sometimes measurements will be done along a one-dimensional axis, but most frequently the measurements are done through a single centralized aperture. Nevertheless, strong correlations are seen between some of the ”global” stellar and gas parameters and the kinematic measures of the galaxies, such as in the Fundamental Plane, the Mg-σ relation, and the Tully-Fisher relation. The presence of these tight correlations proves that there is information to be gleaned about the formation and evolution of galaxies, even from these gross, global measurements.

The formation and evolution of galaxies occurs in the time domain, and there is good reason to believe that if we can look back in time, we might be able to piece together just how galaxies form and evolve. Typically, this is done by studying objects at greater and greater distances, which, due to the finite speed of light, is equivalent to studying objects at earlier and earlier times in the history of the Universe. In this way, we cannot see how an individual galaxy has evolved, but we can see how the population as a whole has changed, and from this infer the mechanisms of that evolution. A study of the change in slope and zeropoint of the aforementioned galaxy correlations is an effective first step to the time-domain methodology. Even though individual measurements of high redshift galaxy parameters are difficult due to their faintness, it is much easier to quantify evolution in the galaxy population through evolution in the correlations. This assumes, of course, that we understand the physical processes which drive the correlations. There is another, perhaps less obvious way to study galaxies in the time domain, and this was hinted at in the discussion of the Milky Way above. The build-up of metals in the gas and stars of a galaxy might be a surrogate clock; furthermore, the timescale to mix together disparate parts of a galaxy is a function of radius from the center of the galaxy. A detailed study of individual galaxies, taking into account the distribution of metals, the ages of the stars, and the dynamical timescales relevant to each part of the galaxy, may be able to rank the relative importance of mergers and secular evolution within different classes of galaxies.

The current trend of belief in the monolithic collapse versus hierarchical galaxy formation dichotomy is leaning towards the hierarchical merging picture.

This is driven as much, if not more, by cosmological arguments and measurements of the cosmic microwave background anisotropy power-spectrum than by detailed studies of galaxy evolution. There are still crucial observational tests that can be made, and must be satisfactorily explained by the models. These tests include a prediction of the number and size of the largest coherent structures present at any given time in the evolution universe, e.g. superclusters of galaxies at the current epoch, or very massive galaxies at higher redshift. The models should also explain the cause of differences in galaxy structure and morphology, and must be able to explain, for instance, the morphology-density relation of galaxies, and what causes the dichotomy between high surface brightess and low surface brightness galaxies at the same total mass.

This thesis includes observational studies of several aspects of the galaxy formation/evolution puzzle. Given the available instrumentation, I have chosen to study objects in the (relatively) nearby universe but with more spatial or spectral detail that was previously possible. Chapter 2, entitled, ”Spectroscopy of Low Surface Brightness Galaxies with the Hobby-Eberly Telescope,” presents observations of 19 low surface brightness galaxies which span a variety of colors, sizes, and absolute magnitudes. These observations serve to clear up some misconceptions about whether or not LSB galaxies follow the Tully-Fisher relation. They also hint at a very wide range of evolutionary histories, comparable to those of high surface brightness galaxies. There are not yet sufficient models to explain the origins of these galaxies. Chapter 4, entitled, ”Accurate Ages of Early-Type Field Galaxies,” uses the latest stellar population models to compare the distribution of ages in early-type field galaxies with the distribution of ages in cluster galaxies, another prediction of the hierarchical clustering models. Internal gradients of age, metallicity, and alpha-enhancement are also measured for these galaxies; the presence of these gradients must be explained within the context of hierarchichal galaxy merger formation models. Chapter 3 is provided as a reference for future work. I derive the local density of spectroscopically catalogued galaxies around every galaxy with cz$<$10,000 km s^{-1}. Additionally, I estimate the completeness of both spectroscopic and photometric galaxy catalogs over the whole sky, which provides correction factors for the derived local galaxy densities. These new measurements are combined for each galaxy with the various published parameters in the LEDA database, into a machine readable/searchable database. This will facilitate the extraction of isolated and cluster galaxy samples for further study.

Chapter 2

Spectroscopy of Low Surface Brightness Galaxies with the Hobby-Eberly Telescope

2.1 Introduction

The class of low surface brightness (LSB) galaxies is a diverse one. LSB galaxies exhibit a range of absolute magnitudes, colors, and morphologies comparable to those of high surface brightness (HSB) galaxies. The defining characteristic of LSB galaxies is, of course, their faint central surface brightness, variously defined as being at least one magnitude fainter than the cannonical Freeman (1970) value of 21.65 B mag/$\square''$, or fainter than 23 B mag/$\square''$; the precise limit varies from investigator to investigator. However, whether the low surface brightness results from a common evolutionary history for these galaxies remains unknown.

Studies of LSB galaxies fall into two broad classes. The first class comprises the surveys to find LSB galaxies, and attempts to quantify what fraction of the total galaxy number density, luminosity density, and mass density are made up by them. The second class comprises studies of the internal structure of LSB galaxies, including investigations into their gas content, star formation history, and evolutionary processes.

The large area surveys which were initially mined for LSB galaxies were photographic surveys, including the Upsala Galaxy Catalog (UGC; Nilson, 1973), the POSS-2 survey (Schombert & Bothun, 1988; Schombert et al., 1992), and the APM survey (Impey et al., 1996). In the past decade, large area CCD surveys have also found a significant population of LSB galaxies. Notable among these are the drift scan survey of Dalcanton et al. (1997), who use well quantified automated detection methods, and the multicolor survey of O'Neil, Bothun, & Cornell (1997, hereafter OBC97) and O'Neil et al. (1997b, hereafter OBSCI97), which turned up a previously unseen population of red LSB galaxies.

These surveys proved the existence of LSB galaxies as more than the occasional oddity. Dalcanton et al. (1997) make a conservative estimate of the number density of LSB galaxies of $N = 0.01^{+0.006}_{-0.005}$ galaxies $h^3_{50}\mathrm{Mpc}^{-3}$, equal to the number density of HSB galaxies. However, the Dalcanton et al. survey suffers from small number statistics, with only 7 LSBs detected. McGaugh, Bothun, & Schombert (1995) have a larger sample, and come to a similar conclusion about the LSB galaxy number density. More recently, de Jong & Lacey (2000) have used a photographic survey of $\simeq 1000$ Sb-Sdm galaxies to calculate the bivariate luminosity and number density of galaxies as a function of both surface brightness and scale length. They find that while the luminosity density is dominated by HSB galaxies (peaked at $\mu_B(0) \simeq 21.0$ mag/$\square''$), the number density of galaxies has an essentially flat distribution at all surface brightnesses fainter than $\mu_B(0) \simeq 21.0$ mag/$\square''$, and therefore LSB galaxies make up a significant fraction of the total number of galaxies (See also the surveys of O'Neil & Bothun (2000) and Cross & Driver (2002)).

The best studied LSB disk galaxies are those in the thesis sample of de Blok

(1997), originally selected from the photographic survey catalogs of Schombert et al. (1992) and the UGC catalog. Observations of these ~ 20 galaxies include multicolor optical surface photometry (de Blok, van der Hulst, & Bothun, 1995), VLA mapping of the HI distribution and kinematics (de Blok, McGaugh, & van der Hulst, 1996; de Blok & McGaugh, 1997), and spectroscopy of the HII regions (de Blok & van der Hulst, 1998). The general picture obtained from these observations is that LSB galaxies are metal poor and gas rich, with a range of sizes (scale lengths) comparable to HSB galaxies, but with much lower surface densities. However, note that de Blok's selection criteria included an existing HI detection. The kinematics, and therefore the gravitational potentials, are dominated by dark matter at all radii (de Blok & McGaugh, 1997; McGaugh, Rubin, & de Blok, 2001), and the low global star formation rates (SFR) are the combined result of both the low surface density, and the low metallicity (Gerritsen & de Blok, 1999).

Sprayberry, Impey, Bothun, & Irwin (1995) obtained photometry, low-resolution optical spectroscopy, and HI spectroscopy for a sample of 8 giant LSB galaxies. Their optical spectroscopic data pertain primarily to the bulges of these galaxies, and they find no difference between the bulges of large LSB and HSB galaxies.

The wide field CCD survey of OBC97 found a large number of LSB galaxies, covering a wider range of colors than those found by previous photographic surveys. In particular, red LSB galaxies with $(\mathrm{B}-\mathrm{V}) > 0.9$, colors consistent with purely old stellar populations, were catalogued for the first time. The follow-up single dish HI observations using the Arecibo 305m single-dish radio telescope (O'Neil, Bothun, & Schombert, 2000a) suggested that many of these red LSBs (and some of the blue LSBs) were quite peculiar indeed, having gas mass-to-light ratios (M/L) in excess of 8, with a few higher than 30. Further, the rotational line widths were far larger than would be expected from their luminosities given the standard Tully-Fisher (1977) relation for spiral galaxies.

Larger scatter in the Tully-Fisher relation among LSB galaxies was also measured by Burkholder, Impey, & Sprayberry (2001). Their survey of over 250 HSB and LSB galaxies selected from the APM survey (Impey et al., 1996) included photometry, HI spectroscopy, and low resolution optical spectroscopy (Impey, Burkholder, & Sprayberry, 2001; Burkholder, Impey, & Sprayberry, 2001). They used emission line ratios to measure the metallicity for 49 HSB and 17 LSB galaxies (where they define $\mu_B = 22 \mathrm{mag}/\square''$as the dividing line) and found there to be a roughly 50% overlap in the metallicity range of the two groups.

Bell et al. (2000) combined optical and near-infrared surface photometry to study the stellar populations in subsets of both the de Blok sample and the red galaxies from the OBSCI97 survey. Broadband optical studies of stellar populations suffer from a degeneracy in color space between age and metallicity; red colors could indicate either older stars or more metal-rich stars, while bluer colors indicate either younger stars or metal-poor stars. The inclusion of near-infrared colors partially breaks this degeneracy, essentially giving a handle on the fractional light contribution from old stars which dominate the light in the near-infrared, and younger stars which will dominate at bluer wavelengths. Bell et al. found that the bluer galaxies from the de Blok sample were younger than similar HSB late-type galaxies. Further, the five red LSB galaxies in their study were a mixture of two types: genuinely red galaxies with old stellar populations, but central surface brightnesses on the bright end of the LSB range ($\sim$ 22.5mag/$\Box''$ in B), and a group of objects with lower surface brightness whose true colors, after correcting for galactic extinction, were in fact as blue as the de Blok sample galaxies and had similar stellar mean ages. Interestingly, the three red galaxies with old stellar populations were not detected in the O'Neil et al. (2000a) HI survey, while the two galaxies with blue extinction corrected colors were detected. However, none of the red galaxies with extreme M_{HI}/L ratios were studied by Bell et al.

We have obtained spectra for a sample of 19 red and blue LSB galaxies chosen from the catalog of OBC97, with the intent of studying the star formation histories of these galaxies. Using a combination of emission and absorption line measures, we compare the chemical enrichment of the stars and gas, and we use the stellar population models of Vazdekis (1999, 2000[1], hereafter V1999 and V2000, respectively) to interpret these data quantitatively. In particular, we attempt to determine whether a single LSB galaxy formation model can be reconciled with the various observational attributes of these galaxies.

This chapter is organized as follows. In Section 2.2 we present the sample, the spectroscopic and photometric observations, and the data reduction. Sections 2.3 through 2.8 presents the LSB spectra, analysis of the emission line and absorption index strengths, and comparison to HSB galaxies. We discuss these results in the context of LSB formation models in Section 2.9. Finally, we summarize our

---

[1] `http://www.iac.es/galeria/vazdekis/MODELS_2000/out_li_BI`

conclusions in Section 2.10.

2.2 Observations, & Data Reduction

2.2.1 Sample selection for the spectroscopic observations

This project began during the early science operations of the Hobby-Eberly Telescope (HET; Ramsey et al., 1998) in 1999 November and observations continued through 2001 January. For the first set of spectroscopic observations, during winter 1999-2000, we chose a group of LSB galaxies from the sample of OBC97 which covered a range of color ($0.3 < \mathrm{B}-\mathrm{V} < 1.35$) and central surface brightness ($22.0 < \mu_B(0) < 24.0$). Twelve galaxies were observed during the first observing period. A new sample of six galaxies was chosen for observation during winter 2000-2001. These objects were selected from the HI follow-up survey of O'Neil et al. (2000a), and stand out due to their extremely high $\mathrm{M_{HI}/L_B}$, and that they lie more than 5 σ from the I-band Tully-Fisher relation (Tully & Fisher, 1977; Pierce & Tully, 1988). Additionally, one galaxy ([OBC97]P06-1[2]) was chosen because it is the first LSB (albeit a giant LSB) galaxy for which CO has been detected (O'Neil, Hofner, & Schinnerer, 2000b; see also Matthews & Gao, 2001). These seven galaxies fall into the same range of color and central surface brightness as the original sample. We obtained spectra for a total of 19 galaxies. Table 2.1 lists the galaxies in our spectroscopic sample, along with positions and relevant data from the literature.

---

[2] The official (IAU) names for the LSB galaxies in this work originated in OBC97, and are listed in full in Table 2.1. For convenience, however, we will use abbreviated galaxy names without [OBC97] for the remainder of this paper.

TABLE 2.1

LITERATURE DATA FOR GALAXIES IN SPECTROSCOPIC SAMPLE[a]

galaxy (1)	RA (J2000) (2)	Dec (J2000) (3)	cz (HI) (km s^{-1}) (4)	r_e (”) (5)	B(5”)[b] (mag) (6)	I_c(5”)[b] (mag) (7)	B_{tot}[b] (mag) (8)	I_{ctot}[b] (mag) (9)	$\mu_B(0)_{cor}$[b] (mag/□″) (10)	i[c] (deg) (11)	E(B-V) (12)
[OBC97]P1-3	23:21:18	08:14:28	3746	7.1	18.28	16.70	17.15	15.81	22.2	45	0.071
[OBC97]P6-1	23:23:33	08:37:25	10882	18.9	19.55	16.79	17.23	15.04	24.2	66	0.061
[OBC97]P9-4	23:18:40	07:30:44	4205	10.9	20.84	18.23	18.86	16.29	25.0	67	0.144
[OBC97]C1-2	08:19:55	20:51:43	8531	5.2	18.99	16.91	18.10	15.84	22.5	21	0.049
[OBC97]C1-4	08:19:24	21:00:12	···	12.6	18.09	15.80	16.55	14.48	22.3	63	0.050
[OBC97]C3-2	08:22:36	20:59:46	···	6.0[d]	18.17	16.06±0.06	16.34	14.14	22.8	47	0.038
[OBC97]C4-1	08:24:33	21:27:04	7905	11.0[d]	18.97	···	17.83	···	23.6	39	0.044
[OBC97]C4-5	08:25:48	21:52:45	···	5.6	18.96	···	18.23	···	23.0	57	0.046
[OBC97]C5-3	08:27:44	22:28:52	12942	8.6	20.12	18.31±0.1	18.88	16.37	24.0	20	0.041
[OBC97]C5-5	08:27:12	22:53:39	5524	23.0	19.90±0.2	18.60±0.2	18.08±0.2	16.19±0.2	24.3	45	0.038
[OBC97]C6-1	08:27:31	21:30:03	4322	6.5	18.57	16.22±0.06	17.53	15.27	22.5	44	0.041
[OBC97]C8-3	08:17:17	21:39:12	3570	4.8	19.22	···	17.69	···	24.3	72	0.039
[OBC97]N3-1	12:32:59	07:29:26	···	8.6	19.05	···	18.02	···	23.5	64	0.023
[OBC97]N9-1	10:20:18	27:45:10	···	7.6	18.41	19.18±1	17.29	17.60±1	22.3	41	0.036
[OBC97]N9-2	10:20:22	28:07:56	7746	6.4	19.80	20.59±0.06	18.89	17.49	24.0	47	0.037
[OBC97]N10-2	11:58:42	20:34:43	···	10.8	18.03	16.22±0.06	16.57	14.85	22.8	52	0.023
[OBC97]N10-4	11:58:52	20:58:28	7478	9.6	19.94	···	18.90	···	24.2	31	0.027
[OBC97]U1-4	11:38:25	17:05:14	3450	32.5	19.00	17.26±0.06	13.08	12.21	23.3	55	0.025
[OBC97]U1-8	11:39:23	16:50:31	···	10.3	19.30	16.55±0.06	18.15	15.65	24.1	70	0.025

[a] Columns (1)-(3) give the names and positions from O’Neil et al. (2000a), and the redshifts of their HI detections are listed in column (4). The exponential scale lengths measured by OBC97 have been converted to half light radii using the formula $r_e = 1.68\alpha$ (Sparks, 1988), and these are listed in column (5). Columns (6)-(7) list the B-band and I-band magnitudes inside apertures of radius 5″, and the corresponding total magnitudes are given in columns (8)-(9) (OBC97, OBSCI97). The inclination corrected B band central surface brightnesses are given in column (10), and the inclinations are in column (11), both from OBC97. Column (12) lists the galactic extinction derived from the Schlegel et al. (1998) dust maps.

[b] Unless otherwise noted, the typical intrinsic uncertainty on the photometry is reported to be ±0.05 mag for the aperture magnitudes, and ±0.1 mag for the total magnitudes and $\mu_B(0)_{cor}$. The uncertainty in the photometric zeropoints are 0.03 mag in the B-band, and 0.04 mag in the I-band (OBC97, OBSCI97).

[c] The intrinsic uncertainty on the inclination angle is ±5° (OBC97).

[d] Not measured by OBC97. We use this value for spectral extraction to optimize the signal-to-noise ratio. (see Sect. 2.2.3.3).

2.2.2 Photometry

2.2.2.1 Observations & Basic Reductions

We obtained new photometry for a subset of the LSB galaxies in the spectroscopic sample, using the Prime Focus Camera (PFC; Claver, 1995) on the McDonald Observatory 0.8m telescope in November and December of 1999. The PFC is a wide-field imager, with a $45' \times 45'$ field of view. The wide-field images include eleven of the nineteen galaxies in the spectroscopic sample, as well as sixteen galaxies from the OBC97 catalog not included in our spectroscopic observations. The instrumental configuration is given in Table 2.2. Images were taken through the B, R_c, and I_c filters, centered on the OBC97 survey fields C1, C3, C4, C5, N9, and U1. Multiple images were taken in each band to aid in cosmic ray rejection. Additionally, we took images of 10 fields containing a total of 217 standard stars included in Landolt (1992) to facilitate photometric calibration of the data. For each field observed, table 2.3 lists the position of the field center, the total integration time and number of exposures through each filter, and the image quality of the coadded data, described in terms of the FWHM and ellipticity of the PSF as determined from gaussian fits to radial profiles of more than 100 stars per image.

TABLE 2.2
INSTRUMENTATION

	Spectroscopy	Photometry
Telescope	Hobby-Eberly Telescope (9.2m)	McDonald Observatory 0.8m
Instrument	Low Resolution Spectrograph	Prime Focus Camera
Dates	10/99-2/01	11/99-12/99
CCD	Ford Aerospace 3072 × 1024 (binned 2 × 2)	Loral-Fairchild 2048 × 2048
Gain	1.82e^-/ADU	1.6 e^-/ADU
RON	7.0 e^-	5.87e^-
Pixel size spatial	$0.465''$	$1.354''$
Wavelength Range	4300Å - 7240 Å	B, R_c, I_c
Slit Width × Length	$2'' \times 4'$	···
Grism	600 l/mm	···
Dispersion	2Å/pix	···
Resolution(σ)	3.3Å (190 km s^{-1} @ 5200Å)	···

TABLE 2.3

PFC PHOTOMETRY OBSERVATIONS

Field[a]	Filter	Exposure Time[b]	N_{obs}[c]	$FWHM_{PSF}$[d]	ε_{PSF}[e]	N_{PSF}[f]
C1	B	300	1	2.8	0.12	176
(08:19:52.6 +21:00:17)	R_c	180	1	2.7	0.13	111
	I_c	120	1	2.4	0.12	101
C3	B	1500	3	3.0	0.08	229
(08:22:46.6 +21:03:34)	R_c	780	3	2.7	0.06	176
	I_c	600	3	3.0	0.04	127
C4	B	2100	4	2.8	0.05	508
(08:26:01.3 +21:57:06)	R_c	1380	5	2.8	0.04	201
	I_c	600	3	3.0	0.06	109
C5	B	2100	4	3.1	0.10	180
(08:26:54.1 +22:35:23)	R_c	1080	4	3.0	0.04	126
	I_c	600	3	3.1	0.07	145
N9	B	2100	4	3.2	0.07	264
(10:20:29.3 +27:55:29)	R_c	780	3	2.8	0.07	141
	I_c	600	3	3.0	0.05	118
U1	B	1200	2	3.8	0.04	147
(11:39:29.1 +17:04:21)	R_c	1200	4	3.2	0.03	101
	I_c	720	3	3.5	0.06	145

[a] First row of each entry is the field name from OBC97. Second row lists the coordinates (J2000) of the field center.

[b] Total exposure time for all observations, in seconds.

[c] Number of individual exposures.

[d] Mean full-width at half-maximum of a gaussian fit to the point-spread-function (PSF), measured in arcsec.

[e] Mean measured ellipticity of the PSF.

[f] Number of stars used in determination of FWHM and ε.

Data reduction was done within the IRAF[3] environment. The images were overscan and bias subtracted, then a shutter correction was applied. Next, the images were divided by a normalized dome flatfield, as well as a normalized illumination correction. The illumination correction is a highly clipped average of all science frames observed at low airmass, in the absence of clouds or moonlight, and corrects large scale gradients not reproduced by the dome flatfield image. After this step, the science images were individually examined for residual real gradients caused by scattered moonlight, clouds, or sky illumination (see Chromey & Hasselbacher, 1996). Any residual gradients larger than 1% across the full image were fit using `imsurfit` and subtracted off, with the mean sky level then added back in as a constant to maintain counting statistics.

Prior to coaddition, a badpixel mask was generated for each image by taking the standard mask file for the CCD, and manually adding all the pixels affected by satellite trails or by ghost images caused by reflections within the PFC optics. The coaddition process was done using the task `imcoadd` (Jørgensen, in prep.) in the Gemini IRAF package. This task determines spatial offsets between all the input images, shifts them accordingly, generates cosmic ray masks, and averages all the good pixel values to produce a coadded output image. The photometric zeropoint offsets between all the input images and the output image were determined. As long as at least one input image was taken during photometric conditions, the coadded output can then be easily calibrated onto a standard system. Finally, we used the

---

[3] IRAF is distributed by the National Optical Astronomy Observatories, which are operated by the Association of Universities for Research in Astronomy, Inc., under cooperative agreement with the National Science Foundation.

HST guide star catalog reference frame to establish the world coordinate system (WCS) for the coadded images.

2.2.2.2 Object Extraction & Standard Photometry

Object extraction was done using SExtractor (version 2.1.6; Bertin & Arnouts 1996), and the output catalogs were matched using the WCS positions to produce a single table with photometry in all three bands (B, R_c, I_c) for each object.

To calibrate the photometry onto a standard system, we used observations of the Landolt (1992) selected area fields SA92, SA95, SA98, SA101, SA104, and SA113, as well as the fields near the standards PG0918+029, PG0231+051, PG1633+091, and PG0233+051. Observations were made each photometric night, interspersing science and standard fields. In total, we have 380 stellar observations in each of the three bands, covering 217 different stars. The standard fields were observed over a range of airmasses spanning from 1 to 3, to better constrain the extinction coefficients. In contrast, the science fields were all observed in the airmass range 1 to 1.25. Average extinction coefficients covering all three photometric nights were used in the standard calibration. The rms scatter of the final standard calibration of the photometric zeropoints was 0.06 mag (B), 0.05 mag (R_c), and 0.05 mag(I_c).

There were no observations of field U1 taken during photometric conditions. To calibrate this field, we used the $\sim$ 1000 stars in our observation in common with the USNO-A2.0 catalog (Monet et al., 1998). We derived relations between the SExtractor “best” magnitudes and the USNO magnitudes for both the U1 and N9 fields, and used the zeropoint offset between these two relations to calibrate the photometry for the U1 field to the standard system. The USNO magnitudes do not have to be on a standard system to make this technique work, merely be internally consistent. The extra uncertainty contributed by this calibration is 0.02 mag, smaller than our zeropoint uncertainty as derived using SExtractor.

We applied galactic extinction corrections to our photometry based on reddening values derived from the Schlegel et al. (1998) dust maps, and the coefficients derived by them for extinction in each band versus color excess (e.g. $A_B/E(B-V) = 4.315$, $A_V/E(B-V) = 3.315$, $A_{R_c}/E(B-V) = 2.673$, $A_{I_c}/E(B-V) = 1.940$). Table 2.4 lists the extinction corrected magnitudes for the 27 galaxies in the OBC97 sample that are included in our observations with the PFC. Also listed are the E(B-V) values used to determine the extinction correction in each band.

Table 2.4

New Photometry from PFC Observations[a]

Name	$B(5'')$	$R_c(5'')$	$I_c(5'')$	B_{tot}	$R_{c,tot}$	$I_{c,tot}$	E(B-V)
C1-1	17.95±0.03	16.31±0.01	15.70±0.01	17.05±0.05	15.59±0.02	15.12±0.02	0.051
C1-2	18.66±0.06	17.26±0.03	16.80±0.04	17.79±0.08	16.57±0.04	15.97±0.06	0.049
C1-4	17.45±0.02	16.01±0.01	15.44±0.01	16.35±0.03	14.89±0.01	14.32±0.02	0.050
C1-6	17.53±0.02	16.48±0.01	15.99±0.02	16.57±0.03	15.49±0.02	15.07±0.03	0.051
C3-1	18.26±0.01	16.63±0.01	16.02±0.01	17.21±0.02	15.84±0.01	15.30±0.01	0.034
C3-2	17.60±0.01	16.24±0.00	15.65±0.00	16.38±0.01	15.02±0.01	14.39±0.01	0.038
C3-6	17.81±0.01	16.60±0.01	16.06±0.01	16.62±0.01	15.42±0.01	14.88±0.01	0.049
C4-1	18.58±0.03	18.00±0.03	17.67±0.03	17.71±0.05	17.08±0.04	16.61±0.05	0.044
C4-2	19.05±0.05	18.32±0.04	17.84±0.04	17.50±0.06	16.62±0.04	16.09±0.04	0.047
C4-3	18.46±0.03	17.67±0.02	17.22±0.02	17.33±0.04	16.55±0.03	16.07±0.03	0.048
C4-5	18.62±0.03	17.50±0.01	16.99±0.04	18.05±0.03	16.85±0.02	16.36±0.06	0.046
C4-6	17.65±0.01	16.23±0.00	15.97±0.02	17.47±0.01	15.41±0.00	15.92±0.01	0.050
C4-7	19.63±0.06	18.73±0.03	18.40±0.16	19.13±0.06	18.08±0.04	17.85±0.15	0.044
C4-8	19.11±0.05	17.92±0.03	17.45±0.03	18.29±0.07	16.98±0.05	16.58±0.04	0.049
C5-1	17.95±0.01	17.12±0.01	16.72±0.01	17.62±0.01	16.82±0.01	16.43±0.02	0.043
C5-2	18.91±0.02	17.68±0.01	17.13±0.02	18.26±0.02	17.09±0.02	16.56±0.02	0.045
C5-3	19.63±0.04	18.94±0.04	18.53±0.06	19.01±0.05	18.43±0.04	18.02±0.06	0.041
C5-4	18.14±0.01	16.76±0.01	16.22±0.01	17.23±0.01	16.01±0.01	15.57±0.01	0.040
C5-5	19.28±0.03	18.56±0.03	18.24±0.05	17.91±0.03	17.12±0.03	16.70±0.05	0.038
N9-1	18.01±0.01	17.14±0.01	16.76±0.01	17.19±0.01	16.40±0.01	16.09±0.02	0.036
N9-2	20.32±0.07	19.13±0.06	18.46±0.06	20.13±0.11	19.04±0.07	18.38±0.10	0.037
U1-1[b]	18.17±0.02	16.96±0.01	16.42±0.01	17.09±0.02	15.91±0.01	15.38±0.01	0.023
U1-2[b]	19.19±0.04	17.85±0.01	17.25±0.02	18.66±0.05	17.47±0.02	16.89±0.03	0.025
U1-3[b]	17.96±0.01	16.08±0.00	15.42±0.00	16.90±0.02	14.96±0.01	14.33±0.01	0.026
U1-4[b]	18.05±0.02	17.09±0.01	16.64±0.01	16.64±0.01	15.81±0.01	15.40±0.01	0.025
U1-6[b]	19.32±0.04	18.37±0.02	17.95±0.03	18.06±0.05	17.08±0.03	16.64±0.05	0.027
U1-8[b]	18.73±0.02	17.05±0.01	16.41±0.01	17.91±0.04	16.47±0.01	15.83±0.01	0.025

[a] The uncertainties included in the table are the intrinsic uncertainties associated with each measurment. Additionally, there is a systematic zeropoint uncertainty of 0.06 mag in the B-band, 0.05 mag in the R_c-band, and 0.05 mag in the I_c-band.

[b] Photometric zeropoints for field U1 were determined relative to field N9. The zeropoint uncertainty for this field is 0.02 mag larger in each band than the other fields. See Section 2.2.2.2 for details.

2.2.2.3 Comparison to literature data

We have compared our photometry with the measurements of OBC97 and OBSCI97 (which were also obtained with the PFC), after applying galactic extinction corrections to their published photometry. Figure 2.1 shows the comparison.

Figures 2.1a and 2.1c show the comparison of the aperture magnitudes in the B-band and I-band, respectively. In the B-band, we find an offset of -0.35 ± 0.04 mag with an rms scatter of 0.19 mag (excluding the two most deviant measurements, N9-2 and C4-2). Offsets are our magnitudes minus OBC97 magnitudes. In the I-band, we find an offset of -0.23 ± 0.08 mag with an rms scatter of 0.34 mag (excluding N9-1 and N9-2). The offsets and the large scatter may be due to the sensitivity of the small apertures used ($5''$) to changes in seeing or image quality. In the interim between when OBC97 obtained their data and the time when we made our observations, the PFC optics were anti-reflection coated and re-aligned, which improved the delivered image quality. In our coadded images, the stellar PSF has a typical FHWM of 2.2 pixels ($2.9''$), with an ellipticity of 0.07. O'Neil has provided some of her images to the NED[1] database, and the typical image quality we measure for these small images is ~ 3 pixels fwhm ($4''$). Poorer image quality will scatter more of the light outside the small $5''$ aperture, resulting in fainter aperture magnitude measurements, consistent with the offsets we see.

OBC97 derive total magnitudes from exponential and King profile fits to the galaxy surface brightness profiles. We compare these to the SExtractor "best" mag-

---

[1] `http://ned.ipac.caltech.edu`

nitudes, which are also a measure of the total magnitude (though systematically too faint by 6%, see Bertin & Arnouts (1996) for details) in Figures 2.1b and 2.1d. The agreement in the B-band is good, except for two outliers, N9-2 and U1-4. Examination of the surface brightness profiles in OBC97 for these two objects shows the profiles to be more complex than could be well fit by a single exponential. Excluding these two points, the offset between the two datasets is 0.06 ± 0.05 mag with an rms scatter of 0.23 mag. In the I-band, the offset is 0.31 ± 0.08 mag with an rms scatter of 0.33 mag.

We have not measured central surface brightness, $\mu(0)$, from our photometry, so we cannot compare to the values in OBC97. However, since they derive total magnitudes based on $\mu(0)$ and the exponential scale length (α, derived over an area with radius typically larger than $12''$), we expect offsets in $\mu(0)$ to be comparable to offsets in the total magnitudes, which are negligible in the B-band.

Figures 2.1e 2.1f show the comparisons of the $(\mathrm{B}-\mathrm{I}_c)$ aperture and total colors, respectively, with the results from OBSCI97. For both the aperture and total colors, we derive a zeropoint offset of -0.15 ± 0.07 mag with an rms scatter of 0.30 mag, when we exclude the two most deviant points (N9-1 and N9-2 for the aperture colors, N9-1 and C5-3 for the total colors). For N9-1 the uncertainty on $(\mathrm{B}-\mathrm{I_c})$ from OBSCI97 is 1 mag. The typical intrinsic uncertainty for our $(\mathrm{B}-\mathrm{I}_c)$ color measurements is 0.05 mag, derived from the SExtractor uncertainties on the individual band magnitudes, added in quadrature. In the following analysis we use our new photometry when available. For the remaining galaxies with spectroscopic observations we use photometry from OBC97. We calibrate the colors from OB-

SCI97 to be consistent with our data by applying an offset of -0.15 mag, and adopt an uncertainty in this calibration of 0.3 mag.

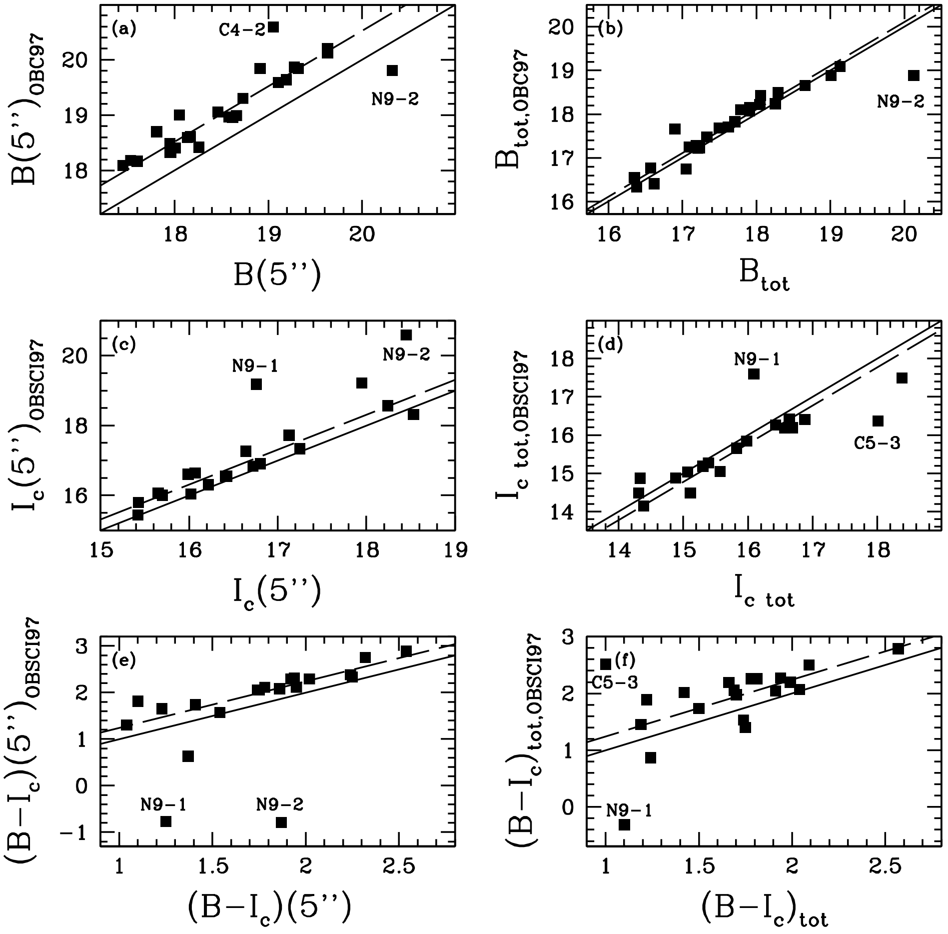

Figure 2.1 Comparison between our photometry and that of OBC97 and OBSCI97. Both datasets have been corrected for galactic extinction. Solid lines denote lines of equality; Dashed lines show the best fit to the zeropoint offset. Typical intrinsic uncertainties for all of the data are less than 0.05 mag, comparable to the size of the boxes. (a) Comparison of B-band magnitudes measured inside apertures of radius 5”. The fit to the zeropoint offset gives $\Delta m_{zero} = -0.52 \pm 0.04$ mag (rms=0.19 mag). The two furthest outliers are labelled and were not included in the fit. (b) Comparison of B-band total magnitudes. The zeropoint offset is $\Delta m_{zero} = -0.11 \pm 0.04$ mag (rms=0.21 mag), excluding the two outliers N9-2 and U1-4 (off the plot). The complex surface brightness profiles of these two galaxies were not well fit by OBC97 using single exponential disk fits. (c) Comparison of I-band 5” radius aperture magnitudes. Excluding N9-1 and N9-2, the mean zeropoint offset is $\Delta m_{zero} = -0.31 \pm 0.08$ mag (rms=0.34 mag). (d) The I-band total magnitude comparison. Excluding N9-1, C5-3, and U1-4 (off the plot) gives a best-fit zeropoint offset of $\Delta m_{zero} = 0.23 \pm 0.08$ mag (rms = 0.33 mag). (e) Comparison of (B$-$I$_c$) aperture colors. We derive a zeropoint offset of $\Delta(\mathrm{B}-\mathrm{I_c})(5'') = -0.24 \pm 0.07$ mag (rms=0.29 mag). The two labelled outliers were not included in the fit. (f) Comparison of the total (B$-$I$_c$) colors. The zeropoint offset is the same as for the aperture colors: $\Delta(\mathrm{B}-\mathrm{I_c})(5'') = -0.24 \pm 0.07$ mag (rms=0.30 mag), excluding the two labelled points.

2.2.3 Spectroscopy

2.2.3.1 Spectroscopic observations

Spectroscopy was obtained using the Marcario Low Resolution Spectrograph (LRS; Hill et al. 1998) on the 9.2m HET. Table 2.2 details the instrumental setup. The weather ranged from photometric to some cirrus. Typical image quality was $\sim$2.6$''$ FWHM during the 1999-2000 season, and $\sim$2.3$''$ FWHM during the 2000-2001 winter, measured on images taken before the spectrum was observed. Additionally, the shape of the point spread function (PSF) was much more regular and symmetric during the second season, as a result of image quality improvements made to the telescope. The only major instrumental change between the two observing seasons was an upgrade of the CCD controller electronics from “version 1” in 1999-2000 to “version 2” in 2000-2001. The version 2 controller provides a much more stable bias and overscan level, faster readout, and lower readout noise.

The typical exposure time was 30 minutes, and multiple observations were made for most of the galaxies to increase the signal-to-noise ratio (S/N) and aid in cosmic ray rejection. Table 2.5 details the spectroscopic observations.

TABLE 2.5

HET SPECTROSCOPIC OBSERVATIONS

Name	Exposure Time[a]	N_{obs}[b]	PA slit[c]	Dates of observations
P1-3	1195	1	46	Nov 30, 2000
P6-1	4200	3	45	Dec 21,22(×2), 2000
P9-4	3600	2	41	Nov 23,24, 2000
C1-2	2014	2	-66	Dec 10, 1999(×2)
C1-4	5160	3	-67	Nov 11, 1999(×2);Mar 11, 2000
C3-2	3300	2	-67	Nov 10, 1999; Dec 7, 1999
C4-1	2770	2	-67, 67	Nov 21, 2000; Jan 26, 2001
C4-5	3750	2	-67, 68	Nov 12, 1999; Mar 6, 2000
C5-3	6700	4	-68, 67	Nov 14, 1999; Dec 14,17, 1999; Mar 13, 2000
C5-5	1666	1	-69	Nov 30, 2000
C6-1	1200	1	-67	Nov 24, 2000
C8-3	4800	4	-67, 67	Dec 22, 2000(×2); Jan 27, 2001(×2)
N3-1	3300	2	-49, 47	Dec 10, 1999; Mar 12, 2000
N9-1	3600	2	-75	Nov 13, 1999; Dec 8, 1999
N9-2	5200	3	-76, 76	Dec 13, 1999; Mar 3, 2000
N10-2	3600	2	-66	Dec 6, 1999; Dec 7, 1999
N10-4	5280	3	-66, 66	Dec 11, 1999; Mar 12,13, 2000
U1-4	3600	2	-62	Dec 13,14, 1999
U1-8	1800	2	-60	Dec 8,10, 1999
NGC 3872	900	1	-59	Dec 7, 1999
UGC 3844	600	1	-82	Dec 7, 1999
NGC 1569	600	1	8	Nov 10, 2000

[a] Total exposure time for all observations, in seconds

[b] Number of individual exposures

[c] Measured in degrees North through East; always parallactic

In total we observed 19 LSB galaxies, two HSB elliptical galaxies (NGC 3872 and UGC 3844) and one HSB post-starburst irregular galaxy (NGC 1569). The HSB observations provide comparisons of old and young stellar populations, respectively. We also observed a K giant star (HD 12402) to use as cross-correlation template for the old stellar populations.

2.2.3.2 Basic reductions of spectroscopic observations

The spectral data reduction was done using IRAF. The observations spanned about 2.5 years beginning with early science operations of the HET, continuing through the telescope and instrument shake-down periods, and into normal operations. Consequently, we will go into some detail about the basic data reductions, and steps taken to find and correct systematic effects which might be present in the data. Readers not interested in the detailed steps of the basic reduction may skip ahead to Section 2.2.3.3. The steps of the basic data reduction are as follows:

1) bias and overscan subtraction
2) dark subtraction
3) flatfielding
4) cosmic ray cleaning
5) wavelength calibration and rectification
6) sky subtraction

The dispersion axis in the LRS runs along rows. The version 1 CCD controller electronics, in use from 1999 October - 2000 March, had a variable overscan level, depending on the flux hitting the CCD. If there were rows with high flux such as the spectroscopic trace for bright objects, then the overscan level for those rows would be depressed. Consequently, for bright traces, the overscan had to be subtracted row by row. For faint traces, or uniform illuminations such as with the flatfields, the overscan level was a smooth function of row number, and we subtracted a fit to the overscan, rather than doing it row by row. The version 2 controller produces a very stable overscan level, which is a constant for all rows regardless of the illumination.

Mean bias frames were produced each month by combining all bias (zero exposure time) images taken on nights when science data was obtained. These images were overscan subtracted, then averaged together, with sigma clipping to eliminate cosmic rays. The coadded bias image was then fit with a low-order surface, and this fit was subtracted from all the science data for that month. The mean of the fit was about 1.4 ADU. Month to month variations were 0.1 ADU.

Flatfield correction was done using lamp flats to correct small scale pixel-to-pixel variations, and using twilight spectra to correct for the slit illumination in the spatial dimension. Mean lamp flats were derived for each night, and checked against each other for variations, which were negligible. While fringing is evident redward of $\sim$7000 Å, it is not seen to vary in the flats over the course of a month. There is some variation between months, caused by shifts in the slit position with respect to the image field center, and the corresponding wavelength range hitting the CCD. The lamp flats taken for each month were combined into a single master flat. The rms uncertainty in these master flats is about 0.1% redward of 6000 Å, increasing slowly blueward to 0.15% at 4800 Å.

Spectra of the sky taken during morning twilight were used to determine the slit illumination. The twilight flats were averaged together, then collapsed along the spectral dimension leaving a one dimensional “image” of the slit. This spatial profile was then applied to the lamp flat to correct for the large scale response of the instrument, along the slit. The way the HET operates, the spherical primary mirror is not moved during an observation. Instead, tracking is accomplished by moving the entire Prime Focus Instrument Package (PFIP) relative to the primary mirror much in the way the Arecibo 305m radio telescope is pointed. As objects are tracked across the mirror, the pupil entering the instrument changes and, consequently, so does the slit illumination. We found that the twilight flats taken with the PFIP location fixed often did not represent the slit illumination during our science exposures. The gross vignetting pattern of the telescope optics was represented, but small gradients remained. These gradients were corrected as part of the sky subtraction procedure, described below.

Cosmic ray rejection was done using an IRAF script called `speccrrej` (a prototype of a task which is planned for the Gemini IRAF package). This task makes a two dimensional model of the longslit spectrum, sensitive to features larger than $\sim$ 30 square pixels. It does a fairly good job of simulating the spectrum, as well as most of the sky lines. However, sharp features are not modeled, and show up in the difference image. Most of these features are cosmic rays, though strong skylines and sometimes strong emission lines or deep absorption troughs are also flagged. The cosmic ray masks were all checked manually to make sure that real spectral features were not flagged. The flagged cosmic rays were then replaced by the values from the model spectrum. Pixels affected by cosmic rays were added to the bad pixel masks for each exposure.

Spectral arc lamps (Ne and HgCdZn) were observed each night with our setup. We used the IRAF tasks `identify`, `reidentify`, and `fitcoords` to establish the spectral dispersion function in the two dimensional spectra. There were 34 lamp lines used over the full wavelength range, and the fifth order polynomial fits typically had an RMS scatter of 0.2 Å. There were small (less than 2 Å) wavelength offsets found for the skylines in many of the science exposures, caused by a shifting of the slit position between setups. These shifts caused a wavelength shift in the dispersion function, but no change in its shape. The wavelengths of several strong skylines (OIλ5577, OIλ6300) were used to correct for these offsets. The `identify` task was also used to find the spectral trace along the spatial dimension. In cases where the trace of a galaxy was too faint to be seen, the fit for a brighter object observed the same night was used instead. We then rectified the two dimensional spectra.

Prior to sky subtraction, we checked the quality of the spatial illumination correction for each spectrum, by measuring the flux of several strong sky lines along the slit. The sky level should be constant along the slit, but due to the varying illumination of the HET image pupil, the simple twilight flatfield was not always effective. In these cases, we fitted any residual illumination gradient with a smooth low order function, and divided it out. Sky regions bracketing the spectral trace were averaged, and then subtracted from the full 2D spectrum. This produced good results, except near the OIλ5577, NaDλ5895, and OIλ6300 skylines, which were simply interpolated over. These bad regions are marked in the spectra presented in Section 2.3.

2.2.3.3 Spectral extraction, coaddition, flux calibration

We extracted the spectra in apertures of length r_e (thus including the signal within $r_e/2$ of the center, rounding off to the nearest integer pixel), by simply summing the appropriate rows. Since the galaxies cover a wide range of distances, the fixed slit width of $2''$ will cover a varying fraction of the galaxy disks. However, since no good spectral gradient data exist for these types of galaxies, we choose to simply note this fact and not attempt any corrections for it. The galaxies C3-2 and C4-1 did not have exponential scale lengths reported in OBC97. We chose the apertures for these galaxies based on their light profiles along the slit and to optimize the S/N; we use an aperture length of $6''$ for C3-2, and $11''$ for C4-1.

A special correction had to be made for the data from 1999 November. During the first month of science observations with the telescope, a glass membrane pellicle was used as part of the telescope guiding system. This membrane caused a fringe pattern to appear in the data, with a fringe wavelength of 300-400 pixels, and a strength and location that varied from one exposure to the next. For each of the galaxies observed in 1999 November, we obtained at least one additional spectrum during a later month. To remove the fringe pattern from the data, we fit the continuum, and normalized the spectrum by this fit. We then multiplied the normalized spectrum with the average continuum fit from the data not affected by the fringing problem.

Most of the galaxies had multiple observations, often taken several months apart. Before coadding the spectra, we corrected the wavelength scales to a consistent velocity with respect to the sun. The spectra were then averaged.

Each night of science observations, a spectrophotometric standard star was observed. The relative flux response of the instrument is very stable (with the exception of the data from 1999 November), and we based the relative flux calibration on all the standard stars observed during an observing season. For the 1999-2000 season, we used 15 standard star observations, and for the 2000-2001 season we averaged 7 observations. The stars observed were: HD 84937, HD 19445, HZ 4, HZ 44, Feige 34, Feige 66, Feige 67, Gl 191B2B, Hiltner 600, BD+25 3941, and BD+26 2606. The observed spectral energy distributions (SED) were scaled to account for grey extinction due to cirrus, and then fit with a sixth order polynomial, with an RMS deviation of less than 0.1%. When the different observations are scaled to the same value at 5800 Å, the full range of measurements at both 4800 Å and 7150 Å spans 0.25%, which we take to be the maximum expected relative uncertainty over large wavelength ranges. We then applied these relative flux calibrations to all the coadded spectra.

In parallel with the spectral reductions and extractions, variance spectra were produced. These are derived by first assuming poisson noise from the sky and object counts, then folding in readout noise, flat-fielding uncertainty, the effects of rectification and extraction, and finally the co-addition of spectra.

2.2.3.4 Redshifts

Redshifts are derived in two separate ways, (1) from cross-correlation with absorption line templates and (2) from measurements of the emission line wavelengths.

We used the IRAF task `xcor` to compute the cross-correlations for galaxies showing stellar absorption features, with an observation of HD12402 (spectral type K1III) as the stellar template. The restframe wavelength range used for the computation was 4300 Å - 6500 Å for galaxies with no significant Hβ emission (C1-2, C1-4, U1-8, N3-1). For galaxies with Hβ emission, the cross-correlation was performed over the range 5000 Å - 6000 Å, which still includes several strong absorption features. The uncertainties determined by the `xcor` task were 60 km/s for the galaxies without Hβ emission and 75 km/s for the systems with both absorption and emission features.

Redshifts for the emission line galaxies were based on positions of the lines Hβ, [O III]λλ4959,5007, Hα, [N II]λ6584, and [S II]λλ6717,6731. We take the mean velocity of all the strong lines as the systemic velocity, and the rms scatter as the uncertainty in the velocity. This uncertainty was typically $\sim$ 30km/s for galaxies with at least four emission lines detected.

For the galaxies where we measure redshifts from both the emission lines and stellar absorption features, the two measurements were always consistent with no velocity offset, to within the uncertainties. We transform the redshifts into the heliocentric reference frame. The measured redshifts are listed in Table 2.7. We list the emission line redshifts when available, otherwise the absorption line redshifts are shown.

2.2.3.5 Emission line measurements

Emission line strengths are measured using the IRAF task `fitprofs`. Nearby lines are measured simultaneously, using the deblend option, and constraining the fit to have a single width for all the nearby lines. We use the variance spectra to estimate the "inverse gain" parameter, used by `fitprofs` in its Monte Carlo estimation of the uncertainties.

In many cases, the measurement of the Hβ emission strength is clearly affected by underlying stellar absorption. We correct this individually for each galaxy. The adopted correction procedure is as follows. The wavelength coverage of the emission line is defined at its base, the widest point. The continuum level is defined with a straight line between the two sides of the base. The emission line flux and equivalent width are then measured above this continuum level. The V1999 single burst stellar population model spectra, convolved to our instrumental resolution, are then used to estimate the effect of the underlying stellar absorption profile on the emission measurements. For each galaxy, we find the model which best fits the absorption lines in the restframe wavelength range $4800\text{Å} < \lambda < 5450\text{Å}$. We also determine what range of model ages and metallicities brackets a reasonable fit to the spectrum. The fits are all done by eye. We define a continuum level on the models, by drawing a straight line between the model values at either side of the emission line wavelength interval, and measure the equivalent width of absorption below this level. We then combine the equivalent width of absorption seen in the models with the equivalent width of emission measured above the interpolated continuum in the data to get a corrected Hβ equivalent width measurement. Finally, we scale the Hβ flux measurement by the ratio of the corrected to uncorrected equivalent widths to determine the total emission line flux corrected for underlying absorption. Examples of this technique applied to two of the galaxies are shown in Figure 2.2. Table 2.6 lists the measured uncorrected Hβ equivalent widths as well as the parameters of the best fitting, youngest, and oldest models, and their corresponding absorption equivalent width corrections.

TABLE 2.6

Hβ EQUIVALENT WIDTH CORRECTIONS

		best-fit model[a]			max EW(Hβ) model[b]			min EW(Hβ) model[c]		
Name	EW(Hβ)$_{em}$ (Å)	age (Gyr)	[Fe/H]	EW(Hβ)$_{abs}$ (Å)	age (Gyr)	[Fe/H]	EW(Hβ)$_{abs}$ (Å)	age (Gyr)	[Fe/H]	EW(Hβ)$_{abs}$ (Å)
C3-2	2.0±0.1	1.58	0.2	-1.3	0.63	0.0	-1.0	11.0	-0.7	-1.9
C4-1	7.5±0.6	0.25	0.0	-2.2	0.10	0.0	-1.8	0.63	0.0	-2.2
C4-5	0.9±0.3	0.79	0.0	-1.2	0.40	0.0	-1.0	1.58	0.0	-1.5
C6-1	2.7±0.3	3.16	-0.4	-1.6	1.00	0.0	-1.3	13.2	-0.7	-2.4
C8-3	3.4±0.4	0.50	0.0	-1.1	0.10	0.0	-0.9	0.79	0.0	-1.2
N10-2	1.3±0.1	7.94	-0.4	-1.0	1.00	0.2	-0.8	17.4	-0.7	-1.4
N9-1	11.5±0.3	0.40	0.0	-2.6	0.03	0.0	-1.7	1.00	0.2	-2.9
N9-2	27.7±0.9	0.25	0.0	-4.4	0.10	0.0	-3.4	0.63	0.0	-4.5
P1-3	7.2±0.4	1.00	0.0	-1.3	0.40	0.0	-1.0	6.31	-0.7	-1.9
P6-1	1.3±0.2	3.16	-0.4	-1.0	1.00	0.2	-0.8	11.0	-0.7	-1.4
U1-4	2.6±0.1	0.63	0.0	-2.0	0.50	0.0	-1.9	0.79	0.0	-2.3

[a] Parameters for the "best-fit" stellar population model and the equivalent width of Hβ absorption over the narrow wavelength region for which we measure emission. The "best fit" as well as the determination of the maximum and minimum reasonable corrections were done by eye. See Section 2.2.3.5 for details.

[b] The model which requires the largest correction to the Hβ equivalent width, but is still a reasonable fit to the other absorption features in the spectrum. This is typically the youngest, highest metallicity, marginally acceptable model.

[c] The model which requires the smallest correction to the Hβ equivalent width, but is still a reasonable fit to the other absorption features in the spectrum. This is typically the oldest, lowest metallicity, marginally acceptable model.

We list two sets of uncertainties for the Hβ fluxes in Table 2.7. The first set are the random uncertainties derived from the fit to the emission line flux, the same as for the other emission lines. Additionally, we include a set of uncertainties showing the range of the absorption corrections consistent with the reasonable fitting models.

The V1999 models, which use an empirical spectral library, are limited in their ability to model young ages at sub-solar metallicities. We also investigated using the Starburst99 models (Leitherer et al., 1999), which cover very young ages at both solar and 1/20 solar metallicity. However, the narrow wavelength coverage of their models does not permit us to fit the metallic absorption features at longer wavelength, which provide the most constraint on the range of reasonable models.

Telluric absorption in the atmospheric B band ($\lambda \simeq 6840$ Å) affected our line strength measurements for two galaxies. The [N II]λ6584 line was absorbed in the galaxy C5-3. Nebular physics predicts [N II]λ6584 = 2.95 · [N II]λ6548 (Osterbrock, 1989, p. 61). For the 9 LSB galaxies with emission and where strong Hα does not make it impossible to measure the [N II]λ6548 line, the mean [N II]λ6584 / [N II]λ6548 ratio is 2.9±0.9. We use the measured value of [N II]λ6548 in C5-3 and the theoretical ratio to calculate the non-absorbed [N II]λ6584 strength (0.27±0.08 relative to Hβ). For the galaxy N9-1, [N II]λλ6548,6584, and Hα all suffered some absorption. For this galaxy, we estimate the additional uncertainty on the [N II]λ6584/Hα ratio to be 10%, and we also likely underestimate the Hα/Hβ ratio by 10%. The uncertainties on the relative emission line fluxes listed for N9-1 in Table 2.7 have been adjusted to account for this. In the following the [N II]λ6584/Hα ratio is simply called [N II]/Hα.

We correct the relative emission line strengths for galactic reddening using the Cardelli extinction law (eqs. 3a and 3b in Cardelli et al. (1989)), with the galactic reddening measurements from Schlegel et al. (1998) as listed in Table 2.1. R_V=3.1 is assumed. The amount of galactic reddening is variable across the field of NGC 1569. We follow Kobulnicky & Skillman (1997) and adopt the value of 0.5 mag (Burstein & Heiles, 1982), so that we may make a direct comparison to their results (see section 2.2.3.7). We have not corrected the emission line strengths for dust reddening internal to the galaxies. We discuss the dust content of these galaxies in Section 2.7. The emission line ratios used for ionization determination and abundance analysis (e.g. [O III]λ5007/Hβ and [N II]/Hα) utilize lines with small wavelength separations, and these ratios are not affected by reddening at the level seen in these galaxies. The Hα equivalent widths are also corrected for the effects of cosmological expansion, $\mathrm{EW}(\lambda_{\mathrm{rest}})=\mathrm{EW}(\lambda_{\mathrm{obs}})\cdot(1+z)$ (see Peterson, 1997, page 156).

We present the measured emission line strengths as well as the equivalent width of Hα in Table 2.7. These data do not have an absolute flux calibration. There are several reasons for this. As objects are tracked across the sky by moving the HET prime focus instrument platform, the region of the primary mirror seen by the instrument changes. Furthermore, not all of the primary mirror is seen all the time, and thus the telescope throughput varies during an object track. Additionally, the PSF at the spectrograph entrance slit changed (sometimes dramatically increasing in size) during exposures, and some of the observations were taken through cirrus clouds. Consequently, we tabulate only relative fluxes, and for convenience we have scaled them to an Hβ flux of 1. For Table 2.7, we list both the random and systematic uncertainties on the scaled Hβ flux, rather than incorporating these into the uncertainties of the other flux measurements and listing line ratios. The uncertainties on Hβ are incorporated into the [O III]λ5007/Hβ ratios plotted in Figure 2.6 and the Hα/Hβ ratios shown in Figure 2.11.

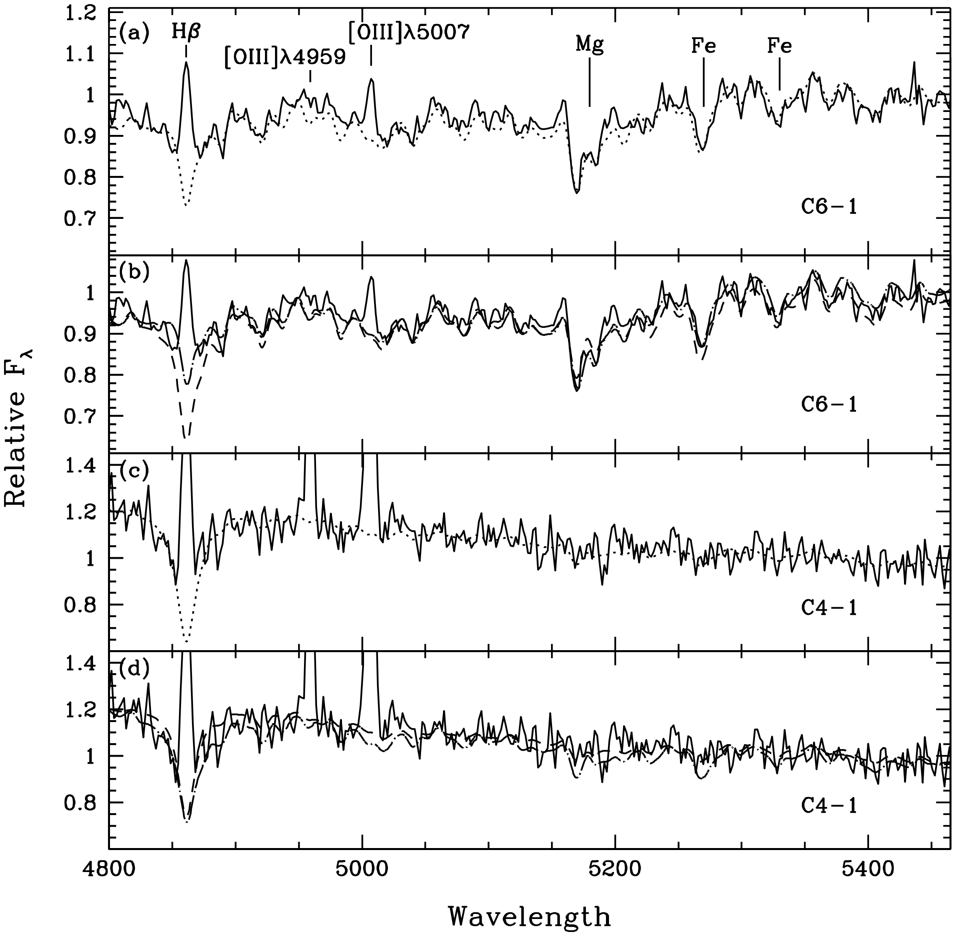

Figure 2.2 Correction of the Hβ emission line strengths for underlying Hβ absorption. Solid lines – observed spectra; dotted lines – best fitting model; dashed lines – youngest acceptable model; dot-dashed lines – oldest acceptable model. The strongest emission and absorption features in this wavelength region are labelled in panel (a). (a) C6-1 with the best fitting model, age=3.2 Gyr, [Fe/H]=-0.4. (b) C6-1 with oldest (age=13.2 Gyr, [Fe/H]=-0.7) and youngest (age=1.0 Gyr, [Fe/H]=0.0) acceptable models. (c) C4-1 with the best fitting model, age=250 Myr, [Fe/H]=0.0. (d) C4-1 with oldest (age=630 Myr, [Fe/H]=0.0) and youngest (age=100 Myr, [Fe/H]=0.0) acceptable models. Note that the depth of the Hβ absorption reaches a maximum for an SSP of 200 Myr, and so appears weaker in both the older and younger models.

TABLE 2.7

SPECTROSCOPIC DATA: ABSORPTION INDICES

Name	S/N[a]	cz_{hel}[b]	M_B[c]	Hβ	Mgb	< Fe >
P1-3	19	17505	-19.67	···	0.9±0.4	1.4±0.4
P6-1	34	10891	-18.53	···	3.1±0.2	2.1±0.2
P9-4	7	4108	-14.67	···	···	···
C1-2	19	4615	-16.26	2.0±0.4	3.0±0.4	2.2±0.3
C1-4	70	3883	-17.35	1.9±0.1	3.5±0.1	2.50±0.09
C3-2	41	4528	-17.63	···	2.4±0.2	2.0±0.2
C4-1	14	4927	-16.48	···	1.0±0.5	0.8±0.5
C4-5	23	4633	-16.01	···	1.1±0.3	1.7±0.3
C5-3	12	12944	-17.21	···	0.9±0.6	1.0±0.5
C5-5	5	5473	-16.49	···	···	···
C6-1	22	25035	-20.13	···	3.1±0.3	2.2±0.3
C8-3	17	3648	-15.91	···	1.1±0.4	1.0±0.4
N3-1	72	25222	-19.67	1.7±0.1	4.7±0.1	3.03±0.09
N9-1	38	15128	-19.38	···	1.6±0.2	···
N9-2	13	73629	-19.84	···	1.3±0.6	1.3±0.5
N10-2	38	20668	-20.69	···	2.8±0.2	2.2±0.2
N10-4	8	7447	-16.20	···	···	···
U1-4	53	3416	-16.86	···	1.0±0.2	0.8±0.1
U1-8	35	32123	-20.27	2.0±0.3	3.0±0.2	2.2±0.2
NGC3872	153	3114	-21.83[d]	1.47±0.05	5.04±0.05	2.83±0.04
UGC3844	38	3192	-20.77[d]	1.5±0.2	4.6±0.2	3.5±0.2
NGC1569[e]	120	-96	-17.23[d]	···	0.68±0.07	0.71±0.06

[a] Signal-to-noise per Å of the continuum, measured between 5050Å and 5150Å.

[b] Heliocentric radial velocity: Based on emission lines, if present. Otherwise based on cross-correlation with absorption line template.

[c] Total absolute magnitude: Based on our photometry, if available, otherwise from OBC97. Assuming H_0=75 $\mathrm{kms}^{-1}\mathrm{Mpc}^{-1}$, and distances based on redshifts in the CMB reference frame.

[d] Data from the LEDA database (`http://leda.univ-lyon1.fr`), and adjusted to H_0=75 $\mathrm{kms}^{-1}\mathrm{Mpc}^{-1}$.

[e] Uncertainties listed as 0.00 are less than 0.005.

Table 2.8

Spectroscopic Data: Emission Line Strengths

Name	EW(Hα)	Hβ[a]	[OIII]λ5007	[NII]λ6548	Hα	[NII]λ6584	[SII]λ6717	[SII]λ6731
P1-3	31±1	$1.00\pm0.05^{+0.07}_{-0.04}$	1.48±0.05	0.20±0.04	3.44±0.07	0.70±0.06	0.89±0.05	0.65±0.05
P6-1	8.0±0.2	$1.00\pm0.17^{+0.15}_{-0.09}$	···	0.75±0.07	5.0±0.1	2.3±0.1	1.70±0.09	1.13±0.08
P9-4	73±7	1.00±0.06	3.1±0.1	0.04±0.04	3.76±0.0.09	0.30±0.05	0.56±0.06	0.36±0.06
C1-2	···	···	···	···	···	···	···	···
C1-4	···	···	···	···	···	···	···	···
C3-2	11.0±0.1	$1.00\pm0.06^{+0.18}_{-0.09}$	···	0.33±0.04	3.84±0.05	1.49±0.04	0.82±0.05	0.76±0.06
C4-1	30±2	$1.00\pm0.07^{+0.00}_{-0.04}$	1.53±0.07	0.09±0.04	2.64±0.09	0.25±0.05	0.56±0.06	0.39±0.05
C4-5	6.3±0.3	$1.00\pm0.25^{+0.12}_{-0.13}$	0.5±0.1	0.47±0.13	2.9±0.1	0.9±0.1	1.3±0.1	0.9±0.1
C5-3	63±1	1.00±0.06	3.78±0.09	0.09±0.03	3.53±0.08	0.27±0.08[b]	0.62±0.05	0.41±0.04
C5-5	25±2	1.00±0.28	4.3±0.4	···	···	5.8±0.4	···	···
C6-1	14.4±0.6	$1.00\pm0.12^{+0.17}_{-0.08}$	···	0.65±0.06	4.3±0.1	1.96±0.09	···	···
C8-3	16.3±0.6	$1.00\pm0.12^{+0.03}_{-0.03}$	3.2±0.2	0.25±0.06	3.2±0.1	0.31±0.07	0.74±0.09	0.42±0.07
N3-1	···	···	···	···	···	···	···	···
N9-1	41±1	$1.00\pm0.02^{+0.02}_{-0.07}$	0.71±0.02	0.12±0.01	2.88±0.02	0.80±0.01	0.81±0.02	0.57±0.02
N9-2	···	$1.00\pm0.03^{+0.00}_{-0.04}$	1.09±0.03	···	···	···	···	···
N10-2	8.1±0.2	$1.00\pm0.11^{+0.17}_{-0.07}$	0.33±0.08	0.70±0.09	3.80±0.08	1.90±0.06	$0.57^{+1.1}_{\pm0.07}$[c]	$0.32^{+0.9}_{\pm0.07}$[c]
N10-4	7±1	···	···	···	···	···	···	···
U1-4	11.9±0.2	$1.00\pm0.05^{+0.06}_{-0.03}$	1.13±0.04	0.11±0.02	2.18±0.03	0.32±0.03	0.57±0.02	0.43±0.02
U1-8	···	···	···	···	···	···	···	···
NGC3872	···	···	···	···	···	···	···	···
UGC3844	···	···	···	···	···	···	···	···
NGC1569[d]	95.6±0.6	1.00±0.00	5.96±0.01	0.06±0.00	3.92±0.00	0.14±0.00	0.20±0.00	0.14±0.00

[a] Emission line fluxes are normalized to f(Hβ)=1. The first set of uncertainties on Hβ are the random uncertainties and the second set are the range of absorption corrections consistent with the stellar population models. If no second set is listed, the correction is negligible compared to the uncertainty due to random error.

[b] Calculated from [NII]λ6548 × 2.95

[c] Lower value is the intrinsic uncertainty, upper value is a systematic uncertainty, caused by poor flux calibration at the extreme red end of the spectrum. See Figure 2.6.

[d] Uncertainties listed as 0.00 are less than 0.005.

2.2.3.6 Absorption line indices

We have measured the strength of the stellar absorption lines Hβ, Mgb, Fe5270, and Fe5335 using the line index definitions of the Lick/IDS system (Worthey et al., 1994). Several calibrations were made to match our observations to the characteristics of the IDS spectrograph and put our measurements onto the Lick system. Before measuring the indices, it was necessary to match our spectra to the instrumental resolution of the IDS spectrograph. We convolved our spectra with a wavelength dependant Gaussian to accomplish this. Additionally, stellar features in galaxy spectra are broadened by the internal velocity dispersion of the galaxies, and this broadening will have an effect on the measured strength of the line indices. To facilitate comparison with stellar population models, we correct our observations to the equivalent strength for a system with zero velocity dispersion, following the method of Davies, Sadler, & Peletier (1993): we determined the correction by taking a spectrum of a K giant star, already convolved to the IDS resolution, and convolving it with Gaussians of increasing velocity width, in 25 km/s increments, up to 400 km/s. We measured the index strengths on this suite of stellar spectra, and used the offsets between each velocity width and the unbroadened spectrum to correct the galaxy measurements. Since we do not actually resolve the velocity dispersion of the LSB galaxies, we assume a value of 75 km/s. The correction factors by which the measurements are multiplied are as follows: Hβ (1.004); Mgb (1.02); Fe5270 (1.02); Fe5335 (1.04). The correction is such that for galaxies whose true velocity dispersion is larger than we have assumed (75 km/s), we will derive index values which are weaker than the actual values for that stellar population if it were observed with zero intrinsic velocity dispersion. If the actual velocity dispersion of the galaxy is 150 km/s instead of 75 km/s, then we will systematically underestimate the Hβ strength by 1%, the Mgb strength by 3%, the Fe5270 strength by 5%, and the Fe5335 strength by 8%. For N3-1 and the two elliptical galaxies we correct for a velocity dispersion of 250 km/s. NGC 3872 has a velocity dispersion of σ=243km/s (Davies et al., 1987), while we simply assume 250 km/s for UGC 3844 and N3-1. The correction factors are Hβ (1.02); Mgb (1.17); Fe5270 (1.16); Fe5335 (1.36).

Uncertainties for the index strengths are derived from the variance spectra. Essentially, we use poisson statistics on the flux in both the line and continuum bandpasses, additionally accounting for the contribution caused by the readout noise, and flatfielding, relative flux calibration, and sky subtraction uncertainties.

In several cases, residuals from imperfect subtraction of strong skylines (Oλ5577, NaD) fall in the index bandpasses. When the residuals lie in the index continuum bandpasses, we correct the residuals by interpolating over the affected region, using values determined from comparison with the V1999 stellar population models. Observations corrected in this way are N10-2 (Mgb red continuum, Fe5270 blue continuum), N3-1 (Mgb blue continuum), U1-8 (Fe5270 red continuum), and C6-1 (Mgb blue continuum). In some cases, the sky residuals lie on the absorption line itself, and this cannot be corrected. Both Fe5270 and Fe5335 are affected in N9-1. The Fe5335 line is affected for C5-3 and U1-8 while the Fe5270 line is affected for P1-3. There are strong correlations between Fe5270, Fe5335, and $<\mathrm{Fe}>$ (defined as $<\mathrm{Fe}>$ = (Fe5270 + Fe5335) / 2). Using the LSB galaxy data not affected by the large sky subtraction uncertainties, we derived the relation Fe5335 $= (1.14 \pm 0.08) \cdot$ Fe5270 $- (0.74 \pm 0.24)$. We use this relation to correct the affected indices.

Intrinsic emission from these galaxies could affect the line indices Mgb and Hβ. Goudfrooij & Emsellem (1996) have found that the [NI] emission doublet at 5199 Å can affect the strength of the Mgb index in early-type galaxies which have ionized gas emission. Many of these LSB galaxies have emission lines, so this is cause for concern. However, the [NI] doublet is strong in LINERs, not HII regions, and none of these galaxies show line ratios consistent with this type of nuclear activity (see Section 2.4). Additionally, since these are integrated spectra, rather than nuclear spectra, we do not expect the Mgb index to be contaminated. The Hβ index, on the other hand, is certainly affected by emission in all but three of the galaxies in our sample. For one more galaxy (U1-8), the Hβ emission must be small. The observed wavelength range for U1-8 does not include either Hα or [O II]λ3727. While the spectrum is dominated by absorption features, there is a small amount of emission seen at [O III]λ5007 which suggests that the Hβ absorption index will also be affected by emission. The equivalent width of [O III]λ5007 emission is 1.2±0.4 Å. Trager et al. (1999) determine the relation between [O III]λ5007 and Hβ emission strength in elliptical galaxies to be EW(Hβ) $\simeq 0.6 \cdot$EW([O III]λ5007). This ratio is metallicity sensitive, and will tend to decrease with decreasing metallicity. The integrated galaxy spectra studied by Kobulnicky, Kennicutt, & Pizagno (1999) show ratios as low as EW(Hβ) $\simeq 0.25 \cdot$EW([O III]λ5007) at the metallicity appropriate for U1-8 ($\simeq 0.4\ Z_{\odot}$; see Figure 2.7). We therefore apply a correction to the Hβ absorption index for U1-8 of 0.5 ± 0.3 Å.

For the 15 LSB galaxies with strong emission lines, a correction of the Hβ absorption index for the Hβ emission (and its uncertainty) would be a significant fraction of the Hβ absorption strength. Consequently, we do not present this absorption index for any of the other LSB galaxies.

The absorption line strengths of Hβ , Mgb, and $<$ Fe $>$ are presented in Table 2.7.

2.2.3.7 Comparison to literature data

Our sample has a very wide range in radial velocities, from 3000 km/s to more than 60,000 km/s (z=0.2). These same galaxies have been observed in the HI survey of O'Neil et al. (2000a), who give detections for twelve of them. We find several discrepancies between our redshift measurements and the redshifts reported in that survey. The HI survey only covered the velocity space out to 13,000 km/s so more distant objects would not have been detected. However, for the galaxies P1-3, C6-1, and N9-2, lower HI redshifts must have been attributed incorrectly to these higher redshift galaxies. The HI detections for P1-3 and C6-1 can be explained by beam confusion. At 21cm, the beam-size of the Arecibo 305m radio telescope is almost $3'$, and both of these galaxies appear in the sky at a projected distance of less than $3'$from a large spiral galaxy at lower redshift. The HI detection ascribed to P1-3 is probably NGC 7631 ($cz_{\mathrm{HI}} = 3746$ km/s; $cz_{\mathrm{opt}} = 3741$ km/s (Falco et al., 1999; hereafter UZC), and the detection ascribed to C6-1 is probably NGC 2595 ($cz_{\mathrm{HI}} = 4322$ km/s; $cz_{\mathrm{opt}} = 4320$ km/s, UZC). The mis-identification also explains why these galaxies appeared to have extreme M_{HI}/L ratios, and lie more than 5σ from the I band Tully-Fisher relation (O'Neil et al., 2000a). Similar cases of beam confusion explain discrepant measurements for the lower redshift LSB galaxies as well. The detection ascribed to C8-3 is probably UGC 4308 ($cz_{HI} = 3570$ km/s; $cz_{opt} = 3566$ km/s, UZC), and the detection of C5-5 is more likely UGC 4416 ($cz_{HI} = 5524$ km/s; $cz_{opt} = 5555 \pm 45$ km/s, UZC).

There are also cases where the optical and HI redshifts are discrepant, but beam confusion is not obviously the reason: N9-2 (listed above), C4-1, C1-2, and possibly P9-4 (where the optical and HI velocities differ by 3σ). C1-2 in particular is a hard case to explain the HI detection. The difference between optical and HI velocities is $\sim$3900 km/s so the HI detection is clearly a different object. However, there are no obvious candidates within $15'$ of the pointing, which lie at the redshift of the HI detection, and very few bright objects in that area for which optical redshifts were not obtained by the redshift survey of Zabludoff & Mulchaey (2000). We are forced to conclude that either the HI observation was errant, due to either noise or incorrect pointing, or that there are very large HI clouds with little associated optical light. Two starless objects have been found by the HIPASS survey (Kilborn et al., 2000; Ryder et al., 2001) but the first one had only a 4 km/s velocity width, and the second was associated with the galaxy NGC 2442, so neither one is a good analogue.

The remaining four galaxies, C5-3, P6-1, N10-4, and U1-4 are in good agreement, less than 1σ separating the optical and HI measurements.

Recently, Chung et al. (2002) used the VLA to map the HI around the galaxies P1-2, P1-3, C6-1, C4-1, and C4-2 from the OBC97 sample. They also discovered the beam contamination issues affecting the O'Neil et al. (2000a) Arecibo 305m single-dish results. The maps for P1-2, P1-3 and C6-1 show clearly that the HI is all at the position of neighboring spiral galaxies. The HI detection for C4-2 was confirmed, but the map of C4-1 did not detect any HI even though the VLA observations were sufficiently deep to detect the HI, if it were present at the level measured at Arecibo. This result suggests that the N9-2 and C1-2 HI detections may also be noise artifacts, and not starless gas clouds.

We compare our emission line strength measurements for the post-starburst dwarf galaxy NGC 1569 with the results of Kobulnicky & Skillman (1997). Our aperture lies perpendicular to the C and D slit placements of their work and near the two super-star clusters. Kobulnicky & Skillman found that the combination of galactic and intrinsic reddening is both large and variable over the face of this galaxy. In accordance with their methods, we choose a value for the total extinction (galactic plus intrinsic) which brings our measured Hα/Hβ ratio to 2.83 after applying the reddening correction. We measure a total E(B$-$V) of 0.83, which is within the range of values found by Kobulnicky & Skillman (following Kobulnicky & Skillman and Burstein & Heiles (1982), we assume that 0.5 mag of the reddening originates in our galaxy). Once we apply the extinction correction to all the emission lines, our relative flux measurements for the lines Hγ (0.45$\pm$0.01), [O III]$\lambda\lambda$4959,5007 (1.94$\pm$0.01, 5.72$\pm$0.01, respectively), [S III]λ6312 (0.008$\pm$0.001), [N II]$\lambda\lambda$6548,6584 (0.042$\pm$0.001, 0.098$\pm$0.001, respectively), HeIλ6678 (0.023$\pm$0.001), and [S II]$\lambda\lambda$6717,6731 (0.137$\pm$0.002, 0.100$\pm$0.001, respectively) all lie within the range covered by the Kobulnicky & Skillman measurements for this part of the galaxy. The only discrepant line is [O III]λ4363 (0.124$\pm$0.007), which lies on the blue end of our spectrum where the flux calibration is less secure. Over the wavelength range 4800 Å to 7000 Å, our emission line measurements are fully consistent with the results of Kobulnicky & Skillman.

The absorption line index strengths for NGC 3872 are compared with the results of Trager et al. (1998). We extract the spectra using a spatial aperture equivalent to the Lick/IDS aperture, and make velocity dispersion corrections appropriate for $\sigma_{\mathrm{NGC3872}} = 250$ km/s. Trager et al. (1998) measure the following values: Hβ: 1.28$\pm$0.22; Mgb: 4.91$\pm$0.30; $<\mathrm{Fe}>$: 2.22$\pm$0.22. Our measurements for Hβ and Mgb are within 1σ of their values. For $<\mathrm{Fe}>$, our measurement is about 2.5σ higher than theirs.

2.3 Presentation of the spectra

We present the spectra in Figures 2.3a-e and 2.4. The spectra for these 19 LSB galaxies qualitatively resemble the spectra of HSB galaxies over the full range of spectra seen for all Hubble types, from ellipticals all the way through late-type spirals and starbursting irregular galaxies. For comparison, we show our spectra of the two elliptical galaxies, NGC 3872 and UGC 3844, in Figure 2.3a, and the spectrum of the post-starburst irregular galaxy NGC 1569 in Figure 2.3d.

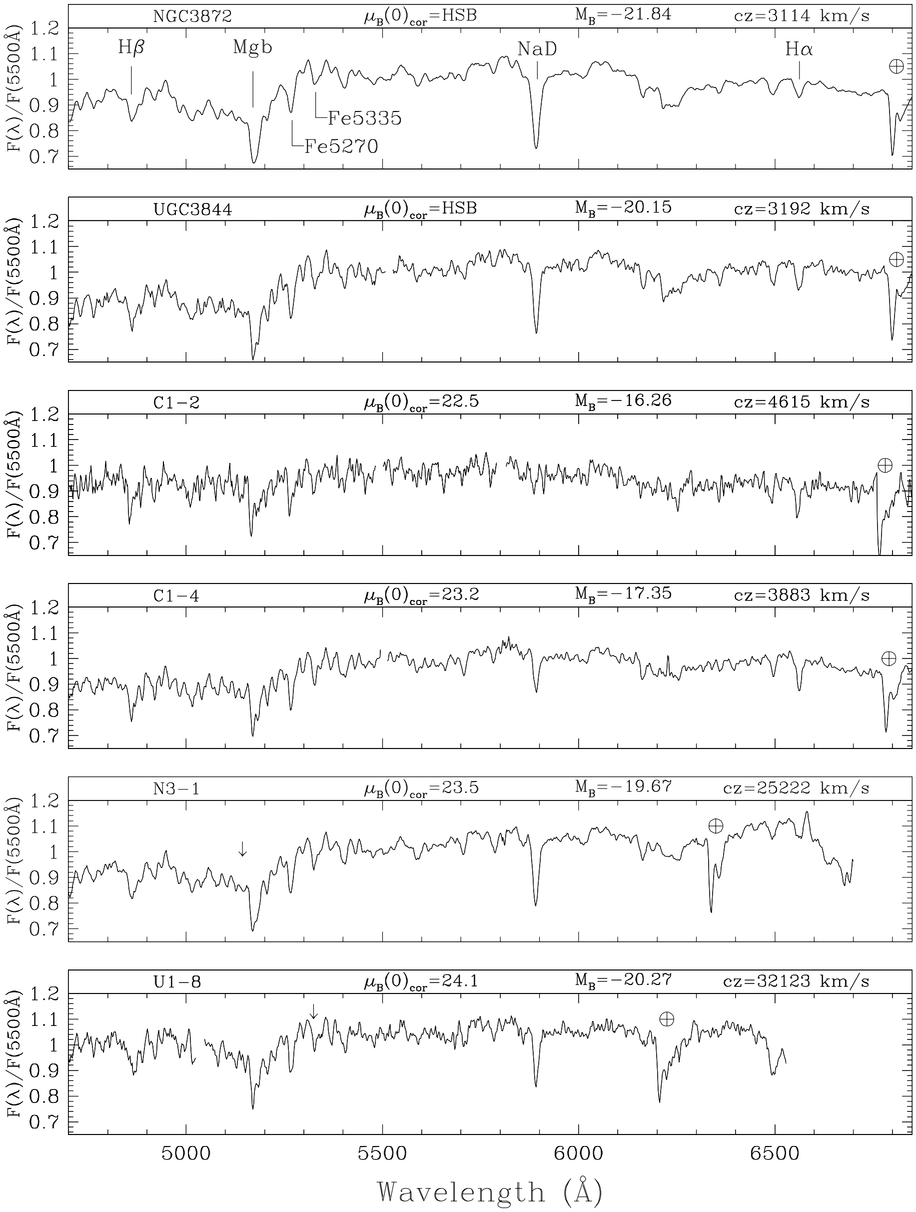
NGC3872
$\mu_B(0)_{cor}$=HSB
M_B=−21.84
cz=3114 km/s
Hβ
Mgb
Fe5270
Fe5335
NaD
Hα
⊕
UGC3844
$\mu_B(0)_{cor}$=HSB
M_B=−20.15
cz=3192 km/s
⊕
C1−2
$\mu_B(0)_{cor}$=22.5
M_B=−16.26
cz=4615 km/s
⊕
C1−4
$\mu_B(0)_{cor}$=23.2
M_B=−17.35
cz=3883 km/s
⊕
N3−1
$\mu_B(0)_{cor}$=23.5
M_B=−19.67
cz=25222 km/s
↓
⊕
U1−8
$\mu_B(0)_{cor}$=24.1
M_B=−20.27
cz=32123 km/s
↓
⊕
F(λ)/F(5500Å)
0.7
0.8
0.9
1
1.1
1.2
5000
5500
6000
6500
Wavelength (Å)

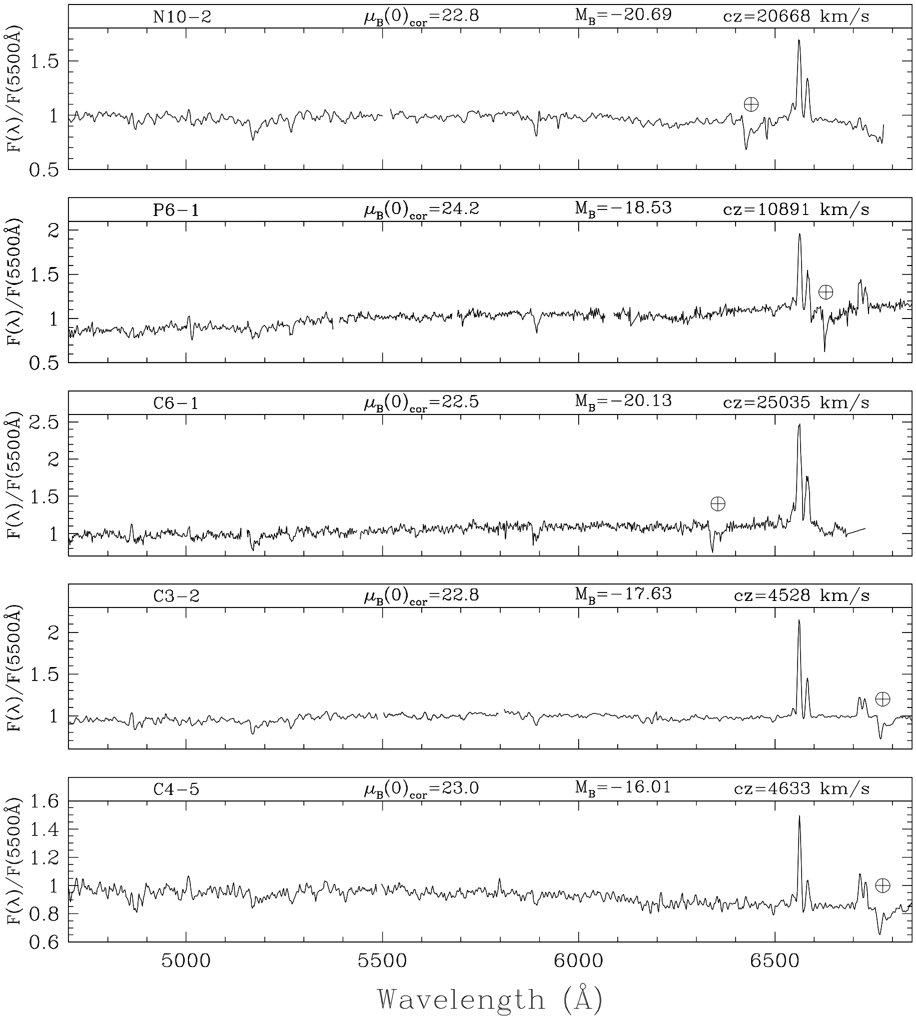
N10-2
$\mu_B(0)_{cor}$=22.8
M_B=−20.69
cz=20668 km/s
P6-1
$\mu_B(0)_{cor}$=24.2
M_B=−18.53
cz=10891 km/s
C6-1
$\mu_B(0)_{cor}$=22.5
M_B=−20.13
cz=25035 km/s
C3-2
$\mu_B(0)_{cor}$=22.8
M_B=−17.63
cz=4528 km/s
C4-5
$\mu_B(0)_{cor}$=23.0
M_B=−16.01
cz=4633 km/s
⊕
F(λ)/F(5500Å)
0.5
1
1.5
2
2.5
0.6
0.8
1.2
1.4
1.6
5000
5500
6000
6500
Wavelength (Å)

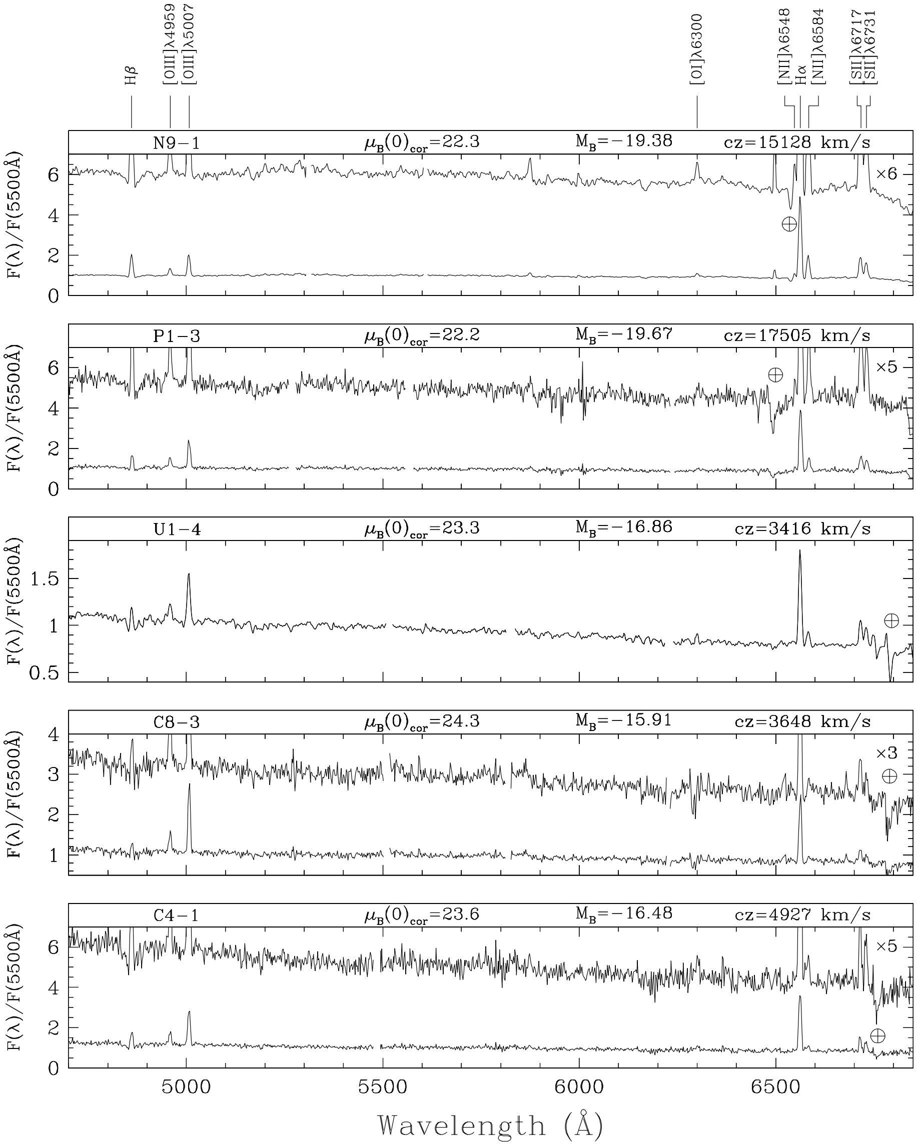
Hβ
[OIII]λ4959
[OIII]λ5007
[OI]λ6300
[NII]λ6548
Hα
[NII]λ6584
[SII]λ6717
[SII]λ6731
N9−1
$\mu_B(0)_{cor}$=22.3
M_B=−19.38
cz=15128 km/s
×6
P1−3
$\mu_B(0)_{cor}$=22.2
M_B=−19.67
cz=17505 km/s
×5
U1−4
$\mu_B(0)_{cor}$=23.3
M_B=−16.86
cz=3416 km/s
C8−3
$\mu_B(0)_{cor}$=24.3
M_B=−15.91
cz=3648 km/s
×3
C4−1
$\mu_B(0)_{cor}$=23.6
M_B=−16.48
cz=4927 km/s
×5
⊕
F(λ)/F(5500Å)
0
2
4
6
0.5
1
1.5
1
2
3
4
5000
5500
6000
6500
Wavelength (Å)

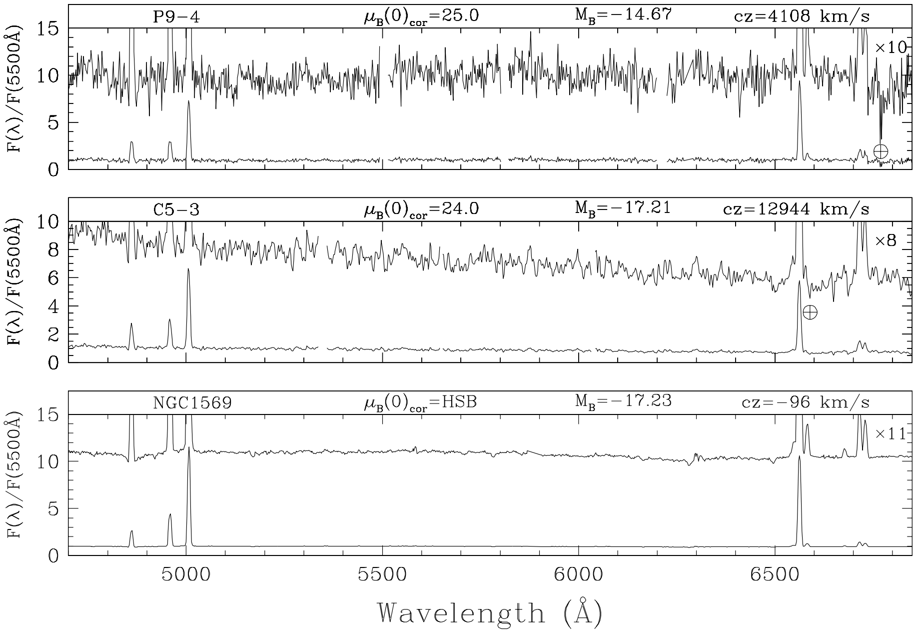
P9-4
$\mu_B(0)_{cor}$=25.0
M_B=−14.67
cz=4108 km/s
×10
C5-3
$\mu_B(0)_{cor}$=24.0
M_B=−17.21
cz=12944 km/s
×8
NGC1569
$\mu_B(0)_{cor}$=HSB
M_B=−17.23
cz=−96 km/s
×11
F(λ)/F(5500Å)
0
5
10
15
0
2
4
6
8
10
5000
5500
6000
6500
Wavelength (Å)

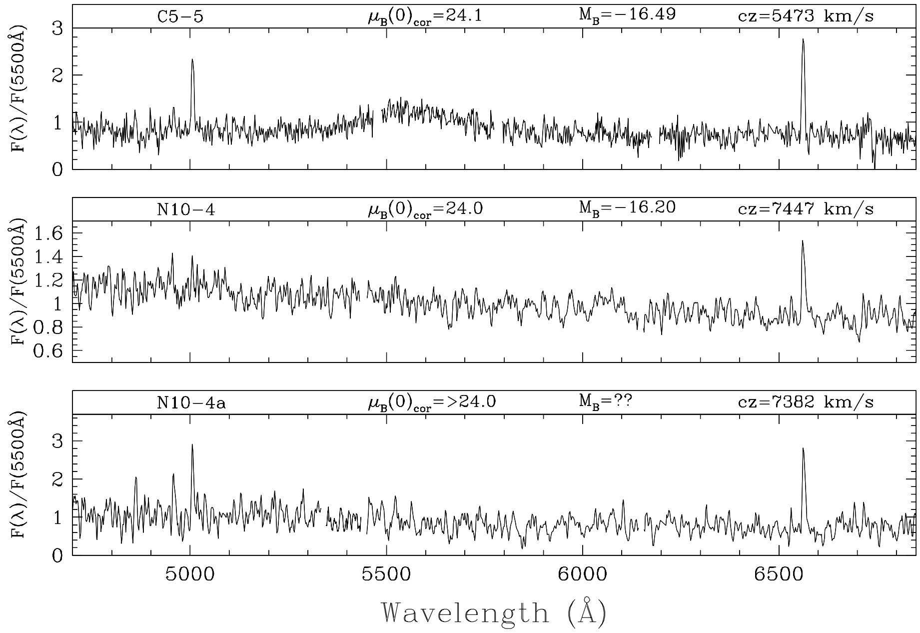

Figure 2.3 Presentation of spectra for galaxies at low redshift ($z < 0.11$). The strongest absorption features are labelled in (a), and the strongest emission lines are labelled in (c). (a) Objects with absorption dominated spectra. The top two galaxies are bright ellipticals for comparison purposes, while the bottom four spectra are LSB galaxies. Gaps in the data mark regions affected by large sky subtraction residuals. The location of the atmospheric B band absorption ($\simeq$ 6840 Å in the observed frame) is marked with $\oplus$. Vertical arrows denote the regions affected by sky subtraction residuals which were corrected via interpolation using the V1999 stellar population model spectra (see Section 2.2.3.6). Note that with the high S/N of the observations for NGC 3872, C1-4, and N3-1, the majority of the bumps and wiggles are real features, and not noise. (b) Spectra for LSB galaxies with emission lines, ordered by the strength of [N II]λ6584 relative to Hα. (c) Spectra for LSB galaxies with emission lines, ordered by the strength of [N II]λ6584 relative to Hα. (d) Spectra for galaxies with very weak [N II]λ6584 and large EW(Hα). NGC 1569 is a high surface brightness post-starburst galaxy. (e) The S/N of the spectra for N10-4 and C5-5 are too low to estimate the galaxies' metallicities, but the spectra are suitable for determining redshifts. See the text for a description of N10-4a.

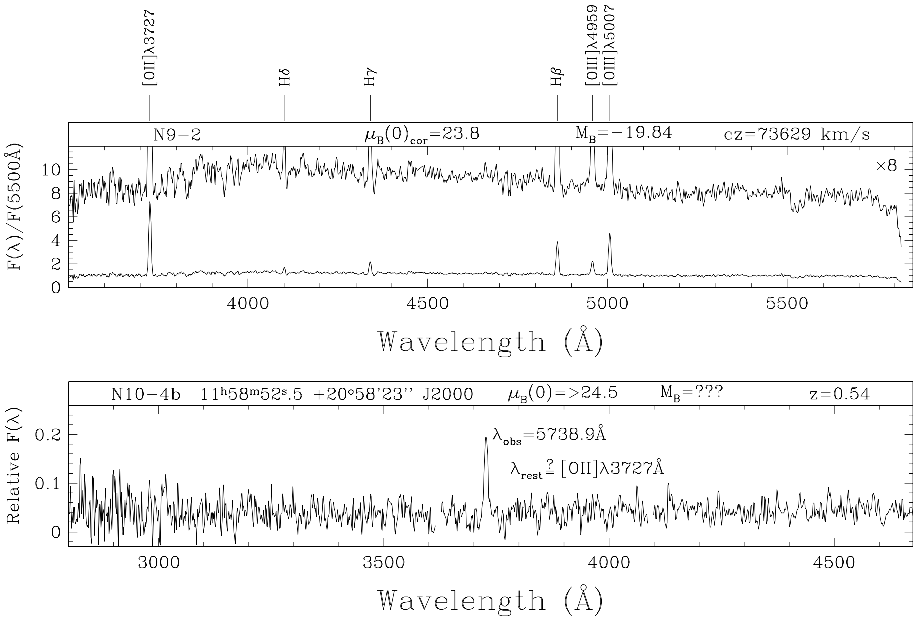

Figure 2.4 Spectra for galaxies with z> 0.2: a) N9-2 is at z≃0.245, and is most likely a normal high surface brightness spiral galaxy affected by cosmological surface brightness dimming. b) N10-4b is detected as a single emission line at $\lambda = 5738.9$Å, which we identify as [O II]λ3727 emission at z=0.54. No object is seen in the broadband imaging with the HET or PFC at the location of this object, suggesting it could be a high redshift LSB galaxy.

The emission line galaxies have been ordered by the strength of their [N II]λ6584 emission relative to Hα, from strongest to weakest. This is essentially a sequence of decreasing metallicity as we will show in Section 2.6. The strength of the [O III]λ5007 emission line increases along the sequence, due to a combination of the decreasing metallicity and the associated decreasing amount of dust reddening in the emission regions. This will be discussed in Section 2.7.

The spectral extraction was done using global apertures, which blend together stellar light and line emission from both HII regions and diffuse emission regions. While we do not generally have sufficient spatial resolution to observe gradients in the galaxy properties, we note that the galaxy U1-4 has a clear inner and outer region. The inner region of radius $3''$ is dominated by a bright continuum with stellar absorption features. Outside this region there is a peak in the emission on both sides of the nucleus at about $5''$. Further out, both the emission and continuum fall off. This is illustrated in Figure 2.5. The spectroscopic aperture we use for this galaxy is $2'' \times 32''$ and includes light from both the inner and outer regions.

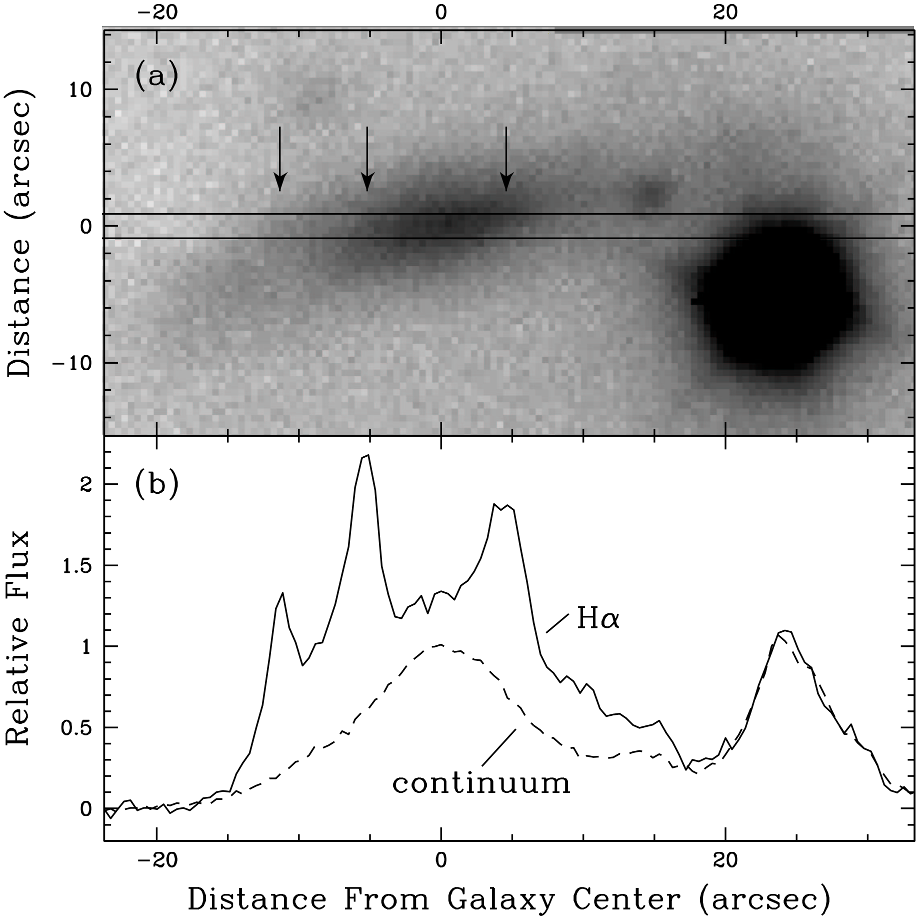

Figure 2.5 The galaxy U1-4: (a) image of U1-4 taken with the HET during set-up for the spectroscopic observation. The object at the lower right is a bright star. The three arrows correspond to the regions of the slit where emission peaks are seen. (b) spatial cut across the 2D spectrum. Solid line - flux of the Hα line (average over 6569.0Å - 6565.9Å in the U1-4 restframe); Dashed line - continuum flux blueward of Hα (average over 6495.3Å - 6540.8Å in the U1-4 restframe). The Hα emission is more spatially extended than the stellar continuum light, and three peaks are seen in the emission (spatial) profile, at -12”, -5” and +5” from the galaxy center. We don’t see the emission regions in (a), which is a broadband image. The spatial profile of the star in (b) shows the image PSF for this observation (the wavelength regions in the restframe of the star are 6633.7Å - 6640.7Å and 6569.3Å - 6615Å).

Analysis of the galaxies in Figure 2.3(a-d) will be presented in the following sections. Here we discuss in detail the galaxies presented in Figures 2.3e and 2.4.

The galaxy N9-2 (Figure 2.4) has a redshift of 0.246 (cz=73629 km s^{-1}). The restframe wavelength coverage for this galaxy is significantly bluer than the rest of the sample, and we do not have observations of the wavelength region near Hα. After applying the $(1+z)^4$ cosmological surface brightness correction and a k_B correction appropriate for an Scd galaxy near z=0.2 of 0.45 mag (Frei & Gunn, 1994), N9-2 has $\mu_B(0) = 22.1$ well within the range of high surface brightness galaxies. N9-2 is just a normal HSB spiral galaxy, seen at moderate redshift, and so we remove it from the rest of the analysis.

The galaxies N10-4 and C5-5 (Figure 2.3e) both have $\mu_B(0) = 24$ and are among the faintest in our sample. The S/N of the observations are sufficient to determine redshifts for these two galaxies, but insufficient for a more detailed analysis. N10-4 is particularly interesting, however, because of its companions. There were two other objects which serendiptously fell onto the slit during the observations. We refer to these as N10-4a and N10-4b. N10-4a ($11^h58^m52^s.5$, $20^\circ58'23''$ J2000) lies 4h^{-1} kpc away ($12''$) from the center of N10-4. We detect emission lines of Hα, Hβ, and [O III]$\lambda\lambda$4959,5007 in the companion, shifted 65 km s^{-1} blueward (cz_{hel}=7382 km s^{-1}). We do not detect anything in the broadband setup image at this position, making it difficult to determine whether this is a separate system, or a knot of emission in the outer disk of N10-4. Additionally, there is another companion $16''.5$ in the opposite direction along the slit (N10-4b, $11^h58^m50^s.8$, $20^\circ58'33''.5$ J2000). This object is also not seen in the setup image, or in images from the digitized sky survey. We do not detect any continuum from this object and only one emission line is seen. This line is detected in all four observations of N10-4. The spectrum is presented in Figure 2.4. The observed wavelength of this emission line is 5738.9 Å, which translates to 5600 Åin the restframe of N10-4. This wavelength does not match any commonly observed galaxy emission lines. Instead, we suggest that this object is a background galaxy, and the single line observed at 5738.9 Å corresponds to [O II]λ3727 seen at a redshift of 0.54. At this redshift, our restframe wavelength coverage is 2790 Å to 4700 Å, where we do not expect to see any other strong emission lines.

The SED of C5-5 (Figure 2.3e) has a bump in it, centered at 5600 Å (5670 Å in the observed frame) which we do not have an explanation for. The bright spiral galaxy UGC 4416 fills the edge of the slit, and some of its light might be scattering in. There is also a spatial offset between the emission line peak and the peak of the continuum for this galaxy, though the emission is still consistent with coming from C5-5. Due to the low S/N of these observations, we do not include either N10-4 or C5-5 in the remainder of the analysis.

2.4 Emission Line Source: HII regions vs. AGN

We use the diagnostic diagrams of Veilleux & Osterbrock (1987) to determine whether the emission lines in the observed LSB galaxies come from active galactic nuclei (AGN) or HII regions. Figure 2.6a shows the [N II]λ6584/Hα vs. [O III]λ5007/Hβ diagnostic. We overplot the theoretical separation line of Kewley et al. (2001a) on the diagram. The LSB galaxies all clearly lie in the HII side of the diagram. They also lie in the same area of the diagram as the HSB galaxies from the Nearby Field Galaxy Survey (NFGS; Jansen et al., 2000). Figure 2.6b shows the [S II]λ6717+λ6731/Hα vs. [O III]λ5007/Hβ emission line diagnostic. The interpretation here is less clear. The LSB galaxies all lie on the separatrix, and there is considerably more scatter amongst the NFGS galaxies as well. Kewley et al. (2001b) note that the [S II]λ6717+λ6731/Hα ratio is sensitive to the local density, and therefore might be a less reliable diagnostic than the [N II]λ6584/Hα ratio. N10-2 shifts dramatically between the two diagnostics, relative to the rest of the LSB galaxies. This is an instrumental effect, as the redshifted [S II] lines fall just at the red end of our spectral coverage, where the flux calibration is less secure. All the galaxies with emission lines are consistent with star formation as the ionizing source, rather than AGN.

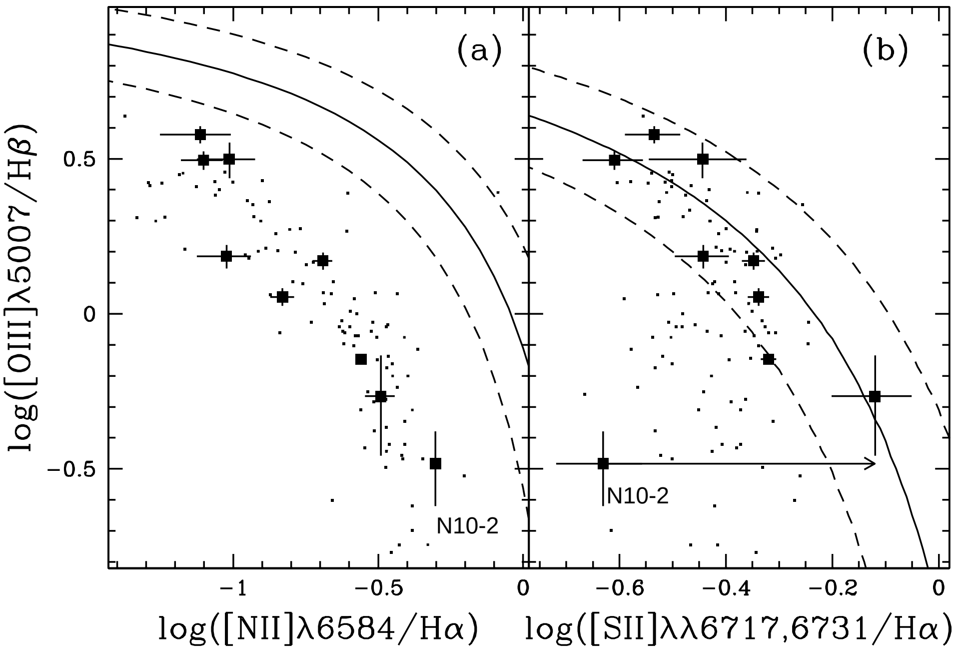

Figure 2.6 Ionization diagnostic diagrams: large boxes – LSB galaxies; small boxes – galaxies in the NFGS sample (Jansen et al., 2000); lines – theoretical classification line and ±0.1 dex error range separating AGN from starburst (HII) galaxies, from Kewley et al. (2001a). The LSB galaxies are all well within the HII region for the [N II]/Hα vs [O III]/Hβ diagnostic. There is a shift in the data with respect to the theoretical separatrix in the [S II]/Hα vs [O III]/Hβ diagnostic. However, the LSB galaxies are all still consistent with starburst like spectra. The shift of N10-2 between (a) and (b) is a result of poor flux calibration at the extreme red end of the spectrum, which affects the [S II] measurements. The arrow shows the uncertainty in [S II]/Hα for N10-2 due to this systematic effect.

2.5 Mean Age and Metallicity of the Stars

The degeneracy between the effects of age and metallicity on broadband optical colors and individual spectral features has been well documented (O'Connell, 1976; Worthey, 1994; Rose, 1994). This degeneracy can be broken by using combinations of two or more absorption features, with different sensitivity to age and metallicity (Worthey et al., 1994; Jørgensen, 1997; Vazdekis, 1999; Kuntschner et al., 2001). We use the line index $H\beta$ which is more age sensitive, in conjunction with the more metal sensitive indices Mgb and $<$Fe$>$. In Figure 2.7 we plot grids of age and metallicity for single stellar populations derived from the V2000 models, on the axes of $H\beta$ vs. Mgb and $H\beta$ vs. $<$Fe$>$. Within this grid, we determine the mean luminosity weighted age and metallicity for the stellar populations of the four absorption line dominated LSB galaxies, C1-2, C1-4, N3-1, and U1-8. We also plot the two elliptical galaxies which we observed, as well as the locus of points covered by the Coma cluster elliptical and S0 galaxies from Jørgensen (1999).

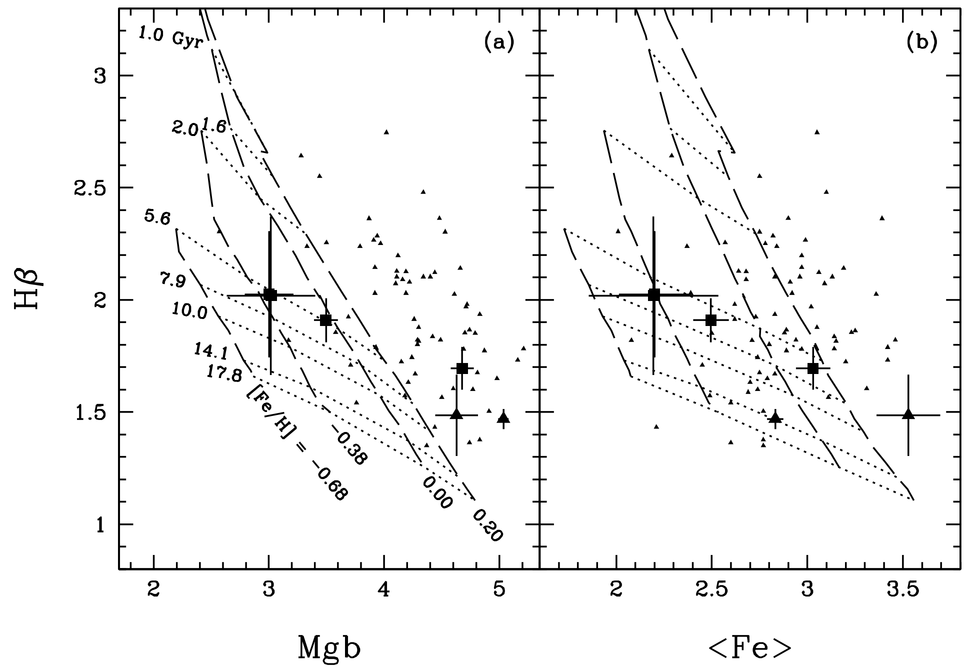

Figure 2.7 Hβ absorption line index vs. the Mgb index (left) and the < Fe > index (right). Boxes: LSB galaxies; Large triangles: our data of HSB ellipticals; small triangles: Coma cluster elliptical and S0 galaxies from Jørgensen (1999). The model grid shows lines of constant age (dotted) and constant metallicity (long dash), from V2000 as labelled. The same age and metallicity values are used for the grid in both panels. The four LSB galaxies plotted are (in order of increasing Mgb, < Fe > strength) U1-8, C1-2, C1-4, and N3-1. Note that the points for C1-2 and U1-8 lie virtually on top of eachother. The Coma cluster galaxies, N3-1, and NGC 3872, shift relative to the model grid in the two plots. This is caused by the well known super-solar [Mg/Fe] ratio in luminous elliptical and S0 galaxies, which is not reproduced by the models.

The three LSB galaxies C1-2, C1-4 and U1-8 all lie together on the plots, in the low metallicity regime. They all have mean ages around 5.5 Gyr. C1-4 has near solar metallicity, while C1-2 and U1-8 have about half solar metallicity.

In contrast, N3-1 has a much higher metallicity, appearing at 1.5 times solar metallicity in the Hβ vs. $<\mathrm{Fe}>$ plot, and even higher in the Hβ vs. Mgb plot. This is the regime shared by luminous elliptical and S0 galaxies. Furthermore, note how N3-1 as well as the elliptical and S0 galaxies shift with respect to the model grid between the two plots. This is the signature of super-solar [Mg/Fe] abundance ratios. This enhancement effect is well known for luminous galaxies, both spirals and ellipticals, and the strength of the enhancement is correlated with galaxy mass and velocity dispersion (Worthey, 1998; Jørgensen, 1999; Kuntschner et al., 2001). The other three LSB galaxies do not move relative to the model grid between the two plots; these galaxies all have solar [Mg/Fe] abundance ratios.

Figure 2.8 more clearly illustrates the [Mg/Fe] issue. This plot shows the $<\mathrm{Fe}>$ index plotted against the Mgb index. Since these two indices have similar metallicity and age sensitivity, the model grid for differing ages and metallicities is not well separated in this plane. Galaxies with solar [Mg/Fe] should fall onto the narrow region covered by the model grid, as indeed most of the LSB galaxies do. On this Figure we also show the LSB galaxies with emission lines which have reliable Mgb and $<\mathrm{Fe}>$ measurements. The bulk of the elliptical and S0 galaxies as well as N3-1 fall to the right of the model grid, a failure of the models to account for the [Mg/Fe] appropriate to these galaxies.

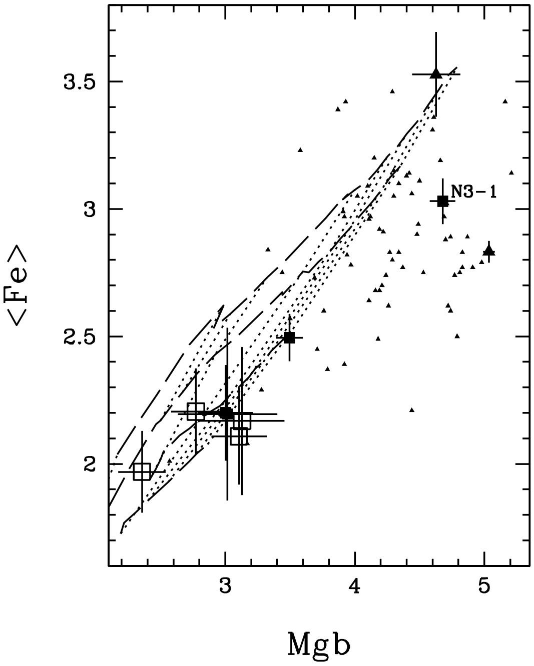

Figure 2.8 The < Fe > index vs. the Mgb index. Filled boxes: LSB galaxies with no Hβ emission; Open boxes: LSB galaxies with measured Hβ emission; Large triangles: our data of HSB ellipticals; small triangles: Coma cluster elliptical and S0 galaxies from Jørgensen (1999). The same models used for the grid in Figure 2.7 are used here. The Mgb and < Fe > indices have similar sensitivity to age and metallicity, so the model grid is very narrow. N3-1, like many of elliptical galaxies, lies off the model grid, suggesting super-solar [Mg/Fe] abundance. See the text for details.

There is another caveat with these models, especially important when dealing with low metallicity stellar populations. These models do not include blue horizontal branch or post-AGB stars, which will have an effect on measured Balmer line strengths (Maraston & Thomas, 2000). However, at the lowest metallicities found here (a tenth solar to a fifth solar), galactic globular clusters do not show a blue horizontal branch, and thus we do not expect contamination by these blue stars to be a significant effect. Furthermore, the effect of these stars on integrated spectra is to increase the strength of the Hβ absorption, leading to younger apparent ages. The main conclusion of this section is that some LSB galaxies do in fact have old mean ages; a correction for these blue stars would only strengthen our conclusion.

2.6 Gas Phase Metallicity and Age Indicators

Much as we used the stellar absorption indices to study the older stellar populations, we would like to use emission line strengths and ratios to characterize the metallicity of the gas and the properties of the young stellar populations. The equivalent width of Hα, EW(Hα), compares the flux from hot young stars, capable of ionizing nebulae, to the red flux from the stellar population, which is dominated by long-lived lower mass stars for a standard (e.g. Salpeter, 1955) initial mass function (IMF). Consequently, the EW(Hα) can be used as a mean age indicator for the integrated stellar population. The conversion between EW(Hα) and the Scalo (1986) birthrate parameter, defined as $b \equiv \frac{\mathrm{SFR}}{<\mathrm{SFR}>_{\mathrm{past}}}$, is sensitive to both the form of the star formation history (SFH) and the IMF, and hence is quite model dependant. A single burst of star formation will only produce Hα emission for ~ 30 Myr after which the massive stars ($M_\star > 15\ M_\odot$) which produce the ionizing flux have all died off. Models with continuous star formation and multiple burst models that produce an underlying old population plus a new burst will both produce Hα emission at later times. Kennicutt, Tamblyn, & Congdon (1994) use stellar population and nebular models to derive a relation between EW(Hα) and *b* appropriate for galaxies with a constant or exponentially decreasing SFR. The relation they derive, based on a Salpeter (1955) IMF with upper and lower mass limits of 100 and 0.1 $M_\odot$, a 10 Gyr age and varying exponential decay times, shows a monotonic increase of *b* with EW(Hα), and has *b*=1 at EW(Hα)=64 Å. van den Hoek et al. (2000) found that chemo-evolutionary models with an exponentially decreasing SFR were sufficient to describe the LSB galaxies in their sample with $(B-V)>0.4$ but that additional star formation bursts were needed to explain bluer galaxies. The measured EW(Hα) for an old-plus-burst stellar population will of course depend on both the age of the burst, and the stellar mass fraction that it embodies. In Figures 2.10 and 2.12 we show the *b* calibration of Kennicut et al. (1994) on the right vertical axis, but give the caveat that this calibration is inappropriate for an old-plus-burst SFH.

Traditional methods of studying gas phase chemical abundances in HII regions require measurements of several H or He recombination lines, along with collisionally excited lines from multiple ionization states of a heavier metallic species. Osterbrock (1989) details the method for studying individual HII regions. Kobulnicky et al. (1999) extend this work and look at the effect on the derived abundances of smearing together the light from multiple HII regions in a single galaxy into a single spectroscopic aperture, using abundance analysis methods such as the semi-empirical strong-line R_{23}[4] method (Pagel et al., 1979; Osterbrock, 1989; McGaugh, 1991, 1994). The wavelength range covered by our spectra rarely includes the [O II]λ3727 Å line used in the R_{23} method. Instead, we choose to use the metallicity indicator [N II]λ6584/Hα (hereafter [N II]/Hα) proposed by Storchi-Bergmann, Calzetti, & Kinney (1994). This measurement has the advantage of being monotonic (as opposed to the double valued nature of the R_{23} method) and is essentially reddening independant by virtue of the small wavelength split between the two lines. Empirical calibrations between [N II]/Hα and log(O/H) (determined using the R_{23} method) have been derived from observations of individual HII regions (e.g. van Zee et al., 1998) and for galaxies (Denicoló, Terlevich, & Terlevich, 2002). The drawback to using [N II]/Hα is that this ratio is sensitive to the ionization state, which will vary between HII regions and the diffuse ISM, and is difficult to determine for globally averaged spectra. Kewley & Dopita (2002) provide a theoretical calibration of [N II]/Hα vs. metallicity for starburst galaxies, including the effects of the ionization parameter. McGaugh (1994) find for HII regions in LSB galaxies that the ionization parameter $\log\langle U\rangle$ varies between -2 and -3.5, while Denicoló et al. find that $\log\langle U\rangle=-2.0$ is most representative for their sample of galaxies. However, a change in $\log\langle U\rangle$ of +0.5 dex or -1.0 dex leads to an uncertainty in the metallicity zeropoint of ±0.3 dex. There was no correlation seen between metallicity and $\log\langle U\rangle$ in the McGaugh dataset. In the plots that follow, we label one axis with the Denicoló et al. empirical calibration of [N II]/Hα, but we give the caveat that the zeropoint of this calibration may be high by $\simeq$0.3 dex and

---

[4] $\log(R_{23}) = \log(\frac{[OII]\lambda3727+[OIII]\lambda\lambda4959,5007}{H\beta})$

that any systematic changes of the ionization parameter with other parameters of these galaxies such as age may lead to a misinterpretation of the [N II]/Hα ranking as a strict metallicity scale.

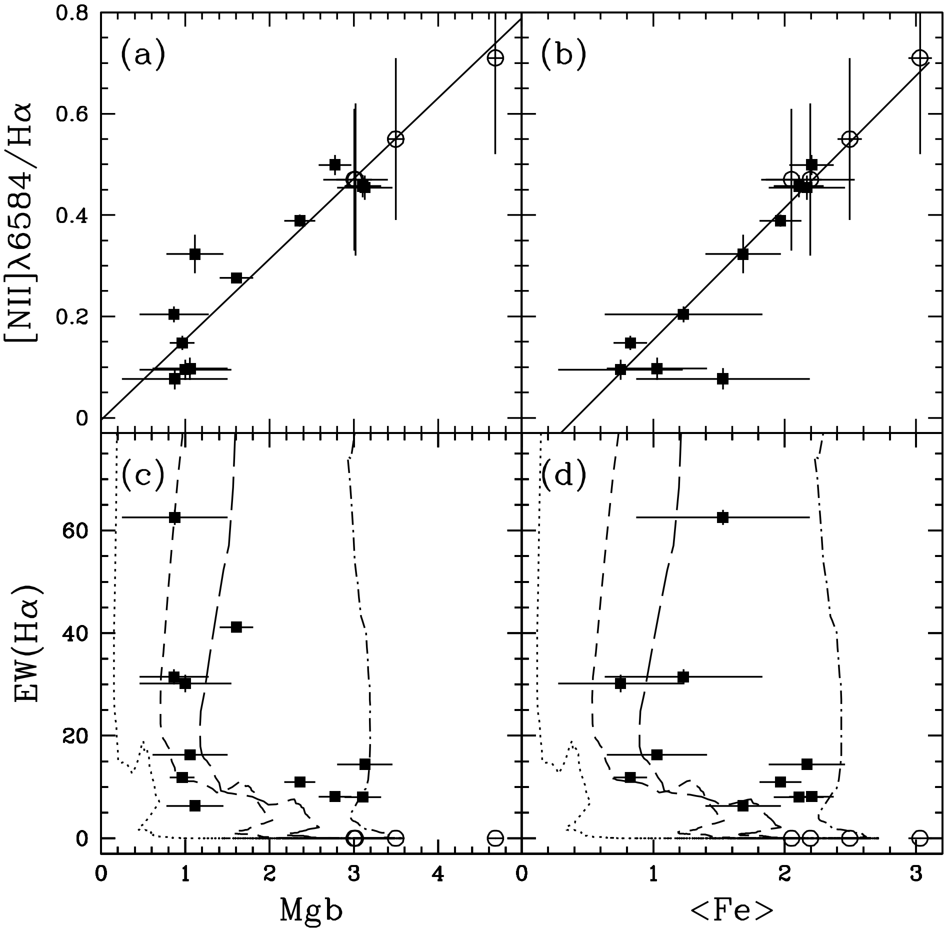

Figure 2.9 Comparison of gas phase indicators and stellar absorption line indices. The gas phase [N II]/Hα ratio plotted against (a) the stellar Mgb line index and (b) the < Fe > line index. The best fitting relations are shown as solid lines. (c) The EW(Hα) vs. the Mgb index. (d) EW(Hα) vs. the < Fe > index. Boxes: LSB galaxies with measured emission lines; circles: LSB galaxies with no measured emission, see Section 2.6 for details. The lines in panels (c) and (d) are evolutionary tracks for an old-plus-burst stellar population, with a 5 Gyr old population, and bursts which comprise (from left to right) of 10% (dotted), 2% (short-dash), 1%(long-dash) and 0.1% (dot-dash) of the total stellar mass. The kink in these evolutionary tracks occurs at $\sim$ 7.5 Myr after the burst, and the EW(Hα) drops below 1 Å within 20 Myr of the burst for all the tracks. The tracks all end at Mgb = 3.6 and < Fe > = 2.7, EW(Hα) $\simeq$ 0, which are the values of the underlying population.

We compare the gas phase metallicity indicator [N II]/Hα with the stellar absorption indices Mgb and $<$Fe$>$ in Figure 2.9. There are clear correlations with each index. A Kendall's τ test gives a probability of 1.6% that [N II]/Hα and Mgb are not correlated, and a probability of 0.08% that [N II]/Hα and $<$Fe$>$ are not correlated. The best fit relations are:

$$[\mathrm{NII}]/\mathrm{H}\alpha = -0.11(\pm 0.13) + 0.26(\pm 0.08) \cdot <\mathrm{Fe}> \tag{2.1}$$

$$[\mathrm{NII}]/\mathrm{H}\alpha = -0.01(\pm 0.09) + 0.16(\pm 0.05) \cdot \mathrm{Mgb} \tag{2.2}$$

It is perhaps surprising that the correlations are so strong, given the age-metallicity degeneracy of the stellar indices and the variation of the [N II]/Hα calibration with ionization parameter. Panels c and d in Figure 2.9 show the age indicator EW(Hα) plotted against the absorption line indices. At low Mgb strength, we see a wide range of EW(Hα) strengths, which diminishes at higher Mgb strengths. In models with continuous, exponentially decreasing SFR, the metallicity increases as the gas fraction decreases. Simultaneously, the SFR drops and the fractional galaxy mass made up by low mass stars increases. This will result in a decrease of EW(Hα) and simultaneous increase of Mgb over time, leading to an upper envelope in the EW(Hα) vs Mgb plane, much as we see here. For "open box" chemical evolution models (models in which enriched gas is allowed to escape due to stellar winds and supernovae), the low EW(Hα) and low Mgb region will get filled in by galaxies with low total mass, where the star formation rate drops once the gas is expelled, and before metallicity builds up. In any case, once star formation stops completely, the EW(Hα) will drop to zero, and the Mgb index will slowly strengthen as the stellar population ages (at constant metallicity). This picture holds equally well for the $<$Fe$>$ strength as for Mgb. A quantitative analysis of where models with continuous star formation would lie on the EW(Hα) vs. metal absorption index plots requires models that contain both nebular emission spectra, and stellar absorption line strengths. Unfortunately, there are not yet any such models in the literature. Within the picture of continuous star formation, we can also give a qualitative explanation for the strong correlation seen between [N II]/Hα and Mgb or $<$Fe$>$. [N II]/Hα reflects the current metallicity of the gas. The ionization parameter is a small source of scatter, but is not (apparently) significant. The Mgb and $<$Fe$>$ strengths are responsive to both the metallicity and age of the stellar population, but since these are linked by the gas consumption and enrichment history, a correlation exists between the current metallicity and the age and enrichment history of the stellar population.

An alternative explanation can be given by a model with an old stellar population underlying a young burst of star formation. In this case, the mass fraction of the burst and metallicity of the old population will determine the evolutionary track of a galaxy through the EW(Hα) vs. Mgb (or $<$Fe$>$) plane. The mass fraction determines how much blue continuum light from the young stellar population there will be to veil the strength of the underlying metal line absorption. The Hα flux is driven by very short-lived stars, while the continuum veiling effect evolves over longer timescales ($\simeq$ 0.5 Gyr vs. $\simeq$ 30 Myr for the Hα). Consequently, the tracks will move vertically down the diagram, and then to the right at late times. The track will end at the absorption line strength of the underlying population for small bursts, and the offset between where the track descends vertically and where it ends depends on the mass fraction of the burst. To illustrate this, we use the Starburst99 models (Leitherer et al., 1999) for the evolution of an instantaneous burst population, along with the V2000 stellar population models for the underlying population. In Figure 2.9(c-d) we plot the data for the LSB galaxies together with model tracks for galaxies with a 5 Gyr old, solar metallicity underlying population, and a 10%, 2%, 1%, and 0.1% (by mass) instantaneous burst. It is clear that by varying the age and metallicity of the underlying population, or by varying the burst mass fraction, it is possible to fill in every part of the plot. While we do not find LSB galaxies in all parts of the plot, we have a small sample and do not strongly constrain against the possibility of galaxies in the high EW(Hα) and high Mgb (or $<$Fe$>$) region of the diagrams.

It is possible to fully explain the EW(Hα), Mgb, and $<$Fe$>$ data with an old ($>$ 5 Gyr) solar metallicity population and varying burst mass fractions. However, with this model the [N II]/Hα vs. Mgb correlation becomes difficult to explain. The [N II]/Hα value should reflect the metallicity of the burst, which is presumably greater than or equal to the metallicity of the underlying stellar population. If the underlying stellar population is always metal rich and the burst mass fractions were random, pushing the absorption line indices to lower levels, there would not be a correlation between [N II]/Hα and the absorption indices. Consequently, it appears that old-plus-burst models are only viable if the old populations have a range of metallicities, and if any one burst constitutes only a small fraction of the stellar mass (less than $\sim$ 0.3%) such that the absorption indices are not perturbed from that of the underlying population.

Our understanding of these correlations is hampered by the small size of our sample, and discontinuity between models which predict nebular emission strengths from young stellar populations, and models which predict the stellar metal absorption line indices for older, cooler populations. Ideally, we could gleen a better understanding of these correlations from a larger sample of LSB or HSB galaxies. However, we have been unable to find published studies of HSB galaxies which include data on both the stellar absorption indices and emission line strengths. The NFGS and Sloan Digital Sky Survey (though the latter is prone to aperture effects) represent two datasets upon which it would be enlightening to make this study.

We cannot measure gas phase abundances for the four absorption line dominated galaxies, but we use the correlations in Equations (2.1) and (2.2) to assign values of [N II]/Hα to these galaxies. We do this primarily so that we can include these four galaxies on the remainder of the diagnostic diagrams, where we use [N II]/Hα as a metallicity indicator. We interpolate the relations get values for C1-2 and U1-8, and extrapolate to get values for C1-4 and N3-1. The values determined from each of the two correlations are averaged, to reduce the uncertainties. The assigned [N II]/Hα values are as follows: 0.47±0.15 for C1-2; 0.47±0.14 for U1-8; 0.55±0.16 for C1-4; 0.71±0.19 for N3-1. These four galaxies are shown as open circles on Figure 2.9. The absorption line dominated galaxies seem to lie at one end of a continuous sequence of spectral properties, as illustrated by Figs. 2.3a - 2.3d. This suggests that the extrapolation of these correlations is reasonable. However, we do note that stellar populations at constant metallicity will evolve to higher

Mgb and $<\text{Fe}>$ with age once the star formation stops. Though we do not see a large age spread among the four absorption dominated systems, age will affect the extrapolation of these relations to higher index strengths. By including both the absorption and emission line galaxies in Figures 2.10 and 2.12 we attempt to show these galaxies potentially have very similar evolutionary histories (though they are perhaps at different stages of that evolution). The emission associated with a small burst of star formation is very short-lived, and though the emission line flux can be significant, the associated effect on the chemical evolution and continuum luminosity could be slight, and so understanding these two ”classes” of LSB galaxies, absorption and emission line galaxies, is necessarily intertwined.

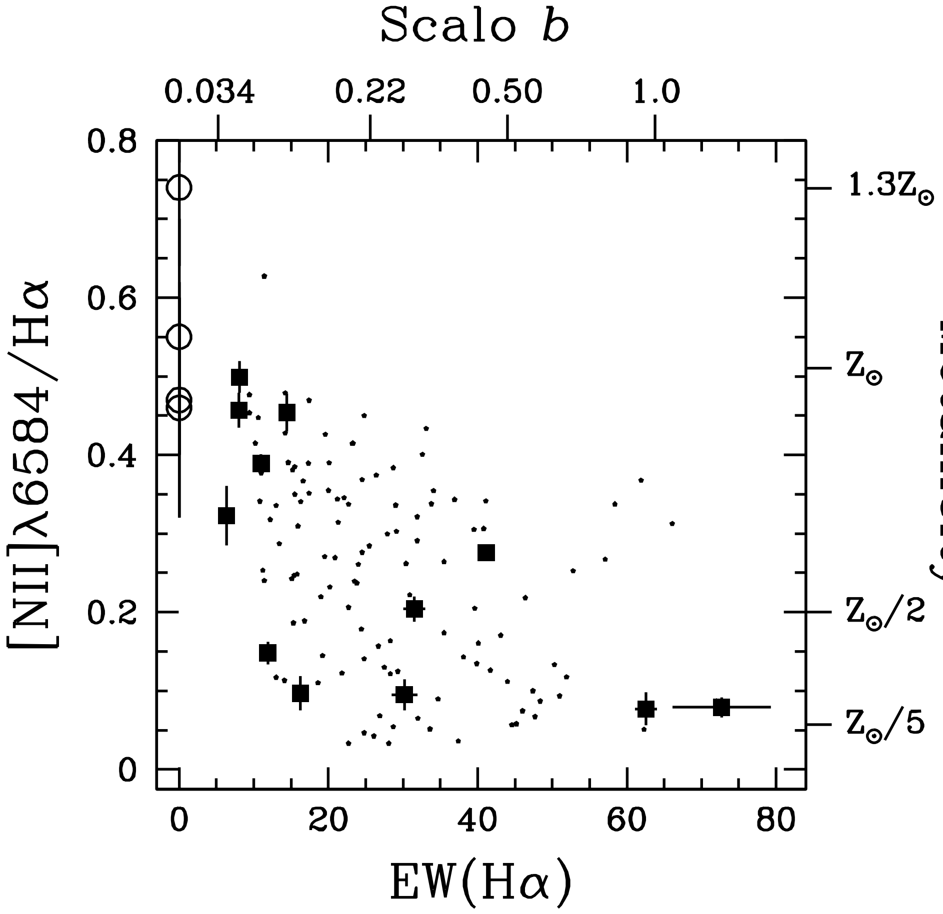

Figure 2.10 The metallicity indicator [N II]/Hα plotted against EW(Hα), a measure of the birthrate parameter. Large boxes: LSB galaxies with measured emission lines; circles: LSB galaxies with no measurable emission lines whose positions are based on the extrapolation described in Section 2.6; small boxes: HSB galaxies from the NFGS (Jansen et al., 2000). The right axis shows the [N II]/Hα metallicity calibration of Denicoló et al. (2002), appropriate for HII regions. The top axis shows the EW(Hα) calibration of the Scalo birthrate parameter for one star formation model detailed in Kennicut et al. (1994). See text for details.

In Figure 2.10 we plot [N II]/Hα against the EW(Hα) for the LSB galaxies. The metallicity and birthrate calibrations discussed at the beginning of this section are included on the axes opposing the measured parameters. We also plot the HSB galaxies from the NFGS (Jansen et al., 2000), which satisfy the condition that EW(Hα)$>$9 Å (i.e. those which have a small measurement uncertainty for the [N II]/Hα line ratio). The LSB galaxies fill the same region of the [N II]/Hα vs. EW(Hα) parameter space, suggesting a similar star formation and chemical enrichment history to that of HSB galaxies. At low metallicities there is a wide range of mean ages, however the relative current SFR decreases as metallicity increases. This makes sense for continuous star formation, as the bulk of the gas in these galaxies must have been previously processed into stars to raise the mean metallicity, and consequently there is less gas around to make new stars.

2.7 Dust Content

The amount of internal reddening in LSB galaxies is not well known, but of great importance to attempts at modelling their formation and evolution. In Figure 2.11a we plot the Balmer ratio, Hα/Hβ, versus the metallicity indicator [N II]/Hα. The Balmer ratio can be used to derive the internal reddening of the emission line regions. Using the Cardelli extinction law (Cardelli et al., 1989), with R_V=3.1, we derive the following relation:

$$\mathrm{E(B-I_c)} = 2.375 \cdot \mathrm{E(B-V)} = \frac{\log(\frac{f(H_\alpha)}{f(H_\beta)})}{0.172} - 2.65 \tag{2.3}$$

This relation is used to place an $E(B-I_c)$ scale on the right axis of Fig.2.11. We use the NFGS (Jansen et al., 2000) as a comparison sample of HSB emission line galaxies. The NFGS galaxies were not observed in the I-band. We convert their $(B-R_c)$ colors to $(B-I_c)$ colors using the relation $(B-I_c) = 1.34 \cdot (B-R_c) + 0.18$, derived from the mean galaxy colors of Fukugita, Shimasaku, & Ichikawa (1995). Central surface brightnesses were not derived for the NFGS galaxies. In the LSB data, we have not corrected the measured Hα fluxes and equivalent widths for underlying stellar absorption. This correction will move points upwards and to the left in the Hα/Hβ vs. [N II]/Hα plane. While the uncorrected data show a trend for LSB galaxies to have lower extinction than HSB galaxies at the same metallicity, an Hα equivalent width correction of 1.5 Å would move most of the LSB galaxies onto the locus of HSB galaxy points.

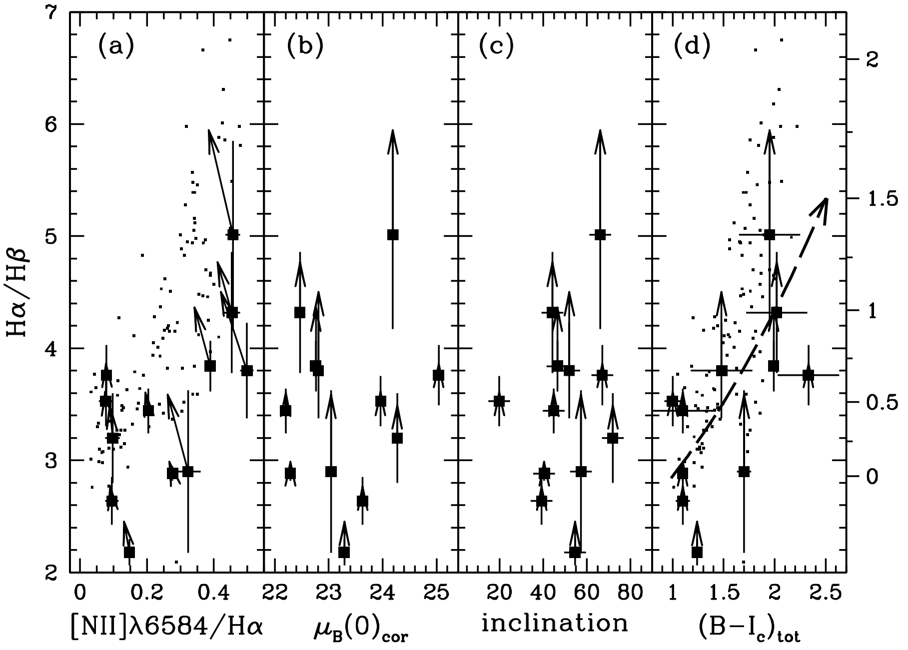

Figure 2.11 The Balmer ratio, Hα/Hβ, plotted against (a) the metallicity indicator [N II]λ6584/Hα, (b) the central surface brightness $\mu_{\mathrm{B}}(0)_{\mathrm{cor}}$, (c) galaxy inclination (edge-on = 90°), and (d) The total (B−I_c) color. Large boxes – LSB galaxies; small points – galaxies from the NFGS (Jansen et al., 2000). The right side y-axis lists the E(B−I_c) values derived from equation 2.3. The vertical arrows show where the LSB galaxies would move if we made a correction of 1.5 Å to the Hα equivalent width to account for underlying stellar absorption. The dashed arrow in panel (d) shows the locus of reddening vectors for the LSB galaxies. The reddening vector for the NFGS galaxies (whose colors have been transformed from observed (B−R_c) colors) would be ≃10% steeper. The uncertainties shown for the Balmer ratios do not include those caused by uncertainties in the absorption correction to Hβ. The NFGS data has not been corrected for underlying stellar absorption at Hα or Hβ. Applying an arbitrary correction of 1.5 Å to the equivalent width of both Hα and Hβ does not significantly shift the location of the locus of HSB galaxy points.

McGaugh (1994), in his study of LSB galaxy HII regions, found evidence for dust in some galaxies, with internal extinctions as high as $\mathrm{E(B-V)} \sim 0.5$ (corresponding to $\mathrm{E(B-I_c)} \sim 1.3$). The galaxies in that study were similar to the lower metallicity galaxies ([N II]/H$\alpha < 0.2$) in Figure 2.11a for which we find a similar range of reddenings. His study did not include any of the red or giant LSB galaxies for which we find generally larger reddening values.

The dust distribution in galaxies tends to be clumped, and these reddening values apply only to the regions where the emission lines are produced. The emission line regions and light from the stellar disk are not spatially resolved in our observations and both contribute to the extracted spectra. Consequently, we cannot constrain the reddening affecting the general stellar disk, which dominates the continuum luminosity of the galaxy, and thus we do not make a correction to the global photometry for internal extinction.

Figure 2.11a shows a trend for the Balmer ratio (and presumed reddening) to increase with increasing gas-phase metallicity. In Figure 2.11(b-d) we plot the Balmer ratio versus photometric parameters dominated by the stellar disk. There is no correlation at all between Hα/Hβ and central surface brightness over the range $22 \leq \mu_B(0)_{\mathrm{cor}} \leq 25$, nor is there a correlation between Hα/Hβ and galaxy inclination. The correlation between $(\mathrm{B-I_c})_{\mathrm{tot}}$ color and the Balmer ratio is shown for the NFGS galaxies in Figure 2.11d. The LSB galaxies fall onto the same locus of points, especially after applying a correction for underlying Hα absorption of 1.5 Å. The LSB galaxies appear to lie along the reddening vector in Figure 2.11d. This might imply that the dust is not local to the emission region, but is instead mixed throughout the galaxy. Alternatively, it is possible that the colors are not caused by dust reddening of the stellar light, and the relation between Hα/Hβ and $(B-I_c)_{tot}$ is not the fundamental one. Rather, the amount of dust increases with increasing metallicity (Fig. 2.11a), and the stellar populations also become redder with increasing metallicity (cf. the tight correlation between [N II]/Hα and $(B-I_c)_{tot}$ shown on Fig. 2.12c, and the corresponding discussion in Section 2.8), which in turn results in the correlation seen here between $H\alpha/H\beta$ and $(B-I_c)_{tot}$. If the colors are driven by dust reddening over the whole galaxy, then we would expect to also see a correlation between galaxy inclination and reddening, with higher reddening measurements for galaxies closer to edge-on. We do not detect any such correlation, and thus conclude that the correlation between $H\alpha/H\beta$ and $(B-I_c)_{tot}$ is secondary, and both parameters are driven primarily by the metallicity.

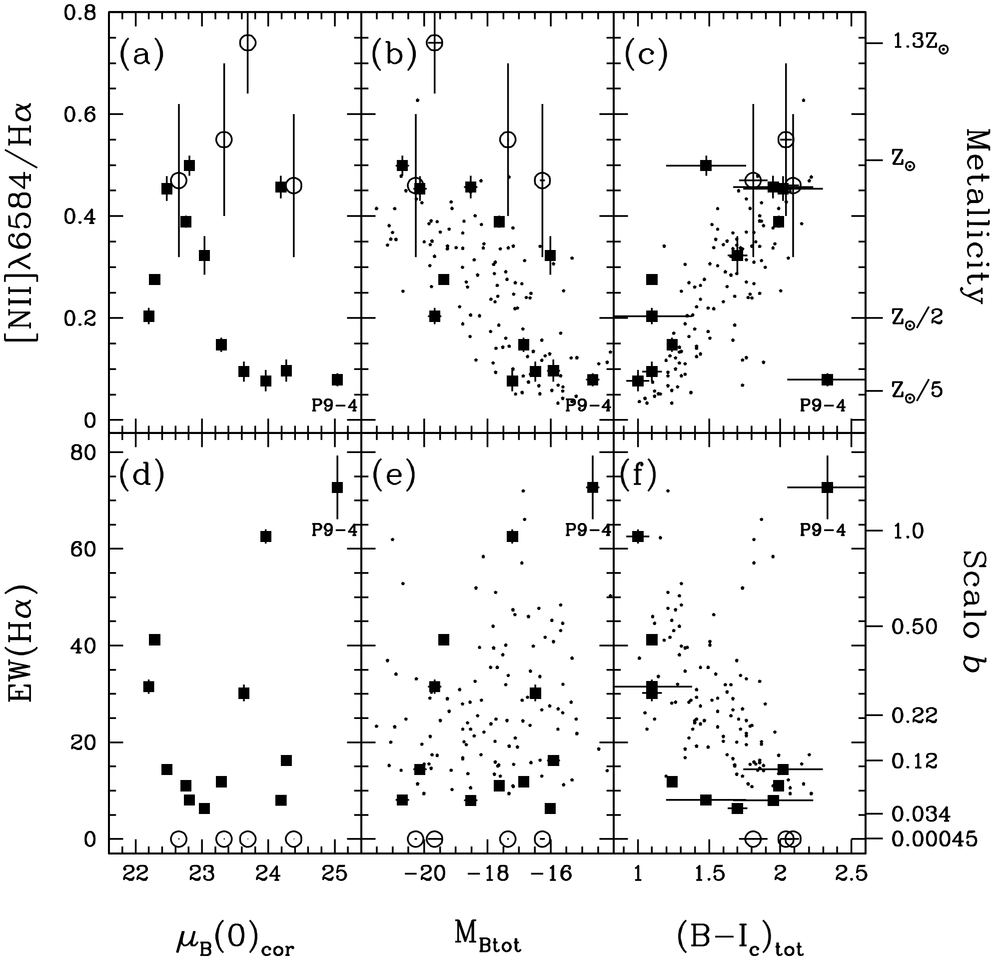

Figure 2.12 The metallicity indicator [N II]/Hα and the age indicator EW(Hα) plotted against central surface brightness, $\mu_B(0)_{cor}$, absolute magnitude, M_{Btot}, and (B−I_c) color. Large boxes: LSB galaxies with measured emission lines; circles: LSB galaxies with no measured emission lines; small pentagons: emission line galaxies in the NFGS (Jansen et al., 2000). On the right side axes are the metallicity and birthrate parameter calibrations described in Section 2.6. The correlation between metallicity and absolute magnitude found for HSB emission-line galaxies is also seen in LSB galaxies. We do not detect a significant correlation between metallicity and surface brightness in this sample. The strongest correlation is between color and [N II]/Hα. See text for comments on the published photometry for P9-4.

Regardless of the interpretation of the galaxy colors, it is clear that dust is present in abundance in some LSB galaxies, particularly the red and high metallicity ones, but the absence of a correlation between dust and $\mu_B(0)_{cor}$ suggests that dust is not the cause of the low surface brightness for LSB galaxies of any color.

The relative emission line strengths presented in Table 2.7 have not been corrected for internal extinction within these galaxies. The line ratios we use in our analysis (e.g. [N II]/Hα) all have narrow wavelength spreads, and are not significantly affected by dust in the amount we detect. The uncertainty of a correction for intrinsic reddening, however, would be significantly larger than the correction itself (which is negligible), and so we do not apply any correction.

2.8 Emission Line Properties Versus Global Photometric Properties

In Figure 2.12, we show [N II]/Hα and EW(Hα) versus central surface brightness, absolute magnitude, and $(B-I_c)_{tot}$. We plot the absorption line galaxies in this figure as well, using the [N II]/Hα values derived and discussed in Section 2.6. However, these four galaxies are never included when we measure correlations between the parameters plotted in Figure 2.12.

In Figures 2.12c and 2.12f, the outlier P9-4 at $(B-I_c)$=2.08 (OBSCI97) is purportedly the reddest object in the sample, despite its high EW(Hα) and metal poor nature. The continuum slope in our HET spectrum of this object is very flat. In comparison, the galaxies at $(B-I_c)$=1.3 have bluer continua, but those at $(B-I_c)$=1.8 have redder continua. The continuum slope of N10-2 $(B-I_c)$=1.57 is also very flat. We suggest that there are errors in the published photometry for P9-4. We label P9-4 in all panels of Figure 2.12 and we do not include the data for P9-4 in the determination of any of the correlations discussed below.

Figures 2.12a and 2.12d show that there is a broad range of both [N II]/Hα and EW(Hα) values for the whole range of surface brightnesses studied. A Kendall's τ test gives a probability of 58% that there is no correlation between EW(Hα) and $\mu_{\mathrm{B}}(0)_{\mathrm{cor}}$. There is a probability of 31% that there is no correlation between [N II]/Hα and $\mu_{\mathrm{B}}(0)_{\mathrm{cor}}$. In contrast, Bell & de Jong (2000) found correlations both between mean age and K-band central surface brightness, and between mean metallicity and K-band central surface brightness. Their modelling involved an assumption of exponentially decreasing star formation rates all beginning at the same time in the past (12 Gyr), with different exponential timescales, τ, which thus produced stellar populations with different luminosity-weighted mean ages at the current epoch. They varied τ and metallicity in their models to produce a grid in the ($\mathrm{R_c}-\mathrm{K}$) vs. ($\mathrm{B}-\mathrm{I_c}$) plane, which was then used to interpret their data. These models have a very similar SFH to the models of Kennicut et al. (1994), which we use for the right side scale on Figure 2.12(d-f) and which predict a monotonic relationship between EW(Hα) and τ, and consequently mean age. However, as mentioned above, we do not see a correlation between EW(Hα) and B-band central surface brightness. Bell & de Jong make an unweighted least-squares fit to their data which produces a change in mean age of 0.84 ± 0.08 Gyr for a change of two magnitudes in central surface brightness, equivalent to the range covered by our sample, with lower luminosity-weighted mean ages occuring at lower central surface brightness. Their fit to the metallicity-surface brightness relation produced a change in the mean metallicity of 0.26 dex for the same two magnitude change in central surface brightness, with higher metallicity at higher surface brightness. Our sample size, though similar to the LSB galaxy study of Bell et al. (2000), is a small fraction of the combined HSB-plus-LSB galaxy sample of Bell & de Jong. It is quite possible that our sample selection, which deliberately covers a wide range of galaxy colors and surface brightnesses, has led to more scatter than would be present in a volume-limited sample of galaxies, and that therefore we might not be sensitive to these predicted modest changes in mean age and metallicity.

The line ratio [N II]/Hα versus the absolute magnitude is shown in Figure 2.12b. This plot makes clear the point that LSB galaxies are not synonomous with dwarf galaxies, but cover a range of absolute magnitudes comparable to that of HSB galaxies. The emission line LSB galaxies show a correlation between [N II]/Hα and absolute magnitude. A Kendall's τ test gives a probability of 5% that no correlation is present. The relation for LSB galaxies matches that of the NFGS galaxies. The LSB galaxies without emission also follow the correlation, but form a ridge on the faint, high metallicity edge of the galaxy distribution. This may be reflecting a higher B-band mass-to-light ratio in these older objects, if the [N II]/Hα-M_{Btot} relation is a result of a more fundamental metallicity-mass relation. Alternatively, it could reflect a systematic error in the interpolation/extrapolation of the [N II]/Hα-Mgb and [N II]/Hα-$<$Fe$>$ relations used for the non-star-forming galaxies.

The distribution of the LSB galaxies is a good match to that of the NFGS galaxies in Figure 2.12e. We do not detect any correlation between EW(Hα) and

M_{Btot}. A Kendall's τ test gives a probability of 30% that there is no correlation for the emission line LSB galaxies. A rough scaling of the absolute SFR can be determined by multiplying the EW(Hα) by the total R-band luminosity, which includes the continuum near Hα. Within our sample, the galaxies with the largest (EW(Hα) $\cdot$ L_B) are the ones at the higher surface brightness end of our range, with $\mu_B(0)_{cor} \lesssim 23.0$ mag/$\square''$. Galaxies with lower total SFR will be found in the lower right of the EW(Hα) vs. M_{Btot} diagram. Our sample selection is neither complete nor representative, so we cannot comment on how the absolute star-formation rates of LSB and HSB galaxies compare. van den Hoek et al. (2000) found that the mean present-day SFR for a sample of late-type LSB galaxies was about one-tenth the SFR of similar HSB galaxies.

The relations between [N II]/Hα and EW(Hα) with (B$-$I$_c$) color, shown in Figs. 2.12c and 2.12f, are comparable in strength to those between [N II]/Hα and the stellar absorption indices Mgb and $<$Fe$>$. A Kendall's τ test applied to the emission line LSB galaxies gives a probability of 3% that there is no correlation between [N II]/Hα and $(B-I_c)_{tot}$. Similarly, there is a probability of only 2% that EW(Hα) and $(B-I_c)_{tot}$ are not correlated for the emission line LSB galaxies. (B$-$I$_c$) color is sensitive to changes in age, metallicity, and dust reddening, and all three may play some role in explaining the correlations. If we use the Denicoló et al. (2002) calibration for [N II]/Hα, the resulting metallicity range spanned by the data is less than one dex. At any constant age less than 5 Gyr, the V2000 stellar population models predict a maximum (B$-$I$_c$) color range of only 0.6 mag for a range in [Fe/H] from -1.0 dex to +0.2 dex. The $(B-I_c)_{tot}$ range spanned by our data is more than one magnitude, so varying only the metallicity of the stellar population is not a sufficient explanation for the colors. Stellar populations with mean ages older than 5 Gyr will show a wider color range over that range of metallicity, but are not supported by the ages determined in Section 2.5 for the four absorption line dominated LSB galaxies.

Including age in the interpretation of the colors requires us to make assumptions about the SFH in these galaxies. In Section 2.6, we discussed three plausible star formation scenarios: (1) continuous, but decreasing star formation rate with a build-up of metallicity, (2) old-plus-burst models with an old stellar population underlying a significant ($>1\%$ by mass) burst of star formation, and (3) old-plus-burst SFH models where the burst was small ($<0.3\%$ by mass) and produced Hα emission, but had little effect on the global photometric properties. Scenario (2) was rejected because it would not maintain the strong correlation between [N II]/Hα and Mgb or $<$Fe$>$. Scenario (3) was acceptable simply because the blue flux from the young population did not significantly veil the strength of the underlying metal absorption strength, and the [N II]/Hα - metal index correlations were unperturbed. However, this assumption also means that the global colors will not be significantly changed by the young burst. Consequently, for this SFH we must invoke a screen of dust as the explanation for the large range of $(B-I_c)$ colors. Scenario (1) predicts a correlation between age and metallicity, which then produces a tight correlation between metallicity and the Mgb, $<$Fe$>$ strengths for the stellar population. By invoking a correlated evolution of age and metallicity, we avoid adding scatter to parameters affected by both, including color. Furthermore, the range of $(B-I_c)$

colors in this picture is at least as great as the range seen in our data. The V2000 models for a 1 Gyr population with one-fifth solar metallicity predict $(B-I_c)=1.57$, while a 4 Gyr solar metallicity stellar population would have $(B-I_c)=2.55$. Mean ages less than 1 Gyr yield colors bluer than $(B-I_c)=1.5$, and while the zeropoint of the model colors is poorly calibrated, the range is more accurate. Dust, while certainly present in the emission line regions, is not necessary to explain the global colors in this scenario.

2.9 Discussion

The previous sections show that LSB galaxies cover a wide range of metallicities, and as a class they may contain both old and young stellar populations. Dust is present in some LSB galaxies, and may affect their global colors. Star formation occurs continuously in these galaxies, but with global rates which have varied exponential decay timescales. The metallicities of the galaxies are coupled to their ages, such that galaxies with older mean ages have reached a higher metallicity. Bursts that occur after long periods without star formation must make up a very small fraction of the total galaxy mass.

The detailed study of LSB galaxies is still a young field, partly because the observations are very difficult to make. The study of LSB galaxies originated with the realization that selection effects in imaging surveys had an impact on our understanding of the galaxy population, and galaxy formation and evolution in general. While we are now more conscious of some of the biases, samples chosen for follow-up study are still subject to selection effects. It is interesting to look at the studies in the literature in the context of our results, and determine what effects selection or observational biases have had on both our and the published conclusions.

Previous spectroscopic studies of LSB galaxy chemical abundances (McGaugh, 1994; Rönnback & Bergvall, 1995; de Blok & van der Hulst, 1998) were done on galaxies selected to have at least one bright HII region. These studies concluded that LSB galaxies were all metal-poor, with gas phase metal abundance less than one-tenth to one-fifth solar. These galaxies were selected from photographic surveys which were much more sensitive to blue galaxies than red galaxies at the surface brightness limit. Furthermore, the HII regions selected were the brightest HII regions in the galaxy, and lower metallicity HII regions will have higher ionization parameters and be brighter than high metallicity HII regions with similar numbers and ages of stars. Compared to our sample, and based on the implicit color criterion imposed by the photographic surveys, these studies were limited to having galaxies as blue or bluer than the five bluest galaxies in our survey. The five bluest galaxies in our study (C5-3, N9-1, U1-4, C4-1, and P1-3) all have active star formation, and define the low metallicity end of the sample. Though they do overlap the range of surface brightnesses and total absolute magnitudes covered by the rest of our sample, they are certainly not representative of the full continuum of LSB galaxy properties found for the sample.

Gerritsen & de Blok (1999) made an N-body simulation of the SFH for one of the blue late-type LSB galaxies from de Blok & van der Hulst (1998), and found that they required both low mass surface density and low metallicity to explain the properties of the galaxy. The SFH they derived has a slowly decreasing SFR when averaged over timescales of order 100 Myr, but has significant (factors of 2) deviations from the mean SFR on timescales of order 20 Myr. It is these deviations from the mean, they say, which explains the color range seen for LSB galaxies in general. Their models do not predict absorption line strengths, but if the colors are significantly affected by the SFR deviations, then the Mgb and $<$Fe$>$ absorption line indices must also be affected. Their simulation cannot be used to explain the full range of LSB galaxy parameters that we see. First of all, despite some uncertainty in the metallicity zeropoints of the [N II]/Hα, Mgb and $<$Fe$>$ indicators, we find LSB galaxies with metallicities near solar, and certainly at least half-solar. Their models require metallicities less then about one-fifth solar to maintain a low SFR. Furthermore, the range of color (and we infer also Mgb, $<$Fe$>$) is decoupled from increases in metallicity, in conflict with the [N II]/Hα-Mgb, [N II]/Hα-$<$Fe$>$, and [N II]/Hα-(B$-$I$_c$) correlations. Determining whether the range of colors (and thus Mgb and $<$Fe$>$) they predict at any given metallicity could be hidden within the scatter of these correlations requires more quantitative modelling than we have done. The Gerritsen & de Blok models predict that $\sim$ 20% of the late-type LSB galaxy population will have red colors, (B-V) $\sim$ 1. However, those galaxies should be gas rich and metal-poor, and while the gas fractions of the red LSB galaxies in our sample remain unconstrained, their metallicities are higher than predicted by Gerritsen & de Blok. In addition, they predict that these red galaxies will have $\mu_B(0) \simeq 24.5$ mag/$\Box''$, which is fainter than the galaxies selected for our sample. This surface brightness is well below the completeness limit of the OBC97 survey, and no other large surveys for red LSB galaxies have yet been published.

van den Hoek et al. (2000) modeled the SFH of the galaxies studied by de Blok & van der Hulst (1998) using a galactic chemical and photometric evolution model. They were able to explain the colors, magnitudes, and gas phase metallicities of most of the blue LSB galaxies with a SFH that had a continous, exponentially decreasing SFR over a period of 14 Gyr. For the bluest galaxies in the sample (with $(B-V) < 0.45$) an additional burst of star formation was needed. While our analysis rejects the possibility for significant late-time, i.e. high metallicity, bursts, none of the galaxies in our sample are that blue.

Bell et al. (2000) used near-infrared and optical colors to study the stellar populations of blue, red, and giant LSB galaxies. They did not require that the galaxies have HII regions, nor that they had previous detections in HI. However, their sample did have a higher average surface brightness than the spectroscopic studies, so that they could get sufficient S/N in the K-band imaging. Their sample has a similar central surface brightness distribution to ours. Like us, they found that LSB galaxies cover a range of metallicities, with some having metallicities near solar. They also found that some red LSB galaxies had rather old luminosity-weighted mean ages. They only had five red LSB galaxies in their survey and they determined that those with old ages and solar metallicities were all at the bright end of the LSB surface brightness range, $\mu_{\rm B}(0) \sim 22.5$ mag/$\square''$. We find old, metal rich stellar populations in some red galaxies with $\mu_{\rm B}(0) \simeq 24.0$ mag/$\square''$. By combining the Bell et al. LSB sample with a sample of HSB disk galaxies, Bell & de Jong (2000) found a clear correlation between mean age and surface brightness, which we do not detect. The discrepancies in both cases can be explained by small sample sizes, especially of the reddest LSB galaxies in the sample.

Impey et al. (2001) obtained low resolution ($\cong 20$Å), low S/N optical spectra for 250 galaxies selected from the APM survey of Impey et al. (1996), 93 of which have central surface brightnesses fainter than $\mu_{\rm B} = 22 {\rm mag}/\Box''$(their LSB cutoff). They also obtained HI spectra for 145 LSB galaxies. Burkholder et al. (2001) analyze these data, and measure Balmer decrements (Hα/Hβ) and [O/H] (using the R_{23} method) when the optical spectra are of sufficient quality (43 HSB and 17 LSB galaxies have measured [O/H]). They also measure the best-fit Tully-Fisher relation for the HI sample. Their sample selection criteria were similar to those of Bell et al. (2000) and ourselves: no requirements for prior HI detections, or the presence of HII regions. Though the quality of their data for individual galaxies may not be as good, they have a larger dataset to draw conclusions from, and their conclusions match ours: there is evidence for old stellar populations in some LSB galaxies, and the range of metallicities for LSB galaxies shows a large overlap with the range of metallicities seen in HSB galaxies.

A complete picture of the formation and evolution of LSB galaxies is still not in hand, as many of the conclusions of these authors and ourselves are clearly still subject to variance due to small and incomplete samples. Future detailed studies should rely on deep, complete, multi-color surveys with well determined detection criteria to gain a better overall picture of LSB galaxy formation and evolution. The constraints on LSB SFH implied by the many correlations we detect are only applicable to LSB galaxies with $1.0 < ({\rm B} - {\rm I_c}) < 2.2$ and $\mu_{\rm B}(0) < 24.3 {\rm mag}/\Box''$.

2.10 Summary & Conclusions

We have used the Marcario Low Resolution Spectrograph on the 9.2m Hobby-Eberly Telescope to obtain deep integrated spectra of the gaseous and stellar components of 19 LSB galaxies, covering a range of colors and surface brightnesses. These spectra have sufficient spectral resolution and S/N in the continuum to measure both emission line ratios and stellar absorption line strengths.

The spectra of these galaxies qualitatively resemble the spectra of HSB galaxies covering the full range of spectra seen in galaxies of Hubble types from E to Irr. In most of the parameters we measure, LSB galaxy properties cover the same broad range as HSB galaxies. Four galaxies have spectra whose features are dominated by old stellar populations, covering a range of abundances from less than half solar to twice solar metallicity. None of these four have been detected in HI. The remainder of the galaxies show evidence for ongoing star formation, in some cases at a significant rate compared to their average past SFR. At least one massive red LSB galaxy shows evidence for super-solar [Mg/Fe] abundance. This is in accord with similar findings for HSB galaxies, and suggests that the mechanism responsible for the super-solar abundance ratios is effective in LSB galaxies as well. All of the emission line galaxies are consistent with star formation, rather than AGN, being the ionizing source.

There are tight correlations between the stellar absorption line indices and the gas phase indicators [N II]/Hα and EW(Hα). These have not been studied before, in LSB or HSB galaxies. We use these correlations to argue that the SFH for these galaxies must be fairly smooth. Large bursts of star formation, or multiple small bursts separated by long quiescent periods, do not fit these relations.

Dust is present in some of these galaxies, with A_V as large as 1.8 mags. We are unable to determine, though, whether the dust is isolated to the emission line regions, or if it is mixed in with the the stellar population.

The redshift distribution for this galaxy sample is very broad, ranging from 3000 to 70000 km/s. Additionally, we find several discrepancies between the published redshifts based on Arecibo 305m telescope HI observations and our new optical observations. In most cases, the discrepancy can be explained by beam confusion affecting the Arecibo detection. All of the galaxies found by O'Neil et al. (2000a) to deviate significantly from the Tully-Fisher relation, we show to suffer from significant redshift errors.

2.11 Acknowledgements

We would like to thank Greg Shields for useful discussions on nebular chemical abundances, and Karl Gebhardt for comments on an early draft of this paper. We also thank the anonymous referee for comments which helped to improve this paper. The Hobby-Eberly Telescope is operated by McDonald Observatory on behalf of The University of Texas at Austin, the Pennsylvania State University, Stanford University, Ludwig-Maximilians-Universität München, and Georg-August-Universität Göttingen. The Marcario Low Resolution Spectrograph is a joint project of the Hobby-Eberly Telescope partnership and the Instituto de Astronoma de la Universidad Nacional Autonoma de México. This material is based in part upon work supported by the Texas Advanced Research Program under Grant No. 009658-

0060-1977. This research was supported in part by the Gemini Observatory, which is operated by the Association of Universities for Research in Astronomy, Inc., on behalf of the international Gemini partnership of Argentina, Australia, Brazil, Canada, Chile, the United Kingdom, and the United States of America. This research has made use of the NASA/IPAC Extragalactic Database (NED) which is operated by the Jet Propulsion Laboratory, California Institute of Technology, under contract with the National Aeronautics and Space Administration. This research has made use of NASA's Astrophysics Data System Service.

2.12 Bibliography

Bell, E. F., Barnaby, D., Bower, R. G., de Jong, R. S., Harper, D. A., Hereld, M., Loewenstein, R. F., & Rauscher, B. J. 2000, MNRAS, 312, 470

Bell, E. F. & de Jong, R. S. 2000, MNRAS, 312, 497

Bertin, E. & Arnouts, S. 1996, A&AS, 117, 393

Burkholder, V., Impey, C., & Sprayberry, D. 2001, AJ, 122, 2318

Burstein, D. & Heiles, C. 1982, AJ, 87, 1165

Cardelli, J. A., Clayton, G. C., & Mathis, J. S. 1989, ApJ, 345, 245

Chromey, F. R. & Hasselbacher, D. A. 1996, PASP, 108, 944

Chung, A., van Gorkom, J. H., O'Neil, K., & Bothun, G. 2002, AJ, 123, 2387

Claver, C. F. 1995, Ph.D. Thesis, University of Texas, Austin

Cross, N. & Driver, S. P. 2002, MNRAS, 329, 579

Dalcanton, J. J., Spergel, D. N., Gunn, J. E., Schmidt, M., & Schneider, D. P. 1997, AJ, 114, 635

Davies, R. L., Burstein, D., Dressler, A., Faber, S. M., Lynden-Bell, D., Terlevich, R. J., & Wegner, G. 1987, ApJS, 64, 581.

Davies, R. L., Sadler, E. M., & Peletier, R. F. 1993, MNRAS, 262, 650.

de Blok, W. J. G. 1997, Ph.D. Thesis, Rijksuniversiteit Groningen

de Blok, W. J. G. & McGaugh, S. S. 1997, MNRAS, 290, 533

de Blok, W. J. G., McGaugh, S. S., & van der Hulst, J. M. 1996, MNRAS, 283, 18

de Blok, W. J. G. & van der Hulst, J. M. 1998, A&A, 335, 421

de Blok, W. J. G., van der Hulst, J. M., & Bothun, G. D. 1995, MNRAS, 274, 235

de Jong, R. S. & Lacey, C. 2000, ApJ, 545, 781

Denicoló, G., Terlevich, R., & Terlevich, E. 2002, MNRAS, 330, 69.

Falco, E. E. et al. 1999, PASP, 111, 438 (UZC)

Freeman, K. C. 1970, ApJ, 160, 811

Frei, Z. & Gunn, J. E. 1994, AJ, 108, 1476

Fukugita, M., Shimasaku, K., & Ichikawa, T. 1995, PASP, 107, 945.

Gerritsen, J. P. E. & de Blok, W. J. G. 1999, A&A, 342, 655

Goudfrooij, P. & Emsellem, E. 1996, A&A, 306, L45

Hill, G. J., Nicklas, H. E., MacQueen, P. J., Tejada, C., Cobos Duenas, F. J., & Mitsch, W. 1998, Proc. SPIE, 3355, 375.

Impey, C., Burkholder, V., & Sprayberry, D. 2001, AJ, 122, 2341

Impey, C. D., Sprayberry, D., Irwin, M. J., & Bothun, G. D. 1996, ApJS, 105, 209

Jansen, R. A., Fabricant, D., Franx, M., & Caldwell, N. 2000, ApJS, 126, 331

Jørgensen, I. 1997, MNRAS, 288, 161.

Jørgensen, I. 1999, MNRAS, 306, 607

Kennicutt, R. C. 1992, ApJ, 388, 310.

Kennicutt, R. C. 1998, ARA&A, 36, 189

Kennicutt, R. C., Tamblyn, P., & Congdon, C. E. 1994, ApJ, 435, 22

Kewley, L. J. & Dopita, M. A. 2002, ApJsubmitted

Kewley, L. J., Dopita, M. A., Sutherland, R. S., Heisler, C. A., & Trevena, J. 2001a, ApJ, 556, 121

Kewley, L. J., Heisler, C. A., Dopita, M. A., & Lumsden, S. 2001b, ApJS, 132, 37

Kilborn, V. A. et al. 2000, AJ, 120, 1342

Kobulnicky, H. A., Kennicutt, R. C., & Pizagno, J. L. 1999, ApJ, 514, 544

Kobulnicky, H. A. & Skillman, E. D. 1997, ApJ, 489, 636

Kuntschner, H., Lucey, J. R., Smith, R. J., Hudson, M. J., & Davies, R. L. 2001, MNRAS, 323, 615.

Landolt, A. U. 1992, AJ, 104, 340

Leitherer, C. et al. 1999, ApJS, 123, 3

Maraston, C. & Thomas, D. 2000, ApJ, 541, 126

Matthews, L. D. & Gao, Y. 2001, ApJ, 549, L191

McGaugh, S. S. 1991, ApJ, 380, 140

McGaugh, S. S. 1994, ApJ, 426, 135

McGaugh, S. S., Bothun, G. D., & Schombert, J. M. 1995, AJ, 110, 573

McGaugh, S. S., Rubin, V. C., & de Blok, W. J. G. 2001, AJ, 122, 2381

Monet, D., et al. 1998, The USNO-SA2.0 Catalog (Washington: US Naval Obs.)

Nilson, P. 1973, Acta Universitatis Upsaliensis. Nova Acta Regiae Societatis Scientiarum Upsaliensis - Uppsala Astronomiska Observatoriums Annaler, Uppsala: Astronomiska Observatorium, 1973 (UGC)

O'connell, R. W. 1976, ApJ, 206, 370.

O'Neil, K. & Bothun, G. D., ApJ, 529, 811

O'Neil, K., Bothun, G. D., & Cornell, M. E. 1997, AJ, 113, 1212 (OBC97)

O'Neil, K., Bothun, G. D., & Schombert, J. 2000a, AJ, 119, 136

O'Neil, K., Bothun, G. D., Schombert, J., Cornell, M. E., & Impey, C. D. 1997, AJ, 114, 2448 (OBSCI97)

O'Neil, K., Hofner, P., & Schinnerer, E. 2000b, ApJ, 545, L99

Osterbrock, D. E. 1989, Astrophysics of Gaseous Nebulae and Active Galactic Nuclei (Mill Valley: University Science Books)

Pagel, B. E. J., Edmunds, M. G., Blackwell, D. E., Chun, M. S., & Smith, G. 1979, MNRAS, 189, 95

Peterson, B. M. 1997, An Introduction to Active Galactic Nuclei (Cambridge: Cambridge University Press)

Pierce, M. J. & Tully, R. B. 1988, ApJ, 330, 579

Ramsey, L. W. et al. 1998, Proc. SPIE, 3352, 34

Rönnback, J. & Bergvall, N. 1995, A&A, 302, 353

Rose, J. A. 1994, AJ, 107, 206.

Ryder, S. D. et al. 2001, ApJ, 555, 232

Salpeter, E. E. 1955, ApJ, 121, 161.

Scalo, J. M. 1986, Fundamentals of Cosmic Physics, 11, 1

Schombert, J. M. & Bothun, G. D. 1988, AJ, 95, 1389

Schombert, J. M., Bothun, G. D., Schneider, S. E., & McGaugh, S. S. 1992, AJ, 103, 1107

Schlegel, D. J., Finkbeiner, D. P., & Davis, M. 1998, ApJ, 500, 525

Sparks, W. B. 1988, AJ, 95, 1569

Sprayberry, D., Impey, C. D., Bothun, G. D., & Irwin, M. J. 1995, AJ, 109, 558

Stasińska, G. & Sodré, L. 2001, A&A, 374, 919

Storchi-Bergmann, T., Calzetti, D., & Kinney, A. L. 1994, ApJ, 429, 572

Trager, S. C., Worthey, G., Faber, S. M., Burstein, D., & Gonzalez, J. J. 1998, ApJS, 116, 1

Tully, R. B. & Fisher, J. R. 1977, A&A, 54, 661

van Zee, L., Salzer, J. J., Haynes, M. P., O'Donoghue, A. A., & Balonek, T. J. 1998, AJ, 116, 2805

van den Hoek, L. B., de Blok, W. J. G., van der Hulst, J. M., & de Jong, T. 2000, A&A, 357, 397.

Vazdekis, A. 1999, ApJ, 513, 224 (V1999)

Vazdekis, A. 2000, `http://www.iac.es/galeria/vazdekis/MODELS\_2000/out\_li\_BI` (V2000)

Veilleux, S. & Osterbrock, D. E. 1987, ApJS, 63, 295

Worthey, G. 1994, ApJS, 95, 107.

Worthey, G. 1998, PASP, 110, 888.

Worthey, G., Faber, S. M., Gonzalez, J. J., & Burstein, D. 1994, ApJS, 94, 687

Zabludoff, A. I. & Mulchaey, J. S. 2000, ApJ, 539, 136

Chapter 3

Determination of Local Galaxy Density

3.1 Introduction

The evolution of galaxies is an environmentally dependent process. The most telling observational example of this is probably the morphology–density relation for galaxies (Dressler, 1980), wherein the fraction of galaxies with early-type (E & S0) morphology increases with increasing local galaxy density. Environmental dependence is also a prediction of the hierarchical clustering galaxy formation scenario, due to the varying likelihood for galaxy interactions and mergers as a function of both local density, and the typical relative velocities of galaxies (which are lower in the field, and hence more conducive to significant gravitational interactions when two galaxies closely approach eachother). These theories predict that the last major merger in a galaxy's hierarchical construction occurred more recently for galaxies in the low density field, compared to galaxies found in clusters.

The best quantification of local galaxy density can only be achieved in volumes of the universe which have been observed with deep and complete redshift surveys. Unfortunately, such surveys typically have not covered a large area of sky, though the ongoing Sloan Digital Sky Survey (SDSS) and 2dF Galaxy Redshift Survey (2dFGRS) are working to rectify that. We wish to study early-type galaxies in both cluster and field environments. The morphology-density relation tells us that this class of galaxies will be found predominantly in clusters, and consequently, the construction of a field sample will require a large survey volume. Detailed, spatially resolved studies of nearby galaxies have the possibility to greatly enhance our understanding of the formation and evolution of galaxies, especially if samples of sufficient size can be produced which allow us to probe general galaxy properties (not just individual galaxies), as a function of environment. Since we want to make detailed studies, the galaxies must be in the nearby universe, and thus our survey volume must be produced with wide-area sky coverage, and relatively shallow depth.

To aid in the selection of suitable field galaxy samples, we have produced an all-sky catalog of local galaxy densities. We describe the source material in Section 3.2, and the derivation of local galaxy density in Section 3.3. Caveats due to galaxy catalog incompleteness are discussed in Section 3.4, and we discuss our derived parameters with regards to published early-type field galaxy samples in Section 3.5. An electronic version of the full catalog accompanies electronic versions of this dissertation, and will also be made available upon request to the author.

3.2 Source Catalog

We use as our basis the Lyon-Meudon Extra-Galactic Database[1] (LEDA). This online resource combines many large catalogs from the literature, and includes

---

[1] The LEDA homepage is at http://leda.univ-lyon1.fr/

listings of nearly one million separate galaxies (close to three million names). It is similar to the NASA Extragalactic Database[2] (NED), however it produces more coherent output catalogs for all-sky queries. Our goal is to measure the local galaxy density around every galaxy whose radial velocity cz$<$ 10000 km s^{-1}. To accomplish this, we extracted information for every galaxy listed in the LEDA database as of 1 August, 2002, for which the radial velocity was less than 10500 km s^{-1}. This includes 42024 galaxies, of which 39829 have cz$<$ 10000 km s^{-1}. The extracted information includes not just positions, velocities, and brightnesses, but also various morphological and kinematics measurements in the database. The full list of extracted parameters is given in Table 3.1. We refer to this extracted data as the "spectroscopic catalog."

Additionally, we extracted a "photometric catalog" from the LEDA database. This contains positions and total apparent magnitudes for every galaxy in the database with $m_{B,tot} < 20$. We use this catalog to ascertain the completeness of the database as a function of position on the sky. This catalog contains 928,636 spatially extended objects. The apparent magnitude distribution of the photometric catalog is shown in Figure 3.1, and the distribution for the spectroscopic catalog is shown in 3.2. Not surprisingly, the spectroscopic catalog is far from complete; this will be discussed in more detail in Section 3.4.

---

[2] The NED homepage is at http://ned.ipac.caltech.edu/

TABLE 3.1

DEFINITION OF PARAMETERS FROM LEDA DATABASE

Parameter	units	Definition
pgc_id	· · ·	ID number in LEDA database
galaxy_name	· · ·	Common/Alternative name for galaxy
al2000	decimal hours	Right Ascenscion
de2000	decimal degrees	Declination
gall	· · ·	Galactic latitude
galb	· · ·	Galactic longitude
type	Hubble	Hubble Type
t	-5 – 10	de Vaucouleurs T-Type
bt	mag	total apparent B magnitude
sbt	mag	error on total apparent B magnitude
it	mag	total apparent I magnitude
sit	mag	error on total apparent I magnitude
ubt	mag	total (U-B) color
bvt	mag	total (B-V) color
ube	mag	error on total (U-B) color
bve	mag	error on total (B-V) color
logr25	· · ·	log10 of axis ratio (major / minor)
slogr25	· · ·	error on logr25
pa	degrees	Position Angle of major axis, measure N→E
brief	mag/$\square''$	surface brightness at the effective radius
sbrief	mag/$\square''$	error on brief
logs	km/s	log10 of the central velocity dispersion
slogs	km/s	error on logs
v	km/s	mean heliocentric radial velocity
sv	km/s	error on mean recessional velocity
lgg	· · ·	group number from Lyon Galaxy Groups
ag	mag	galactic extinction in B band
mucin	mag	kinematical distance modulus (H_o=75 km s^{-1}Mpc^{-1})
mabsr	mag	absolute magnitude in B band

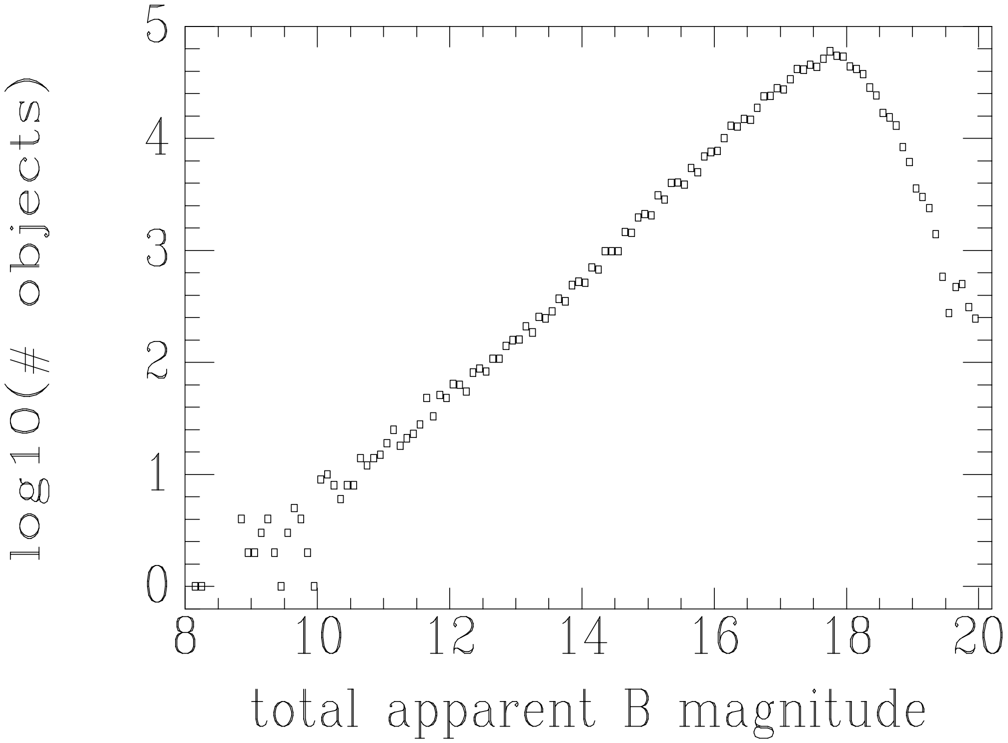

Figure 3.1 Photometric galaxy catalog apparent magnitude distribution, integrated over the whole sky. The total number of galaxies in the plot is 928,636.

3.3 Galaxy Volume Density

The algorithm to determine the local space volume density around every galaxy in the database is a very simple one. We assume that redshift (radial velocity) is a perfect surrogate for distance, i.e. we do not take any peculiar velocities into account, and assume a Hubble constant of H_o = 65 km $s^{-1}Mpc^{-1}$. For ease of computation, we transform the three polar space coordinates, (RA, Dec, cz), into three spatial cartesian coordinates, which we call (mgalX, mgalY, mgalZ). The

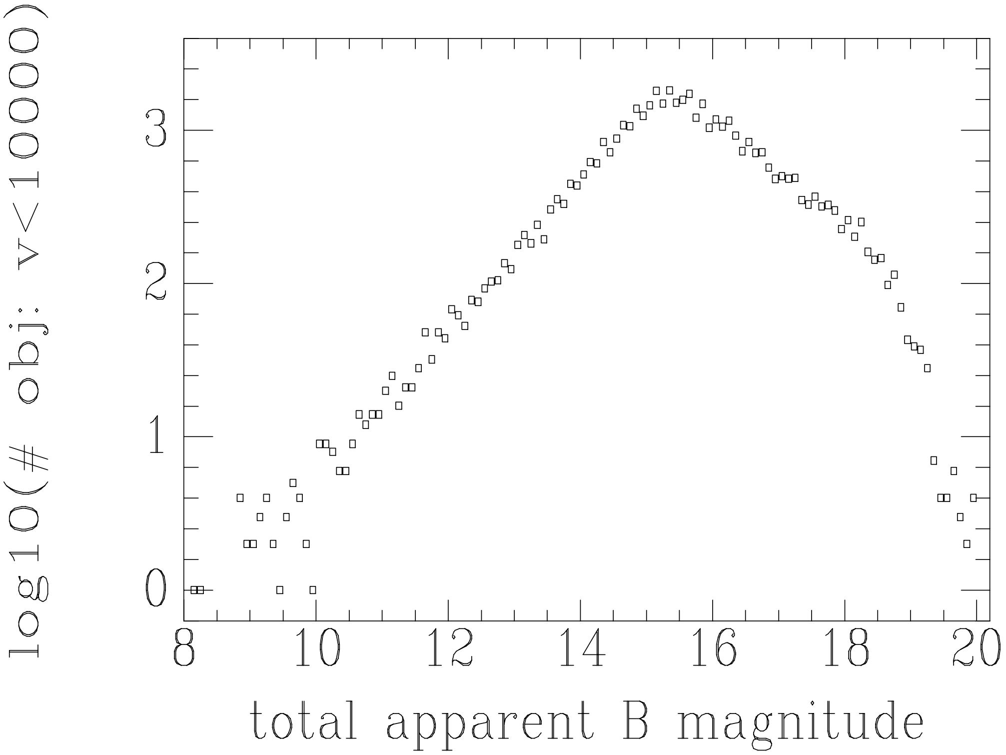

Figure 3.2 Spectroscopic galaxy catalog apparent luminosity distribution for all the galaxies with cz < 10,000 km/s, integrated over the whole sky. The total number of galaxies in the plot is 39,829.

transformation equations used were:

$$\mathrm{mgalX} = \mathrm{cz}/65 \times \cos(\mathrm{RA})\cos(\mathrm{Dec}) \tag{3.1}$$

$$\mathrm{mgalY} = \mathrm{cz}/65 \times \sin(\mathrm{RA})\cos(\mathrm{Dec}) \tag{3.2}$$

$$\mathrm{mgalZ} = \mathrm{cz}/65 \times \sin(\mathrm{Dec}) \tag{3.3}$$

Around each of the $\sim$ 39000 galaxies with spectra, we extracted the subset of the galaxies within a sphere of radius 10 Mpc (650 km s^{-1}). The distance between each of those galaxies and the target galaxy was derived, and the distance to the nearest neighbor determined. Additionally, we counted the number of galaxies within concentric spheres of radius 5 Mpc, 7.5 Mpc, and 10 Mpc from the target galaxy. We also derived the mean distance from the target galaxy to all of the galaxies within those three spheres. These measurements were all tabulated, and the parameter names and descriptions are listed in Table 3.2. There were some cases where the nearest observed neighbor was at a distance greater than 10 Mpc. In these cases, the value for "neimindist" was set to 9999. in the density table. Similarly, for any of the radii, if there were no neighbors within that radius, the value for the mean distance to the neighbors was set to 9999. in the output table.

The local density around all the galaxies in the spectroscopic catalog can be seen in Figure 3.3, where we plot the number of neighbors within 5 Mpc versus the radial velocity of the target galaxy. We have separated the plot into two panels, based on declination. Galaxy clusters show up as large and obvious features in this plot, and we have labelled several of the largest clusters. The galaxy cluster features are stretched out in velocity space due to the intrinsic velocity dispersions within the clusters, and not due to large spatial extent along the line of sight. Clearly, since we assumed distances based on velocity, with no peculiar velocity correction, we will underestimate the local density for galaxies belonging to these peaks. Field galaxies make up the large bulk of galaxies with few local neighbors, and are fairly uniformly distributed over the whole sky, and over the entire redshift range.

TABLE 3.2

DEFINITION OF DERIVED PARAMETERS FOR LOCAL DENSITY CATALOG

Column name	units	Definition
mgalX	h_{65}^{-1}Mpc	X – cartesian space coordinate
mgalY	h_{65}^{-1}Mpc	Y – cartesian space coordinate
mgalZ	h_{65}^{-1}Mpc	Z – cartesian space coordinate
neimindist	h_{65}^{-1}Mpc	distance to nearest cataloged neighbor
nnei50	···	Number of galaxies within a sphere of radius 5h_{65}^{-1}Mpc
nnei75	···	Number of galaxies within a sphere of radius 7.5h_{65}^{-1}Mpc
nnei100	···	Number of galaxies within a sphere of radius 10h_{65}^{-1}Mpc
nei50meandist	h_{65}^{-1}Mpc	Mean distance to all galaxies within 5h_{65}^{-1}Mpc
nei75meandist	h_{65}^{-1}Mpc	Mean distance to all galaxies within 7.5h_{65}^{-1}Mpc
nei100meandist	h_{65}^{-1}Mpc	Mean distance to all galaxies within 10h_{65}^{-1}Mpc
catbinsize	$\square^\circ$	area of bin for local surface density determination
photdens	#/$\square^\circ$	local number density of objects in photometric catalog
specdens	#/$\square^\circ$	local number density of objects with redshifts
photdensb15	#/$\square^\circ$	local number density of objects with $\mathrm{m_B} < 15$
specdensb15	#/$\square^\circ$	local number density of objects with redshifts and $\mathrm{m_B} < 15$
specfrac	···	local fraction of photometrically cataloged objects with redshifts
specfracb15	···	local fraction of photometrically cataloged objects with redshifts and $\mathrm{m_B} < 15$
photnorm	···	local photometric catalog density, divided by 89.6 objects/$\square^\circ$
photnormb15	···	local photometric catalog density for objects with $\mathrm{m_B} < 15$, divided by 5.5 objects/$\square^\circ$
specnorm	···	local spectroscopic catalog density, divided by 46.7 objects/$\square^\circ$
specnorb15m	···	local spectroscopic catalog density for objects with $\mathrm{m_B} < 15$, divided by 4.8 objects/$\square^\circ$

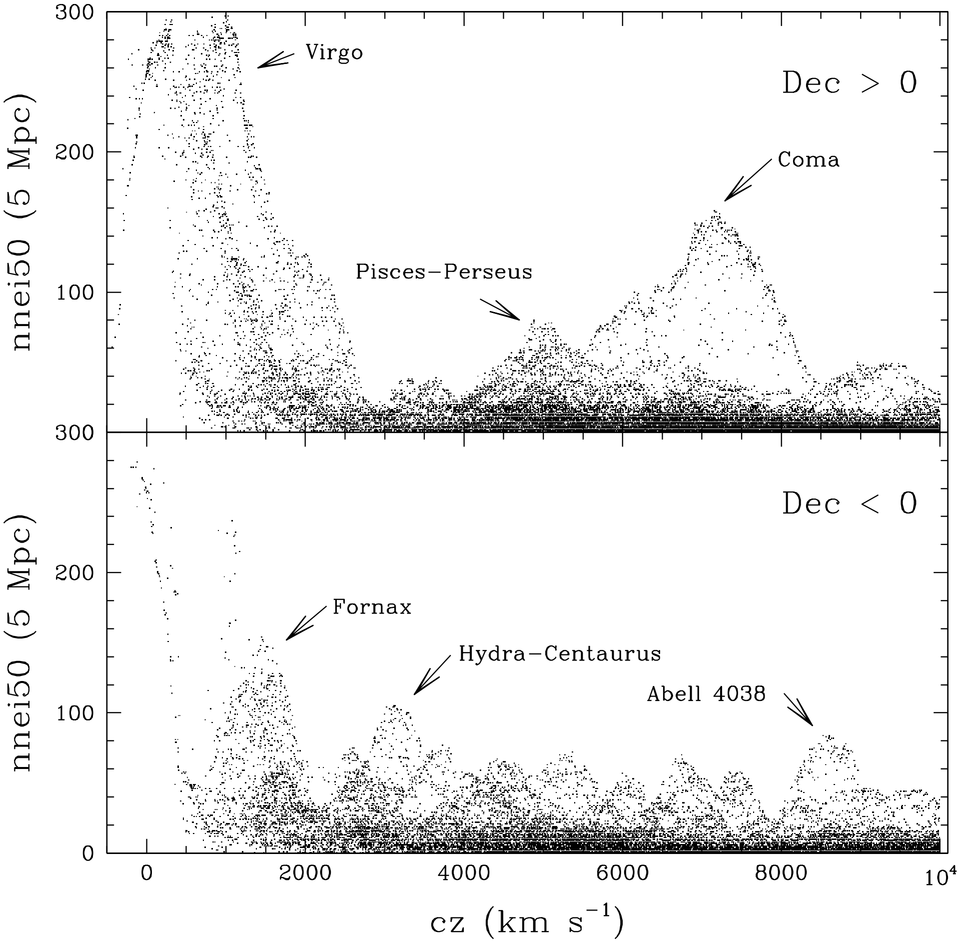

Figure 3.3 Number of neighbors within 5 Mpc as a function of radial velocity for all the early-type galaxies in the spectroscopic catalog. Top: all the galaxies at declinations > 0. Bottom: All the galaxies with declination < 0. Some of the obvious peaks are labelled with their corresponding cluster names.

3.4 Catalog Completeness

The primary fault of this all-sky galaxy density catalog is the varying completeness level, over different parts of the sky, of the input galaxy catalogs. Regions which have been studied more intensively with both deeper imaging and deeper spectroscopy will appear to have higher local galaxy densities, when the actual local density might not be higher. There is no perfect way to correct for this. We have, however, derived both photometric and spectroscopic completeness diagnostics which may be of use when extracting field galaxy samples from the density catalog.

We divided up the sky into 7200 spatial regions, by making simple bins in both RA and Dec. The bins were chosen to be one degree of declination high, and 7.5 or 15 degrees (0.5 or 1 hour) of RA wide, with the larger RA coverage used for bins at declinations, $|\delta| > 60^o$. We separated up the photometric catalog into these 7200 bins, and counted up how many objects were in each one, and what fraction of those object had an observed redshift (not limited to cz$<$ 10000km s^{-1}). We normalized the counting by the solid angle covered by each bin (which ranged from 0.131 sq. deg. up to 7.5 sq. deg.). In doing so, we assume that the intrinsic galaxy distribution down to 20th magnitude is uniform across the whole sky, on scales $\sim$ 5 sq. deg. Given this assumption, the spatially varying observed surface density distribution then reflects the varying completeness level of the LEDA catalog. For each galaxy in our local (volume) density catalog, we tabulate the local surface density of objects in the photometric catalog, as well as the local spectroscopic fraction. These parameters are named “photdens” and “specfrac” respectively, and the two are used together to define a “specdens” parameter which is the local surface density of objects with redshifts. We also tabulate the bin size in square degrees for the bin in which the galaxy is found. This parameter is named “catbinsize”. These parameters are all listed in Table 3.2. We also normalize these parameters by the highest photometric and spectroscopic object densities found anywhere on the sky, which are 89.6 objects per sq. deg. and 47.6 objects per sq. deg., respectively. These parameters are named “photnorm” and “specnorm.”

Figures 3.4 and 3.5 show the spatial distribution of the object (number) densities in the photometric and spectroscopic catalogs. The images have been smoothed with a 3×3 bins tophat filter, for clarity. The plane of our Galaxy makes an obvious sinusoidal pattern through both figures; the combined effects of Galactic extinction and crowded stellar fields make it practically impossible to catalog external galaxies through and beyond the disk of the Milky Way. Several other bright “features” are seen, corresponding to regions of the sky where spectroscopic and deep photometric surveys have been made. The swaths near -35^{o} and 0^{o} Declination are the survey regions made with the UK Schmidt Telescope, with follow-up spectroscopy from the Las Campanas Redshift Survey (LCRS) and the Two-degree Field Galaxy Redshift Survey (2dFGRS). The extensive imaging and spectroscopy of the Coma Cluster (near $13^{h}00^{m}$ $+30^{o}$ J2000) is apparent, as well as several other pointed survey regions.

In addition to spatially varying survey levels, there is also the problem of incomplete survey depth, shown in Figure 3.6. This will result in lower apparent densities for galaxies at larger distances. The fall-off in completeness starts around

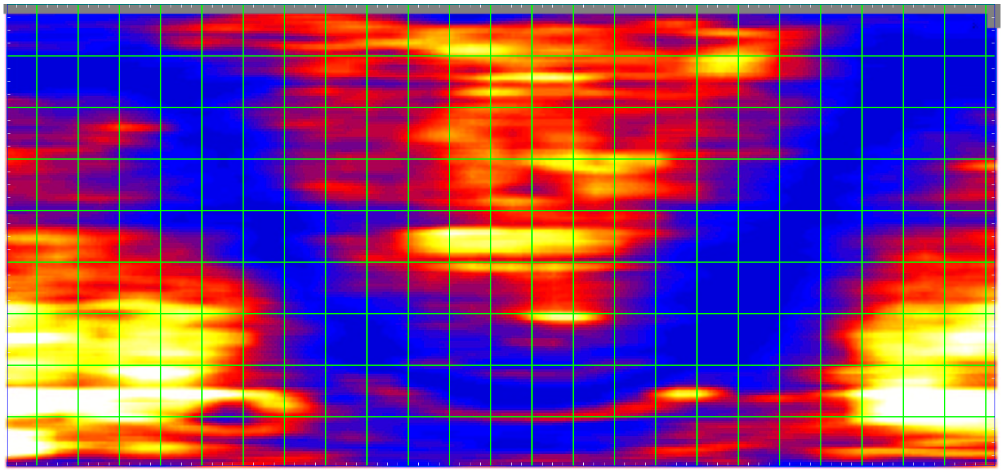

Figure 3.4 Spatial distribution of Photometric Catalog. x-axis is RA in hours, while the y-axis is declination in degrees (grid goes from -90 to +90 in 20 degree increments). White is high density, and blue is low density.

a total apparent magnitude $m_{B,tot} = 15$. The increase in the spectroscopic fraction at faint magnitudes, $m_{B,tot} \geq 18$, reflects the spatial incompleteness of both the photometric and spectroscopic catalogs. The few regions for which the LEDA database includes galaxies at these faint magnitudes are the subject of deep imaging/spectroscopic surveys, and thus the fractional spectroscopic coverage is higher than for the intermediate magnitudes where wide-area photometric surveys have been conducted (and included in the database), without deep spectroscopy. We rederived all of the local surface density parameters described above, but with a limiting magnitude of $m_{B,tot} = 15$. These are included in the density table with parameters named as above, but with "b15" appended (e.g. photdensb15). These parameters, along with the normalizations, are listed in Table 3.2.

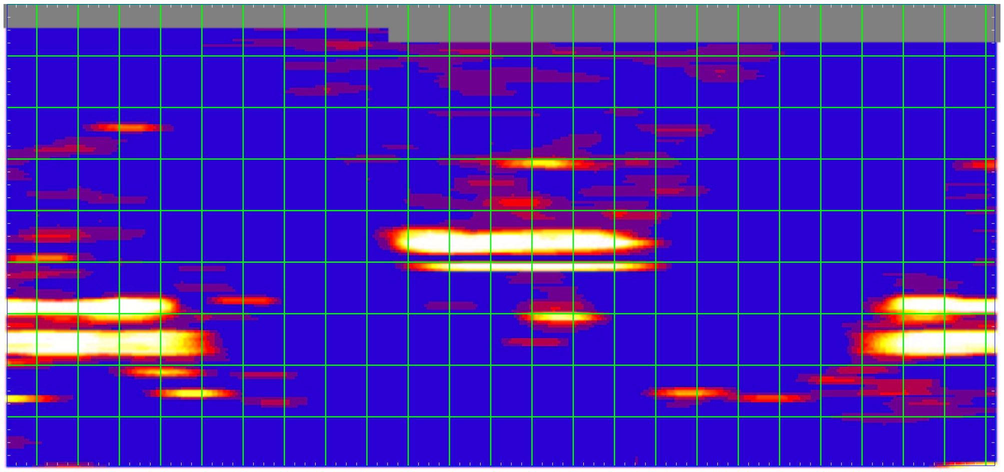

Figure 3.5 Spatial distribution of Spectrocopic Catalog. x-axis is RA in hours, while the y-axis is declination in degrees (grid goes from -90 to +90 in 20 degree increments). White is high density, and blue is low density.

3.5 Field Galaxy Samples

The first step in selecting a field galaxy sample is determining what is meant by the term “field galaxy.” There are two extremes of opinion, and to a large extent it depends on what exactly is the purpose of the study. On one end of the range, a field galaxy is defined as an isolated galaxy, with no neighbors within some suitable radius, say 5 Mpc. This isolation then defines a minimum time since the last possible dynamical encounter, given the mean pair-wise velocities of galaxies.The opposite extreme is to say that any galaxy, chosen at random, is a field galaxy. This will include galaxies in all density environments, but will be weighted towards low densities since the majority of all galaxies lie outside of clusters (this is not true for early-type galaxies, though). This latter definition is what is often used by theorist/modelers when describing the field galaxy population. It is also the definition frequently adopted by observers studying galaxies at high redshift using randomly

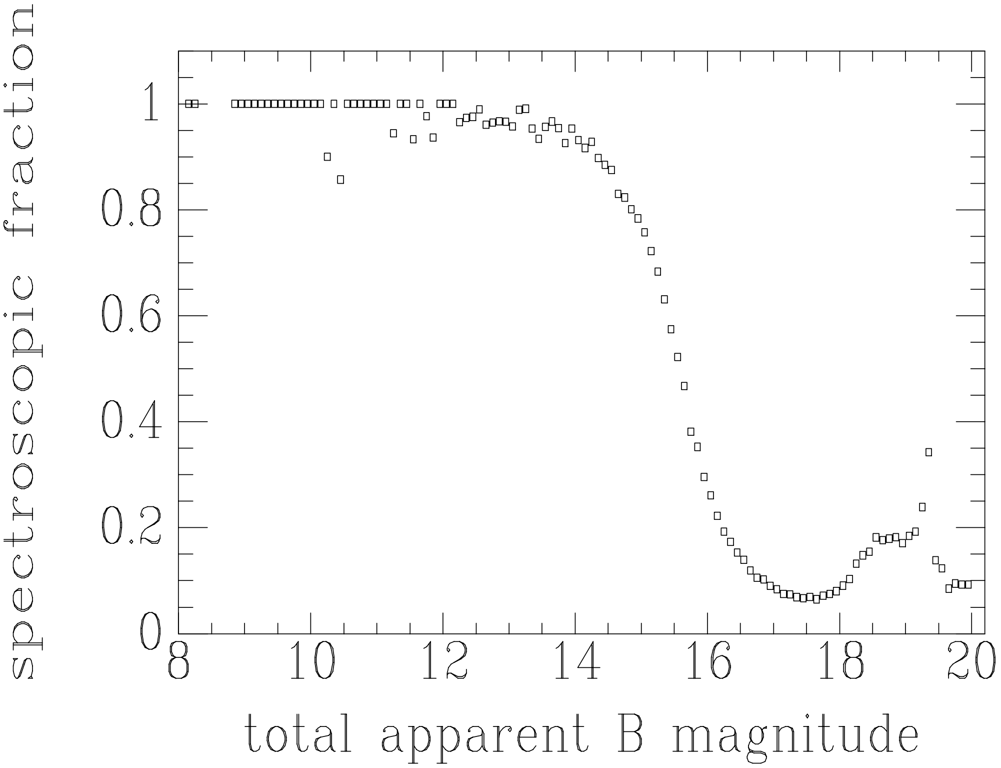

Figure 3.6 Fraction of cataloged galaxies with redshifts, as a function of apparent magnitude, integrated over the whole sky.

pointed fields (i.e. not specifically pointed at clusters). These studies aim to assess the general properties of galaxies, and are well suited to comparison with the cosmological models. However, when attempting to directly assess the impact of environment on galaxy evolution, the choice of a field galaxy sample is more appropriately tuned to the former definition.

The local density parameters which we have derived are useful for selecting samples from low density, or isolated environments. We present our measurements for two sets of early-type field galaxy samples already present in the literature:

Colbert, Mulchaey, & Zabludoff (2001) and Kuntschner et al. (2002). Colbert et al. (2001) defined an isolated galaxy sample based on the galaxies listed in the RC3 catalog (de Vaucouleurs et al., 1991). They choose galaxies for which there are no known neighbors within a projected radius of 1 Mpc_{100}^{-1} on the sky, and a velocity of ± 1000 km s^{-1}. Kuntschner et al. (2002) choose their sample from the region of sky covered by the FLASH spectroscopic survey (Kaldare et al., 2002), which has both deep imaging and spectroscopy. Their sample requirements are a projected radius of 1.3 Mpc, and a velocity spread of ± 350 km s^{-1}. The galaxies in those two samples are listed in Table 3.3, along with our measurements for nearest neighbor distance, and the number of galaxies within volumes of radius 5, 7.5, and 10 Mpc. We also list the mean and median values found for our full catalog, as well as the mean and median values for just the early-type galaxies in our catalog (those with de Vaucouleurs T-type < 1).

Scanning the table, it is clear that the distance to the nearest neighbor for galaxies in the field typically larger than the mean for either our full or earlyt-type galaxy catalog. Similarly, the number of neighbors is typically lower for the isolated field samples, though notable exceptions exist where the photometric catalog density and spectroscopic fraction are high. We find objects which are closer than the minimum cutoffs used by either survey, due to the inclusion of newer, redshift catalogs which improve the completeness. Both Colbert et al. (2001) and Kuntschner et al. (2002) stress the necessity of visual follow-up of all preliminary galaxy samples, to cull out possible neighbors without redshift observations. Even in regions with high spectroscopic follow-up density, there are many galaxies without mea-

TABLE 3.3

LOCAL DENSITIES FOR PUBLISHED FIELD SAMPLES[a]

PGC_ID	Galaxy_Name	al2000 (J2000)	de2000 (J2000)	v (km s^{-1})	neimindist (h_{65}^{-1}Mpc)	nnei50	nnei75	nnei100	photnorm	specfrac
Colbert, Zabludoff, & Mulchaey (2000) Sample:										
2253	NGC179	0:37:46.2	-17:50:56.0	6007	3.454	4	9	23	0.27	0.03
7468	NGC766	1:58:41.8	8:20:47.4	8110	2.317	4	6	11	0.11	0.10
10891	NGC1132	2:52:51.9	-1:16:28.2	6952	1.252	7	16	43	0.17	0.07
11499	A0300+16	3:03:15.0	16:26:19.7	9738	4.229	4	24	34	0.10	0.10
12909	UGC2748	3:27:54.2	2:33:41.8	9438	2.168	10	15	22	0.12	0.12
14213	A0356+10	3:58:54.5	10:26:03.8	9136	9.594	0	0	1	0.05	0.10
15579	2ZW17	4:35:17.3	-1:43:52.0	9738	2.784	1	3	4	0.12	0.07
18030	NGC2110	5:52:11.4	-7:27:22.0	2205	1.742	5	18	43	0.01	0.11
20731	A0718-34	7:20:48.2	-34:07:12.4	8965	2.239	4	5	5	0.09	0.04
30242	NGC3209	10:20:38.5	25:30:18.0	6182	2.036	12	22	42	0.15	0.04
31768	NGC3332	10:40:28.4	9:10:58.1	5833	4.124	3	9	19	0.18	0.09
34199	IC2637	11:13:49.8	9:35:10.0	8694	2.475	4	5	11	0.12	0.13
37612	IC2980	11:57:31.1	-73:41:02.0	8372	> 10	0	0	0	0.02	0.24
38450	ESO505-15	12:07:07.5	-25:41:29.8	7557	1.036	3	4	12	0.14	0.04
42119	ESO65-1	12:37:12.1	-72:35:31.6	7115	1.324	3	5	10	0.19	0.07
42470	ESO574-17	12:40:35.1	-20:33:44.6	8569	2.161	4	6	8	0.19	0.08
49677	NGC5413	13:57:53.5	64:54:38.9	9619	2.987	3	3	2	0.15	0.04
55123	UGC9874	15:27:15.2	77:09:23.8	5380	7.132	0	1	2	0.14	0.05
56460	UGC10115	15:57:07.8	63:55:03.0	9218	2.311	5	8	14	0.15	0.03
56650	IC1156	16:00:37.3	19:43:23.2	9475	2.105	5	11	34	0.20	0.09
57937	NGC6172	16:22:10.3	-1:30:53.3	4956	3.890	4	4	4	0.05	0.10
62176	MCG3-47-10	18:38:26.3	17:11:50.6	5096	2.782	6	15	27	0.02	0.07
62395	NGC6702	18:46:57.8	45:42:22.3	4714	2.593	3	10	21	0.10	0.07
63339	NGC6799	19:32:16.7	-55:54:27.4	5028	1.953	7	30	55	0.26	0.38
64097	NGC6849	20:06:16.2	-40:11:51.7	6042	2.204	10	26	44	0.14	0.07
65117	NGC6944	20:38:23.8	6:59:47.8	4442	2.688	11	29	47	0.03	0.18
66039	NGC7010	21:04:39.4	-12:20:18.2	8487	2.419	2	11	17	0.12	0.02
67017	IC1392	21:35:32.7	35:23:53.2	4361	3.401	2	3	12	0.01	0.44
69869	IC5258	22:51:31.6	23:04:50.2	7775	5.744	0	5	23	0.08	0.12
71090	NGC7618	23:19:47.3	42:51:10.1	5210	0.518	8	19	34	0.07	0.08
Kuntschner et al. (2002) Sample:										
34310	ESO503-5	11:15:15.8	-27:39:40.0	3961	3.122	4	14	90	0.07	0.06
34513	NGC3617	11:17:50.6	-26:08:06.4	2198	2.308	7	49	116	0.08	0.05
41784	ESO442-6	12:34:06.2	-31:13:01.2	5803	5.277	0	7	10	0.19	0.06
44770	ESO381-41	13:00:30.3	-34:22:33.2	2573	0.825	19	96	216	0.26	0.32
45919	ESO382-16	13:13:12.3	-36:43:22.1	3206	1.480	17	132	259	0.11	0.26
49162	ESO445-56	13:50:53.6	-30:17:20.0	5659	0.756	5	14	27	0.36	0.15
51229	ESO446-49	14:20:14.5	-29:44:49.9	3854	1.940	6	38	76	0.20	0.05
Full Leda Catalog mean values:				6053	1.944	21	48	87	0.21	0.20
Full Leda Catalog median values:				6201	1.444	9	21	41	0.18	0.12
Leda Catalog Early-Type[b] mean values:				5940	1.529	31	65	112	0.24	0.20
Leda Catalog Early-Type[b] median values:				5981	1.108	13	31	57	0.21	0.14

[a] Column names are the same as used in the electronic table. A description of each parameter may be found in Table 3.2.

[b] Galaxies in the Leda Catalog with de Vaucouleurs T-type < -1 (5909 galaxies total).

sured redshifts. That same caveat is thus also true of samples selected from our new catalog.

3.6 Summary

We have measured diagnostics of local galaxy density for approximately 40,000 galaxies in the local universe. These measurements can be used as an aid in the selection of field galaxy samples for further study, particularly into galaxy traits which might be a function of environment. The density parameters are all included in a comprehensive electronic table, along with many parameters already measured for the galaxies in the LEDA database. We have compared the measured density parameters for galaxies in two field galaxy samples from the literature. Similar, but larger samples can be selected based on nearest neighbor distance, local density of neighbors, or some combination of these parameters. The sample of galaxies observed in Chapter 4 was selected using an early version of this catalog.

3.7 Bibliography

Colbert, Mulchaey, & Zabludoff Colbert, J. W., Mulchaey, J. S., & Zabludoff, A. I. 2001, AJ, 121, 808

de Vaucouleurs, G., de Vaucouleurs, A., Corwin, H. G., Buta, R. J., Paturel, G., & Fouque, P. 1991, "Third Reference Catalog of Bright Galaxies (RC3)" (Springer-Verlag: New York)

Dressler, A. 1980, ApJ, 236, 351

Kaldare, R., Colless, M. M., Raychauddhury, S., Peterson, B. A., 2002, MNRAS-submitted, astro-ph/0109415

Kuntschner, H., Smith, R. J., Colless, M., Davies, R. L., Kaldare, R., & Vazdekis, A. 2002, 29 pages, 19 figures, Latex, MNRAS accepted., astro-ph/0207504

Chapter 4

Accurate Ages of Early-Type Field Galaxies

4.1 Introduction

The difficulty in obtaining even moderate quality spectra of Low Surface Brightness galaxies forced us to study their global properties, without much capability to investigate substructure within individual galaxies. This is unfortunate, because there is much to be learned by studying the detailed inner-workings of galaxies. The structure of a galaxy: it's detailed chemical composition and dynamical state, give us very strong clues to the processes most relevant to the formation and evolution of galaxies.

Hierarchical clustering models predict that galaxies form by the agglomeration of small bits into bigger ones over the course of cosmic history. If these models are correct, then galaxies are expected to have undergone many mergers during their formation, and a large fraction of the galaxies should have undergone a major merger in the past $\sim$ 8 Gyr (since z=1). The timescale for galaxy growth is most likely environment dependent. In low density environments, galaxies will only infrequently pass near other galaxies, allowing the possibility of a merger. In clusters, galaxy interactions are much more frequent. However, the large velocity differences between galaxies makes nearby encounters very short-lived, and it may be hard to have significant merging once a cluster has grown large.

Early-type (E and S0) galaxies are observed to follow several strong scaling relations, such as the Fundamental Plane (Djorgovski & Davis, 1987; Jørgensen, Franx, & Kjaergaard, 1996) and the Mg-σ relation (Bender, Burstein, & Faber, 1993). The evolution of these scaling relations with lookback time (redshift) has been used to place constraints on possible star formation histories for this class of galaxies (Ziegler & Bender, 1997; Jørgensen, Franx, Hjorth, & van Dokkum, 1999). The standard result is that the bulk of stars in early-type cluster galaxies must have formed at $z > 2$.

The stellar populations of galaxies can also be modelled directly, and ages derived for them. This has been a very active field for the past decade, with several groups obtaining large observational samples (Gonzalez, 1993; Jørgensen, 1997; Trager et al., 1998; Kuntschner & Davies, 1998) and analysing the data with increasingly sophisticated stellar population models (Worthey et al., 1994; Bruzual A. & Charlot, 1993; Vazdekis et al., 1996; Vazdekis, 1999; Thomas, Maraston, & Bender, 2002). Work during the first half of the 1990's discovered two major difficulties in the proper interpretation of the data. First of all, there was a degeneracy between the effects of age and metallicity on both broadband colors and stellar absorption line strengths. The effects of a change in metallicity by a factor of two could be matched by a change in metallicity by a factor of 3 for most indicators(Worthey et al., 1994). Additionally, non-solar elemental abundance ratios were found, which were not matched by the stellar population models. In most massive early-type galaxies, the ratio of Mg to Fe was larger than in the sun, by nearly a factor of two (0.2 - 0.3 dex).

The models that was applied were single stellar population (SSP) synthesis models. The methodology of building an SSP is simple: A star formation history is defined, with a chosen IMF and metallicity at each epoch. Stars evolve along theoretical tracks which move from the Main-Sequence onto the Giant Branch, and eventually towards stellar remnants, though there is usually no feedback mechanism in the population synthesis models. For any given epoch, then, it is known how many stars (or what mass fraction of the total population) fit into each mass and age interval. This translates into a stellar temperature and surface gravity (spectral and luminosity class), which is then translated into an SED. These are added for all the stars in the population, weighted by their luminosity and mass fraction, to predict the global SED of the model population.

The basic mechanics of most stellar population models are the same. They differ in two main ways. The first is the translation from mass and age into stellar temperature and surface gravity, which depends on model isochrones. Different stellar population models use different model isochrones (e.g. the padua isochrones, or the yale isochrones; note that there is an alternative for modelling stars on the giant branch, using the fuel consumption theorem (Renzini & Buzzoni, 1986; Maraston, 1998)). The second difference between stellar population synthesis models is how they translate from stellar temperature and surface gravity into an output SED. The two main techniques are the use of so-called ”fitting functions” and the use of empirical stellar spectra.

The fitting function technique is the one employed the Lick group (Worthey et al. 1994, Trager et al 1998), and has been expanded by Tripicco & Bell (1995) and more recently by Thomas, Maraston, & Bender (2002). These models do not produce output synthesized spectra. Rather, they predict the strengths of line ”indices”, akin to absorption line equivalent widths. Line indices are used as a surrogate for absorption line equivalent widths in galaxies, where it is nigh impossible to determine the continuum level in the velocity broadened spectra. Each line index has three defined wavelength bandpasses, one covering the absorption line itself, and two defined in the neighboring continuum regions. The index strength is effectively the difference in flux between the line bandpass, and mean of the continuum bandpasses (weighted by their width in Angstroms). The Lick group measured the strengths of 21 line indices in ~ 400 stars covering a range of temperature and surface gravities (Worthey et al., 1994). They then fit polynomials to the strength of each index as a function of temperature and surface gravity, and it is these fitting functions which are now used in stellar population models to predict the index strengths of synthesized populations.

The alternative approach taken by some stellar population modelers (e.g. Vazdekis et al., 1996; Vazdekis, 1999) is to use a large library of observed stellar spectra, covering a range of stellar parameters. Each star has a measured temperature and surface gravity. A grid covering the whole range of possible (relevant) temperature and surface gravities is defined, and each library star is assigned to one part of this grid. It is possible to have multiple stars assigned to the same area of the grid. When the synthesized model population contains a stellar mass fraction from a certain part of the grid, the actual spectra of the star or stars from that area are added to the output SED (weighted by the mass/luminosity fraction for this type of star in the whole population).

The advantage to the latter technique is that it predicts model spectra, at the resolution and with the wavelength coverage of the stellar library. In contrast, the fitting function method only predicts derived measurements of the SED, and does not easily allow the study of new spectral features. Additionally, the fitting functions in the literature are mainly for the low resolution Lick indices, which were established on stellar spectra with $\sim$ 9Å resolution, and the index bandpasses are typically 20Å–40Å wide. Information is lost by using such low resolution (as shown by Jones & Worthey (1995) and Vazdekis (1999)), and cannot be regained in the fitting function models. The disadvantage to the empirical stellar library approach is that it requires a large observational library; if there are no stars observed within a given grid region of stellar temperature and surface gravity, then the output SED will be lacking. With the fitting functions, interpolation within the temperature/gravity plane is more smoothly accomplished.

Working with the basic models, tentative solutions were devised for both the age-metallicity degeneracy, and the mismatch to non-solar elemental abundances. By simultaneously using two indices, one which was more age sensitive (typically a Hydrogen Balmer line), and one which was more metallicity sensitive, the degeneracy could be partly broken. This was used in Chapter 2 in the analysis of the LSB galaxies. Extending from two dimensions to a third (or more) dimension is also the path for solving the non-solar abundance problem. Jørgensen (1997) analysed the stellar populations and dark matter content in a sample of Coma cluster galaxies using the correlations between $H\beta_G$, Mg_2, and $<\mathrm{Fe}>$ with velocity dispersion, σ, simultaneously. Trager et al. (2000, hereafter TFWG) used the results of Tripicco & Bell (1995) to "correct" the Worthey et al. (1994) SSP models for non-solar [E/Fe] (here we introduce the [] notation, which is the logarithm of the elemental abundance ratio, relative to that ratio for the Sun). Based on those corrections, TFWG derived ages (*t*), metallicities ([Fe/H]), and elemental abundance ratios ([E/Fe]) for a sample of ~ 40 early-type field galaxies. The transformation couples together the $H\beta$, Mgb, and Fe line indices in a way that leads to correlated errors in age, metallicity, and [E/Fe]. If the data quality were insufficient, the correlated errors would lead to the appearance of correlations in the derived parameters. Consequently, TFWG urge the necessity of using only high quality data (S/N ~ 100, yielding uncertainties on $H\beta$, Mgb, and $<\mathrm{Fe}>$of ~ 0.1Å) to study the stellar populations.

A new generation of stellar population models have now been developed, aiming to solve these two problems, and accurately model the stellar populations of galaxies. Vazdekis has used his modelling code (Vazdekis et al., 1996), combined with a large empirical stellar spectral library (Jones, 1998) to produce model galaxy spectra at 1.8Å resolution, over the wavelength ranges 3820–4500 Å and 4780–5460 Å. Using these model spectra, a new index near the $H\gamma$ line has been defined which shows age sensitivity, but is insensitive to metallicity (Vazdekis & Arimoto 1999). This index, called $[H\gamma + 1/2(\mathrm{Fe\ I}+\mathrm{Mg\ I})]_\sigma$ is very carefully defined so that metallic absorption lines in the continuum bandpasses are precisely cancelled out by similar metal sensitive features in the line bandpass. This index solves the age-metallicity degeneracy by itself; consequently, it is also independent of the

Mg/Fe ratio of the observed population. Unfortunately, this comes at a cost. Since the metallicity insensitivity of the index is achieved by carefully balancing metal absorption in the line and continuum bandpasses, the index is very sensitive to wavelength offsets, and intrinsic velocity broadening of the galaxy spectra. In fact, three different indices were defined, for galaxies whose velocity dispersion fit into the intervals 100-175 km s^{-1}, 150-225 km s^{-1}, and 225-300 km s^{-1}. To accurately measure the $[\mathrm{H}\gamma + 1/2(\mathrm{Fe\ I}+\mathrm{Mg\ I})]_\sigma$ index requires spectra with S/N per Å of $\sim$ 200, $\sim$ 300, and $\sim$ 400, respectively, depending on the velocity broadening of the spectrum.

An alternative solution to the age-metallicity-abundance ratio is proposed by the simple stellar population models of Thomas, Maraston, & Bender (2002). These models are based on the old Lick fitting functions, however they explicitly account for non-solar abundance ratios. Following the work of Tripicco & Bell (1995), Jørgensen (1997), and TFWG. Thomas, Maraston, & Bender (2002) have derived the effect of non-solar abundances on the fitting functions, and have calibrated this using spectra of Galactic globular clusters. Their models explicitly include the α/Fe abundance ratio as a parameter, and predict the full set of lick index strengths as a function of age, metallicity, and α/Fe for simple stellar populations.

We set out to obtain the high quality data necessary to measure the Vazdekis & Arimoto $[\mathrm{H}\gamma + 1/2(\mathrm{Fe\ I}+\mathrm{Mg\ I})]_\sigma$ index, in a small sample of field early-type galaxies. We wish to constrain the distribution of stellar population ages in field galaxies, compared to cluster galaxies. Hierarchical clustering models predict that on average, field galaxies should be younger (less time since the last major merger) than cluster early-type galaxies (Kauffmann, 1996). Such high quality data have many other uses, of course, and so in addition to measuring the $[\mathrm{H}\gamma+1/2(\mathrm{Fe\,I}+\mathrm{Mg\,I})]_\sigma$ index in the centers of these galaxies, we measure accurate lick indices as a function of radius to $\sim \pm 1$ $R_e$for all the galaxies, and interpret the measured indices using the new Thomas, Maraston, & Bender (2002) models. This is a work in progress. We have obtained and reduced the data. The Lick indices have been measured, and the data has been put onto the Lick system. We present here a preliminary analysis of the line strength gradients, and the inferred age, metallicity, and abundance ratio gradients. The organization of this chapter is as follows: sample selection, observations, and data reduction are described in Section 4.2. The kinematic measurements are described in Section 4.3. We derive the Lick index measurements in Section 4.4. The model grids are described in Section 4.5.Section 4.6 is a description of future plans for the dataset and its analysis.

4.2 Observations & Data Reduction

4.2.1 Sample Selection

Measurement of the $[\mathrm{H}\gamma+1/2(\mathrm{Fe\,I}+\mathrm{Mg\,I})]_\sigma$ index requires very high quality spectra, with S/N/Å of $\sim 200-400$, depending on the internal velocity dispersion of the galaxy. This requirement placed the strongest constraint on the sample selection, as there are very few field early-type galaxies for which spectra of such quality can be obtained with a 4m-class telescope in a reasonable amount of integration time. We compiled a list of E and S0 (de Vaucouleurs T–type < 0) galaxies with $22^{\mathrm{h}}30^{\mathrm{m}} < \mathrm{RA} < 10^{\mathrm{h}}30^{\mathrm{m}}$ and $\mathrm{DEC} > -15^\circ 00'$. For this list of galaxies, we

TABLE 4.1
FIELD GALAXY SAMPLE

Galaxy	RA (J2000)	DEC (J2000)	cz (km s^{-1})	M_{abs} (mag)	T-type	σ (km s^{-1})	R_e (arcsec)	PA (deg)	ϵ
NGC 661	01:44:14.6	+28:42:24.1	3817	-20.84	-4.3	181	15.0	60	0.24
NGC 821	02:08:21.2	+10:59:41.0	1735	-20.57	-4.8	208	39.5	25	0.24
NGC 890	02:22:01.0	+33:15:58.0	3994	-21.58	-2.7	213	27.1	1	0.31
NGC 1172	03:01:36.0	-14:50:12.0	1669	-19.10	-3.8	116	33.4	25	0.24
NGC 1700	04:56:56.3	-04:51:55.0	3895	-21.80	-4.6	234	20.4	65	0.37
NGC 2300	07:32:19.5	+85:22:30.0	2099	-20.85	-3.4	263	27.5	78	0.24
NGC 2872	09:25:42.5	+11:25:55.0	3241	-20.59	-4.8	288	17.6	22	0.24
NGC 3115	10:05:13.9	-07:43:06.8	720	-19.77	-2.8	265	35.5	43	0.55
NGC 7457	23:00:59.9	+30:08:42.0	812	-18.75	-2.6	75	31.9	130	0.41

then derived local density statistics, in a manner similar to that described in chapter 3. Given the difficulty of the observations, and the limited time allocation (3 nights), observing any sort of complete sample was unrealistic. Instead, we chose a representative sample of (apparently) bright field early-type galaxies which cover a range of internal velocity dispersions. From a technical standpoint, this sample allows the evaluation of the $[\mathrm{H}\gamma + 1/2(\mathrm{Fe\ I}+\mathrm{Mg\ I})]_{\sigma}$ index on real galaxy data, in comparison with the more traditional analysis of the low resolution lick indices, and can be used to establish the science case for larger, and complete samples of field and cluster galaxies. The galaxies which were observed are listed in Table 4.1, along with relevant data from the literature.

4.2.2 Spectroscopic Observations

Spectroscopy was obtained with the ISIS spectrograph on the 4.2m William Herschel Telescope over three nights, 20-22 November 2000. The instrumental set-

TABLE 4.2
INSTRUMENTATION

	Spectroscopy
Telescope	William Herschel Telescope (4.2m)
Instrument	ISIS (blue arm)
Dates	20-22 November, 2000
CCD	EEV12 2048 × 4096 pixels (binned 2 × 1)
Gain	1.46 e^-/ADU
RON	5.3 e^-
Pixel size spatial	0.38″ (binned)
Wavelength Range	3855 Å - 5648 Å
Slit Width × Length	1.6″× 4′
Grism	R600B (600 l/mm)
Dispersion	0.44 Å/pix
Resolution(σ)	1.02 Å (59 km s^{-1} @ 5200 Å)

up is described in Table 4.2. ISIS is a dual beam spectrograph, however we only obtained data through the blue channel. The dichroic used to separate light to the blue and red spectrograph arms causes a variable fringing pattern which makes accurate flat-fielding impossible. Consequently, we opted to use a mirror rather than the dichroic, and observed with only the blue channel. The first and third nights were mostly clear, but the middle night had moderate to thick cloudcover. Seeing the first night was 1.8″ FWHM, improving to 1.3″ the second night, and 0.9″ on the final night. Multiple exposures typically of length 35 minutes were taken for each galaxy, interspersed with flatfield and arc-lamp spectra. We observed a selection of F, G, and K stars from the Lick (Worthey et al., 1994) sample to act both as templates for the kinematic measurements, and also to secure the calibration onto the Lick absorption index system. The kinematic templates must have the same instrumental dispersion profile as the galaxy observations. The stars were moved across

TABLE 4.3
WHT SPECTROSCOPIC OBSERVATIONS

Name	Exposure Time[a]	N_{obs}[b]	PA slit[c]	Notes
NGC 661	8,400	4	60	major axis
NGC 821	8,400	4	25	major axis
NGC 890	1,300	1	55	major axis
NGC 1172	8,400	4	25	major axis
NGC 1700	8,400	4	90	major axis
NGC 2300	3,100	2	78	major axis
NGC 2872	6,090	4	291.5	intermediate PA
NGC 3115	2,600	3	133	minor axis
NGC 7457	10,500	5	130	major axis

[a] Total exposure time, in seconds

[b] Number of exposures

[c] Measured North through East, in degrees

and along the spectrograph slit during the observations to fully illuminate the slit, mimicking the galaxies' light entering the spectrograph. Several of the stars were observed multiple times, to help assess uncertainties in both the velocity zeropoint and the Lick index measurements. We detail the galaxy observations in Table 4.3. Table 4.4 lists the stars observed, with their spectral types and metallicities.

4.2.3 Basic Reductions

Data reduction was done within the IRAF software environment. The basic steps of the reduction follow those described for the LSB galaxy spectra in Chapter 2, though with appropriate modifications to account for the different telescope and instrument configuration. In particular, flexure is present in the ISIS spectrograph to a much greater degree than in the LRS, and this modifies the reductions somewhat.

TABLE 4.4
STELLAR TEMPLATES

Name	Spectral Type[a]	[Fe/H][b]	N_{obs}[b]	Notes
HD 75632	K5	···	1	velocity standard
HD 75732	G8V	0.13	1	
HD 82328	F6IV	-0.06	1	
HD 85503	K2III	0.46	3	Lick system standard
HD 90508	F9V	-0.23	1	
HD 97907	K3III	-0.04	2	
HD 184406	K3IIIb	0.22	1	Lick system standard
HD 198149	K0IV	-0.14	1	
HD 199580	K0III-IV	-0.1	2	
HD 201891	F8V-VI	-1.23	1	
HD 203344	K1III	-0.09	1	
HD 219449	K0III	-0.13	1	

[a] Spectral type from Simbad, http://simbad.u-strasbg.fr/sim-fid.pl

[b] Metallicity, relative to Solar, from Worthey et al. (1994)

[c] Number of individual observations

The first step in the reductions was to subtract off the bias and overscan. No structure was seen in the overscan regions, so the mean overscan level was subtracted off as a constant from the whole image. We took a set of ten bias frames each night. When combined, we determined the bias level to be negligible, less than one ADU over the whole array. No correction was made for dark current, as it has historically not been an issue with this CCD.

Each night, we observed the twilight sky to determine the spatial flatfield illumination along the slit, and we exposed continuum lamp flatfields using the internal calibration unit, to determine the pixel-to-pixel variations on the chip. Internal flatfields were also observed with each telescope pointing, but since fringing is not a problem for this blue wavelength setup, we did not use these flatfields.

These flatfield pointings at various telescope positions did expose issues of telescope and instrument flexure; it is clear that the entrance slit is moving relative to the CCD, and consequently the small-scale spatial variations of throughput caused by non-uniformity in the slit jaws move over the CCD from one exposure to the next. With the exception of two colums far from the center of the slit, however, the column-to-column throughput variation is less than 2%. The two obvious features, each 1-2 pixels wide, have roughly 5% lower througput. Inability to account for these throughput variations might affect the extracted spectra in several ways. First, they will limit the ultimate accuracy with which we can subtract off the sky. Second, they will subtly affect the luminosity weighting of spatially summed bins. Neither point should be a concern for this project, however. In a typical 35 minute galaxy spectrum, the number of sky counts is only $\sim$15 ADU/pixel, corresponding to an uncertainty due to poisson noise of 20%. Even when the spectra are coadded, the sky noise per pixel is roughly 10% of the summed sky level. Flatfield illumination uncertainties of 2% may be safely ignored in the sky subtraction. We are not attempting to derive galaxy surface brightness profiles from our spectra, so the inaccuracies in the spatial flatfielding at the 2% level can also be ignored. Variability in the slit width will also result in fluctuating spectral resolution along the slit, which will affect our kinematic measurements. However, over most of the slit, the variability is small. The two obvious features are not near the center of the chip, and galaxy spectra extracted from the affected regions will have large spatial windows (many pixels), which will further minimize the effects of these few columns.

For each night, the series of ten continuum flatfield spectra were coadded. These two dimensional spectra were collapsed in the spatial dimension yielding the one dimensional spectral signature of the lamp. This one dimensional spectrum was replicated into two dimensions, and divided out of the flatfield image. Next, the flatfield was collapsed in the spectral dimension to reveal a one dimensional slit function. This was also divided out of the two dimensional spectrum, leaving only small scale pixel-to-pixel variations in the flatfield. Similar reductions were done to the nightly set of twilight flatfields, except that the (spatial) slit function is the thing of interest. With the exception of small movement in the slit position, the spatial structure in the twilight flat was identical from one night to the next, and this slit function was multiplied into the three nightly flatfields, which were then compared. Over most of the chip, these three flatfields were very similar. However, on the red end of the spectrum, near 5300Å, there was a variation between the flatfield from the first night and the latter two. It is unknown what caused this difference, but it shows up only near this wavelength (±100Å), and results in a flatter spatial profile than is seen for the rest of the wavelength coverage. It should be noted that because of the way the spectral normalization was done (to divide out the signature of the lamp), there is no difference between the nightly flatfields for the central columns of the chip, so there should certainly be no effect for stellar observations, and in the galaxy centers. Nevertheless, because of the variation, we opted to use separate flatfields for each night.

After the galaxy spectra were bias subtracted and flatfielded, we cleaned them for cosmic rays. This was done individually for each spectrum, by convolving the 2D spectrum with a 9×3 pixel tophat filter, and then marking pixels which differed between the smoothed and unsmoothed image by more than 3σ (poisson noise) as potential cosmic rays. This selects sharp features, such as cosmic rays, bad pixels, and potentially emission lines in the galaxies. Cleaning was not done in the central columns of the galaxy trace where the galaxy brightness changed much more rapidly than the convolution kernel, causing all pixels to be flagged. The flagged pixels were all checked by hand, and those which were not cosmic rays or bad pixels were removed from the mask. All pixels immediately adjacent to a flagged pixel were now also flagged, to account for moderately affected pixels. All of the flagged pixels were then interpolated over, along the spatial dimension.

The spectral dispersion was traced using the IRAF task `IDENTIFY` and `REIDENTIFY`. CuNe+CuAr arc lamp spectra were taken either before or after (or both) each galaxy spectrum, and we identified approximately 75 spectral lines spanning the full wavelength coverage. We fit the dispersion function with a sixth order chebyshev polynomial, with a typical RMS uncertainty of 0.2Å. The galaxies were almost always centered in the slit, though some stellar spectra were taken $\sim$10$''$from the slit center. We combined two stellar observations taken at the extremes of this small range, and used them to determine the spatial distortions of the spectral trace. There was only a small ($<$ 3 pixel) spatial shift across the full spectrum. We used the `TRANSFORM` task in IRAF to rectify the science spectra, correcting the spatial slant and placing the spectra on a linear wavelength scale.

Sky regions were defined for each spectrum on both sides of the rectified galaxy trace, near the edges of the slit. The sky regions typically covered 100 pixels (40$''$) on either side of the galaxy, and had a mean level of $\sim$ 15 ADU/pixel. The flux in the two sky regions was averaged at each wavelength, and this was subtracted from the 2D spectra.

Multiple spectra of the same galaxy were summed together, after spatially aligning the galaxy centers. The spatial alignment involved making only integer pixel shifts, which could introduce up to an additional 0.2$''$ of spatial broadening. Added in quadrature to the $\sim$ 1$''$ seeing, however, this is a small effect.

Starting from the center of each galaxy, we extracted apertures with spatial bins chosen so as to reach a total S/N per Å (at 5100 Å) of at least 55 in each bin. In the outermost $\sim 1-2$ apertures, the S/N is lower, however, typically 20–40 per Å. Additionally, we extracted apertures centered on the galaxy, which extended along the major axis to $\pm$a$_\mathrm{e}$/16, $\pm$a$_\mathrm{e}$/10, $\pm$a$_\mathrm{e}$/8 and $\pm$a$_\mathrm{e}$/4 (For NGC 3115, we used b$_\mathrm{e}$ instead of a$_\mathrm{e}$, and for NGC 2872, where the longslit was rotated to an intermediate position angle, we used r_e instead of a_e). Finally, we extracted an aperture designed to match as closely as possible the aperture used by the Lick group. This was an aperture of dimension $1.6'' \times 3.5''$ (compared to the Lick aperture dimensions of $1.4'' \times 4.0''$), centered on the galaxy.

We observed six spectrophotometric standards over three nights. The stars observed were Feige 15, Feige 34 (twice), HD19445 (twice) and BD +28 4211. All the stellar observations were made with the slit at the parallactic angle. We used wide extraction apertures so that any differential image quality at the red and the blue ends of the spectrum would not cause a systematic tilt in the sensitivity function. The variable cloudcover and variable seeing over three nights makes it impossible for us to derive absolute spectrophotometry, but the relative sensitivity function was stable, and any extinction due to cloudcover seems to have been grey (i.e. wavelength independent). We use all six observations together to determine the relative sensitivity function, using the IRAF tasks `STANDARD` and `SENSFUNC`. The resulting one-dimensional sensitivity function was then applied to the galaxy and template star spectra.

4.3 Kinematic Measurements

We used the kinematic modelling software of Karl Gebhardt (Gebhardt et al. (2000); based on the method of Saha & Williams (1994)) to derive the line-of-sight velocity distribution (LOSVD) for each aperture. The method employed is a non-parametric penalized maximumum-likelihood fit in pixel space to determine the broadening function which produces the best match between a broadened stellar template and the observed galaxy spectrum for each aperture. The penalty function is used to impose some level of smoothness to the LOSVD. The penalty function employed is the integral over all velocities of the square of the second derivative of the LOSVD. The software works with multiple input template stars, and simultaneously determines the best linear combination of templates, and the best-fit LOSVD. Both the LOSVD and the weighting of individual templates are constrained to be non-negative at all all points, e.g. the convolved template fit is made up of only positive (or zero) flux components. Uncertainties on the LOSVD fit are determined for each velocity bin, using a Monte-Carlo technique.

Each step of the process will now be described in more detail.

We start with the extracted one dimensional spectra for both the galaxy radial aperture bins, and the stellar template spectra. Velocity offsets between the template stars are determined (using this same LOSVD fitting software) and removed, so that each template is on the same velocity reference frame. All of the stars have published heliocentric velocities. The relative offsets we measure between these stars, compared to their actual (published) velocity offsets, reflects our uncertainty in the wavelength calibration and stability. We measured an offset of

-5±2 km s^{-1} (RMS = 7 km s^{-1}) for the sample as a whole (rejecting HD 75732 which had an offset of -55 km s^{-1}; including this star yields an RMS uncertainty of ±14 km s^{-1}). This adopted mean velocity reference is offset by -10 km $s^{-1}$from the reference frame if we used only the velocity standard star HD 75632. A 10 km s^{-1} shift translates to a wavelength difference of 0.17Å at 5200Å, and 0.14Å at Hγ. Independent of the reference frames, we observed two stars twice, and one star three times. The RMS difference between multiple observations was 7 km s^{-1}.

The first step of the kinematic measurements is to remove the continuum from both the template and galaxy observations. A low order polynomial fit is made to the spectrum, with sigma clipping to reject low points, which are presumably real absorption features. We did two iterations of this fit, and an example is shown in Figure 4.1. The spectrum is normalized by the polynomial fit. Next, the peak values are averaged within user defined wavelength bins (we used seventeen bins, but did not fit the region near the Mgb absorption feature), and a continuum ”fit” is made which is simply the mean value for each bin, connected by straight lines. This is illustrated in Figure 4.2. The spectrum is normalized by this fit, and is now ready for the LOSVD determination. The placement of the wavelength bins, and the resultant continuum normalization, does not have a large impact on the measured kinematics, so long as the same wavelength bins are used for both the stellar templates and the galaxy spectra.

The next step is the determination of the full LOSVD. We start with an initial guess for the radial velocity and velocity dispersion, taken from the literature. We also choose a smoothing parameter, dependent on the quality (S/N) of the extracted spectra. The LOSVD fitting software employs a maximum penalized likelihood technique. Rather than simply minimizing the χ^2 of a fit to the LOSVD, the software minimizes the function:

$$\mathrm{L(v)} = \chi^2 + \beta \int\limits_{\mathrm{V}} \left(\frac{\partial^2 f}{\partial v^2} \right)^2 \mathrm{dv}$$

where *f*(v) is the LOSVD and β is a (constant) smoothing parameter, chosen by the user. These spectra were extracted such that each aperture has a S/N/Å $>$ 55 until the outermost $\sim$2-3 apertures in the galaxy profile. This is very high quality data, and consequently we can use a small smoothing parameter. For most of the apertures we used something between 0.2 and 0.8. The LOSVD is determined over a velocity span equal to five times the input velocity dispersion guess, split into 29 equally spaced bins. The fit was done using the rest-frame wavelength interval 5000Å-5400Å. In some cases, small wavelength ranges were excluded from the fit due to bad sky subtraction residuals from strong sky lines in the galaxy spectrum. The initial guess is a uniform velocity profile over the full velocity interval, at the appropriate redshift, and the template spectra are convolved with this profile. The galaxy spectrum is compared to the model fit, and χ^2 is calculated. The penalty function is measured, and added to the χ^2 (with the penalty function weighted by the smoothing parameter). Then, the velocity profile is modified, a new fit performed, and a new χ^2 + penalty function calculated. Iterative modifications to the velocity profile and optimal template combination are made to minimize the value of χ^2 + penalty function. The minimization routine runs locally, and is not guaranteed of finding a global minimum/best fit. Once a ”robust” local minimum is found, the program stops, and outputs the best-fit to the LOSVD for each velocity bin, the χ^2 of the fit, and the optimal weighting of the input templates. Figure 4.3 shows an example of the template spectrum being fit to a galaxy spectrum.

The LOSVD derived from this fit is shown in Figure 4.4 for three different choices of the smoothing parameter, 0.0, 0.2, and 30. When the smoothing is turned off, the best-fit LOSVD is very jagged (Panel 4.4a). Formally, this has the lowest χ^2 of any of the fits. However, it does not seem physically reasonable to have the stellar velocity distribution so segmented into small groups. The velocity bins used in this example (~ 47 km s^{-1}) subsample the resolution of the data (which has a FWHM resolution of 140 km s^{-1}at 5200Å). Consequently, neighboring velocity bins in the unsmoothed LOSVD are not independent, and the best fit LOSVD doesn't require use of every velocity bin. Physically more realistic profiles are produced by only slightly increasing the smoothing. Figure 4.4b shows the LOSVD derived with a smoothing of 0.2, and Figure 4.4c shows the LOSVD derived with a smoothing of 30. The intermediate smoothing level shows a double peaked profile, which is smoothed out in the latter profile. The reported σ in each panel is the second gauss-hermite moment of a fourth order Gauss-Hermite expansion of the LOSVD. Though this sort of expansion cannot properly describe a double peaked profile, the second moment alone is a fairly robust measure. The value reported in the zero smoothing case is an error, because the Gauss-Hermite fit did not cover the whole distribution, but only the highest peak of the LOSVD. While a broad range of the smoothing parameter will produce the same first and second moment (radial velocity and velocity dispersion), it is more difficult to determine the proper smoothing parameter to produce a physically accurate description of the higher order shape. As stated above, there is a large range of smoothing parameters for which the σ is stable; when the derived σ starts to increase, the smoothing parameter is clearly too high. Similarly, double peaked features, or significant skew or kurtosis, should be stable for a range of smoothing values, if they reflect the underlying physical structure, and not just noise in the fitting process. We experimented with several smoothing values to determine what seemed to be the most reasonable values. In the case of the aperture from NGC 661 displayed in Figure 4.4, the double peaked profile seems to be real. This aperture (app10) is at a radius of +5.7” from the center of the galaxy along the major axis, which is near the peak of the signature of the decoupled core in this galaxy (see Figure 4.6). We are actually resolving the two counter-rotating stellar components, thus producing the two peaks in the LOSVD.

We describe the LOSVD with 29 separate values, the relative fractions of the velocity distribution in each velocity bin. The shape of the LOSVD can be distilled further, however, by fitting the derived profile with an expansion in Gauss-Hermite polynomials. Gauss-Hermite polynomials are ortho-normal functions, whose lowest order terms resemble a standard gaussian. van der Marel & Franx (1993) showed that using only the first four Gauss-Hermite polynomials was sufficient to describe most of the information contained in the LOSVDs of hot stellar systems. They suggest using the expansion:

$$\mathcal{L}(v) = [\gamma\alpha(w)/\sigma]\left\{1+\sum_{j=3}^{4} h_j H_j(w)\right\}, \qquad w \equiv (v-V)/\sigma \tag{4.1}$$

where γ normalizes the height of the LOSVD, V sets the center of the profile, σ sets the width of the profile, H_j are the Hermite polynomials, h_j are the coefficients which we solve for, and

$$\alpha(y) = \frac{1}{\sqrt{2\pi}} e^{-(1/2)y^2}.$$

In Figure 4.5 we show the effect of the H_3 and H_4 polynomials when added to a Gaussian profile (this plot is a copy of Fig. 1 from van der Marel & Franx (1993)). A positive h_3 leads to a prograde wing on the LOSVD, while a negative h_3 results in a retrograde wing. A positive h_4 leads to pointier profiles than a pure Gaussian, while a negative $h4$ leads to a more flattened profile. These non-Gaussian profiles have clear physical interpretations in terms of rotation and the relative importance of radial and tangential orbits for the galaxy structure (van der Marel & Franx, 1993; Rix et al., 1997). However, when the true velocity distribution is double peaked, for instance due to multiple physical components, like a decoupled core, the higher order coefficients can be easily mis-interpreted, and the full, non-parametric LOSVD yields a better understanding.

For each galaxy aperture, we measure the shape of the LOSVD, and we derive the first four coefficients (velocity, σ, h3, and h4) of a Gauss-Hermite expansion to the best-fit LOSVD. These values are plotted as a function of luminosity-weighted radius for all the apertures of each observed galaxy in Figures 4.6 – 4.14. The uncertainties for all these measurements, both the LOSVD bin heights and the Gauss-Hermite coefficients, are determined with Monte-Carlo simulations of the observations. The best-fitting template combination is convolved with the derived LOSVD. We add random noise at each wavelength, such that the noise spectrum is gaussian with a FWHM determined by the input S/N of the spectrum in that aperture. Then the LOSVD fitting routine is run on this model spectrum, and a new

LOSVD is measured and tabulated. The new fit is compared to the original spectrum, and the χ^2 of that fit is used to make a new estimate of the S/N in the original spectrum. A second realization of the convolved template with the best-fit LOSVD is made, with new noise added in, and the fitting routine is run again. This continues for 100 iterations. By allowing the S/N to vary, we are partially accounting for the effects of template mismatch between the input galaxy spectrum and the best-fitting template. The 100 realizations are used to derive 68% confidence bands for all of the measured LOSVD bin heights, as well as the first four moments of the Gauss-Hermite expansion. These uncertainties are plotted in Figures 4.6 – 4.14.

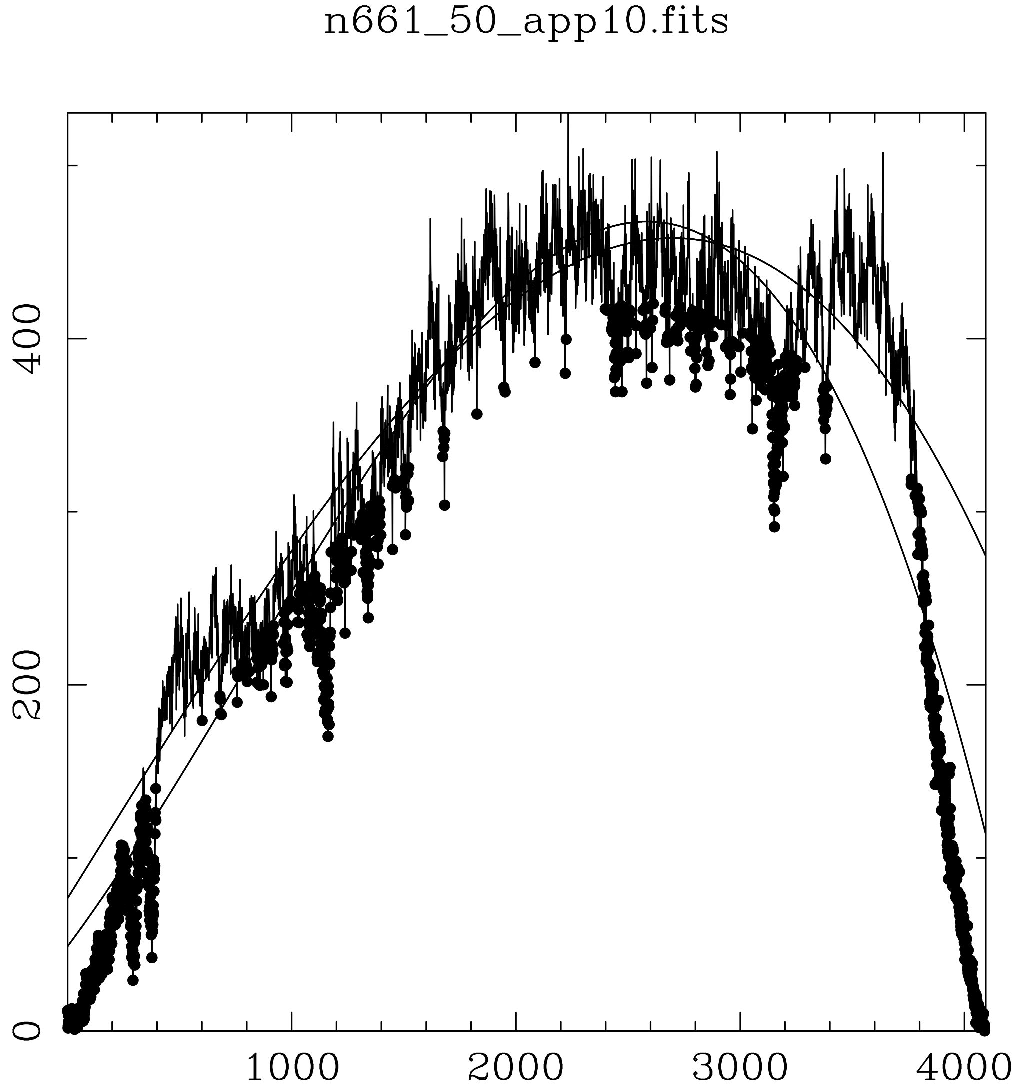

Figure 4.1 Continuum normalization step 1: a low order polynomial fit is made to the full spectrum, with sigma clipping of the low points. Two iterations are done, and the spectrum is normalized by the fit.

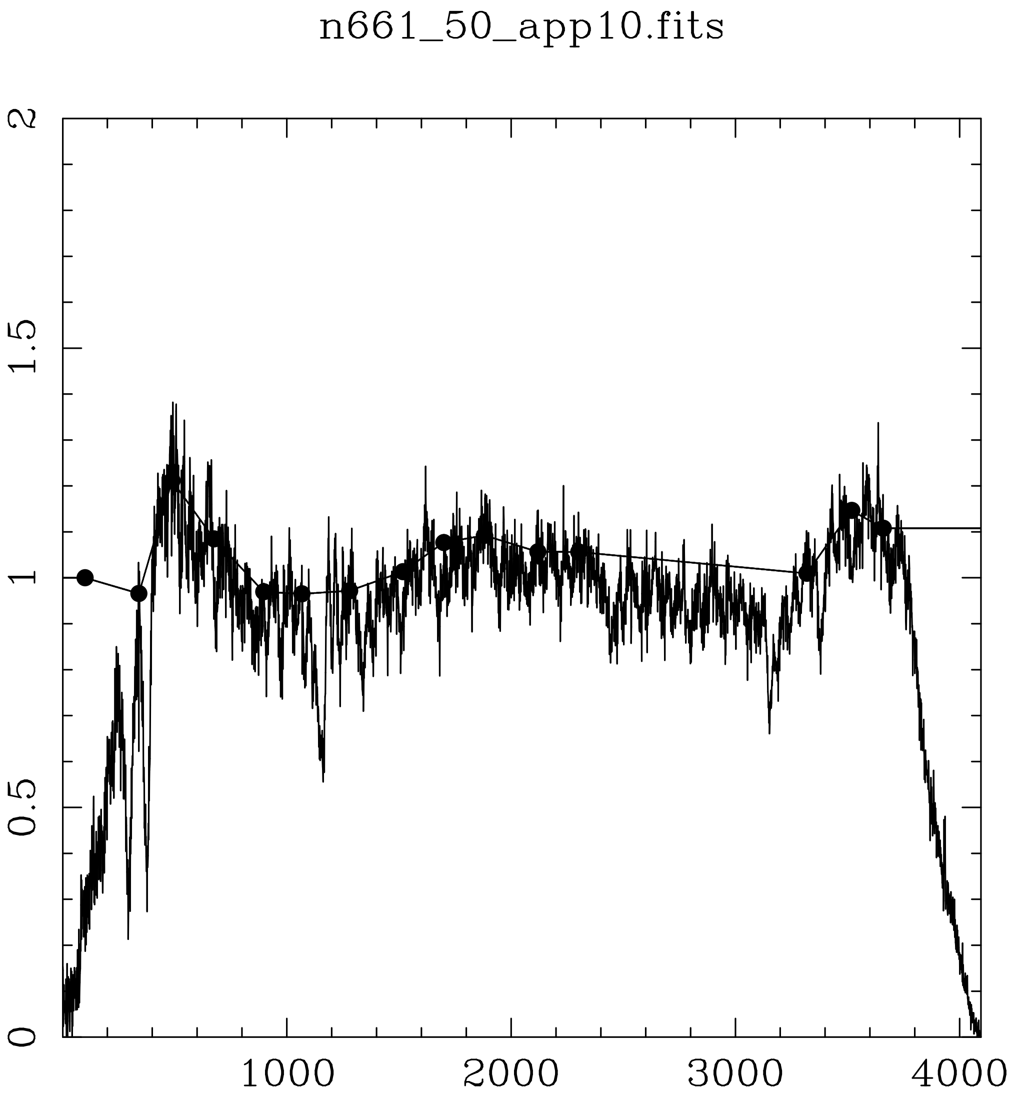

Figure 4.2 Continuum normalization step 2: the flux of the peaks inside each bandpass window are averaged, and a straight line fit is made between the mean within each window. The spectrum is then normalized by this piecewise fit. The number and placement of the windows can be toggled by the user, but the kinematic measurements are robust to a wide range of window sizes and placements.

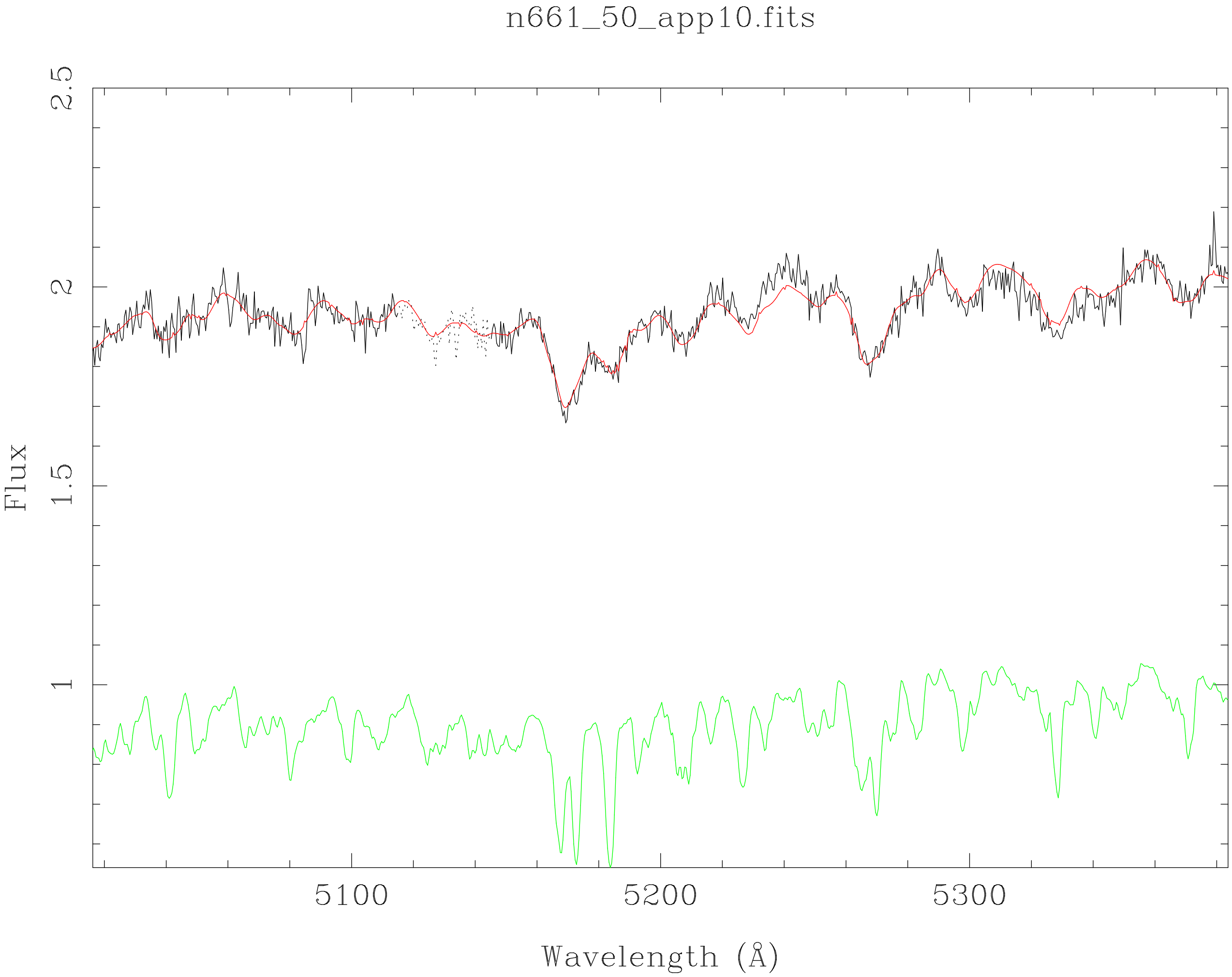

Figure 4.3 Fitting the LOSVD: the galaxy spectrum is shown on top (solid line with noise), and the best-fitting composite template is shown on the bottom. Overlayed on the galaxy spectrum is the template after being convolved with the MPL best-fit LOSVD, for a smoothing parameter of 0.2. The dashed portion of the galaxy spectrum near 5130Å was contaminated with sky emission, and not used during the fitting. The spectrum is from aperture app10 of NGC 661, at a radius of 5.5” from the center of the galaxy, in the region where the signature of the counter-rotating core reaches its maximum.

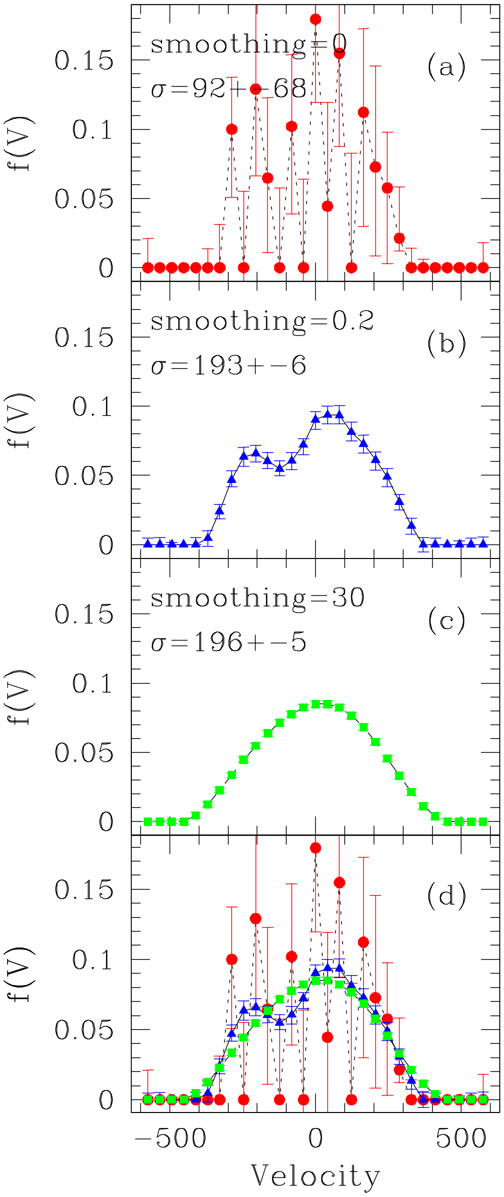

Figure 4.4 Comparison of derived LOSVD for different smoothing parameters: a) no smoothing applied; b) smoothing of 0.2; c) smoothing of 30; d) all three LOSVDs plotted together. The spectrum being fit is the same one as in Figure 4.3, in the region of the galaxy NGC 661 where the signature of the counter-rotating core reaches its maximum.

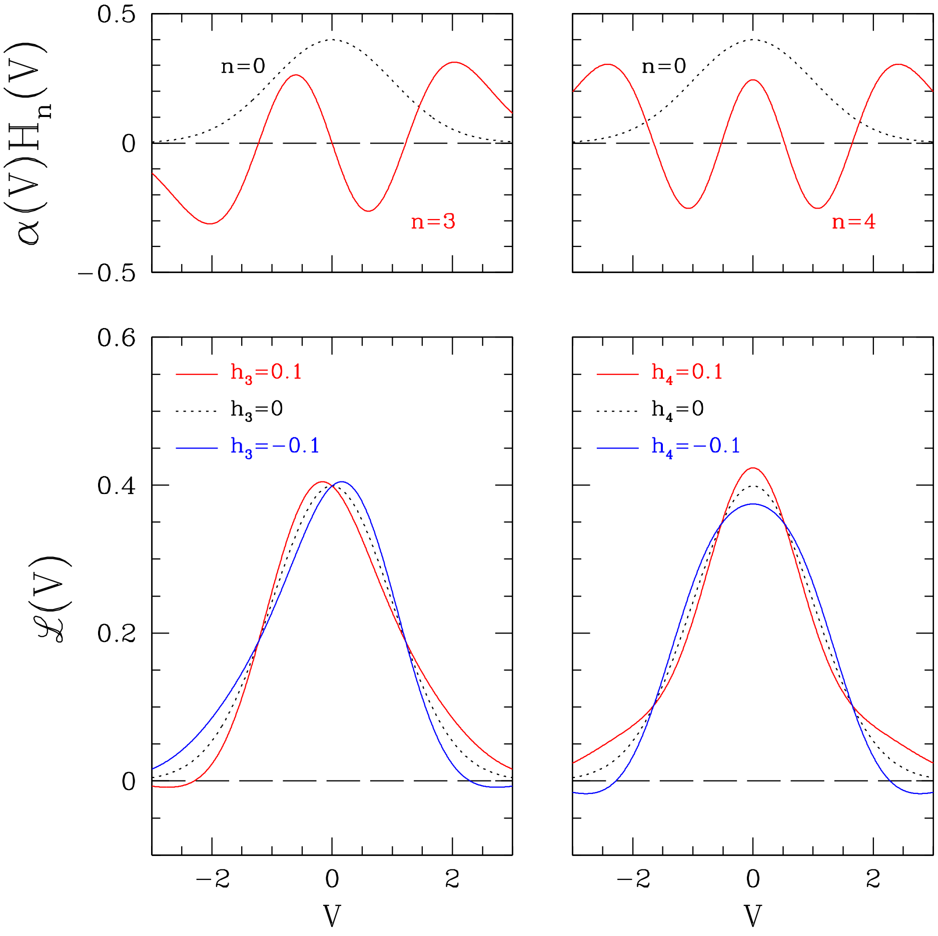

Figure 4.5 Examples of the effect of the H_3 and H_4 polynomials on Gaussians. Top panels: the lowest odd (left) and even (right) Gauss-Hermite functions used to describe the deviations of the LOSVD from a pure Gaussian profile. Bottom panels: the standard Gaussian (dotted line), and the higher order LOSVD profiles produced by various values of h_3 and h_4. The h_3 term produces a skew to the LOSVD, while h_4 produces either flattened or pointy profiles. This figure is a copy of Figure 1 from van der Marel & Franx (1993)

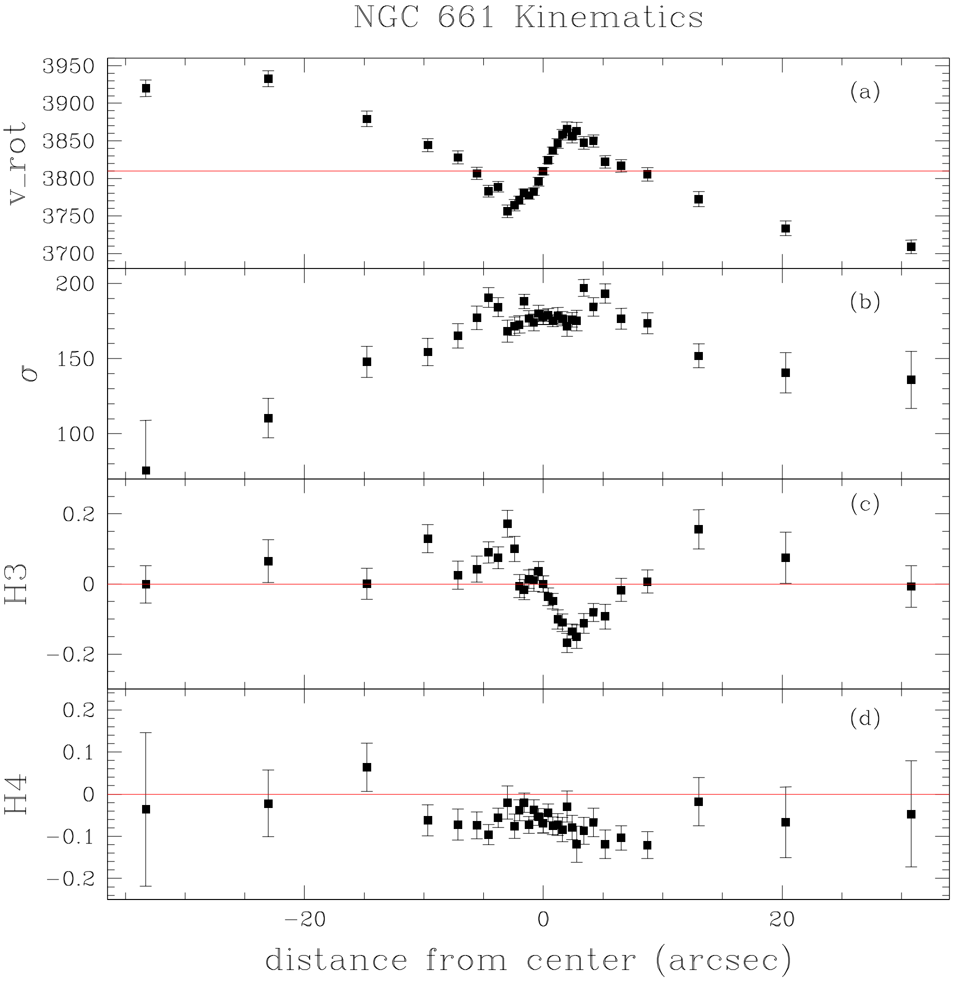

Figure 4.6 Kinematic measurements for NGC 661, as a function of distance from the galaxy center along the major axis. a) heliocentric radial velocity. b) velocity dispersion c) H3, the third order Gauss-Hermite moment of the LOSVD d) H4, the fourth order Gauss-Hermite moment of the LOSVD.

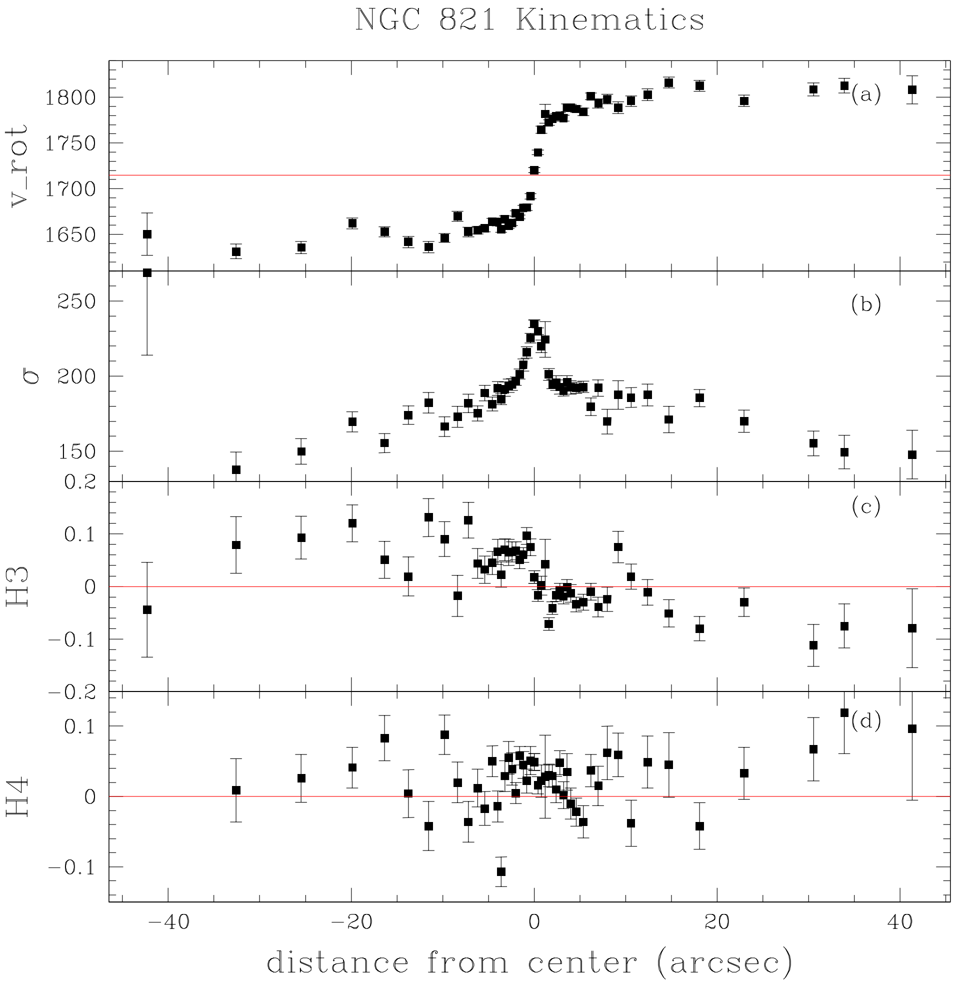

Figure 4.7 Kinematic measurements for NGC 821, as a function of distance from the galaxy center along the major axis. a) heliocentric radial velocity. b) velocity dispersion c) H3, the third order Gauss-Hermite moment of the LOSVD d) H4, the fourth order Gauss-Hermite moment of the LOSVD.

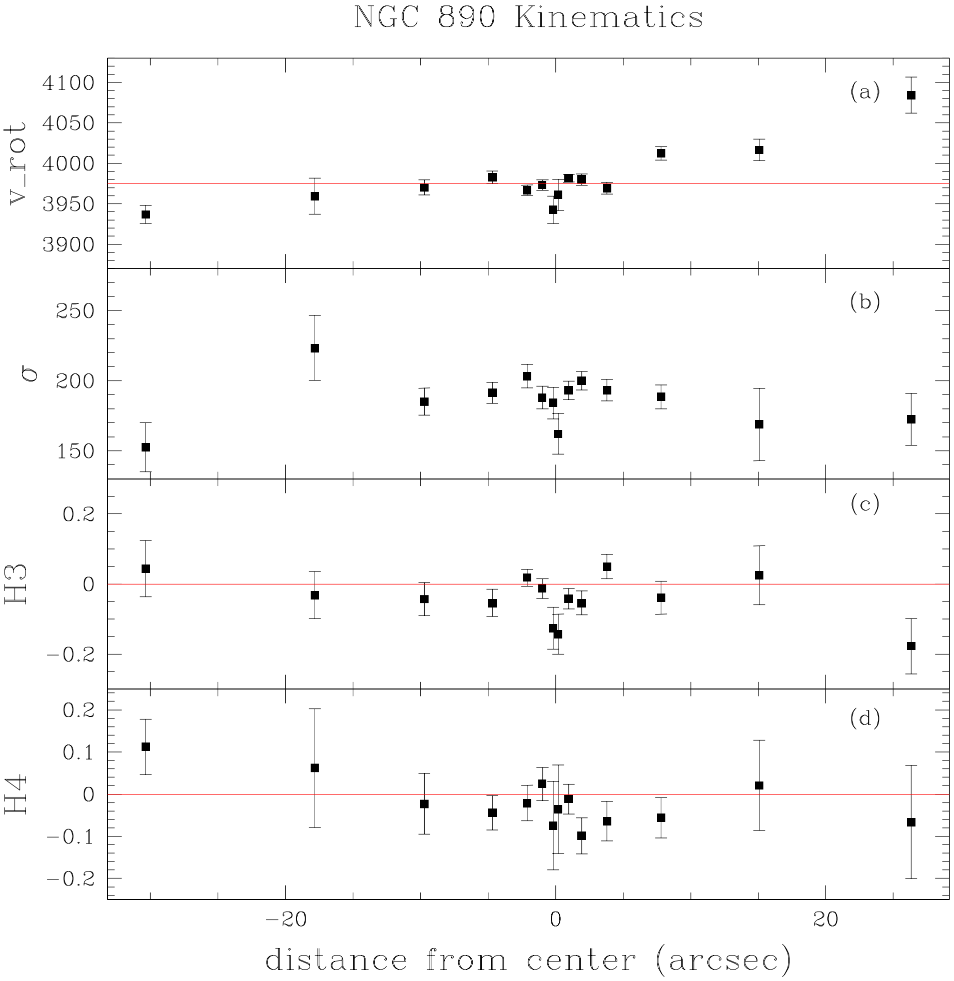

Figure 4.8 Kinematic measurements for NGC 890, as a function of distance from the galaxy center along the major axis. a) heliocentric radial velocity. b) velocity dispersion c) H3, the third order Gauss-Hermite moment of the LOSVD d) H4, the fourth order Gauss-Hermite moment of the LOSVD.

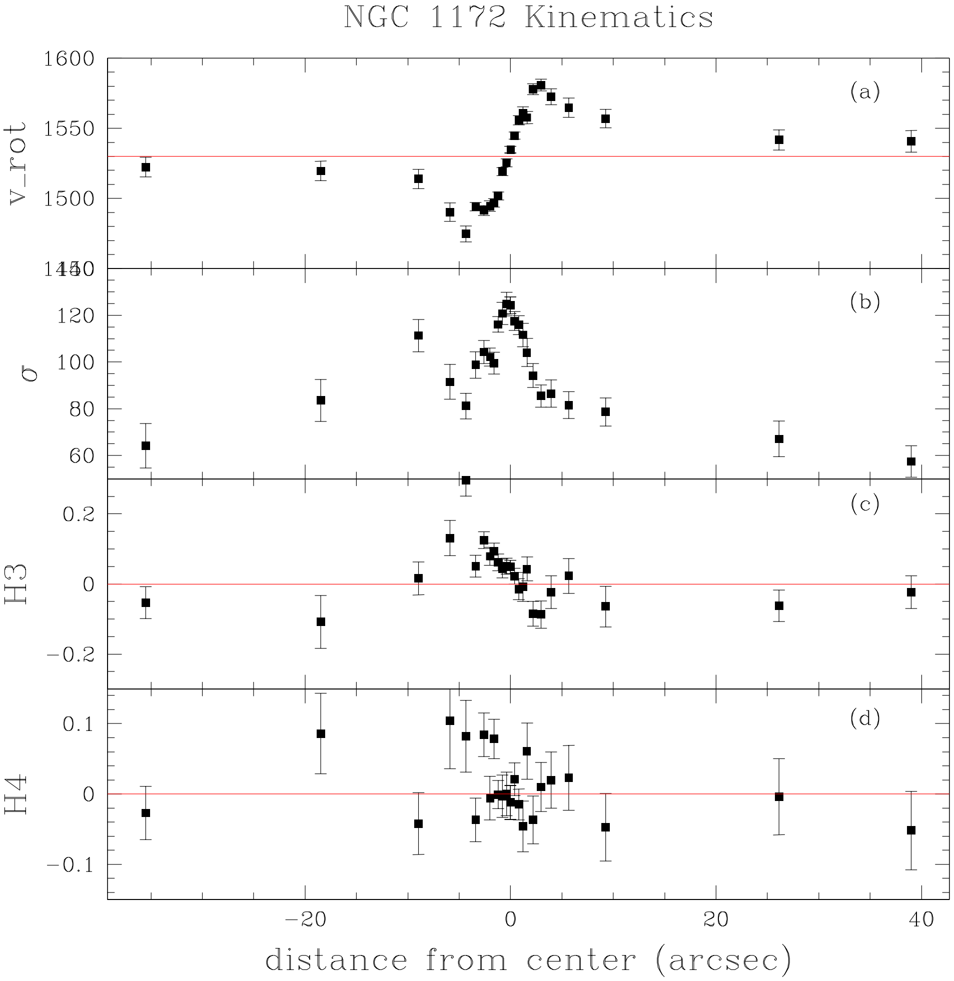

Figure 4.9 Kinematic measurements for NGC 1172, as a function of distance from the galaxy center along the major axis. a) heliocentric radial velocity. b) velocity dispersion c) H3, the third order Gauss-Hermite moment of the LOSVD d) H4, the fourth order Gauss-Hermite moment of the LOSVD.

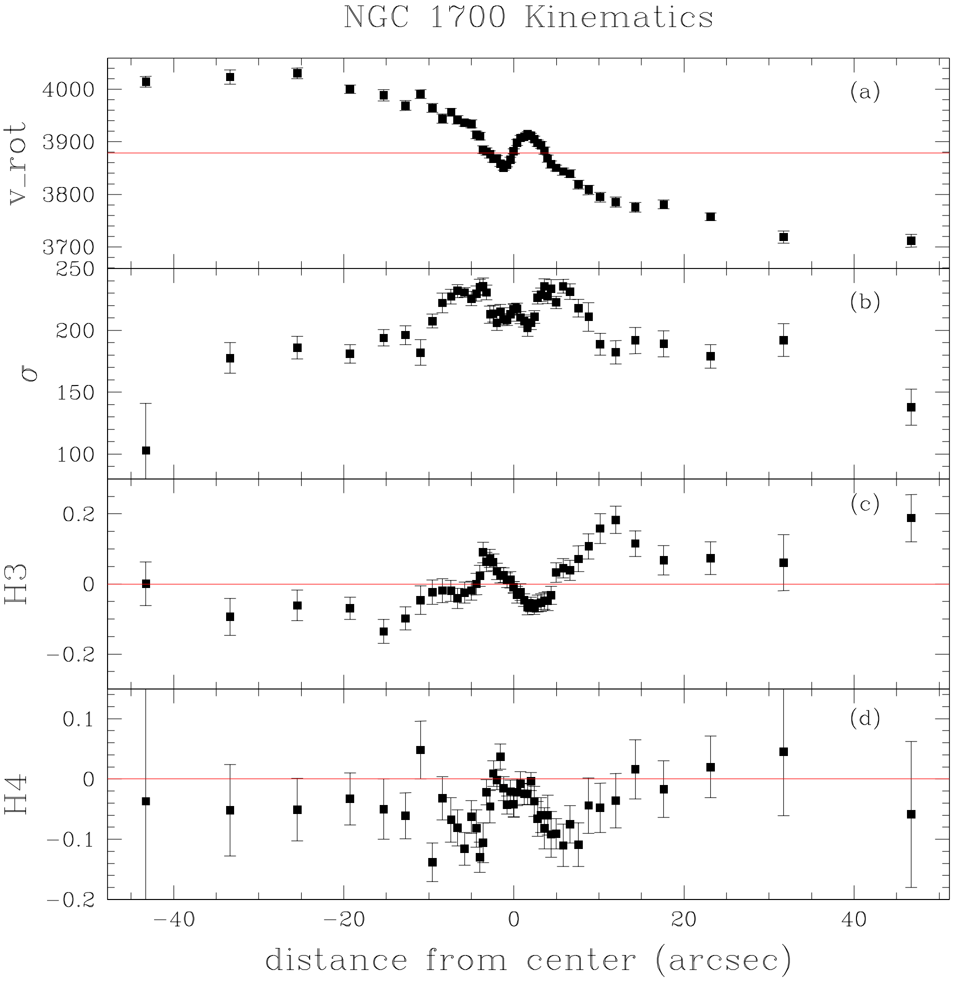

Figure 4.10 Kinematic measurements for NGC 1700, as a function of distance from the galaxy center along the major axis. a) heliocentric radial velocity. b) velocity dispersion c) H3, the third order Gauss-Hermite moment of the LOSVD d) H4, the fourth order Gauss-Hermite moment of the LOSVD.

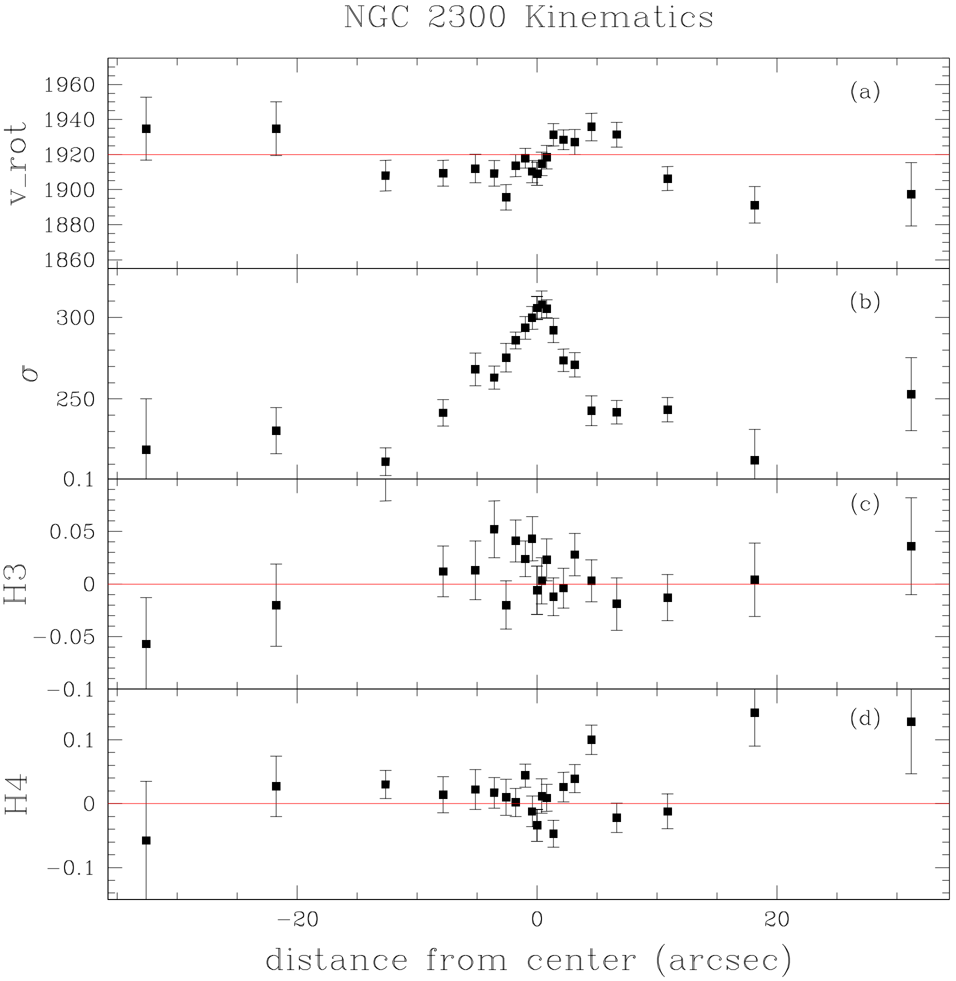

Figure 4.11 Kinematic measurements for NGC 2300, as a function of distance from the galaxy center along the major axis. a) heliocentric radial velocity. b) velocity dispersion c) H3, the third order Gauss-Hermite moment of the LOSVD d) H4, the fourth order Gauss-Hermite moment of the LOSVD.

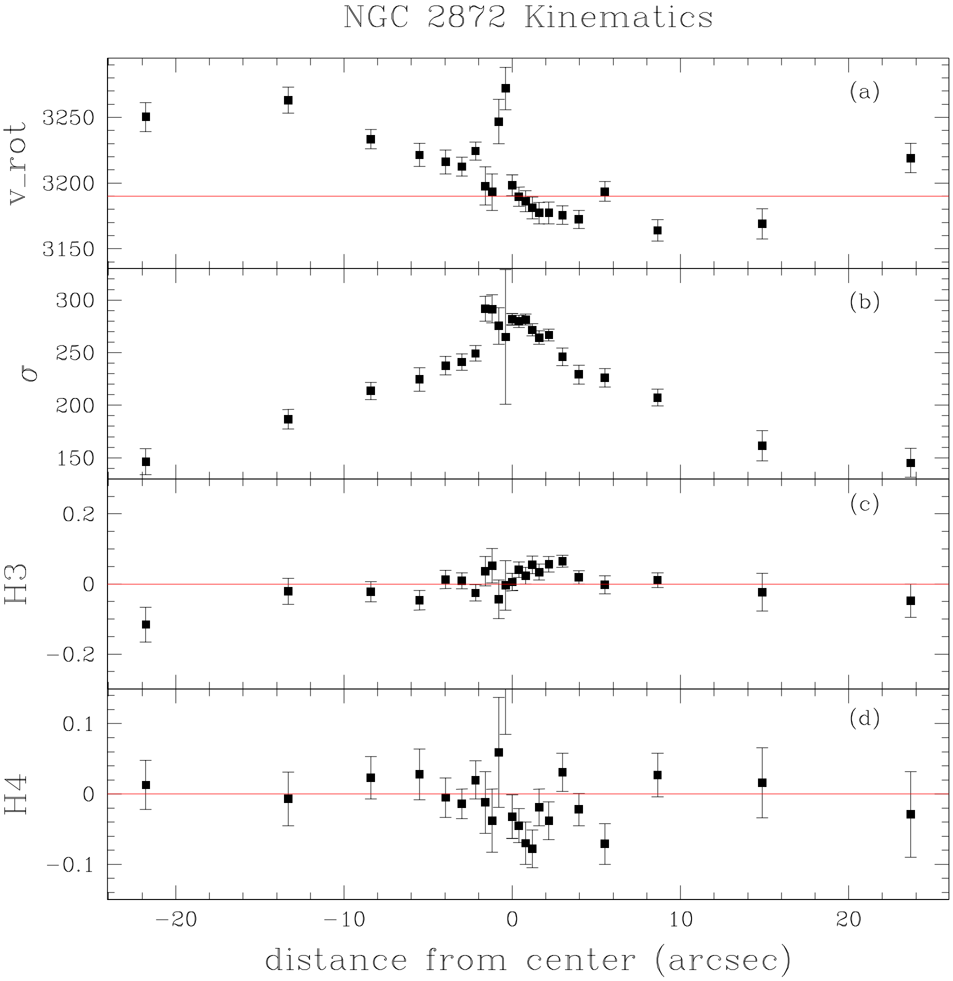

Figure 4.12 Kinematic measurements for NGC 2872, as a function of distance from the galaxy center along PA=291.5. a) heliocentric radial velocity. b) velocity dispersion c) H3, the third order Gauss-Hermite moment of the LOSVD d) H4, the fourth order Gauss-Hermite moment of the LOSVD.

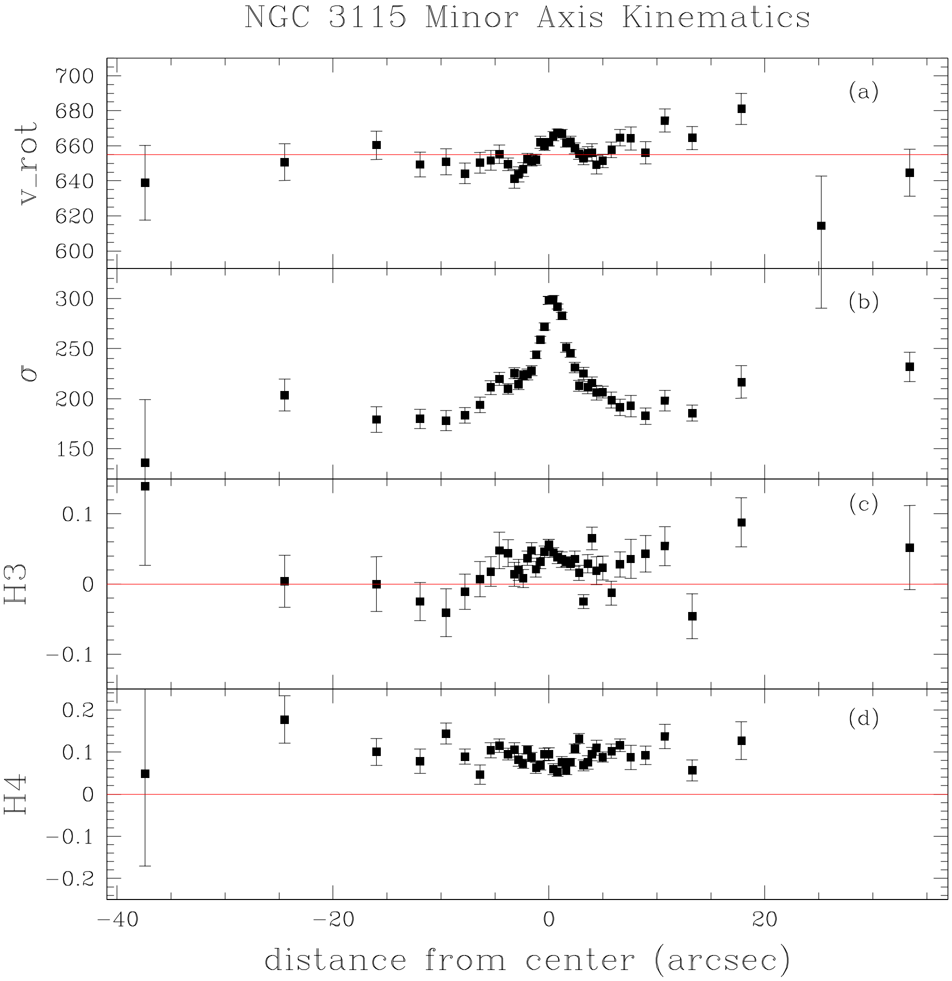

Figure 4.13 Kinematic measurements for NGC 3115, as a function of distance from the galaxy center along the minor axis. a) heliocentric radial velocity. b) velocity dispersion c) H3, the third order Gauss-Hermite moment of the LOSVD d) H4, the fourth order Gauss-Hermite moment of the LOSVD.

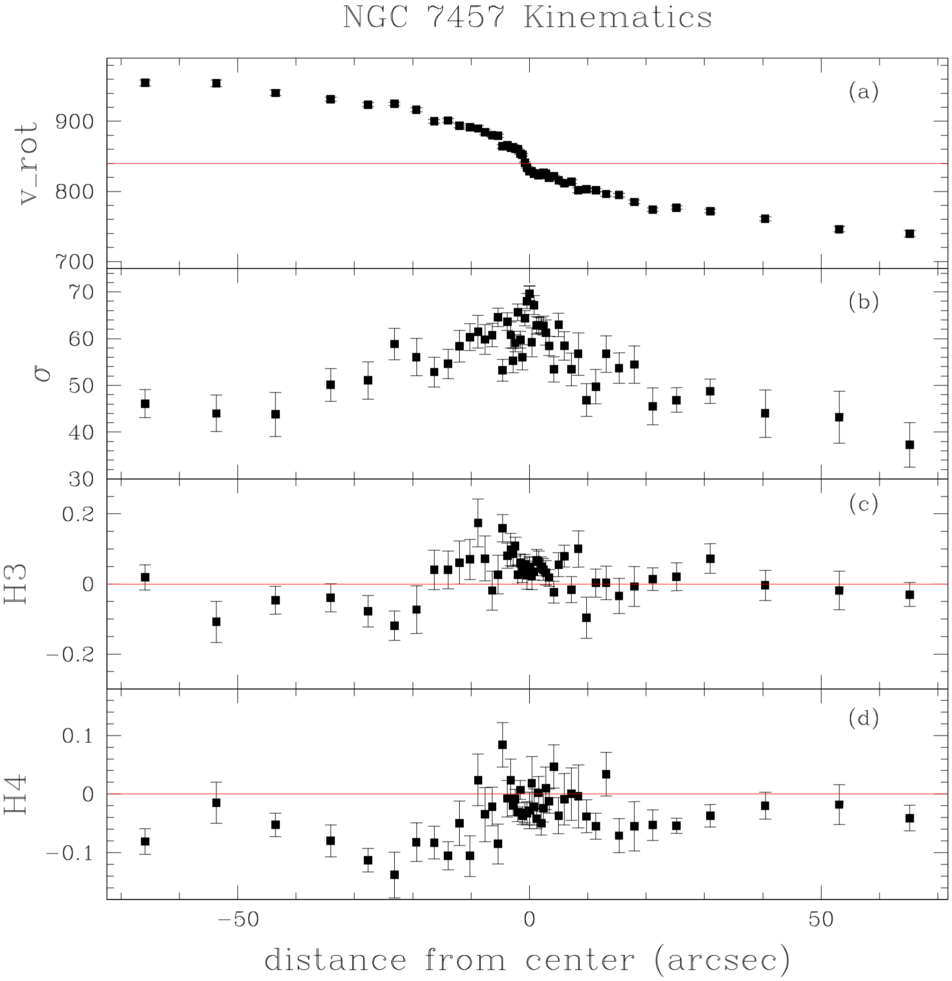

Figure 4.14 Kinematic measurements for NGC 7457, as a function of distance from the galaxy center along the major axis. a) heliocentric radial velocity. b) velocity dispersion c) H3, the third order Gauss-Hermite moment of the LOSVD d) H4, the fourth order Gauss-Hermite moment of the LOSVD.

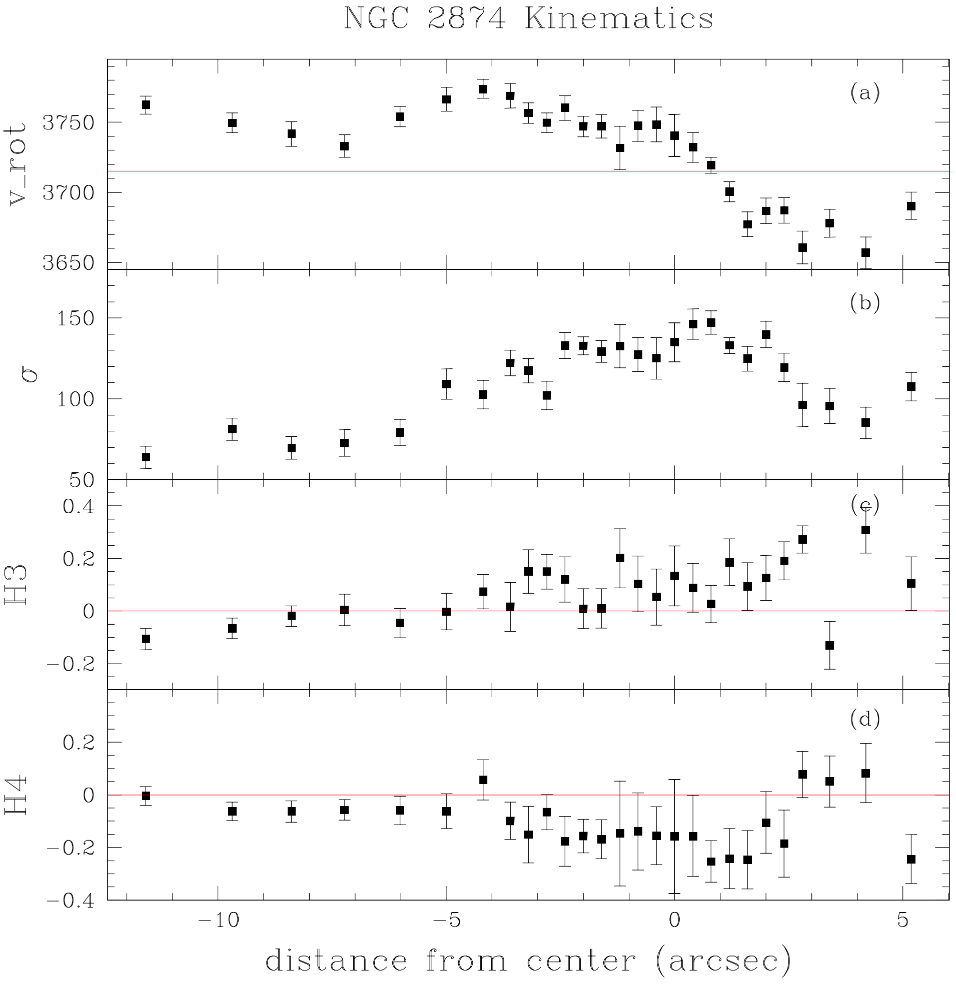

Figure 4.15 Kinematic measurements for the Sbc galaxy NGC 2874, as a function of distance from the galaxy center along PA=291.5. The data along the positive axis is truncated, where it begins to overlap with NGC 2872 (which is shifted 500 km/s to the blue). a) heliocentric radial velocity. b) velocity dispersion c) H3, the third order Gauss-Hermite moment of the LOSVD d) H4, the fourth order Gauss-Hermite moment of the LOSVD.

4.3.1 Notes On Kinematics Measurements for Select Galaxies

NGC 661: The kinematically decoupled core that we observe has not previously been reported in the literature. The h_3 and h_4 profiles in the decoupled core region should be interpreted warily, as the double peaked LOSVD is not well fit by the fourth order Gauss-Hermite decomposition.

NGC 821: Our observations show a central peak in the velocity dispersion, which was not seen in the observations of Bender, Saglia, & Gerhard (1994). The rotation curve we measure is also steeper in the central region than the one they published. Presumably both of these differences are due to better spatial resolution for our observations ($\sim 1.2''$ vs. $\sim 1.8''$). This galaxy is in both the SAURON sample, and the Planetary Nebula Spectrograph sample, and will have well sampled two-dimensional kinematics soon available.

NGC 1172: This is the only galaxy in the sample which shows significant emission, with a strong [O III]λ5007 line. The emission line kinematics have not yet been measured, however.

NGC 1700: This galaxy has been extensively observed by Statler, Dejonghe, & Smecker-Hane (1999), along four different position angles. The kinematically decoupled core is well known. The caveats about interpretating h_3 and h_4 given for NGC 661 apply here as well.

NGC 3115: Previous observations of NGC 3115 (e.g. Bender, Saglia, & Gerhard, 1994) have shown that this galaxy has rapid rotation along the major axis. Though we lined up the spectrograph slit parallel to the minor axis, it is clear that we did not pass through the center of the galaxy, but offset from it. This leads to a bump in the velocity profile which is symmetric about the major axis of the galaxy. We do not have a good determination of the radial velocity at the galaxy center.

NGC 7457: This is the smallest galaxy in our sample, and the velocity dispersion is not resolved in the outermost apertures. This will lead to poor measurements of the higher order Gauss-Hermite coefficients as well.

NGC 2854: This galaxy is not in our early-type sample. It is a companion to NGC 2872, and has a morphological classification of Sbc. The position angle of the slit was not aligned with the galaxy major axis, though we did attempt to go through the center of the galaxy. We could not extract fully symmetric apertures because NGC 2872 filled the positive side of the slit.

4.4 Lick Indices

The Lick absorption line indices were introduced in Chapter 2. With much higher quality data, and with a bluer wavelength range, we have measured a larger set of indices on these data than we did for the LSB galaxies. The full list of Lick/IDS indices we measure, along with the definitions used for the line and continuum passbands are taken from Trager et al. (1998) and shown in Table 4.5. Additionally, we measure the $H\beta_G$ index as defined by Gonzalez (1993), and the $H\gamma$ and $H\delta$ indices defined by Worthey & Ottaviani (1997), which are listed in Table 4.6.

Several steps must be undertaken to put our index measurements onto the

TABLE 4.5

LICK INDEX DEFINITIONS[a]

Name	Index Bandpass	Pseudocontinua	Units
CN_1	4142.125–4177.125	4080.125–4117.625 4244.125–4284.125	mag
CN_2	4142.125–4177.125	4083.875–4096.375 4244.125–4284.125	mag
Ca4227	4222.250–4234.750	4211.000–4219.750 4241.000–4251.000	Å
G4300	4281.375–4316.375	4266.375–4282.625 4318.875–4335.125	Å
Fe4383	4369.125–4420.375	4359.125–4370.375 4442.875–4455.375	Å
Ca4455	4452.125–4474.625	4445.875–4454.625 4477.125–4492.125	Å
Fe4531	4514.250–4559.250	4504.250–4514.250 4560.500–4579.250	Å
C4668[b]	4634.000–4720.250	4611.500–4630.250 4742.750–4756.500	Å
$H\beta$	4847.875–4876.625	4827.875–4847.875 4876.625–4891.625	Å
Fe5015	4977.750–5054.000	4946.500–4977.750 5054.000–5065.250	Å
Mg_1	5069.125–5134.125	4895.125–4957.625 5301.125–5366.125	mag
Mg_2	5154.125–5196.625	4895.125–4957.625 5301.125–5366.125	mag
Mg*b*	5160.125–5192.625	5142.625–5161.375 5191.375–5206.375	Å
Fe5270	5245.650–5285.650	5233.150–5248.150 5285.650–5318.150	Å
Fe5335	5312.125–5352.125	5304.625–5315.875 5353.375–5363.375	Å
Fe5406	5387.500–5415.000	5376.250–5387.500 5415.000–5425.000	Å

[a] All indices as defined in Trager et al. (1998).

[b] Formerly called Fe4668, but renamed after Tripicco & Bell (1995) found that this index was more sensitive to Carbon than Iron.

TABLE 4.6
OTHER INDEX DEFINITIONS

Name	Index Bandpass	Pseudocontinua	Units
Hβ_G[a]	4851.32–4871.32	4815.00–4845.00 4880.00–4930.00	Å
Hδ_A[b]	4083.50–4122.25	4041.60–4079.75 4128.50–4161.00	Å
Hδ_F[b]	4091.00–4112.25	4057.25–4088.50 4114.75–4137.25	Å
Hγ_A[b]	4319.75–4363.50	4283.50–4319.75 4367.25–4419.75	Å
Hγ_F[b]	4331.25–4352.25	4283.50–4319.75 4354.75–4384.75	Å

[a] Defined in Jørgensen (1997).

[b] Defined in Worthey & Ottaviani (1997).

Lick system, and ensure that the models used to interpret the data are appropriate. We first degrade the resolution of our data to match that of the Lick spectrograph. This ranges from 8.4Å FWHM near the Mgb index up to 11Å for the bluest indices (Worthey & Ottaviani, 1997).

After matching the resolution, we measure the indices for all of our stellar observations. The stellar observations serve two purposes. First, they provide templates from which we can determine the correction back to zero velocity dispersion. Secondly, they are used to determine additive offsets between our measurements and those of the Lick group. These offsets are often caused by differences in the continuum shape; the original Lick data were not flux calibrated (even in a relative sense), whereas we have removed the instrumental response from our data.

The velocity dispersion correction was derived in a similar manner to the one described in Chapter 2. We convolve all of the templates with gaussians of width 25–400 km s^{-1}, in steps of 25 km s^{-1}. The measurements for each star are then normalized to the value for that star without any velocity broadening, and all the stars are used together. We show the effects of the broadening on all the indices in Figures 4.16–4.19. In the figures, we have color-coded the stars by spectral type: F stars are blue, the G star is green, and the K stars are red. Some of the corrections are definitely type dependent. We have used only the G and K stars for determining the corrections. We fit a third order polynomial to the index corrections, excluding any stars which strongly deviate from the mean variation. The fits are shown in Figures 4.16–4.19 as a black line in the left panels. The right panels show the residuals after subtracting off or dividing by the fit, as appropriate. The spread of the different template residuals is a measurement of the systematic uncertainty for these corrections.

We compare the measured indices for the stars with the published measurements from the Lick group (Worthey et al., 1994). The comparisons for all the indices are shown in Figures 4.20–4.23. We list the mean offset and scatter for all the indices in Table 4.7. Two stars were observed twice, and one star was observed three times. Even for indices where our comparison to the published values shows a great deal of scatter, the multiple observations of a single star (taken on different nights) match closely. We applied the measured offsets to the galaxy index observations, after the velocity dispersion correction had been applied.

We determine the uncertainties for each line index measurement using Poisson statistics. These uncertainties should be compounded by the uncertainty in

TABLE 4.7

LICK INDEX STELLAR OFFSETS

Index	Offset[a]	rms	N_{obs}
CN_1	0.024±0.008	0.031	15
CN_2	0.015±0.004	0.017	15
Ca4227	-0.000±0.025	0.097	15
G4300	0.110±0.083	0.321	15
Fe4383	-0.180±0.102	0.394	15
Ca4455	-0.250±0.080	0.311	15
Fe4531	-0.011±0.067	0.261	15
Fe4668	-0.120±0.110	0.425	15
Hbeta	0.170±0.025	0.098	15
Fe5015	0.710±0.084	0.326	15
Mg_1	-0.040±0.003	0.013	15
Mg_2	-0.050±0.002	0.009	15
Mg b	-0.050±0.049	0.191	15
Fe5270	0.083±0.043	0.166	15
Fe5335	0.287±0.049	0.191	15
FE5406	0.239±0.051	0.199	15
$H\gamma_A$	-0.230±0.082	0.317	15
$H\gamma_F$	-0.110±0.050	0.192	15
$H\delta_A$	0.434±0.107	0.415	15
$H\delta_F$	0.156±0.071	0.276	15

[a] Offsets are defined as our measurements minus Worthey et al. (1994) values.

TABLE 4.8

CENTRAL LICK APERTURE LINE INDEX STRENGTHS: CN_1–C4668

Name	CN_1	CN_2	Ca4227	G4300	Fe4383	Ca4455	Fe4531	C4668
NGC 661	0.104±0.001	0.150±0.001	1.03±0.02	-1.45±0.03	-1.17±0.05	1.57±0.02	3.50±0.04	8.46±0.06
NGC 821	0.126±0.001	0.172±0.001	1.19±0.01	4.02±0.03	3.83±0.04	1.59±0.02	3.57±0.03	8.53±0.05
NGC 890	0.070±0.002	0.116±0.002	0.90±0.04	-1.68±0.07	-0.79±0.11	1.51±0.05	3.32±0.09	7.70±0.14
NGC 1172	0.056±0.001	0.098±0.001	1.04±0.02	4.93±0.03	4.24±0.05	1.44±0.03	3.30±0.04	5.25±0.07
NGC 1700	0.095±0.001	0.137±0.001	0.88±0.01	-1.91±0.02	-1.62±0.04	1.45±0.02	3.39±0.03	8.36±0.05
NGC 2300	0.125±0.002	0.168±0.002	0.93±0.03	3.27±0.05	3.63±0.08	1.36±0.04	3.36±0.07	7.59±0.11
NGC 2872	0.126±0.001	0.171±0.001	0.99±0.02	-1.94±0.04	1.71±0.06	1.38±0.03	3.47±0.05	7.79±0.08
NGC 3115	0.126±0.001	0.168±0.001	1.08±0.01	4.81±0.02	3.47±0.03	1.38±0.02	3.43±0.03	8.13±0.05

the velocity dispersion corrections as evidenced in the right-side panels of Figures 4.16–4.19. For instance, for a dispersion of $\sim$ 250–300 km s^{-1}, the additional uncertainty is $\sim$ 3% on Hβ, $\sim$ 1% on Mgb, and $\sim$ 2% on Fe5270 and Fe5335. Additionally, there is a zeropoint uncertainty for each index from additive offsets in the stellar observations. These will equally affect every measurement of a particular index, and we do not add them to the intrinsic uncertainty for each datapoint.

Finally, we compare our measurements for galaxies with the measurements from Trager et al. (1998). Our central index strengths, measured through apertures equivalent to the Lick aperture, are listed in Tables 4.8–4.10. Small offsets remain for many of the indices (and large ones for others). In particular, we find on offset of -0.1±0.09 Å for Hβ, -0.1±0.2 Å for Mgb, and -0.48±0.15 for $<$Fe$>$.

The radial profiles for each index are shown in Appendix A for all of the galaxies. These profiles have not had any offset applied to correct for differences between our measurements and the galaxy observations of Trager et al. (1998).

TABLE 4.9
CENTRAL LICK APERTURE LINE INDEX STRENGTHS: Hβ–FE5270

Name	Hβ	$H\beta_G$	Fe4930	Fe5015	Mg_1	Mg_2	Mg b	Fe5270
NGC 661	1.41±0.02	1.86±0.02	1.85±0.04	3.96±0.05	0.148±0.001	0.334±0.001	4.29±0.03	2.95±0.03
NGC 821	1.47±0.02	1.87±0.02	1.64±0.03	4.87±0.04	0.157±0.001	0.342±0.001	4.66±0.02	2.93±0.03
NGC 890	2.27±0.06	2.32±0.04	1.87±0.09	4.03±0.12	0.121±0.001	0.305±0.002	3.72±0.06	2.91±0.07
NGC 1172	1.41±0.03	1.84±0.02	1.87±0.04	3.98±0.06	0.094±0.001	0.255±0.001	4.01±0.03	2.73±0.03
NGC 1700	1.66±0.02	2.02±0.01	1.57±0.03	4.03±0.04	0.139±0.000	0.323±0.001	3.96±0.02	2.88±0.02
NGC 2300	1.49±0.05	1.81±0.03	1.36±0.07	4.71±0.09	0.155±0.001	0.344±0.001	4.48±0.05	2.67±0.05
NGC 2872	1.16±0.03	1.55±0.02	1.45±0.05	3.72±0.07	0.160±0.001	0.359±0.001	4.61±0.03	2.68±0.04
NGC 3115	1.48±0.02	1.87±0.01	1.28±0.03	5.33±0.04	0.153±0.000	0.337±0.001	4.47±0.02	2.89±0.02

TABLE 4.10
CENTRAL LICK APERTURE LINE INDEX STRENGTHS: FE5335–$H\delta_F$

Name	Fe5335	Fe5406	$H\gamma_A$	$H\gamma_F$	$H\delta_A$	$H\delta_F$
NGC 661	2.36±0.04	1.72±0.03	0.24±0.03	-6.31±0.02	9.57±0.02	-2.38 ±0.02
NGC 821	2.34±0.03	1.20±0.02	0.02±0.03	-6.88±0.02	9.57±0.02	-3.02 ±0.02
NGC 890	2.20±0.09	1.40±0.06	0.82±0.07	-5.19±0.05	9.57±0.05	-1.33 ±0.05
NGC 1172	2.19±0.04	1.22±0.03	0.46±0.03	-5.79±0.03	9.57±0.03	-1.87 ±0.02
NGC 1700	2.20±0.03	1.49±0.02	0.49±0.02	-5.85±0.02	9.57±0.02	-1.89 ±0.02
NGC 2300	2.01±0.07	1.10±0.05	0.27±0.05	-6.19±0.04	9.57±0.04	-2.31 ±0.04
NGC 2872	1.68±0.05	1.31±0.04	0.17±0.04	-6.60±0.03	9.57±0.03	-2.40 ±0.03
NGC 3115	2.18±0.03	1.38±0.02	0.10±0.02	-6.80±0.02	9.57±0.02	-2.85 ±0.02

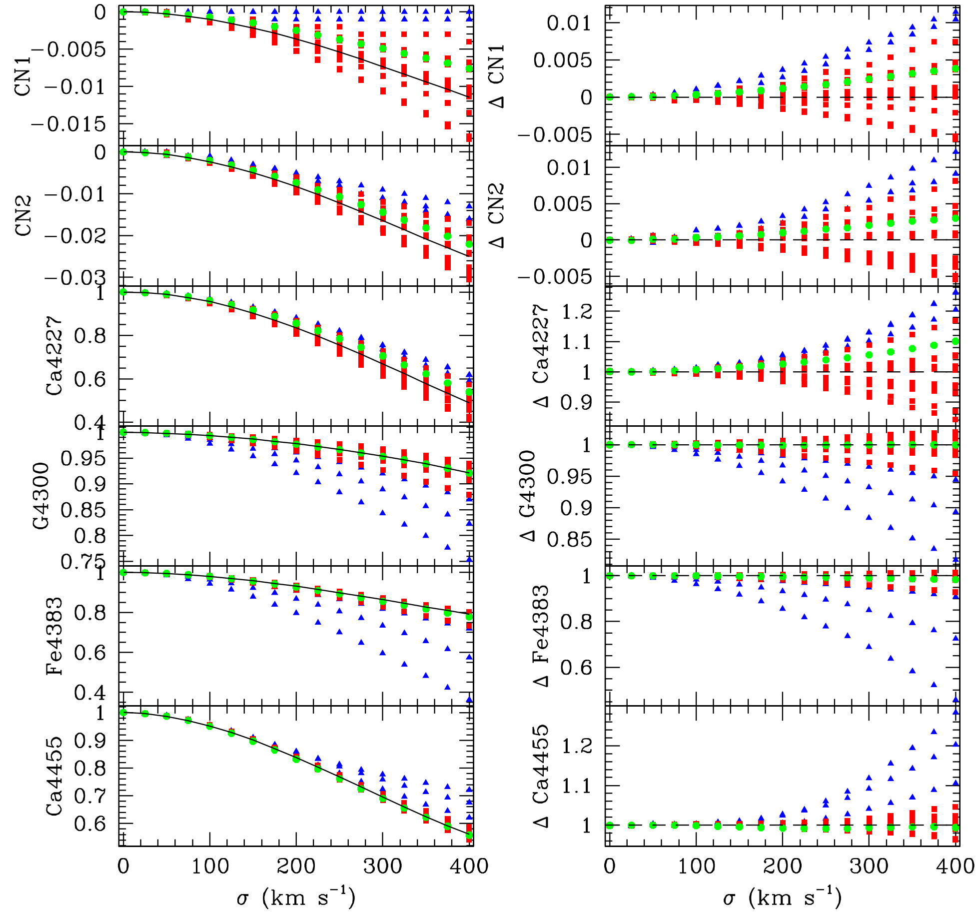

Figure 4.16 Line Index Corrections to Zero Velocity Dispersion: CN_1–Ca4455. *Blue Triangles*: stars with spectral type F; *Green Dots*: stars with spectral type G; *Red Boxes*: stars with spectral type K. *Solid Line*: Best fit to the G and K stars. The panels on the right show the residuals after normalizing by the best-fit line.

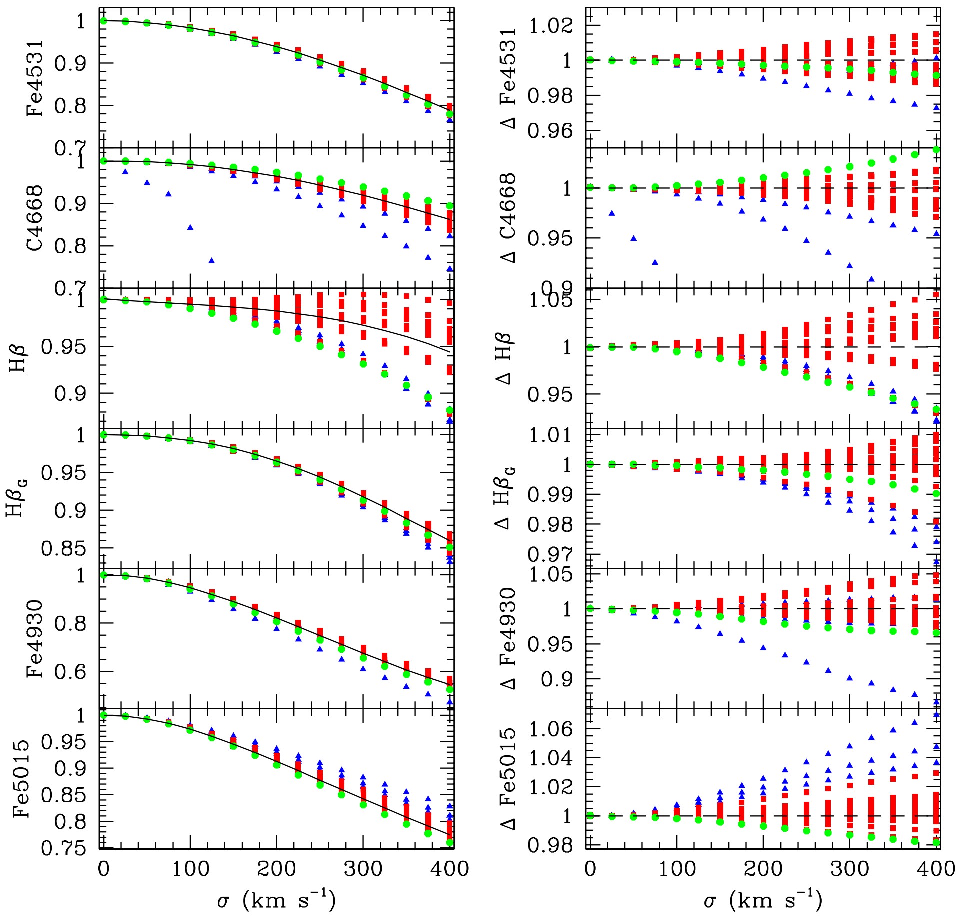

Figure 4.17 Line Index Corrections to Zero Velocity Dispersion: Fe4531–Fe5015. Symbols as in Figure 4.16.

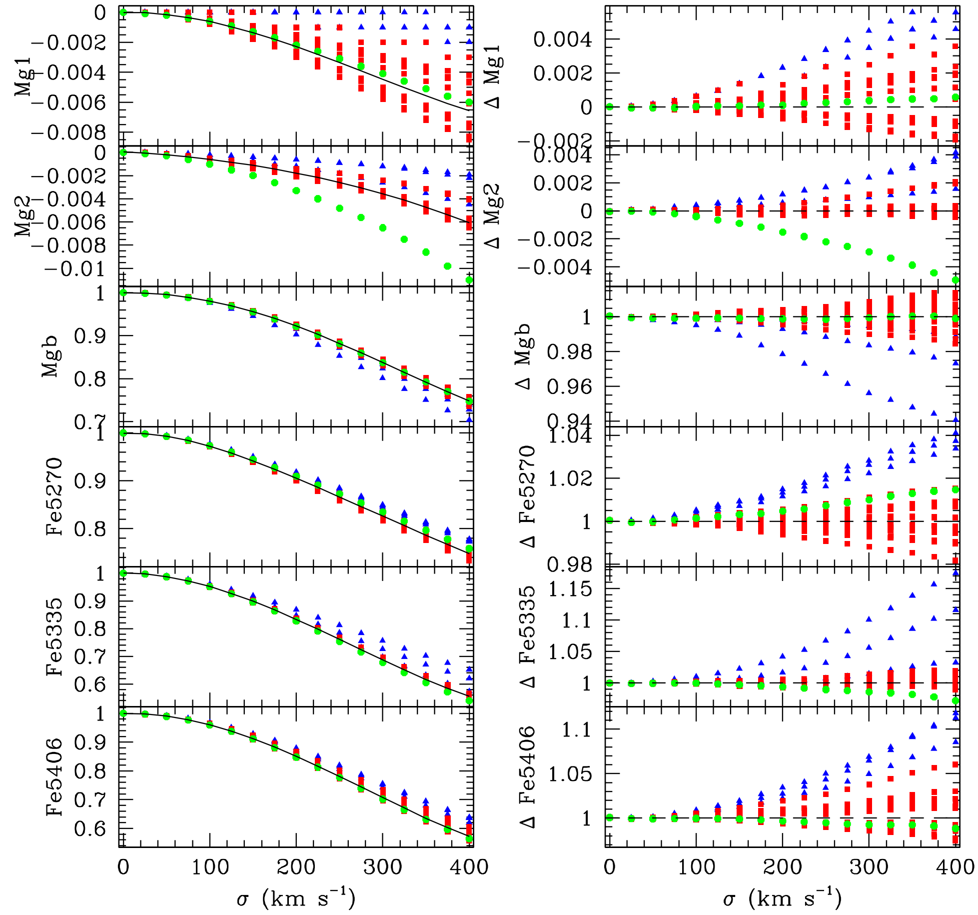

Figure 4.18 Line Index Corrections to Zero Velocity Dispersion: Mg_1–Fe5406. Symbols as in Figure 4.16.

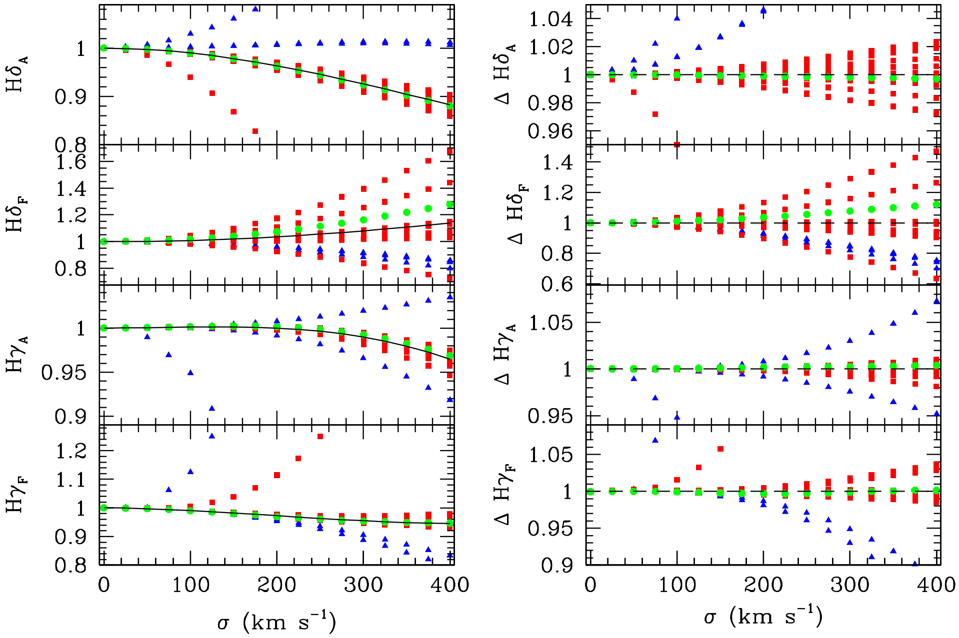

Figure 4.19 Line Index Corrections to Zero Velocity Dispersion: Hδ_A–Hγ_F. Symbols as in Figure 4.16.

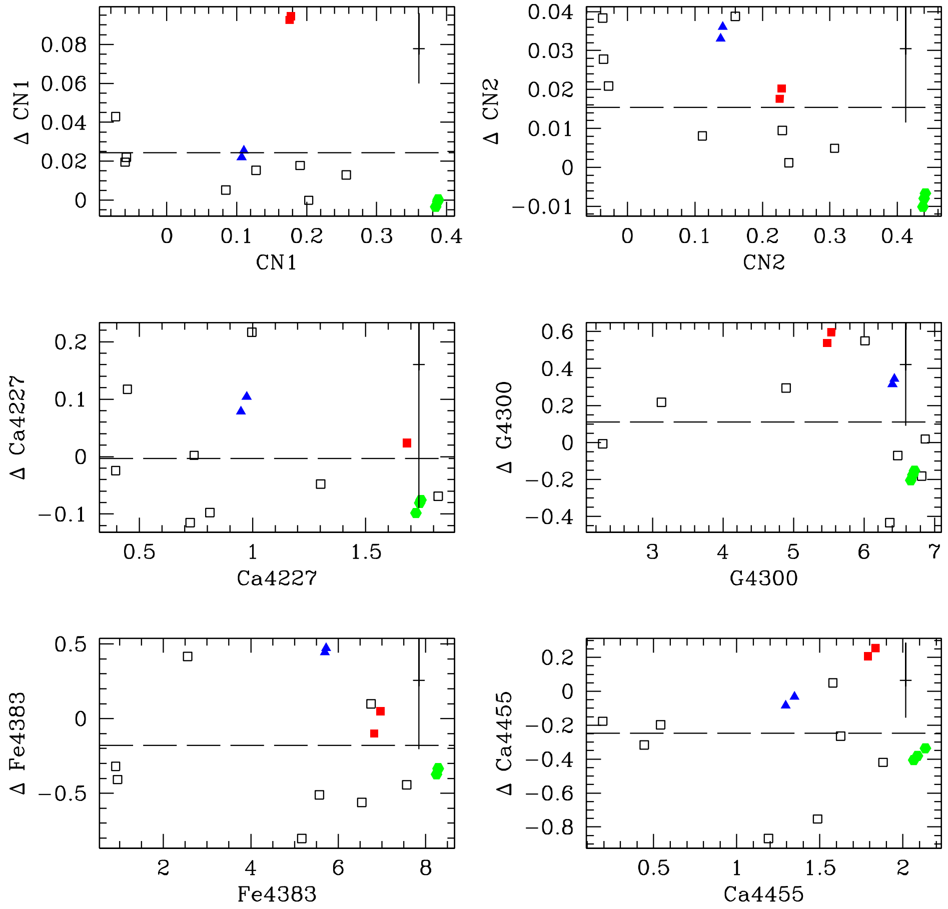

Figure 4.20 Offsets between the measured Lick indices and the published values for our stellar observations, for the indices CN$_1$, CN$_2$, Ca4227, G4300, Fe4383 and Ca4455. *Open Boxes*: stars which we only observed once, including HD 75732, HD 82328, HD 90508, HD 184406, HD 198149, HD 201891, HD 203344, and HD 219449; *Filled Boxes*: the two observations of HD 97907; *Filled Triangles*: the two observations of HD 199580; *Filled Circles*: the three observations of HD 85503. Dashed lines show the mean measured offsets, as tabulated in Table 4.7. The typical index uncertainties reported for the stellar measurements by the Lick group (Worthey et al., 1994) are shown as naked error bars in the upper right corner of each plot.

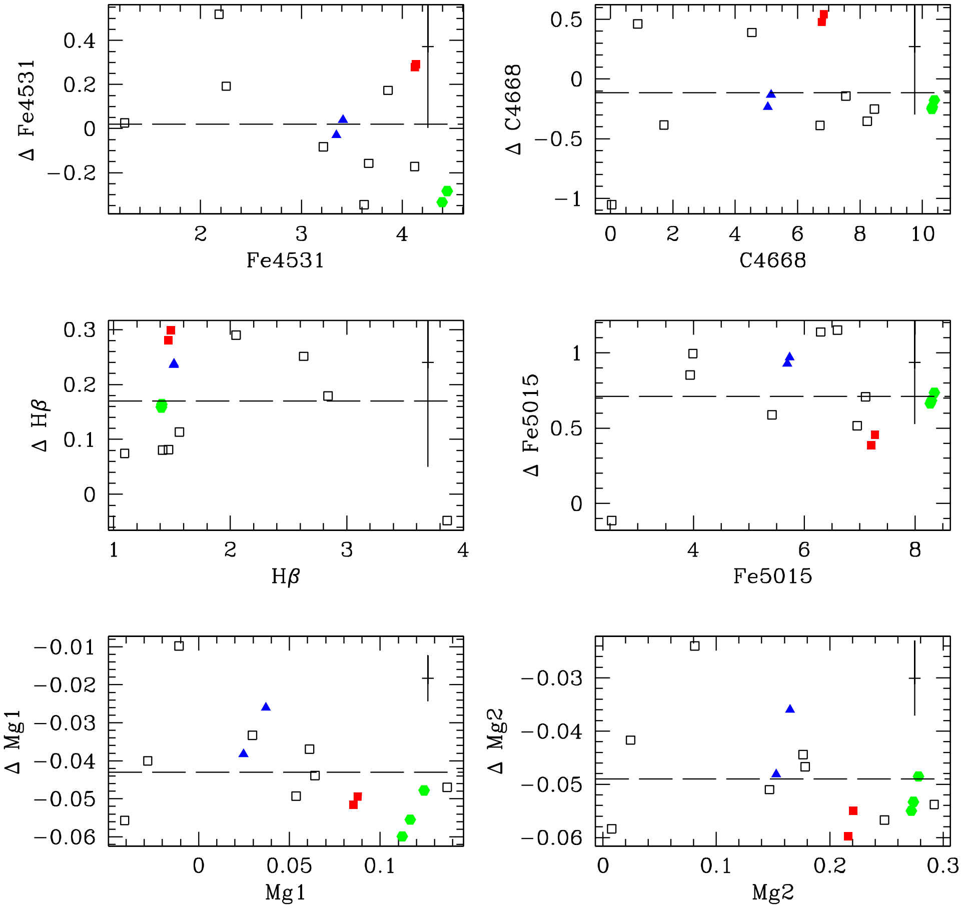

Figure 4.21 Offsets between the measured Lick indices and the published values for our stellar observations, for the indices Fe4531, C4668, Hβ, Fe5015, Mg_1, and Mg_2. Symbols as in Figure 4.20.

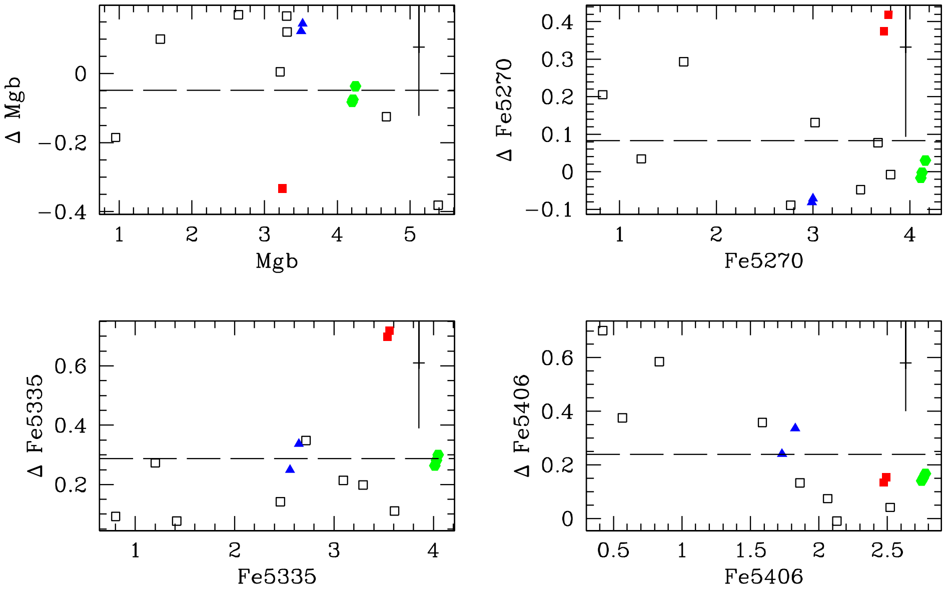

Figure 4.22 Offsets between the measured Lick indices and the published values for our stellar observations, for the indices Mgb, Fe5270, Fe5335, and Fe5406. Symbols as in Figure 4.20.

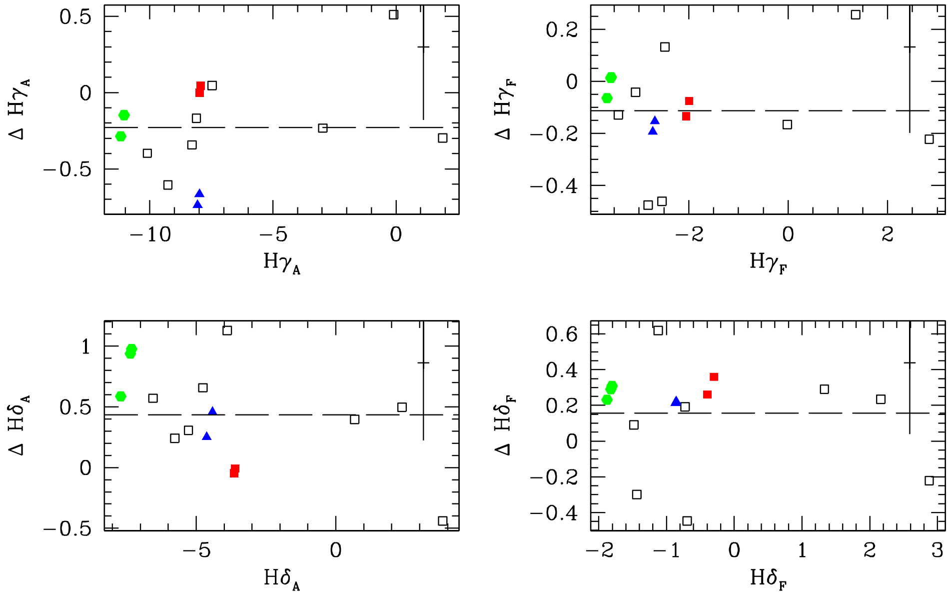

Figure 4.23 Offsets between the measured Lick indices and the published values for our stellar observations, for the indices Hγ_A, Hγ_F, Hδ_A, and Hδ_F. Symbols as in Figure 4.20.

4.5 Stellar Population Models: Age, [Z/H], and [α/Fe]

The Thomas, Maraston, & Bender (2002) models predict the full set of Lick Indices as an explicit function age, [Z/H], and [α/Fe]. We plot a single grid of models in Figure 4.24, in the two-space of the parameters Hβ vs. MgFe[1]. The dotted lines in the grid are lines of constant age, including 2, 6, 8, 10, 14, 15 Gyr. The dot-dash lines are show lines of constant metallicity ([Z/H] = -0.33, 0.0, +0.35, +0.67). The grid that is plotted has an [α/Fe] of +0.3. We will use different colors for grids with different [α/Fe], as noted in the figure. The grid will change shape when plotted against different line indices, however we always use the same values of age, metallicity for the gridlines. Additionally, in the lower left corner of the plot, we show the typical uncertainties on the line indices, for apertures in the center of the galaxy, in the outermost 2-3 bins, and in the intermediate region, as marked.

4.6 Future Work

There are many things to be done with this high quality dataset. We will start by checking the Lick index calibration; there are some significant offsets in the bluer indices which we need to understand before attempting to measure the Vazdekis indices.

Aside from residual cosmic rays in the core of the spectral trace, which will be easily removed by re-doing the spectral co-addition, the largest uncertainty for interpreting the index gradients will come from the emission correction. We plan to

---

[1] MgFe = $\sqrt{\mathrm{Mgb} < Fe >}$

fit Vazdekis template spectra and subtract off the stellar population to determine the emission spectrum. We will look for correlations between the O IIIλ5007 and Hβ emission lines, to aid in their cleaning. Also, we plan to make full use of the blue end of our spectra range, by analysing the Hγ and Hδ features, where emission will be a lesser effect.

We will interpret the gradients within these galaxies in terms of age, [Fe/H] and [α/Fe]. In particular, we will attempt to reconcile our findings (young central ages) with the metallicity hyperplane found by TFWG, and their drizzled star formation model. We will also tie the kinematics in more directly, by looking at correlations between, for example, σ and gradient slope.

Two of our galaxies have decoupled cores. NGC 1700 seems to have a break in the line strength gradient for several indices (Fe4383, Mgb, Hβ, Hδ). The gradient slope is shallower in the central region. This contrasts with previous studies which found enhancements of Mg_2 in the central parts of decoupled core galaxies. However, previous investigators (Carollo & Danziger, 1994; Surma & Bender, 1995), fit gradients in index vs. r, not index vs. log(r) (or log(index) vs. log(r). The gradients are centrally peaked for many galaxies when viewed against linear radius, and it is difficult to see the difference for decoupled core galaxies. We will investigate for both NGC 1700, and NGC 661 in which we newly discovered a decoupled core. We have already begun to obtain very deep longslit data on NGC 661 with the HET, to study the stellar kinematics and population gradients to large radii.

4.7 Bibliography

Bender, R., Burstein, D., & Faber, S. M. 1993, ApJ, 411, 153

Bender, R., Saglia, R. P., & Gerhard, O. E. 1994, MNRAS, 269, 785

Bruzual A., G. & Charlot, S. 1993, ApJ, 405, 538

Carollo, C. M. & Danziger, I. J. 1994, MNRAS, 270, 523

Djorgovski, S. & Davis, M. 1987, ApJ, 313, 59

Gebhardt, K. et al. 2000, AJ, 119, 1157

Gonzalez, J.J. 1993, Ph.D. thesis, Univ. of California, Santa Cruz

Jones, L. A. 1998, Ph.D. Thesis, Univ. of North Carolina, Chapel Hill

Jones, L. A. & Worthey, G. 1995, ApJ, 446, L31

Jørgensen, I., Franx, M., Hjorth, J., & van Dokkum, P. G. 1999, MNRAS, 308, 833

Jørgensen, I., Franx, M., & Kjaergaard, P. 1996, MNRAS, 280, 167

Kauffmann, G. 1996, MNRAS, 281, 487

Kuntschner, H. & Davies, R. L. 1998, MNRAS, 295, L29

Maraston, C. 1998, MNRAS, 300, 872

Renzini, A. & Buzzoni, A. 1986, ASSL Vol. 122: Spectral Evolution of Galaxies, 195

Rix, H., de Zeeuw, P. T., Cretton, N., van der Marel, R. P., & Carollo, C. M. 1997, ApJ, 488, 702

Saha, P. & Williams, T. B. 1994, AJ, 107, 1295

Statler, T. S., Dejonghe, H., & Smecker-Hane, T. 1999, AJ, 117, 126

Surma, P. & Bender, R. 1995, A&A, 298, 405

Thomas, D., Maraston, C., & Bender, R. 2002, astro-ph/0209250

Trager, S. C., Faber, S. M., Worthey, G., & González, J. J. ;. 2000, AJ, 119, 1645

Trager, S. C., Worthey, G., Faber, S. M., Burstein, D., & Gonzalez, J. J. 1998, ApJS, 116, 1

Tripicco, M. J. & Bell, R. A. 1995, AJ, 110, 3035

van der Marel, R. P. & Franx, M. 1993, ApJ, 407, 525

Vazdekis, A., Casuso, E., Peletier, R. F., & Beckman, J. E. 1996, ApJS, 106, 307

Worthey, G., Faber, S. M., Gonzalez, J. J., & Burstein, D. 1994, ApJS, 94, 687

Worthey, G. & Ottaviani, D. L. 1997, ApJS, 111, 377

Ziegler, B. L. & Bender, R. 1997, MNRAS, 291, 527

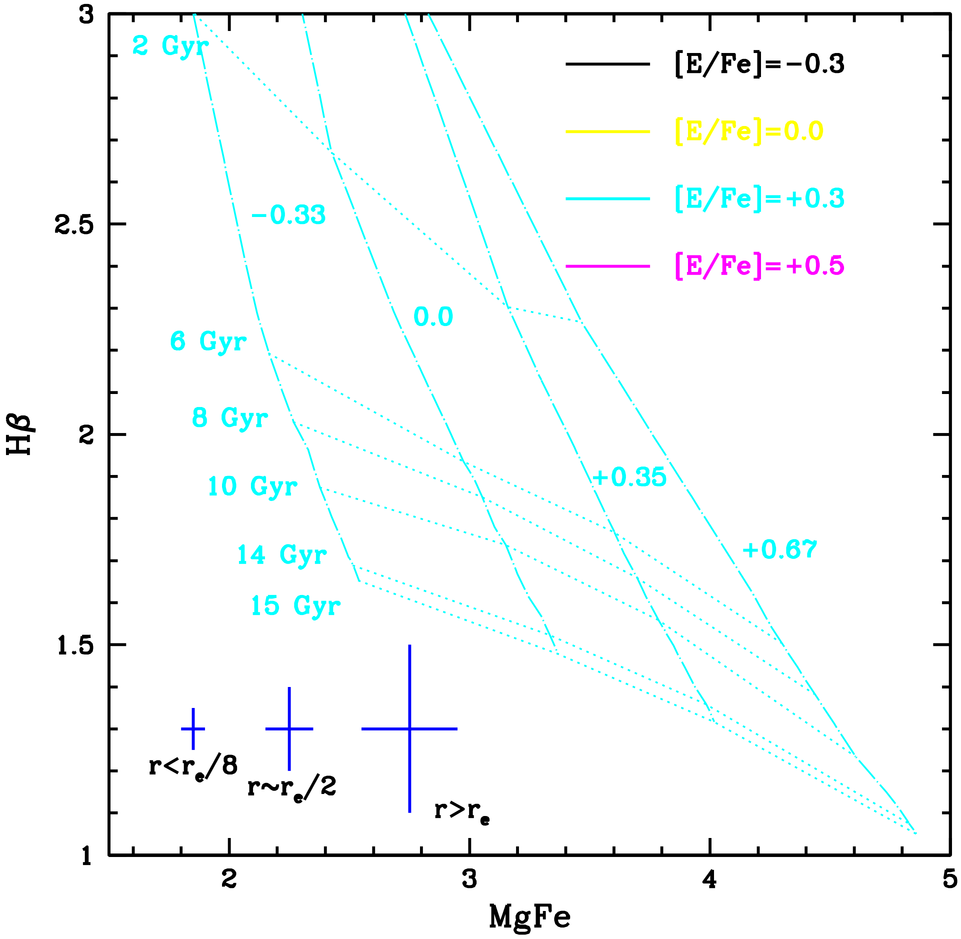

Figure 4.24 Model grid using the Thomas, Maraston, & Bender (2002) models. *dotted lines*: lines of constant age, running from top to bottom they are 2, 6, 8, 10, 14, and 15 Gyr SSP ages. *dot-dash lines*: lines of constant [Z/H], running from left to right they are -0.33, 0.0, +0.35, +0.67 dex. The grid which is shown here has [α/Fe] = +0.3. We will color-code other grids when we use them, with [α/Fe]=-0.3 in black, [α/Fe]=0.0 in yellow, and [α/Fe]=+0.5 in magenta. The typical uncertainties for are index measurements are shown in the lower left corner; apertures near the center of the galaxy typically have S/N per Å greater than 100, and the smallest uncertainties. The outermost radii typical have S/N per Å of 20 – 35, and the largest uncertaintis. In the intermediate range, the apertures each have S/N per Å of at least 56, and uncertainties in the index strengths as shown.

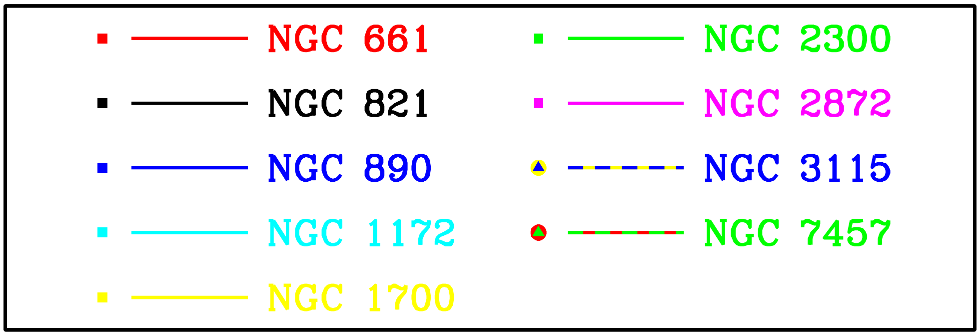

Figure 4.25 We use color coding to identify the data from each galaxy in Figures 4.26 – 4.31. The coding is as follows: *red*: NGC 661; *black*: NGC 821; *blue*: NGC 890; *cyan*: NGC 1172; *yellow*: NGC 1700; *green*: NGC 2300; *magenta*: NGC 2872; *blue/yellow stripe*: NGC 3115; *green/red stripe*: NGC 7457.

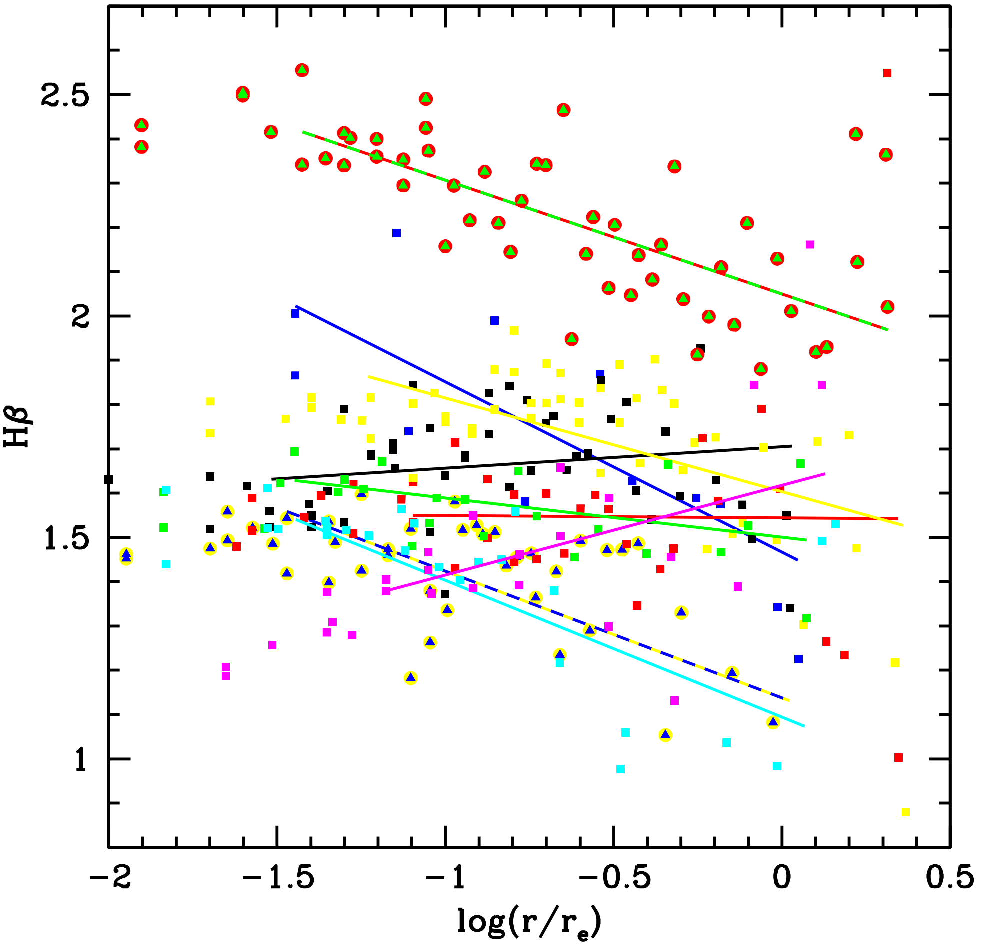

Figure 4.26 Radial gradients in Hβ vs. log(r/r$_e$ for the nine galaxies in our sample. Symbols and colors as in Figure 4.25. Individual gradients are plotted in Appendix A. NGC 1172 and NGC 3115 definitely have some Hβ emission contamination. NGC 890 is affected by a cosmic ray in the central apertures. NGC 7457 is well separated from the rest of the galaxies. This galaxy is a candidate "peanut-bulge" galaxy, formed by secular evolutionary processes which may be very different from the way elliptical galaxies form (Kormendy 2002, private communication).

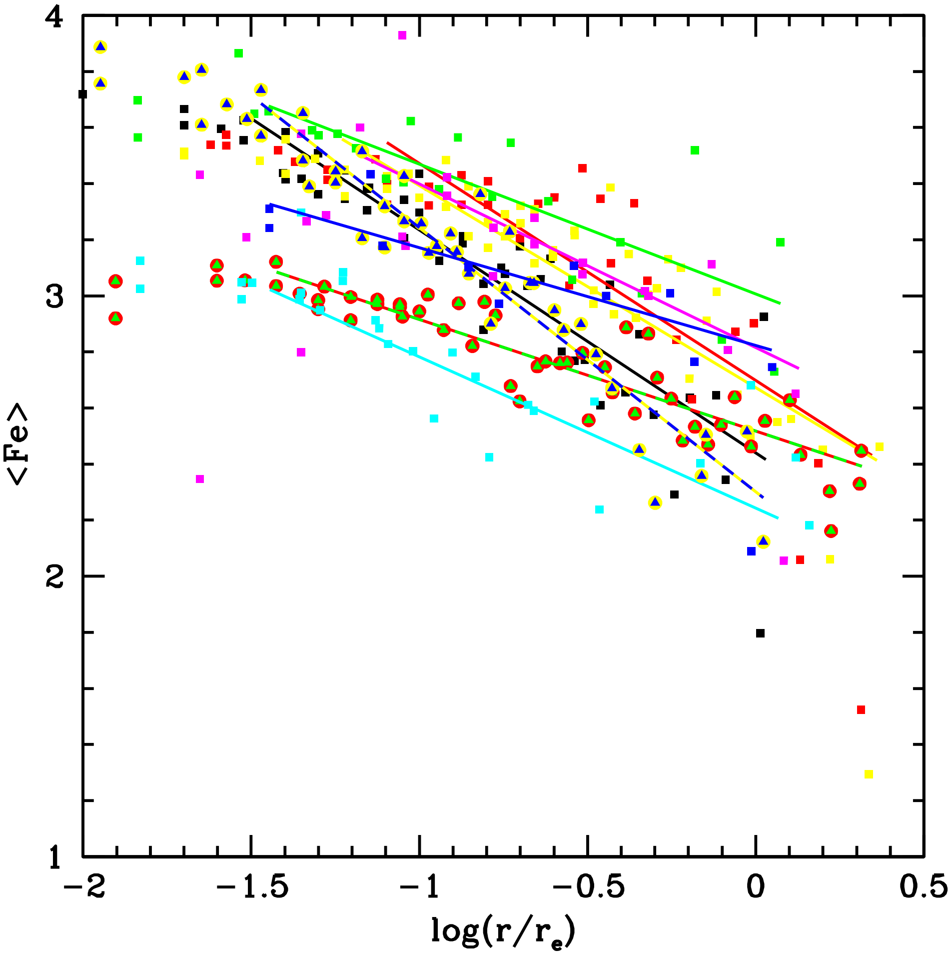

Figure 4.27 Radial gradients in <Fe>vs. log(r/r_e for the nine galaxies in our sample. Symbols and colors as in Figure 4.25. Individual gradients are plotted in Appendix A.

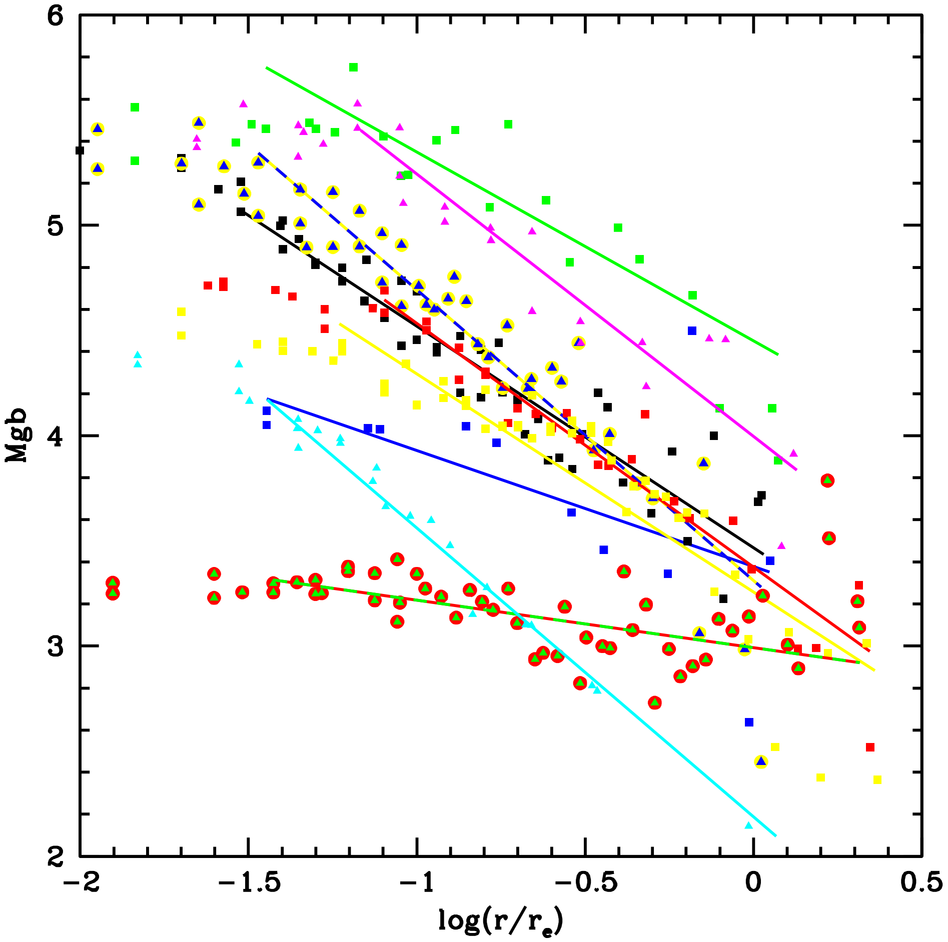

Figure 4.28 Radial gradients in Mg b vs. log(r/r$_e$ for the nine galaxies in our sample. Symbols and colors as in Figure 4.25. Individual gradients are plotted in Appendix A. The gradient for NGC 1700 (yellow) is non-linear; it appears to have a break near the outer edge of the decoupled core. Any break in the gradient of NGC 661 (the other decoupled core galaxy) is less obvious.

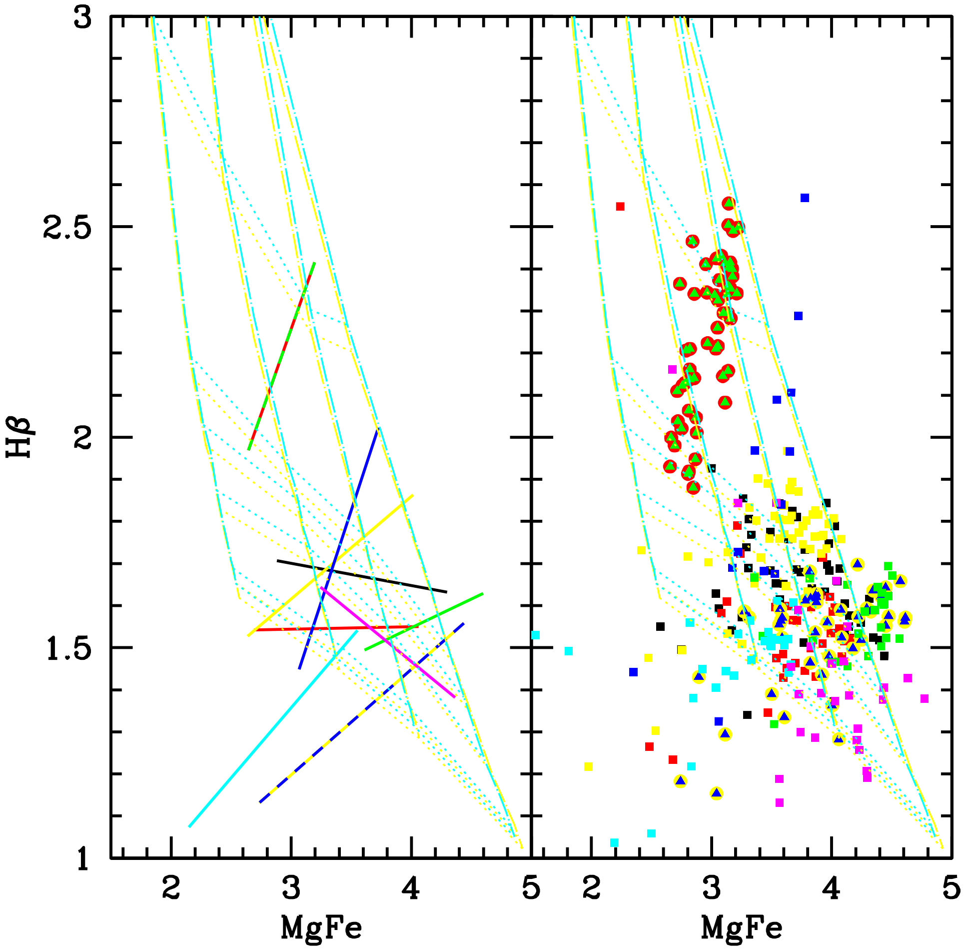

Figure 4.29 Hβ vs. MgFe. Right Panel: Model grids and the galaxy data. Left Panel: Model grids and the fits to the galaxy index gradients. The model grids are all degenerate in [α/Fe] vs. MgFe, so this projection is a stable one from which to derive age, [Z/H]. This sample of field galaxies shows a broad range of central ages. In every case except NGC 2872 (magenta), the gradients are consistent with the galaxy centers being younger by ∼ 2 Gyr, and also more metal rich. NGC 2872 seems to have a uniform age, and a pure metallicity gradient, 0.6 dex higher in the center than the outer parts.

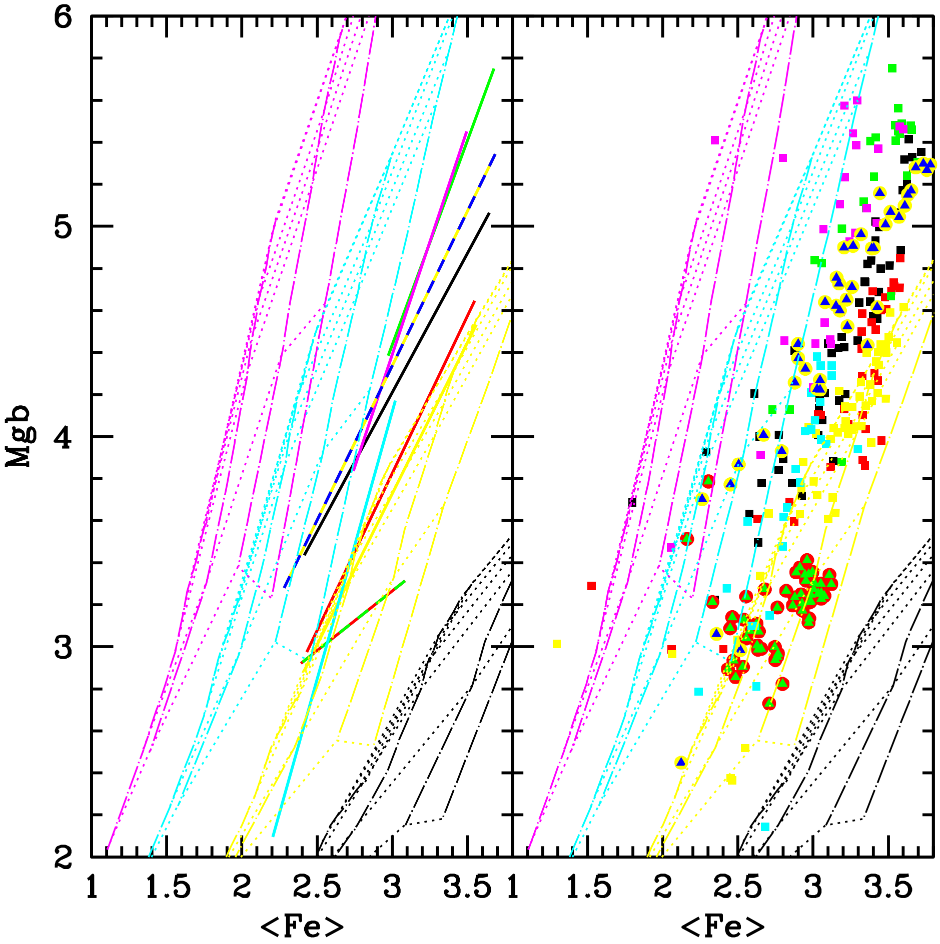

Figure 4.30 Mgb vs. <Fe>. Mgb and <Fe>have very similar response to age and metallicity, so the model grids are collapsed in this projection. Element abundance, [α/Fe], is almost orthogonal to this projection, however, making it possible to determine the [α/Fe] ratio for each aperture. The gradients within each galaxy run almost parallel to the model grids, suggesting that the [α/Fe] is uniform in any given galaxy. TFWG found that [α/Fe] was correlated with central velocity dispersion, increasing for higher σ.

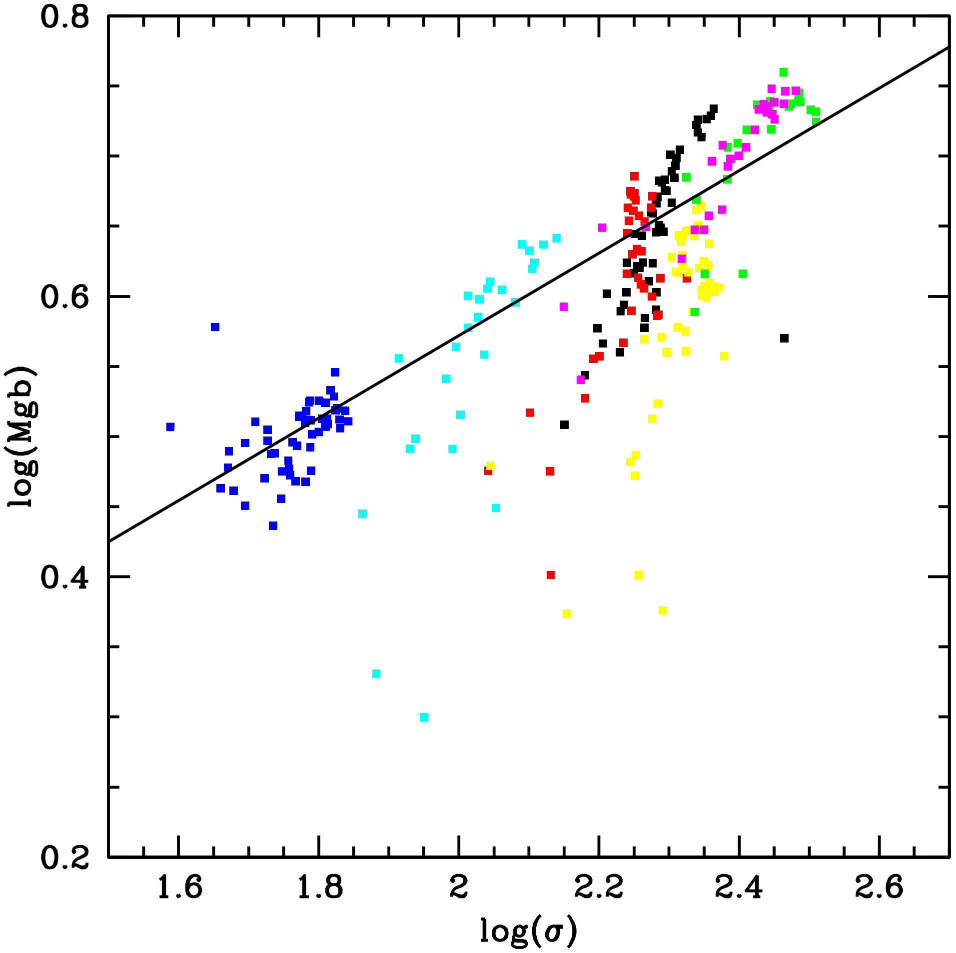

Figure 4.31 Local Mgb vs. local σ. The solid line is the best-fit Mgb-σ relation from TFWG. It runs parallel to locus defined by the centers of all these galaxies.

Appendices

Appendix A

Line Index Gradient Plots

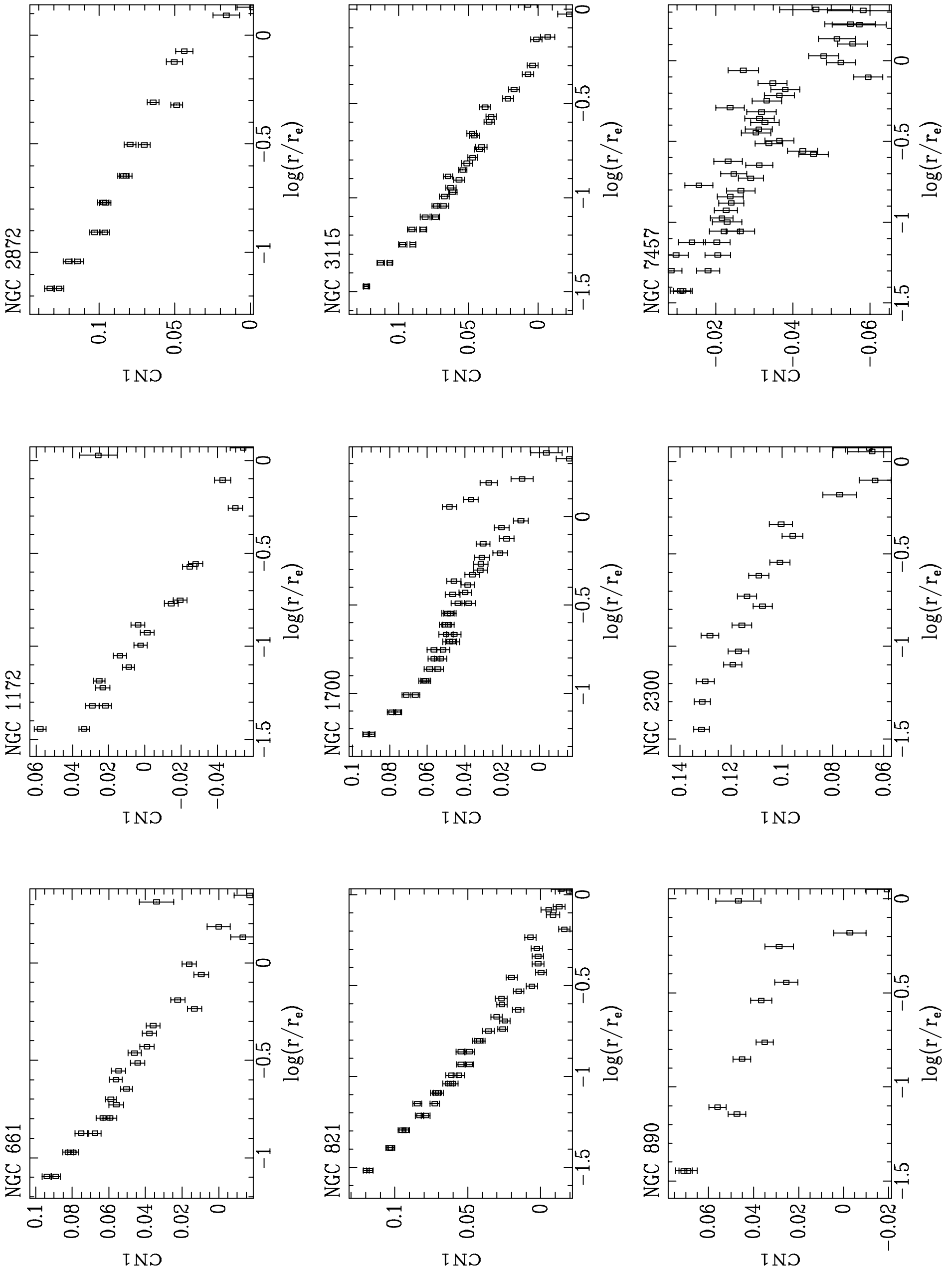

Figure A.1 Radial profiles of the CN_1 index for all nine galaxies.

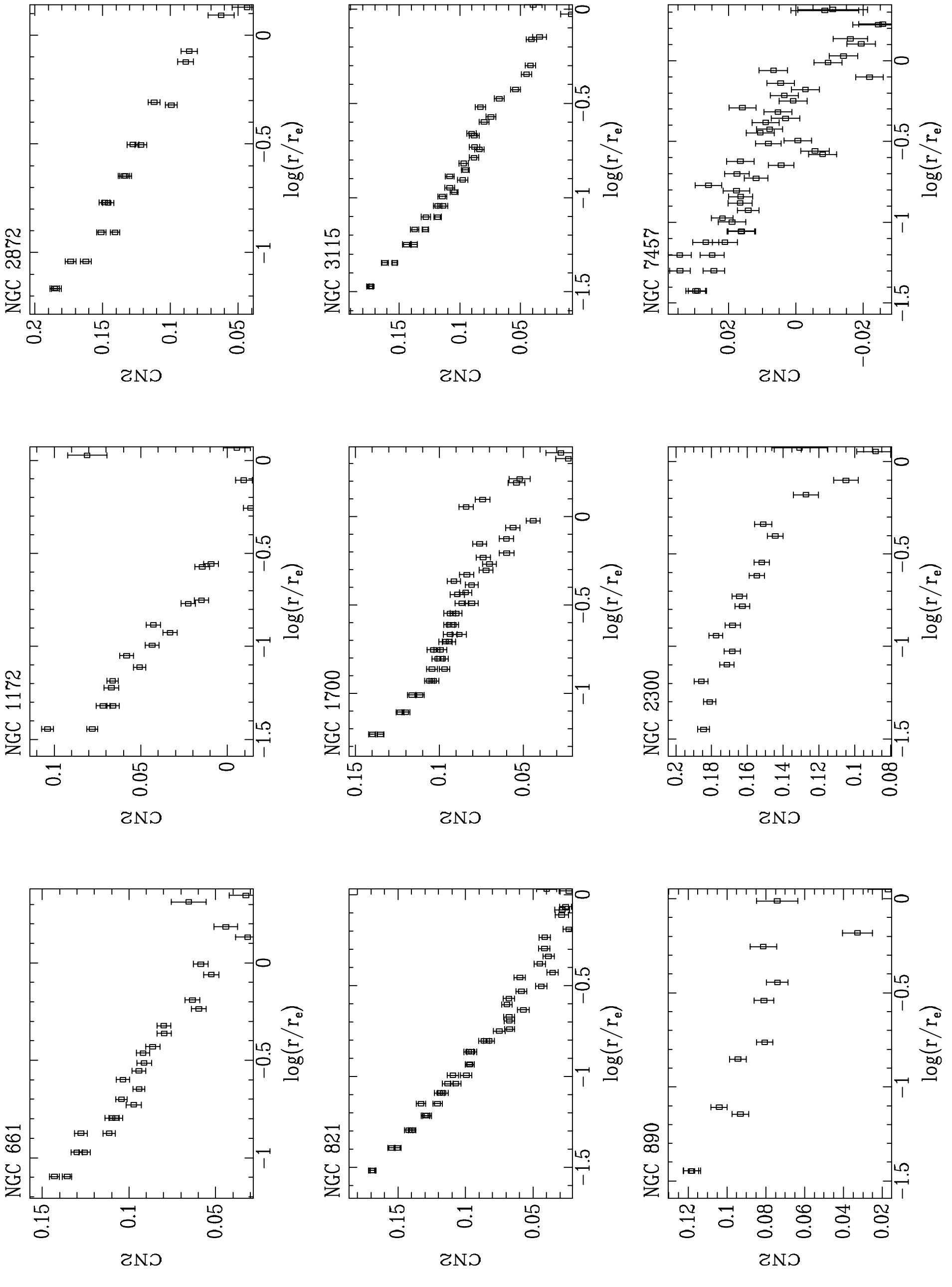

Figure A.2 Radial profiles of the CN_2 index for all nine galaxies.

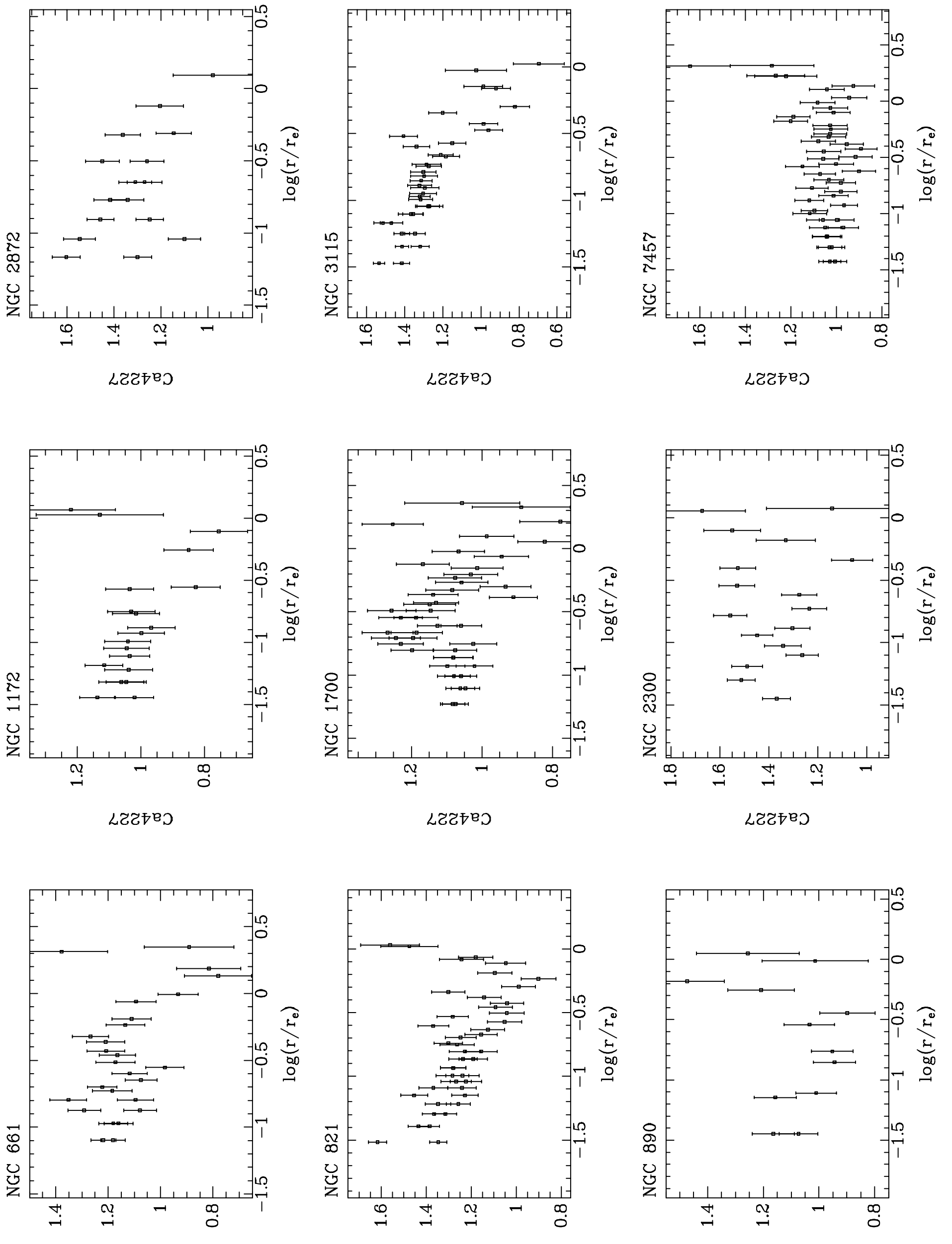

Figure A.3 Radial profiles of the Ca4227 index for all nine galaxies.

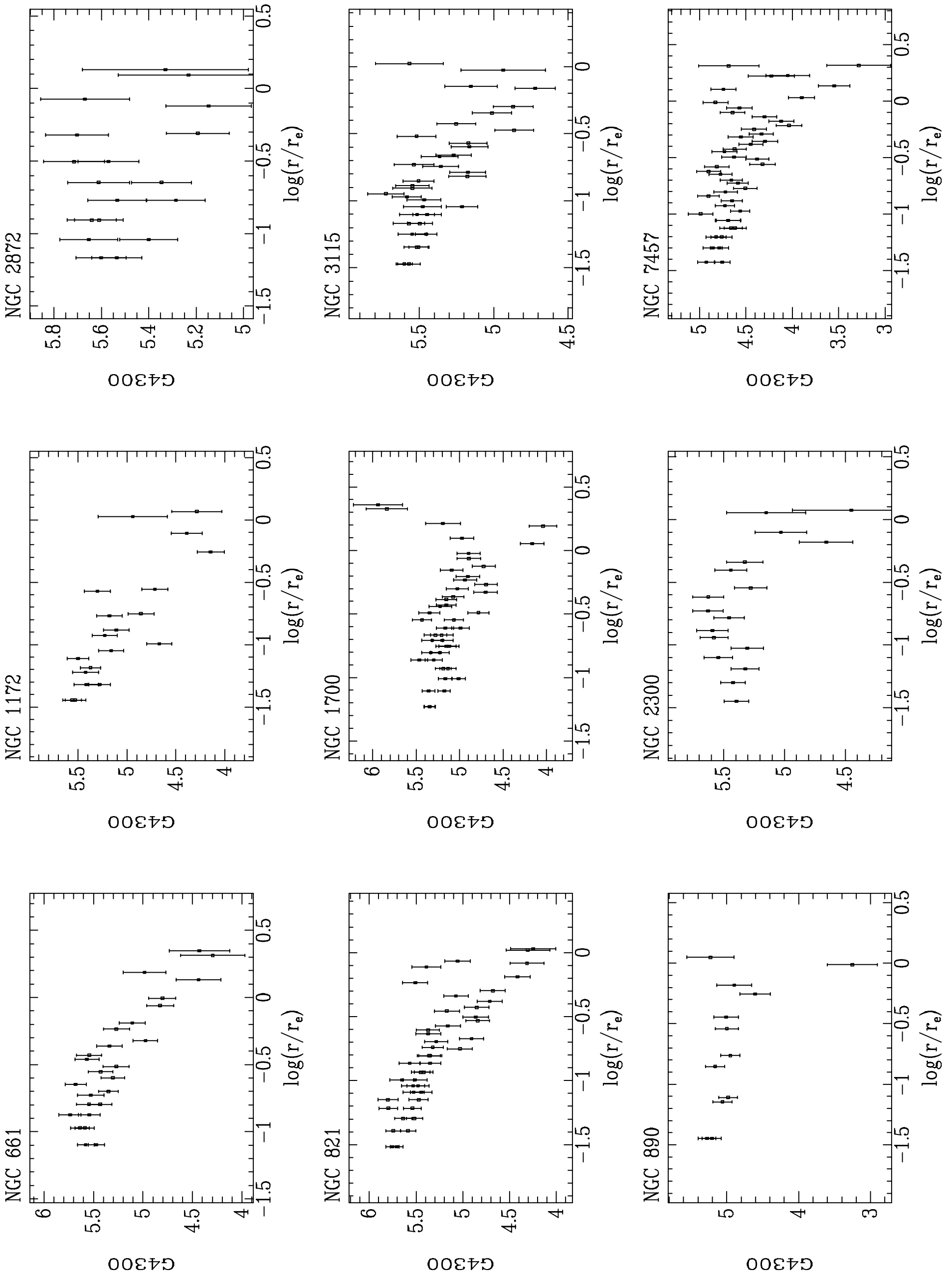

Figure A.4 Radial profiles of the G4300 line index for all nine galaxies.

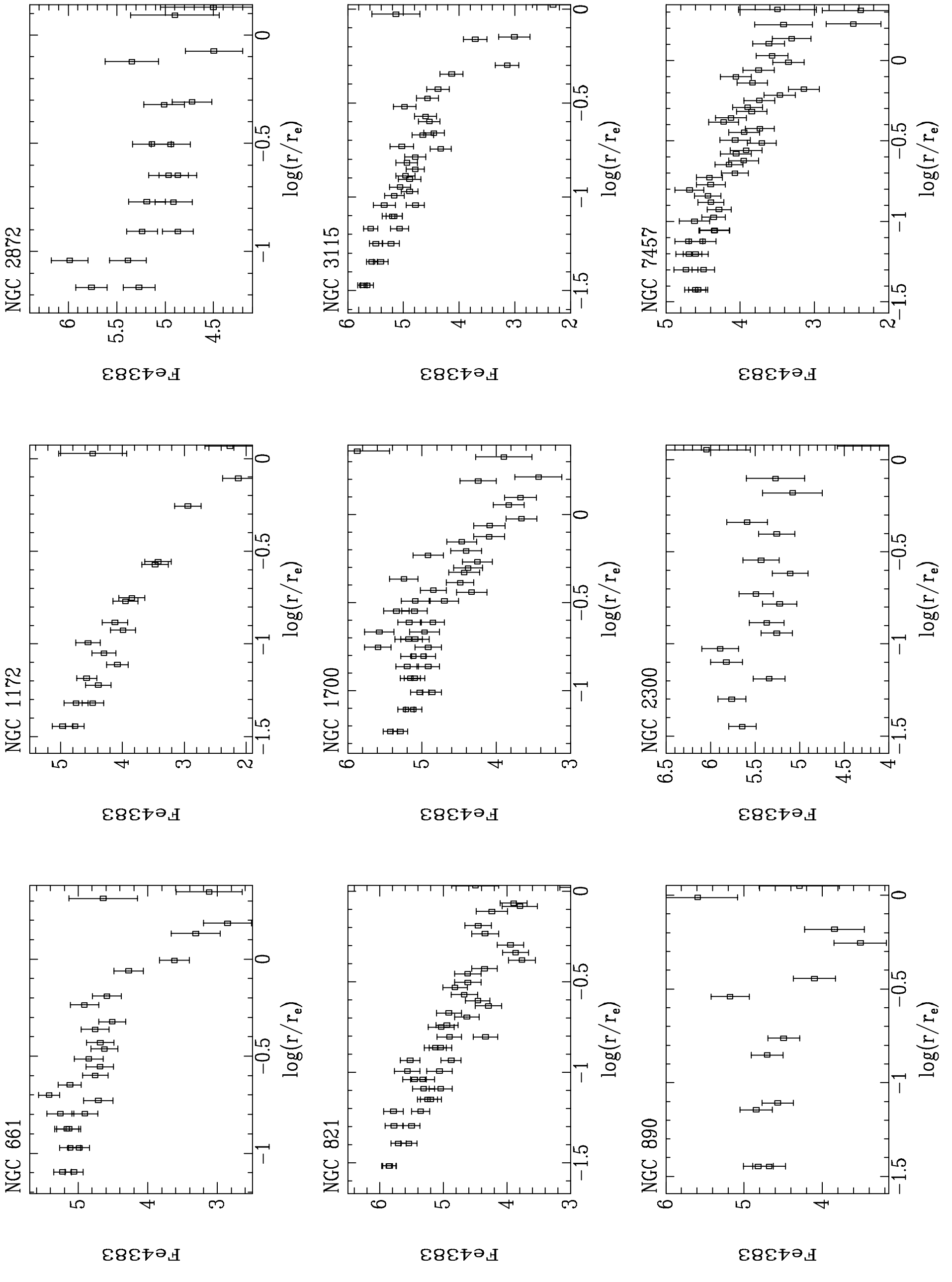

Figure A.5 Radial profiles of the Fe4383 line index for all nine galaxies.

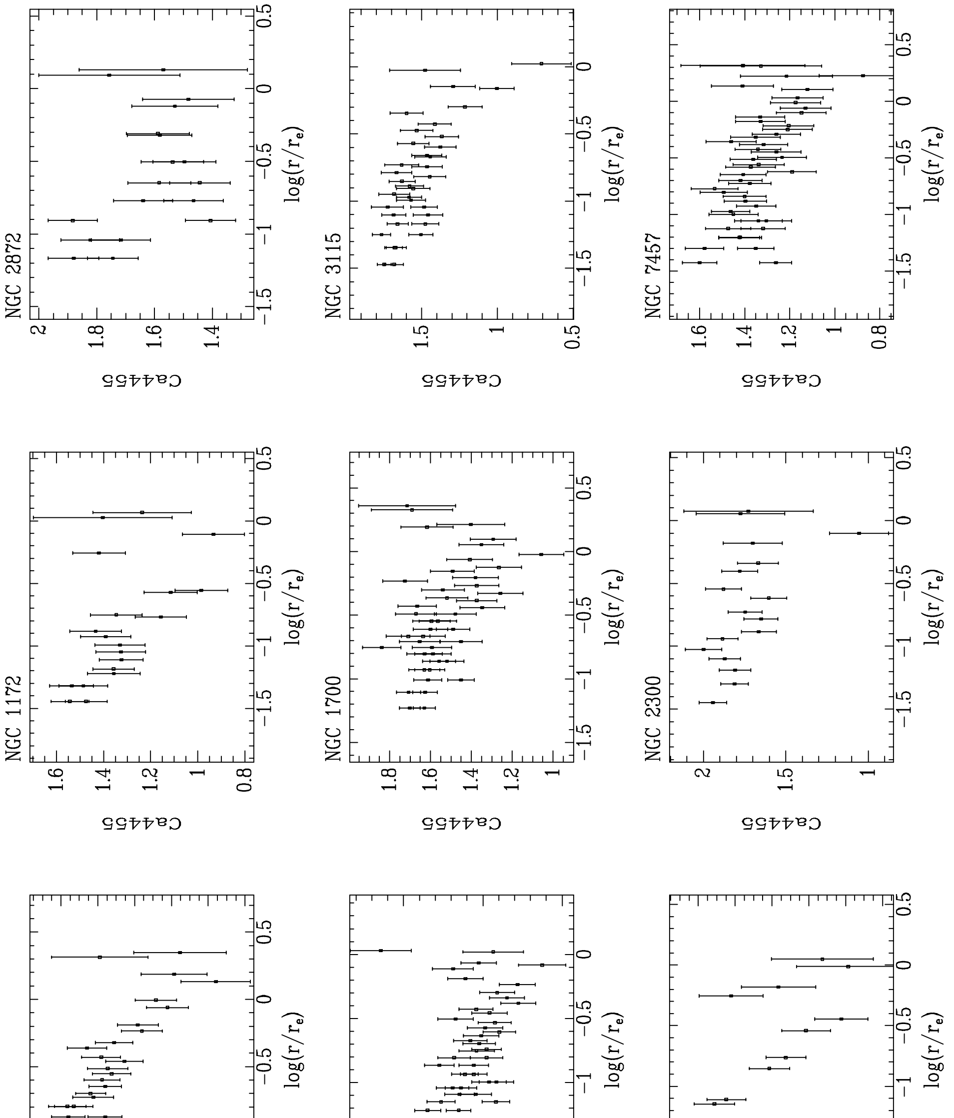

Figure A.6 Radial profiles of the Ca4455 line index for all nine galaxies.

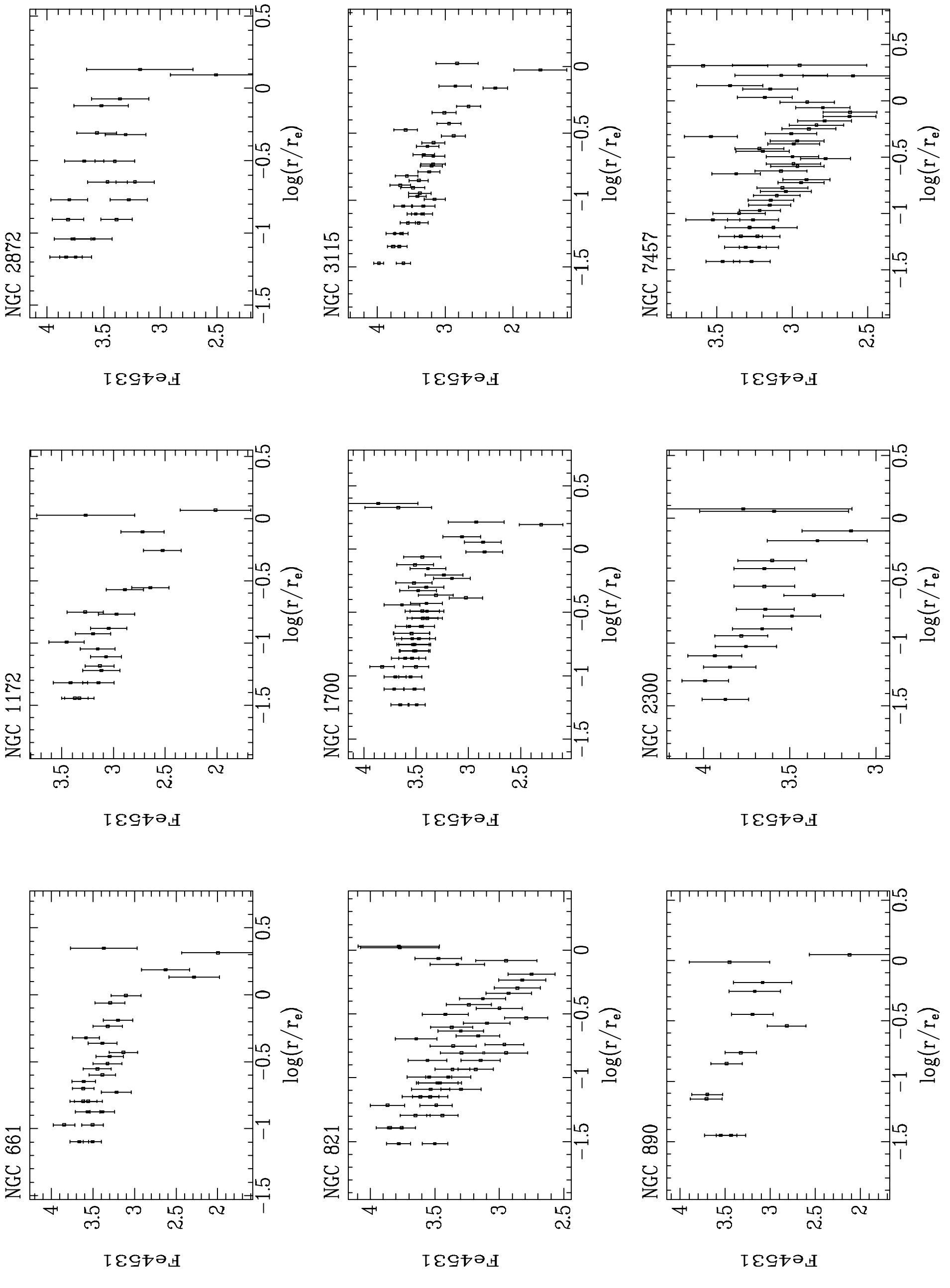

Figure A.7 Radial profiles of the Fe4531 line index for all nine galaxies.

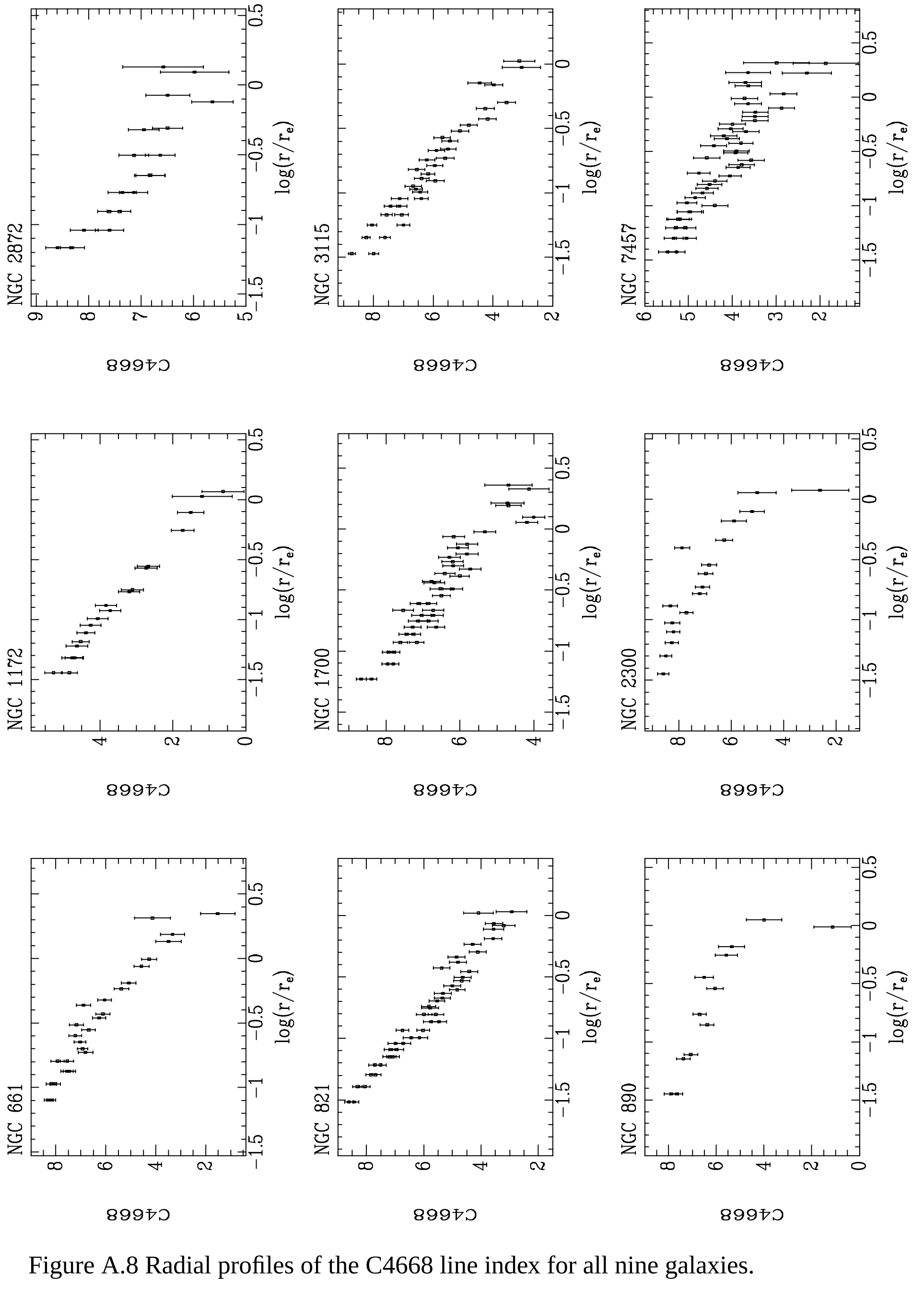

Figure A.8 Radial profiles of the C4668 line index for all nine galaxies.

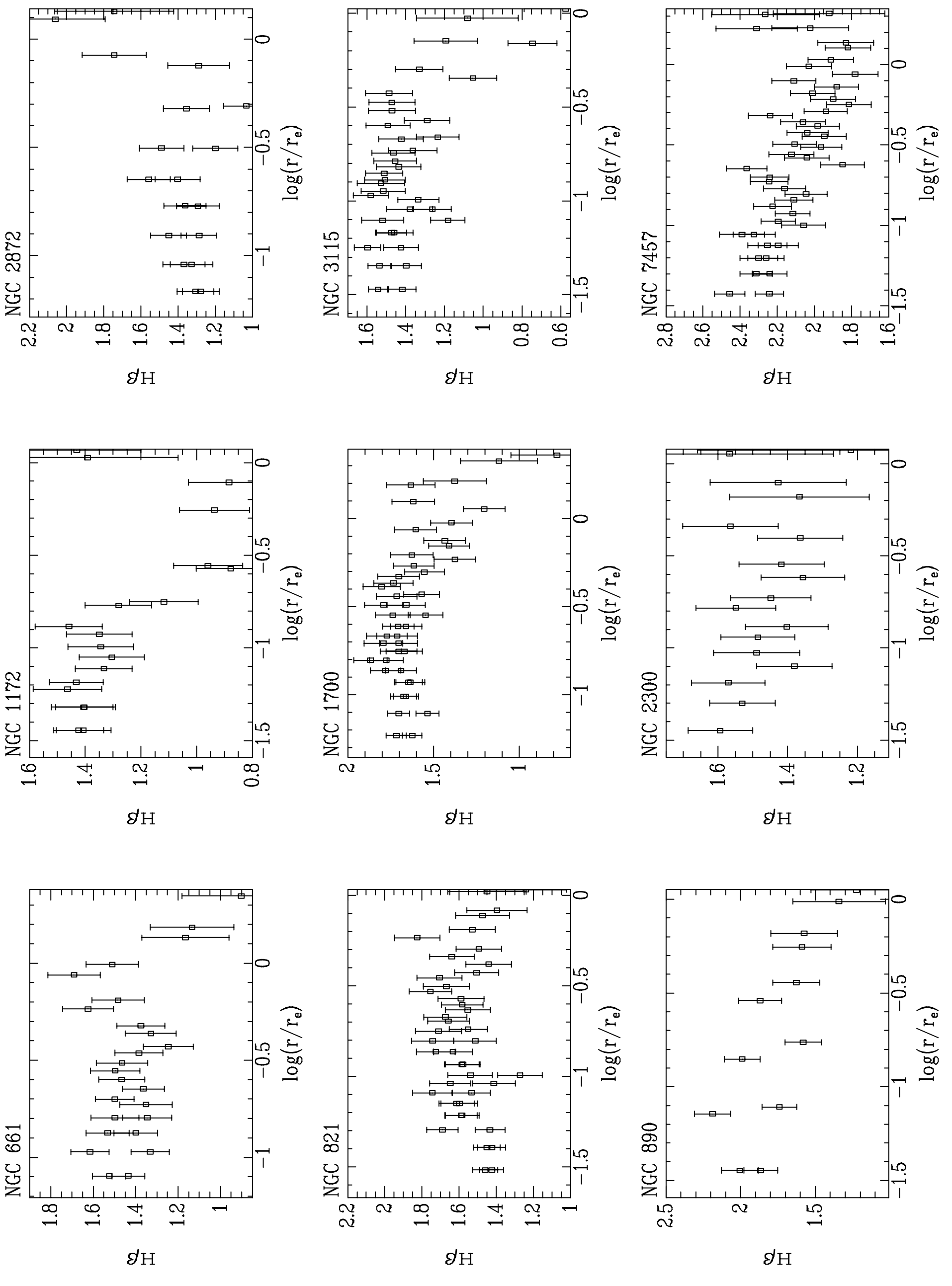

Figure A.9 Radial profiles of the Hβ index for all nine galaxies.

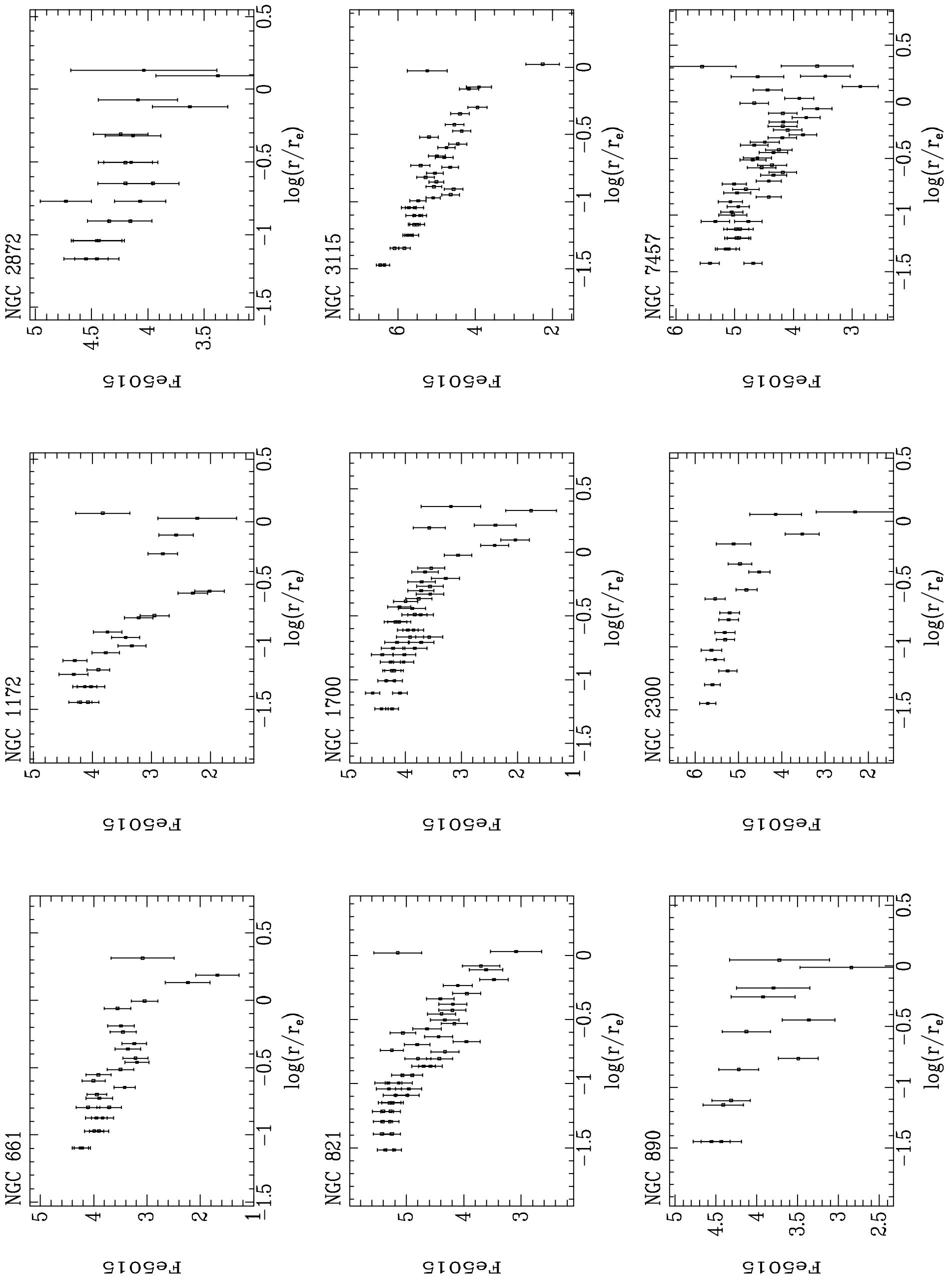

Figure A.10 Radial profiles of the Fe5015 line index for all nine galaxies.

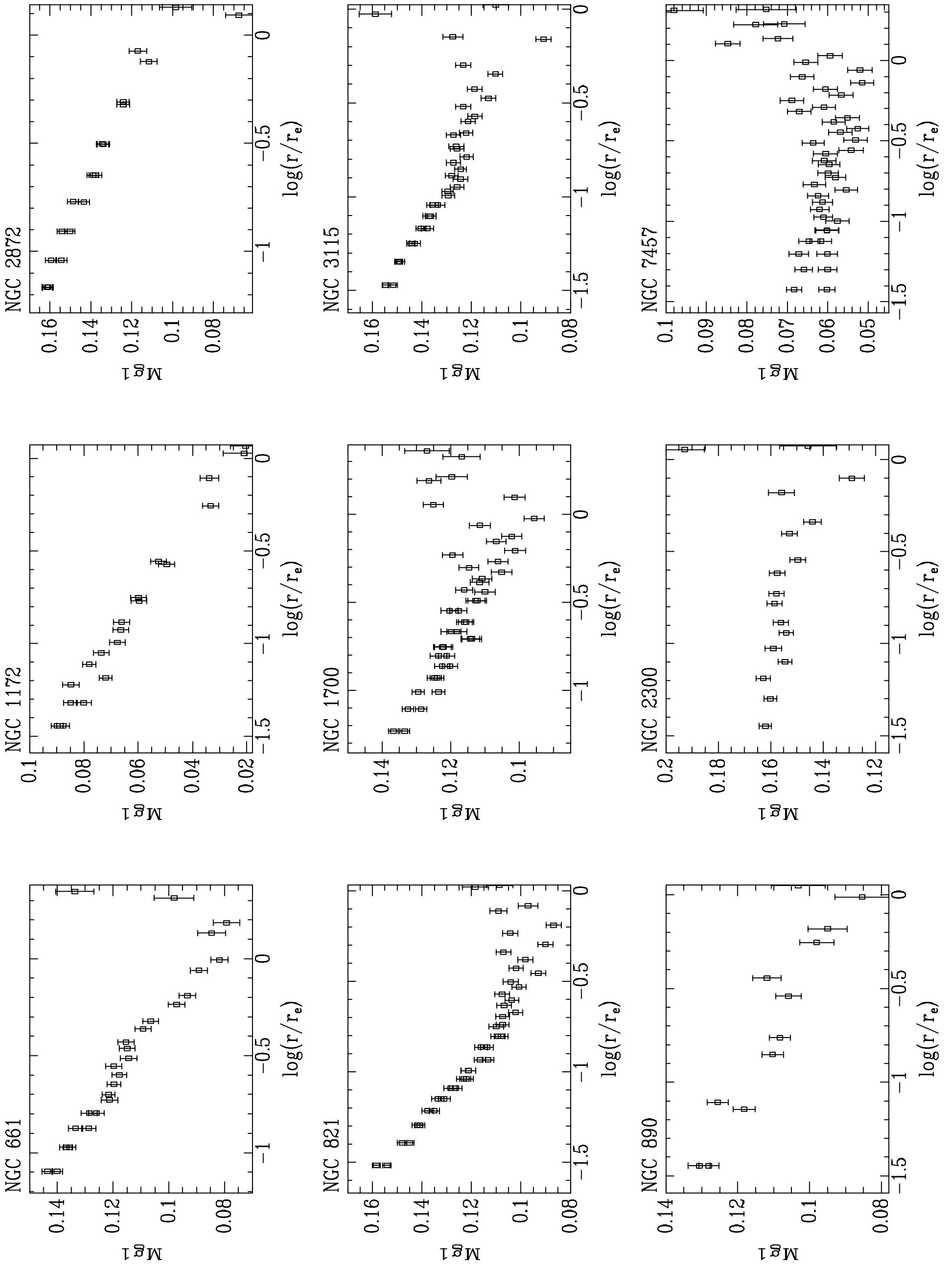

Figure A.11 Radial profiles of the Mg_1 index for all nine galaxies.

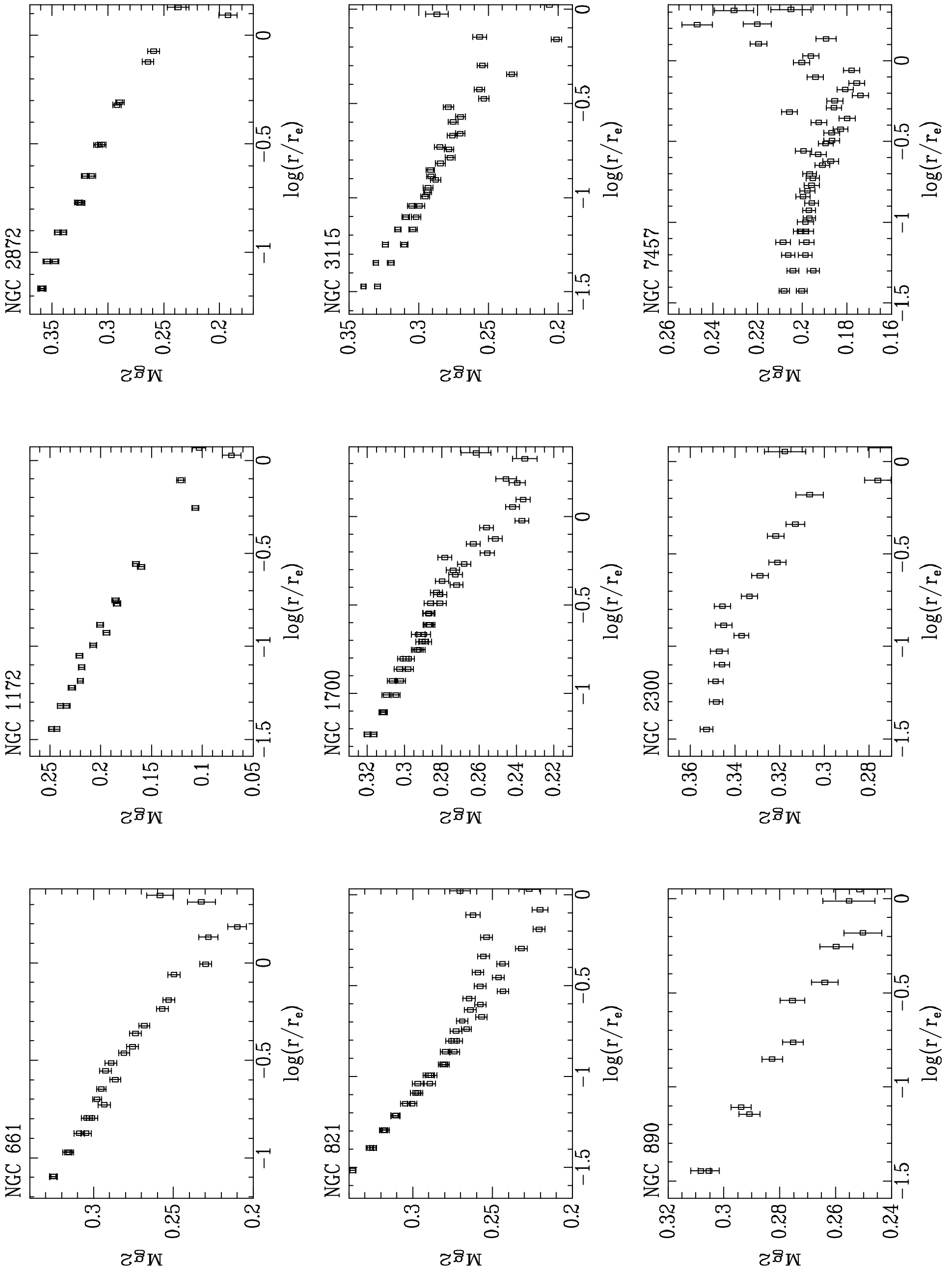

Figure A.12 Radial profiles of the Mg_2 index for all nine galaxies.

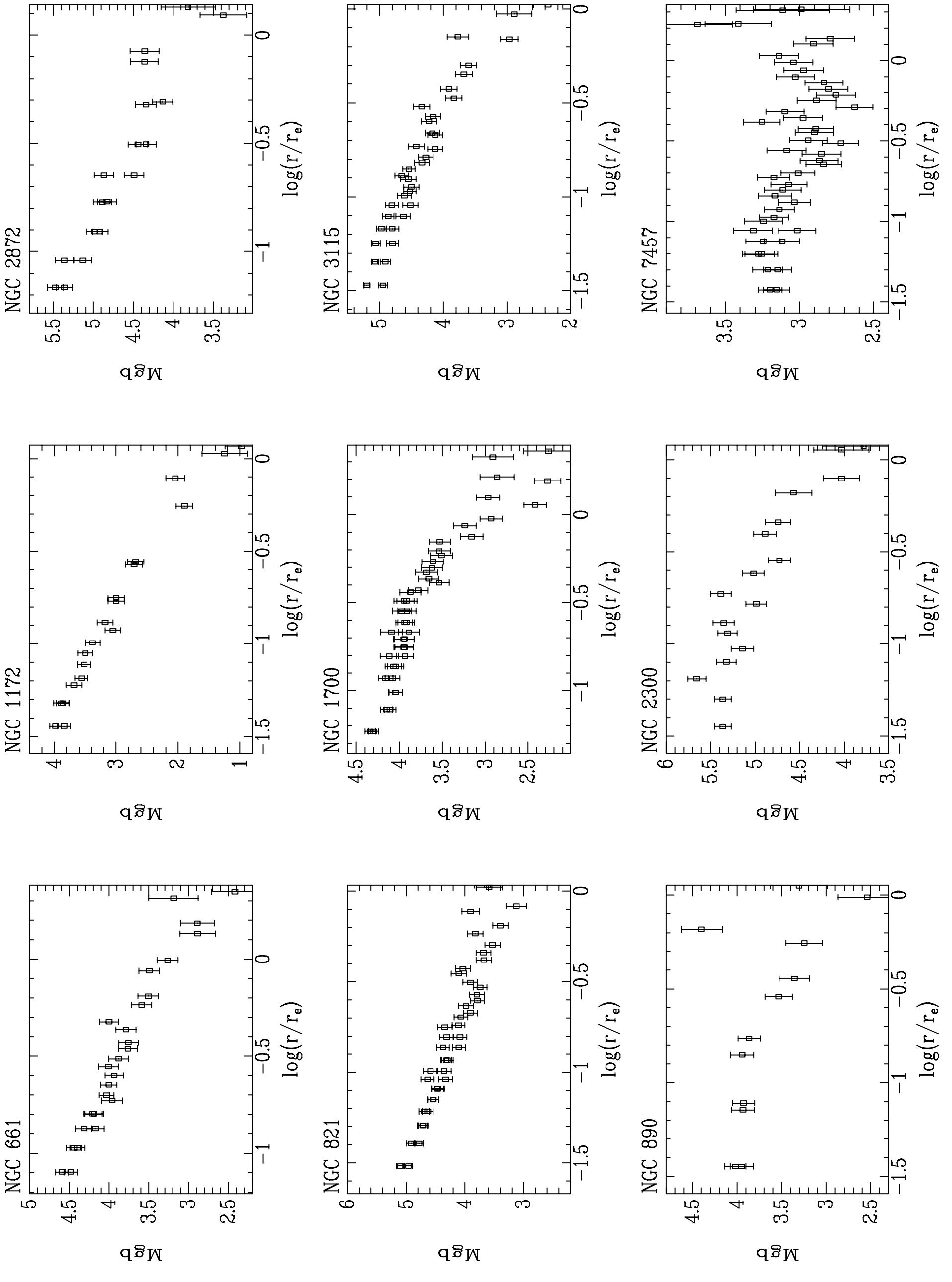

Figure A.13 Radial profiles of the Mg b index for all nine galaxies.

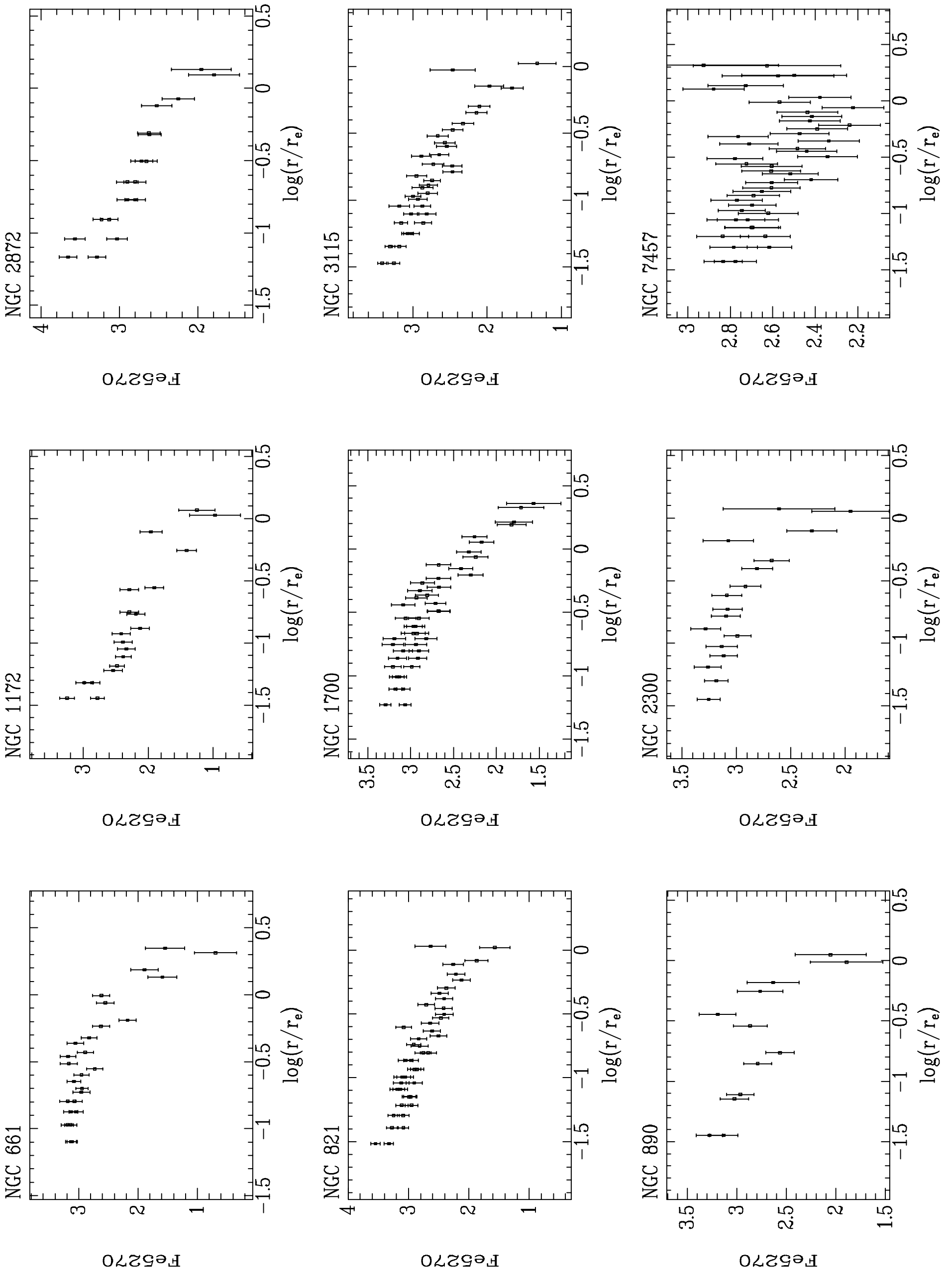

Figure A.14 Radial profiles of the Fe5270 line index for all nine galaxies.

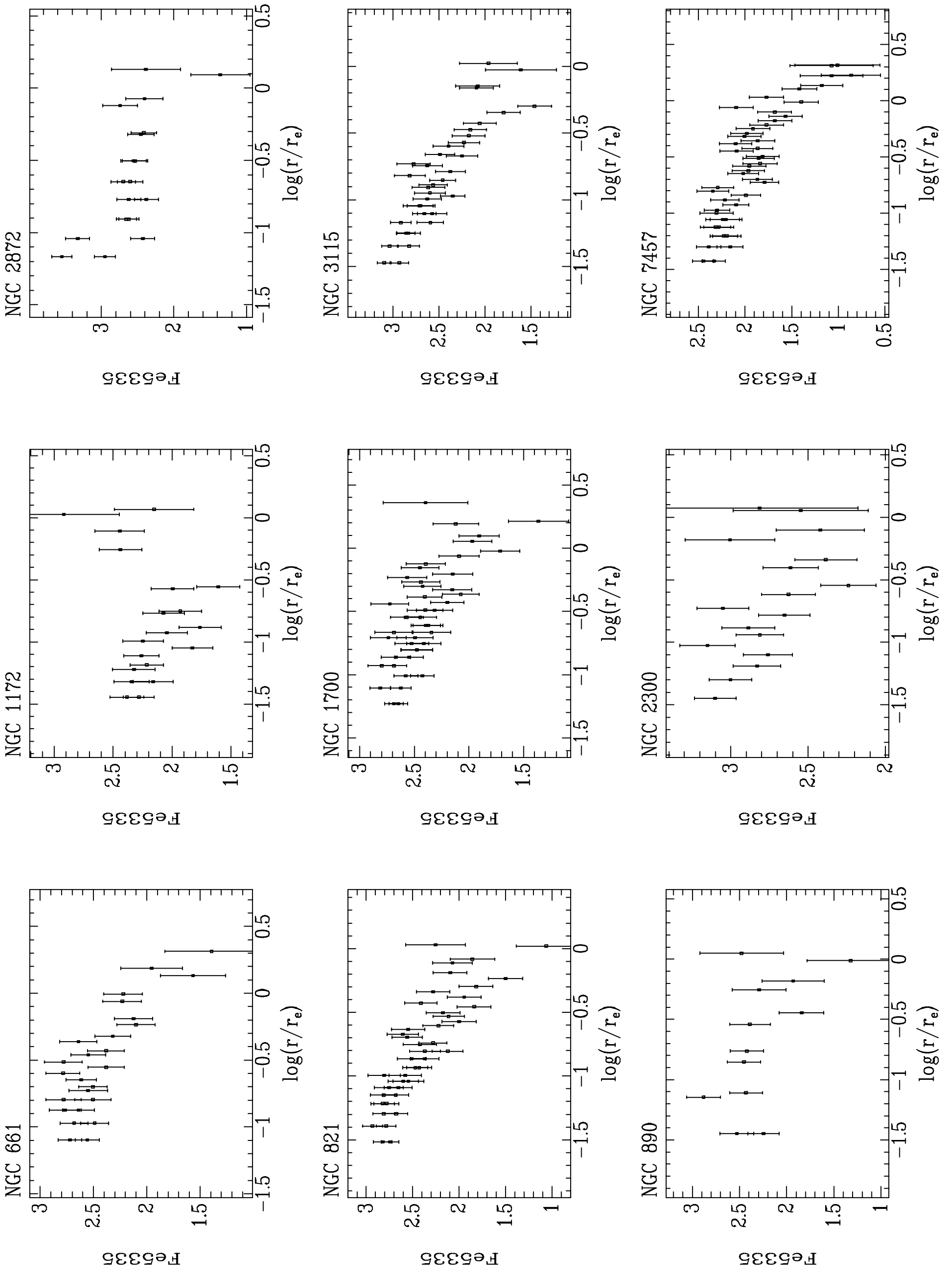

Figure A.15 Radial profiles of the Fe5335 line index for all nine galaxies.

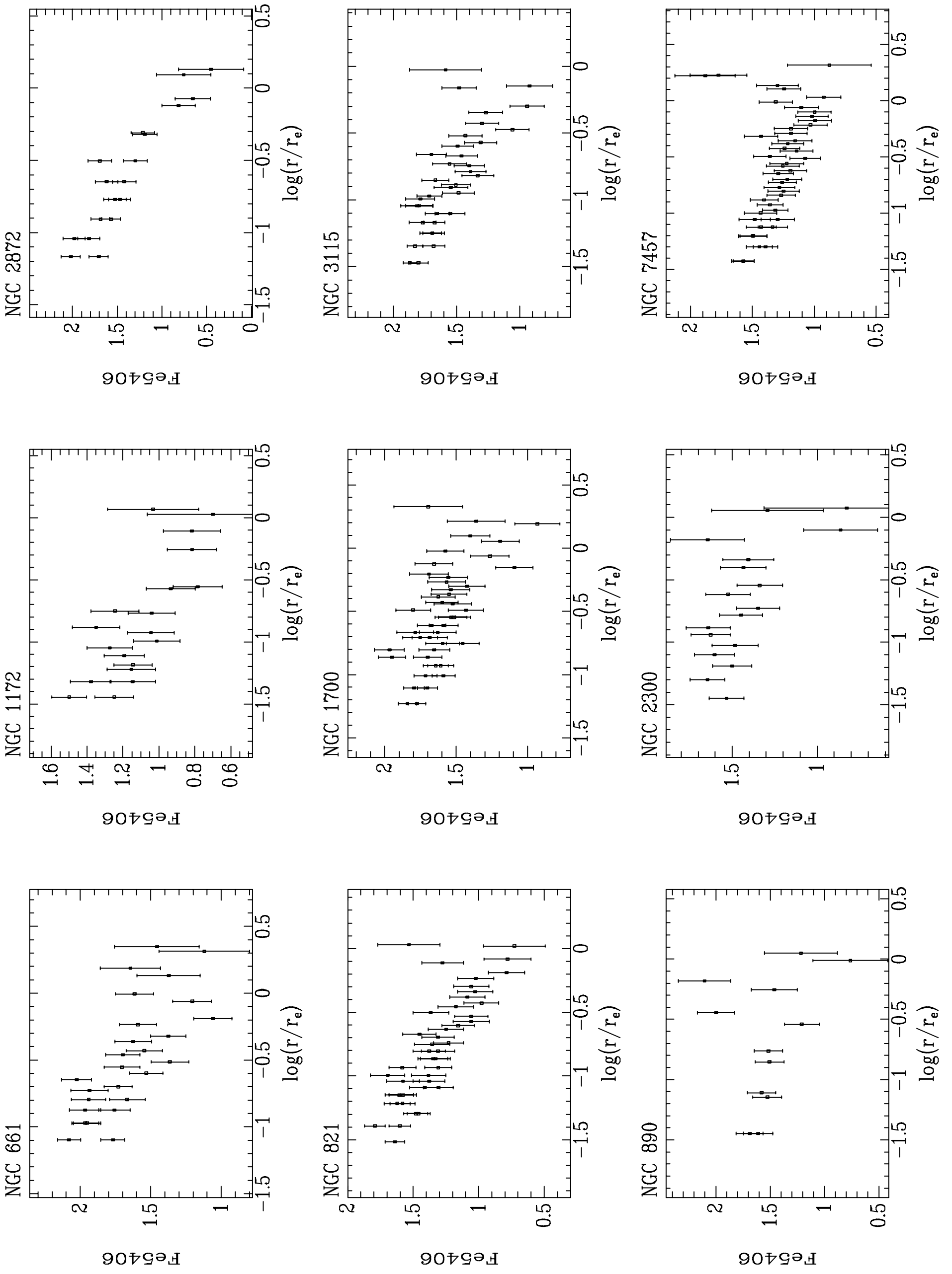

Figure A.16 Radial profiles of the Fe5406 line index for all nine galaxies.

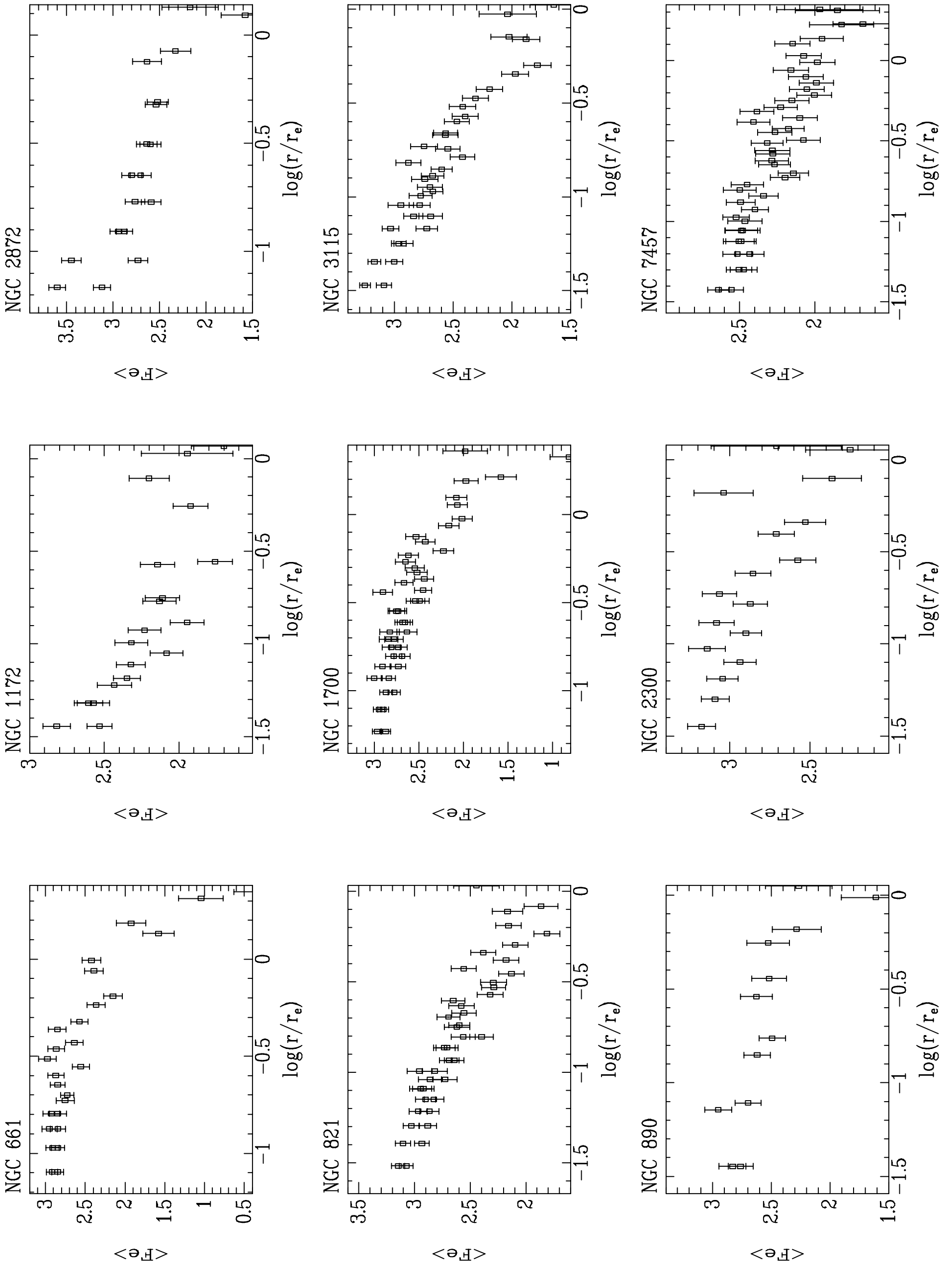

Figure A.17 Radial profiles of the <Fe>line index for all nine galaxies.

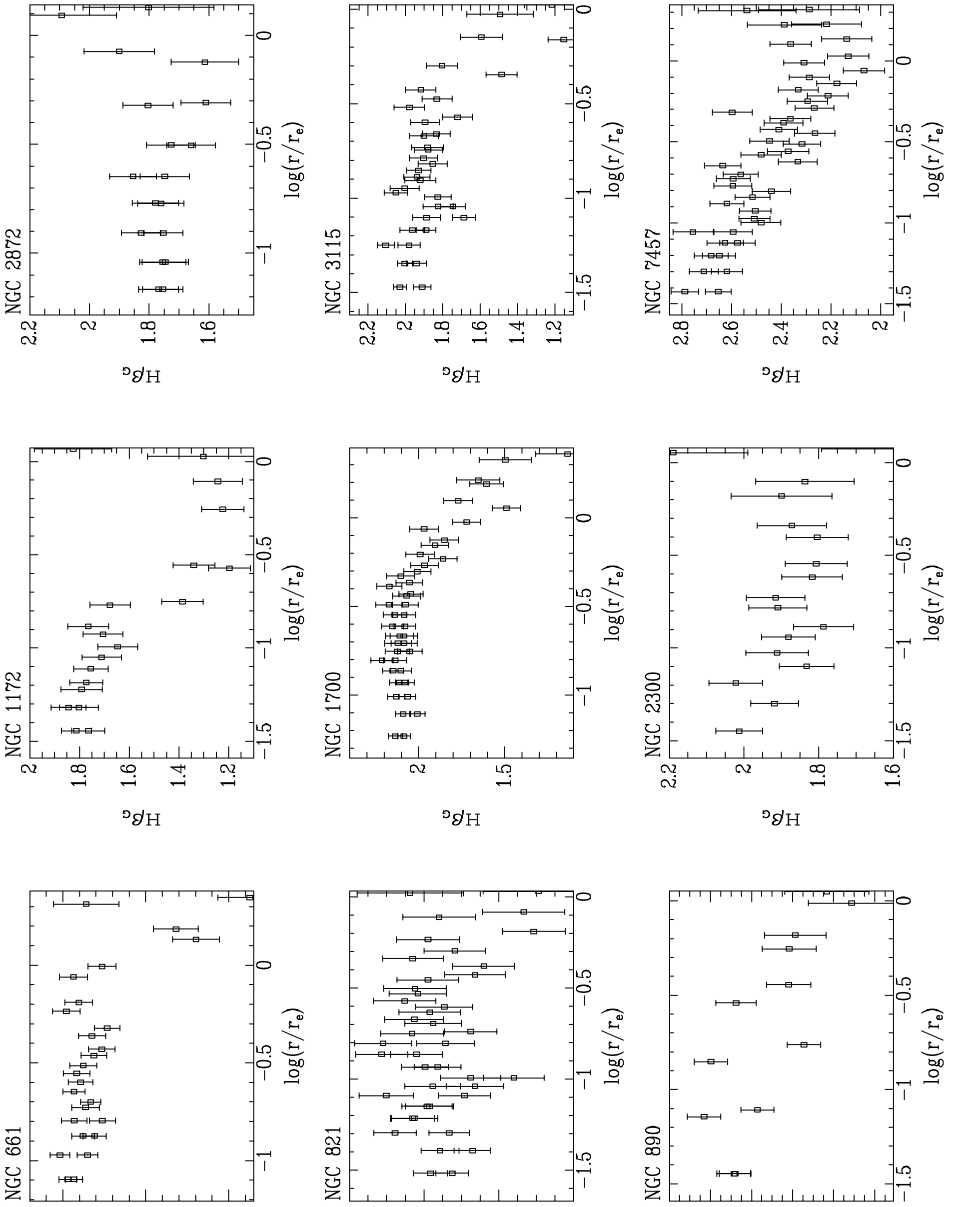

Figure A.18 Radial profiles of the Hβ_G index for all nine galaxies.

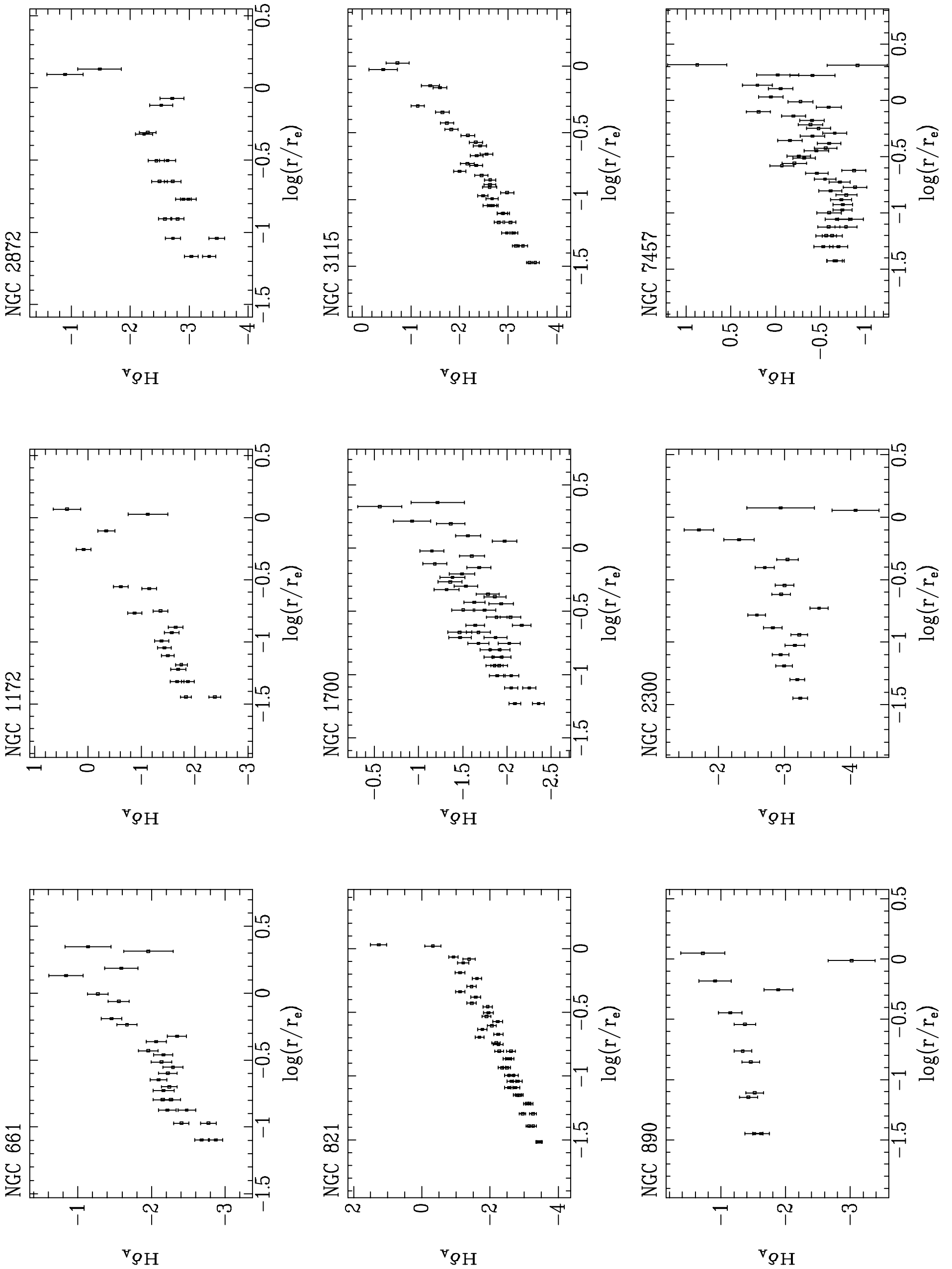

Figure A.19 Radial profiles of the Hδ_A index for all nine galaxies.

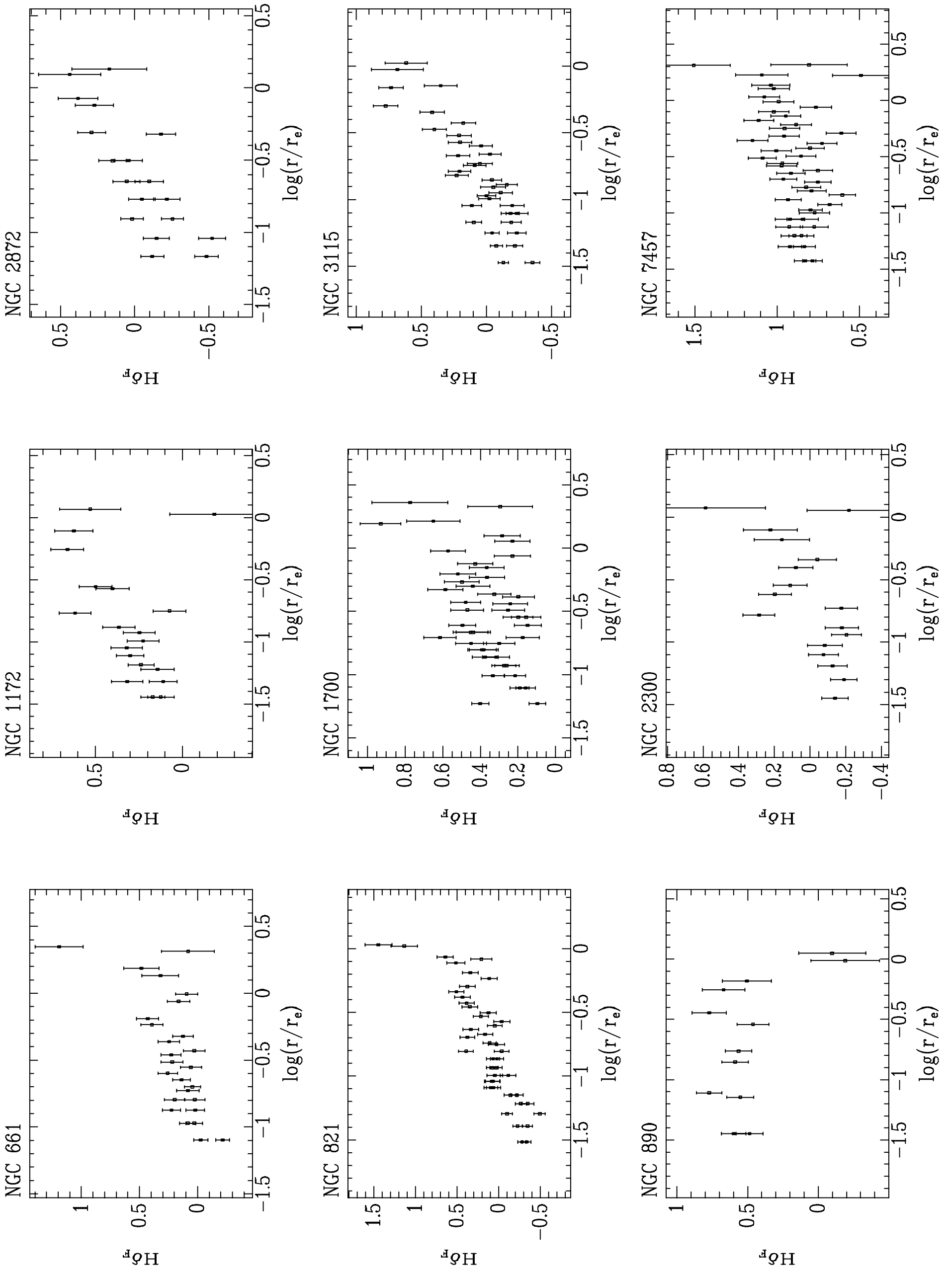

Figure A.20 Radial profiles of the Hδ_F index for all nine galaxies.

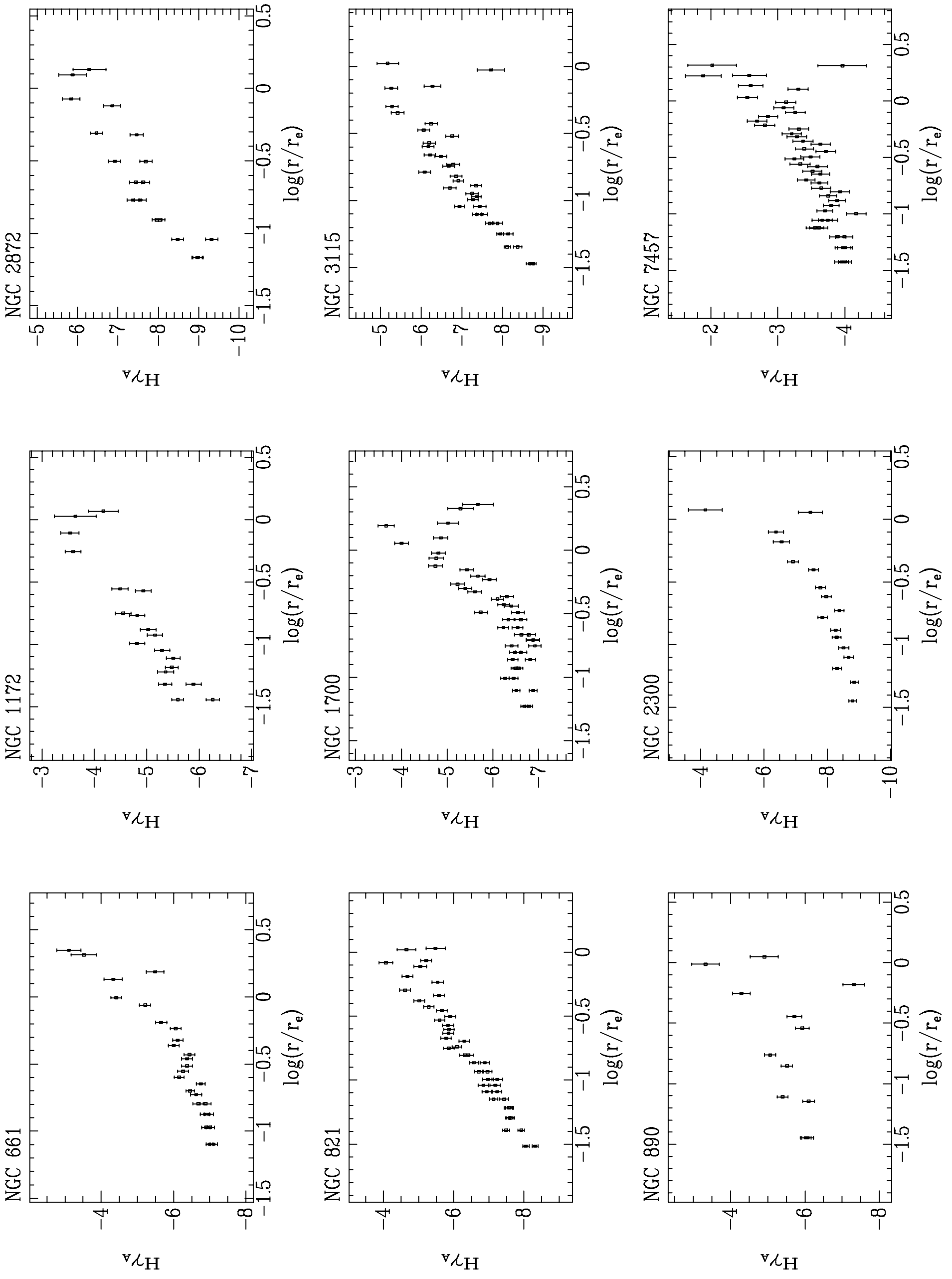

Figure A.21 Radial profiles of the Hγ_A index for all nine galaxies.

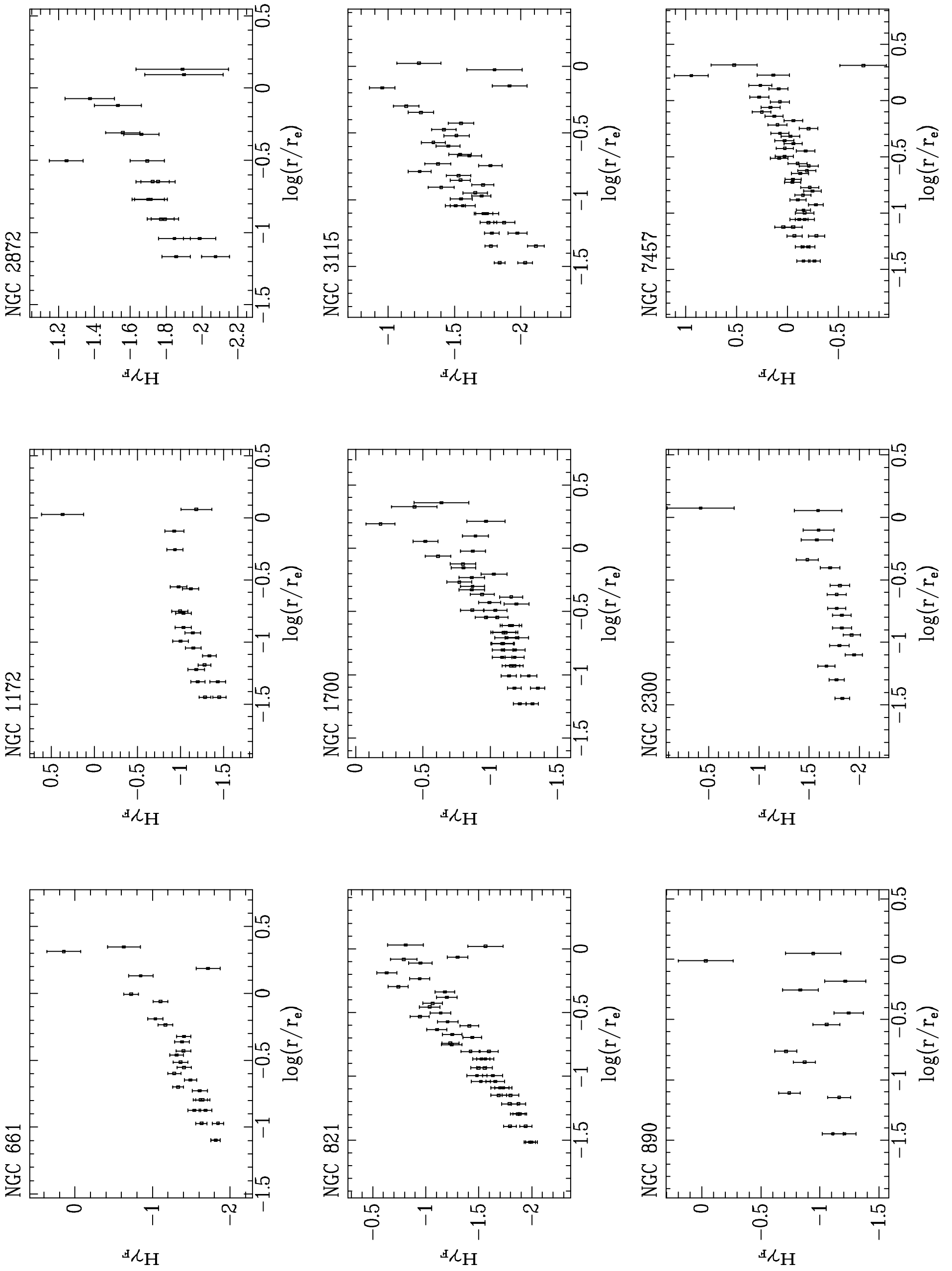

Figure A.22 Radial profiles of the Hγ$_F$ index for all nine galaxies.

Appendix B

Line Index Gradient Fits

TABLE B.1
NGC 661 LINE INDEX GRADIENT FITS[a]

Index	Δindex/Δlog(r/r$_e$)	zeropoint	χ^2	rms$_{\mathrm{fit}}$
CN1	-0.07±0.03	0.01±0.02	3.0	0.010
CN2	-0.07±0.03	0.05±0.02	2.8	0.009
Ca4227	-0.19±0.14	1.03±0.10	1.9	0.102
G4300	-0.73±0.18	4.92±0.13	2.1	0.191
Fe4383	-1.17±0.23	4.09±0.16	2.5	0.390
Ca4455	-0.41±0.17	1.30±0.12	0.9	0.100
Fe4531	-0.61±0.21	3.03±0.15	1.4	0.282
Fe4668	-3.71±0.27	4.50±0.19	2.2	0.519
Hβ	-0.01±0.17	1.44±0.12	1.7	0.258
Hβ_G	-0.08±0.18	1.82±0.13	1.1	0.073
Fe4930	-0.31±0.21	1.85±0.15	1.2	0.248
Fe5015	-1.43±0.25	2.75±0.17	2.3	0.602
Mg1	-0.05±0.03	0.09±0.02	1.0	0.003
Mg2	-0.08±0.03	0.24±0.02	1.7	0.005
MgB	-1.16±0.18	3.28±0.12	0.9	0.151
Fe5270	-0.98±0.19	2.29±0.13	3.5	0.352
Fe5335	-0.61±0.22	2.12±0.15	1.2	0.207
Fe5406	-0.52±0.18	1.39±0.13	2.1	0.184
<Fe>	-0.77±0.18	2.22±0.12	3.5	0.269
Hγ_A	2.08±0.20	-5.07±0.13	5.2	0.435
Hγ_F	0.77±0.15	-0.97±0.11	3.4	0.263
Hδ_A	1.05±0.19	-1.53±0.13	2.4	0.253
Hδ_F	0.27±0.16	0.29±0.11	1.9	0.124

[a] Coefficients for a linear fit to each index versus log(r/r$_e$). The fit was conducted over the radius range log(r/r$_e$) $\in \{-1.10, 0.35\}$ made up of 26 separate apertures.

TABLE B.2

NGC 821 LINE INDEX GRADIENT FITS[a]

Index	Δindex/Δlog(r/r_e)	zeropoint	χ^2	$\mathrm{rms}_{\mathrm{fit}}$
CN1	-0.09±0.02	-0.03±0.02	4.3	0.008
CN2	-0.10±0.02	0.01±0.02	4.1	0.008
Ca4227	-0.20±0.09	1.09±0.09	2.9	0.133
G4300	-0.73±0.12	4.70±0.12	3.0	0.237
Fe4383	-1.31±0.16	3.86±0.15	1.8	0.261
Ca4455	-0.32±0.11	1.33±0.11	1.7	0.128
Fe4531	-0.44±0.14	3.00±0.13	2.1	0.266
Fe4668	-3.51±0.18	3.13±0.17	1.3	0.322
Hβ	0.05±0.12	1.60±0.12	1.2	0.129
Hβ_G	-0.05±0.10	1.92±0.10	1.5	0.097
Fe4930	-0.44±0.15	1.52±0.14	1.3	0.200
Fe5015	-1.24±0.18	3.70±0.17	1.6	0.265
Mg1	-0.04±0.02	0.09±0.02	8.0	0.009
Mg2	-0.07±0.02	0.22±0.02	9.0	0.012
MgB	-1.05±0.12	3.37±0.12	1.5	0.155
Fe5270	-0.83±0.13	2.13±0.13	1.6	0.184
Fe5335	-0.76±0.15	1.79±0.14	1.3	0.213
Fe5406	-0.30±0.13	1.05±0.12	9.7	0.265
$<$Fe$>$	-0.79±0.12	1.96±0.11	1.8	0.173
Hγ_A	2.38±0.13	-4.52±0.13	3.6	0.304
Hγ_F	0.87±0.11	-0.71±0.11	1.6	0.109
Hδ_A	1.67±0.13	-0.94±0.12	2.0	0.194
Hδ_F	0.57±0.11	0.54±0.11	2.8	0.141

[a] Coefficients for a linear fit to each index versus log(r/r_e). The fit was conducted over the radius range log(r/r_e) $\in \{-1.51, 0.03\}$ made up of 43 separate apertures.

TABLE B.3
NGC 890 LINE INDEX GRADIENT FITS[a]

Index	Δindex/Δlog(r/r$_e$)	zeropoint	χ^2	rms$_{fit}$
CN1	-0.04±0.04	0.01±0.04	4.0	0.015
CN2	-0.05±0.04	0.05±0.04	4.3	0.015
Ca4227	0.05±0.19	1.12±0.18	2.4	0.151
G4300	-0.22±0.27	4.86±0.26	0.7	0.162
Fe4383	-0.33±0.31	4.31±0.29	2.6	0.529
Ca4455	-0.28±0.23	1.38±0.21	2.0	0.183
Fe4531	-0.37±0.31	3.07±0.30	1.1	0.211
Fe4668	-1.96±0.39	4.99±0.38	0.7	0.358
Hβ[b]	-0.38±0.24	1.47±0.22	1.6	0.159
$H\beta_G$[b]	-0.30±0.20	1.92±0.18	2.6	0.137
Fe4930	-0.26±0.29	1.76±0.28	1.0	0.279
Fe5015	-0.75±0.34	3.42±0.32	1.0	0.311
Mg1	-0.02±0.04	0.09±0.04	1.7	0.005
Mg2	-0.04±0.04	0.25±0.04	0.5	0.003
MgB	-0.55±0.28	3.28±0.28	0.9	0.122
Fe5270	-0.53±0.26	2.42±0.24	1.8	0.268
Fe5335	-0.26±0.31	2.16±0.30	1.5	0.244
Fe5406	-0.13±0.25	1.45±0.24	2.4	0.326
<Fe>	-0.35±0.25	2.34±0.24	0.7	0.097
$H\gamma_A$	0.68±0.27	-5.02±0.25	12.5	0.883
$H\gamma_F$	0.06±0.22	-0.95±0.22	3.8	0.188
$H\delta_A$	0.21±0.30	-1.24±0.30	1.4	0.233
$H\delta_F$	0.03±0.25	0.62±0.24	1.2	0.104

[a] Coefficients for a linear fit to each index versus log(r/r$_e$). The fit was conducted over the radius range log(r/r$_e$) $\in \{-1.45, 0.05\}$ made up of 12 separate apertures.

[b] This measurement is bad, due to an uncorrected cosmic ray in one of the continuum bandpasses, near the center of the galaxy.

TABLE B.4

NGC 1172 LINE INDEX GRADIENT FITS[a]

Index	Δindex/$\Delta\log(r/r_e)$			
CN1	-0.07±0.03	-0.06±0.04	5.4	0.008
CN2	-0.07±0.04	-0.02±0.04	3.4	0.008
Ca4227	-0.21±0.17	0.81±0.18	0.7	0.054
G4300	-0.80±0.20	4.38±0.20	3.1	0.248
Fe4383	-1.73±0.26	2.42±0.27	1.0	0.195
Ca4455	-0.25±0.18	1.10±0.18	1.3	0.139
Fe4531	-0.55±0.23	2.56±0.23	1.0	0.248
Fe4668	-2.81±0.29	1.12±0.30	0.3	0.154
Hβ[b]	-0.31±0.19	0.99±0.19	1.3	0.180
Hβ_G[b]	-0.50±0.17	1.15±0.17	1.7	0.105
Fe4930	-0.30±0.25	1.60±0.26	0.9	0.156
Fe5015	-1.56±0.29	2.02±0.30	2.4	0.354
Mg1	-0.04±0.03	0.03±0.03	1.4	0.003
Mg2	-0.10±0.03	0.10±0.03	4.7	0.010
Mgb	-1.44±0.25	1.89±0.27	0.4	0.069
Fe5270	-1.06±0.20	1.38±0.21	2.2	0.212
Fe5335	-0.01±0.23	2.15±0.23	2.0	0.287
Fe5406	-0.38±0.20	0.78±0.20	1.1	0.133
$<$Fe$>$	-0.54±0.18	1.76±0.18	2.4	0.169
Hγ_A[b]	1.54±0.21	-3.62±0.21	3.5	0.279
Hγ_F[b]	0.36±0.19	-0.81±0.20	1.2	0.089
Hδ_A[b]	1.43±0.23	-0.01±0.24	3.6	0.234
Hδ_F[b]	0.36±0.17	0.67±0.18	0.9	0.090

[a] Coefficients for a linear fit to each index versus log(r/r$_e$). The fit was conducted over the radius range log(r/r$_e$) $\in \{-1.45, 0.07\}$ made up of 19 separate apertures.

[b] This galaxy clearly shows emission at $\lambda = 5007$Å. This suggests that the Balmer line strengths and gradients will all be contaminated by emission, less so for the higher order lines.

TABLE B.5

NGC 1700 LINE INDEX GRADIENT FITS[a]

Index	Δindex/$\Delta\log(r/r_e)$	zeropoint	χ^2	$\mathrm{rms}_{\mathrm{fit}}$
CN1	-0.05±0.02	0.02±0.02	5.8	0.009
CN2	-0.06±0.02	0.06±0.02	5.4	0.008
Ca4227	-0.06±0.09	1.05±0.07	2.2	0.105
G4300	-0.32±0.13	4.93±0.09	4.0	0.325
Fe4383	-0.92±0.16	4.30±0.11	3.3	0.427
Ca4455	-0.19±0.11	1.43±0.08	1.7	0.144
Fe4531	-0.39±0.14	3.21±0.11	1.5	0.243
Fe4668	-2.53±0.19	5.24±0.14	1.9	0.354
$\mathrm{H}\beta$	-0.21±0.12	1.50±0.09	1.6	0.159
$\mathrm{H}\beta_{\mathrm{G}}$	-0.31±0.10	1.84±0.07	2.9	0.144
Fe4930	-0.26±0.15	1.76±0.11	1.3	0.187
Fe5015	-1.12±0.17	3.18±0.13	2.1	0.352
Mg1	-0.02±0.02	0.11±0.01	6.5	0.008
Mg2	-0.05±0.02	0.25±0.02	2.4	0.007
MgB	-1.04±0.12	3.16±0.09	3.3	0.221
Fe5270	-0.81±0.13	2.35±0.10	2.2	0.198
Fe5335	-0.63±0.15	2.03±0.11	2.2	0.358
Fe5406	-0.38±0.13	1.37±0.09	1.9	0.226
$<$Fe$>$	-0.72±0.12	2.19±0.09	2.9	0.230
$\mathrm{H}\gamma_A$	1.52±0.13	-5.21±0.10	11.2	0.474
$\mathrm{H}\gamma_F$	0.46±0.11	-0.76±0.08	2.1	0.131
$\mathrm{H}\delta_A$	0.63±0.13	-1.38±0.09	3.1	0.228
$\mathrm{H}\delta_F$	0.19±0.11	0.46±0.08	3.2	0.152

[a] Coefficients for a linear fit to each index versus $\log(r/r_e)$. The fit was conducted over the radius range $\log(r/r_e) \in \{-1.23, 0.36\}$ made up of 43 separate apertures.

TABLE B.6
NGC 2300 LINE INDEX GRADIENT FITS[a]

Index	Δindex/Δlog(r/r$_e$)	zeropoint	χ^2	rms$_{\rm fit}$
CN1	-0.04±0.04	0.08±0.03	2.4	0.007
CN2	-0.05±0.04	0.12±0.04	3.5	0.011
Ca4227	-0.01±0.16	1.38±0.15	3.6	0.160
G4300	-0.12±0.24	5.33±0.22	1.3	0.154
Fe4383	-0.24±0.28	5.28±0.26	1.4	0.281
Ca4455	-0.15±0.21	1.67±0.20	0.9	0.096
Fe4531	-0.42±0.26	3.34±0.24	0.5	0.139
Fe4668	-2.20±0.34	5.71±0.31	2.4	0.457
Hβ	-0.09±0.22	1.40±0.20	0.4	0.079
Hβ_G	-0.11±0.19	1.79±0.18	0.6	0.058
Fe4930	-0.04±0.26	1.99±0.23	1.1	0.204
Fe5015	-0.98±0.31	4.39±0.28	1.4	0.343
Mg1	-0.01±0.03	0.14±0.03	2.2	0.006
Mg2	-0.04±0.04	0.30±0.03	4.2	0.012
MgB	-0.90±0.21	4.35±0.19	2.9	0.236
Fe5270	-0.54±0.23	2.58±0.21	1.1	0.214
Fe5335	-0.38±0.25	2.48±0.23	1.2	0.222
Fe5406	-0.14±0.25	1.39±0.23	0.5	0.100
$<$Fe$>$	-0.46±0.20	2.53±0.18	1.4	0.172
Hγ_A	1.54±0.25	-6.80±0.23	3.2	0.343
Hγ_F	0.18±0.20	-1.62±0.18	1.1	0.092
Hδ_A	0.54±0.24	-2.51±0.22	4.3	0.341
Hδ_F	0.25±0.19	0.18±0.17	2.1	0.179

[a] Coefficients for a linear fit to each index versus log(r/r$_e$). The fit was conducted over the radius range log(r/r$_e$) $\in \{-1.45, 0.07\}$ made up of 17 separate apertures.

TABLE B.7

NGC 2872 LINE INDEX GRADIENT FITS[a]

Index	Δindex/Δlog(r/r_e)	zeropoint	χ^2	$\mathrm{rms_{fit}}$
CN1	-0.08±0.04	0.03±0.03	2.5	0.007
CN2	-0.09±0.04	0.07±0.03	3.3	0.008
Ca4227	-0.06±0.19	1.31±0.15	5.4	0.247
G4300	-0.15±0.24	5.40±0.18	1.6	0.167
Fe4383	-0.65±0.30	4.68±0.23	2.1	0.276
Ca4455	-0.21±0.22	1.48±0.17	1.8	0.136
Fe4531	-0.35±0.29	3.30±0.23	1.2	0.168
Fe4668	-1.81±0.35	5.99±0.27	1.2	0.347
Hβ	0.20±0.23	1.52±0.18	1.8	0.199
Hβ_G	-0.03±0.20	1.73±0.16	0.7	0.074
Fe4930	-0.34±0.28	1.51±0.22	1.4	0.200
Fe5015	-0.54±0.32	3.86±0.25	0.6	0.210
Mg1	-0.04±0.04	0.11±0.03	0.7	0.003
Mg2	-0.09±0.04	0.26±0.03	1.2	0.004
MgB	-1.25±0.23	3.90±0.18	1.5	0.184
Fe5270	-1.08±0.25	2.17±0.19	1.3	0.156
Fe5335	-0.70±0.28	2.18±0.21	2.9	0.318
Fe5406	-0.96±0.24	0.83±0.19	1.4	0.157
$<$Fe$>$	-0.89±0.22	2.18±0.17	3.9	0.228
Hγ_A	2.34±0.26	-6.10±0.20	6.2	0.384
Hγ_F	0.33±0.20	-1.51±0.16	2.4	0.188
Hδ_A	1.02±0.25	-1.99±0.19	3.8	0.356
Hδ_F	0.54±0.20	0.31±0.16	3.0	0.153

[a] Coefficients for a linear fit to each index versus log(r/r_e). The fit was conducted over the radius range log(r/r_e) $\in \{-1.17, 0.13\}$ made up of 18 separate apertures.

TABLE B.8

NGC 3115 LINE INDEX GRADIENT FITS[a]

Index	Δindex/$\Delta\log(r/r_e)$	zeropoint	χ^2	rms_{fit}
CN1	-0.09±0.03	-0.02±0.03	3.0	0.005
CN2	-0.10±0.03	0.01±0.03	3.7	0.006
Ca4227	-0.38±0.11	0.94±0.11	2.3	0.102
G4300	-0.42±0.14	5.01±0.14	1.9	0.183
Fe4383	-1.51±0.18	3.54±0.18	2.7	0.431
Ca4455	-0.35±0.13	1.23±0.13	1.5	0.144
Fe4531	-0.86±0.17	2.59±0.17	1.7	0.256
Fe4668	-3.54±0.22	3.20±0.21	2.3	0.342
Hβ[b]	-0.29±0.14	1.14±0.14	2.1	0.170
$H\beta_G$[b]	-0.32±0.11	1.57±0.11	3.9	0.149
Fe4930	-0.41±0.17	1.26±0.17	1.3	0.257
Fe5015	-1.71±0.20	3.66±0.19	2.2	0.431
Mg1	-0.03±0.02	0.10±0.02	4.7	0.006
Mg2	-0.07±0.02	0.22±0.02	8.5	0.014
MgB	-1.38±0.14	3.21±0.14	2.9	0.226
Fe5270	-1.01±0.15	1.88±0.15	1.6	0.194
Fe5335	-0.87±0.17	1.76±0.17	1.2	0.177
Fe5406	-0.50±0.15	1.12±0.15	1.4	0.160
<Fe>	-0.94±0.13	1.82±0.13	1.6	0.127
$H\gamma_A$	2.45±0.16	-4.88±0.16	4.7	0.312
$H\gamma_F$	0.59±0.13	-1.07±0.13	3.0	0.137
$H\delta_A$	1.61±0.15	-1.10±0.15	2.5	0.227
$H\delta_F$	0.58±0.12	0.57±0.12	3.5	0.140

[a] Coefficients for a linear fit to each index versus $\log(r/r_e)$. The fit was conducted over the radius range $\log(r/r_e) \in \{-1.47, 0.02\}$ made up of 35 separate apertures.

[b] There are hints of emission at both $\lambda = 5007$Å and at the Hβ line. Proper characterization of the emission will require subtraction of a stellar population template.

TABLE B.9

NGC 7457 LINE INDEX GRADIENT FITS[a]

Index	Δindex/$\Delta\log(r/r_e)$	zeropoint	χ^2	rms_{fit}
CN1	-0.02±0.02	-0.04±0.02	2.8	0.007
CN2	-0.03±0.02	-0.01±0.02	3.3	0.007
Ca4227	0.05±0.08	1.08±0.07	1.3	0.116
G4300	-0.40±0.11	4.32±0.09	2.9	0.269
Fe4383	-0.89±0.14	3.52±0.11	1.2	0.266
Ca4455	-0.15±0.10	1.25±0.08	0.9	0.096
Fe4531	-0.25±0.13	2.95±0.10	1.2	0.219
Fe4668	-1.47±0.17	3.34±0.13	1.1	0.353
Hβ	-0.26±0.11	1.95±0.09	1.1	0.137
$H\beta_G$	-0.32±0.09	2.26±0.07	1.5	0.111
Fe4930	-0.26±0.13	1.59±0.11	0.9	0.226
Fe5015	-0.79±0.15	4.06±0.12	1.9	0.415
Mg1	0.00±0.02	0.06±0.01	4.5	0.007
Mg2	-0.00±0.02	0.19±0.01	8.1	0.014
MgB	-0.22±0.12	2.89±0.09	1.1	0.138
Fe5270	-0.18±0.12	2.50±0.09	1.1	0.159
Fe5335	-0.62±0.13	1.58±0.10	1.0	0.199
Fe5406	-0.21±0.11	1.16±0.09	1.1	0.188
<Fe>	-0.40±0.10	2.04±0.08	0.7	0.098
$H\gamma_A$	0.80±0.12	-2.97±0.09	2.7	0.324
$H\gamma_F$	0.23±0.10	0.09±0.08	1.5	0.103
$H\delta_A$	0.40±0.11	-0.23±0.09	2.7	0.274
$H\delta_F$	0.12±0.10	0.96±0.08	1.9	0.116

[a] Coefficients for a linear fit to each index versus $\log(r/r_e)$. The fit was conducted over the radius range $\log(r/r_e) \in \{-1.43, 0.32\}$ made up of 45 separate apertures.

Bibliography

Bell, E. F., Barnaby, D., Bower, R. G., de Jong, R. S., Harper, D. A., Hereld, M., Loewenstein, R. F., & Rauscher, B. J. 2000, MNRAS, 312, 470

Bell, E. F. & de Jong, R. S. 2000, MNRAS, 312, 497

Bender, R., Burstein, D., & Faber, S. M. 1993, ApJ, 411, 153

Bender, R., Saglia, R. P., & Gerhard, O. E. 1994, MNRAS, 269, 785

Bertin, E. & Arnouts, S. 1996, A&AS, 117, 393

Bruzual A., G. & Charlot, S. 1993, ApJ, 405, 538

Burkholder, V., Impey, C., & Sprayberry, D. 2001, AJ, 122, 2318

Burstein, D. & Heiles, C. 1982, AJ, 87, 1165

Cardelli, J. A., Clayton, G. C., & Mathis, J. S. 1989, ApJ, 345, 245

Carollo, C. M. & Danziger, I. J. 1994, MNRAS, 270, 523

Chromey, F. R. & Hasselbacher, D. A. 1996, PASP, 108, 944

Chung, A., van Gorkom, J. H., O’Neil, K., & Bothun, G. 2002, AJ, 123, 2387

Claver, C. F. 1995, Ph.D. Thesis, University of Texas, Austin

Colbert, J. W., Mulchaey, J. S., & Zabludoff, A. I. 2001, AJ, 121, 808

Cross, N. & Driver, S. P. 2002, MNRAS, 329, 579

Dalcanton, J. J., Spergel, D. N., Gunn, J. E., Schmidt, M., & Schneider, D. P. 1997, AJ, 114, 635

Davies, R. L., Burstein, D., Dressler, A., Faber, S. M., Lynden-Bell, D., Terlevich, R. J., & Wegner, G. 1987, ApJS, 64, 581.

Davies, R. L., Sadler, E. M., & Peletier, R. F. 1993, MNRAS, 262, 650.

de Blok, W. J. G. 1997, Ph.D. Thesis, Rijksuniversiteit Groningen

de Blok, W. J. G. & McGaugh, S. S. 1997, MNRAS, 290, 533

de Blok, W. J. G., McGaugh, S. S., & van der Hulst, J. M. 1996, MNRAS, 283, 18

de Blok, W. J. G. & van der Hulst, J. M. 1998, A&A, 335, 421

de Blok, W. J. G., van der Hulst, J. M., & Bothun, G. D. 1995, MNRAS, 274, 235

de Jong, R. S. & Lacey, C. 2000, ApJ, 545, 781

de Vaucouleurs, G., de Vaucouleurs, A., Corwin, H. G., Buta, R. J., Paturel, G., & Fouque, P. 1991, “Third Reference Catalog of Bright Galaxies (RC3)” (Springer-Verlag: New York)

Denicoló, G., Terlevich, R., & Terlevich, E. 2002, MNRAS, 330, 69.

Djorgovski, S. & Davis, M. 1987, ApJ, 313, 59

Dressler, A. 1980, ApJ, 236, 351

Falco, E. E. et al. 1999, PASP, 111, 438 (UZC)

Freeman, K. C. 1970, ApJ, 160, 811

Frei, Z. & Gunn, J. E. 1994, AJ, 108, 1476

Fukugita, M., Shimasaku, K., & Ichikawa, T. 1995, PASP, 107, 945.

Gebhardt, K. et al. 2000, AJ, 119, 1157

Gerritsen, J. P. E. & de Blok, W. J. G. 1999, A&A, 342, 655

Gonzalez, J.J. 1993, Ph.D. thesis, Univ. California, Santa Cruz

Goudfrooij, P. & Emsellem, E. 1996, A&A, 306, L45

Hill, G. J., Nicklas, H. E., MacQueen, P. J., Tejada, C., Cobos Duenas, F. J., & Mitsch, W. 1998, Proc. SPIE, 3355, 375.

Impey, C., Burkholder, V., & Sprayberry, D. 2001, AJ, 122, 2341

Impey, C. D., Sprayberry, D., Irwin, M. J., & Bothun, G. D. 1996, ApJS, 105, 209

Jansen, R. A., Fabricant, D., Franx, M., & Caldwell, N. 2000, ApJS, 126, 331

Jones, L. A. 1998, Ph.D. Thesis, Univ. of North Carolina, Chapel Hill

Jones, L. A. & Worthey, G. 1995, ApJ, 446, L31

Jørgensen, I. 1997, MNRAS, 288, 161.

Jørgensen, I. 1999, MNRAS, 306, 607

Jørgensen, I., Franx, M., Hjorth, J., & van Dokkum, P. G. 1999, MNRAS, 308, 833

Jørgensen, I., Franx, M., & Kjaergaard, P. 1996, MNRAS, 280, 167

Kaldare, R., Colless, M. M., Raychauddhury, S., Peterson, B. A., 2002, MNRAS-submitted, astro-ph/0109415

Kauffmann, G. 1996, MNRAS, 281, 487

Kennicutt, R. C. 1992, ApJ, 388, 310.

Kennicutt, R. C. 1998, ARA&A, 36, 189

Kennicutt, R. C., Tamblyn, P., & Congdon, C. E. 1994, ApJ, 435, 22

Kewley, L. J. & Dopita, M. A. 2002, ApJsubmitted

Kewley, L. J., Dopita, M. A., Sutherland, R. S., Heisler, C. A., & Trevena, J. 2001a, ApJ, 556, 121

Kewley, L. J., Heisler, C. A., Dopita, M. A., & Lumsden, S. 2001b, ApJS, 132, 37

Kilborn, V. A. et al. 2000, AJ, 120, 1342

Kobulnicky, H. A., Kennicutt, R. C., & Pizagno, J. L. 1999, ApJ, 514, 544

Kobulnicky, H. A. & Skillman, E. D. 1997, ApJ, 489, 636

Kuntschner, H. & Davies, R. L. 1998, MNRAS, 295, L29

Kuntschner, H., Lucey, J. R., Smith, R. J., Hudson, M. J., & Davies, R. L. 2001, MNRAS, 323, 615.

Kuntschner, H., Smith, R. J., Colless, M., Davies, R. L., Kaldare, R., & Vazdekis,

A. 2002, 29 pages, 19 figures, Latex, MNRAS accepted., astro-ph/0207504

Landolt, A. U. 1992, AJ, 104, 340

Leitherer, C. et al. 1999, ApJS, 123, 3

Maraston, C. 1998, MNRAS, 300, 872

Maraston, C. & Thomas, D. 2000, ApJ, 541, 126

Matthews, L. D. & Gao, Y. 2001, ApJ, 549, L191

McGaugh, S. S. 1991, ApJ, 380, 140

McGaugh, S. S. 1994, ApJ, 426, 135

McGaugh, S. S., Bothun, G. D., & Schombert, J. M. 1995, AJ, 110, 573

McGaugh, S. S., Rubin, V. C., & de Blok, W. J. G. 2001, AJ, 122, 2381

Monet, D., et al. 1998, The USNO-SA2.0 Catalog (Washington: US Naval Obs.)

Nilson, P. 1973, Acta Universitatis Upsaliensis. Nova Acta Regiae Societatis Scientiarum Upsaliensis - Uppsala Astronomiska Observatoriums Annaler, Uppsala: Astronomiska Observatorium, 1973 (UGC)

O'connell, R. W. 1976, ApJ, 206, 370.

O'Neil, K. & Bothun, G. D., ApJ, 529, 811

O'Neil, K., Bothun, G. D., & Cornell, M. E. 1997, AJ, 113, 1212 (OBC97)

O'Neil, K., Bothun, G. D., & Schombert, J. 2000a, AJ, 119, 136

O'Neil, K., Bothun, G. D., Schombert, J., Cornell, M. E., & Impey, C. D. 1997, AJ, 114, 2448 (OBSCI97)

O'Neil, K., Hofner, P., & Schinnerer, E. 2000b, ApJ, 545, L99

Osterbrock, D. E. 1989, Astrophysics of Gaseous Nebulae and Active Galactic Nuclei (Mill Valley: University Science Books)

Pagel, B. E. J., Edmunds, M. G., Blackwell, D. E., Chun, M. S., & Smith, G. 1979, MNRAS, 189, 95

Peterson, B. M. 1997, An Introduction to Active Galactic Nuclei (Cambridge: Cambridge University Press)

Pierce, M. J. & Tully, R. B. 1988, ApJ, 330, 579

Ramsey, L. W. et al. 1998, Proc. SPIE, 3352, 34

Renzini, A. & Buzzoni, A. 1986, ASSL Vol. 122: Spectral Evolution of Galaxies, 195

Rix, H., de Zeeuw, P. T., Cretton, N., van der Marel, R. P., & Carollo, C. M. 1997, ApJ, 488, 702

Rönnback, J. & Bergvall, N. 1995, A&A, 302, 353

Rose, J. A. 1994, AJ, 107, 206.

Ryder, S. D. et al. 2001, ApJ, 555, 232

Saha, P. & Williams, T. B. 1994, AJ, 107, 1295

Salpeter, E. E. 1955, ApJ, 121, 161.

Scalo, J. M. 1986, Fundamentals of Cosmic Physics, 11, 1

Schombert, J. M. & Bothun, G. D. 1988, AJ, 95, 1389

Schombert, J. M., Bothun, G. D., Schneider, S. E., & McGaugh, S. S. 1992, AJ, 103, 1107

Schlegel, D. J., Finkbeiner, D. P., & Davis, M. 1998, ApJ, 500, 525

Sparks, W. B. 1988, AJ, 95, 1569

Sprayberry, D., Impey, C. D., Bothun, G. D., & Irwin, M. J. 1995, AJ, 109, 558

Stasińska, G. & Sodré, L. 2001, A&A, 374, 919

Statler, T. S., Dejonghe, H., & Smecker-Hane, T. 1999, AJ, 117, 126

Storchi-Bergmann, T., Calzetti, D., & Kinney, A. L. 1994, ApJ, 429, 572

Surma, P. & Bender, R. 1995, A&A, 298, 405

Thomas, D., Maraston, C., & Bender, R. 2002, astro-ph/0209250

Trager, S. C., Worthey, G., Faber, S. M., Burstein, D., & Gonzalez, J. J. 1998, ApJS, 116, 1

Trager, S. C., Faber, S. M., Worthey, G., & González, J. J. ;. 2000, AJ, 119, 1645

Tripicco, M. J. & Bell, R. A. 1995, AJ, 110, 3035

Tully, R. B. & Fisher, J. R. 1977, A&A, 54, 661 van Zee, L., Salzer, J. J., Haynes, M. P., O'Donoghue, A. A., & Balonek, T. J. 1998, AJ, 116, 2805

van den Hoek, L. B., de Blok, W. J. G., van der Hulst, J. M., & de Jong, T. 2000, A&A, 357, 397.

van der Marel, R. P. & Franx, M. 1993, ApJ, 407, 525

Vazdekis, A., Casuso, E., Peletier, R. F., & Beckman, J. E. 1996, ApJS, 106, 307

Vazdekis, A. 1999, ApJ, 513, 224 (V1999)

Vazdekis, A. 2000, `http://www.iac.es/galeria/vazdekis/MODELS_2000/out_li_BI` (V2000)

Veilleux, S. & Osterbrock, D. E. 1987, ApJS, 63, 295

Worthey, G. 1994, ApJS, 95, 107.

Worthey, G. 1998, PASP, 110, 888.

Worthey, G., Faber, S. M., Gonzalez, J. J., & Burstein, D. 1994, ApJS, 94, 687

Worthey, G. & Ottaviani, D. L. 1997, ApJS, 111, 377

Zabludoff, A. I. & Mulchaey, J. S. 2000, ApJ, 539, 136

Ziegler, B. L. & Bender, R. 1997, MNRAS, 291, 527

Vita

Marcel Peter Bergmann was born in Allentown, Pennsylvania on September 7, 1973, briefly after receiving a swift kick to the head from his twin sister Gabrielle. Despite the resulting slightly eggshaped cranium, his parents Marianne and Ernest, and his older sister Dominique, loved and raised him well. He graduated from Liberty High School, Bethlehem, Pennsylvania, in 1991, and proceeded to college at the California Institute of Technology (where he met many other eggheads). He delayed graduation for a year, travelling to such exotic locales as Lijiang, Upstream Bravo Camp, Kennesaw, and the intersection of CA routes 62 & 177, before finally finishing his Bachelor of Science in June, 1996. He entered The Graduate School at the University of Texas at Austin in September, 1996.

Permanent address: 730 Seneca St.
Bethlehem, Pennsylvania 18015

This dissertation was typeset with LaTeX[†] by the author.

[†] LaTeX is a document preparation system developed by Leslie Lamport as a special version of Donald Knuth's TeX Program.